

THE LOOKING-GLASS AND BEYOND:
USING OBSERVATIONS AND MODELING OF STELLAR ACTINIDE
ABUNDANCES AS A WINDOW INTO *R*-PROCESS EVENTS

A Dissertation

Submitted to the Graduate School
of the University of Notre Dame
in Partial Fulfillment of the Requirements
for the Degree of

Doctor of Philosophy

by
Erika M. Holmbeck

Rebecca Surman, Co-Director

Timothy Beers, Co-Director

Graduate Program in Physics

Notre Dame, Indiana

July 2020

© Copyright by
Erika M. Holmbeck
2020
All Rights Reserved

THE LOOKING-GLASS AND BEYOND:
USING OBSERVATIONS AND MODELING OF STELLAR ACTINIDE
ABUNDANCES AS A WINDOW INTO *R*-PROCESS EVENTS

Abstract

by

Erika M. Holmbeck

Nucleosynthesis by rapid neutron capture—the *r*-process—accounts for the production of roughly half of the heavy elements in the Solar System. Not only are these heavy elements found locally, but they are also found in very old, chemically simple stars, providing evidence that this process must occur astrophysically. Yet the exact environment that made the heavy elements is unknown. Through the combination of *r*-process network calculations and observational signatures of *r*-process events, I utilize actinide production by the *r*-process to investigate questions regarding the source of heavy-element abundance variations in metal-poor stars, the effect of fission cycling on the *r*-process abundance pattern, limits on *r*-process ejecta by candidate sites, and constraints on primordial neutron star binary systems. I find that neutron star mergers have the potential to synthesize all observed levels of actinide abundances measured in metal-poor stars if astrophysical variations on the composition of the ejecta are allowed within the merger site. Using this principle, I then determine that if neutron star mergers produced the majority of *r*-process elements in the Galaxy, then the first mergers were primarily mass-asymmetric. This thesis demonstrates a unique and adaptable route by which the elemental signatures of metal-poor stars can disentangle the complex chemical-enrichment history of the Universe.

DEDICATION

She who saves a single soul, saves the universe.

— Lewis Carroll

To my grandmother and godmother, Evangeline Martínez, whose intellectual freedom was stifled simply for being a woman.

CONTENTS

Figures	vi
Tables	x
Acknowledgments	xi
Symbols	xii
Chapter 1: Introduction	1
1.1 The Origin of the Heavy Elements	1
1.2 Neutron-Capture Nucleosynthesis	2
1.2.1 The Equilibrium <i>r</i> -Process	4
1.2.2 The Dynamic <i>r</i> -Process	6
1.3 The Observational <i>r</i> -Process	8
1.4 Current Challenges	11
Chapter 2: Astrophysical Variations and Nuclear Uncertainty	13
2.1 Ingredients for an <i>r</i> -Process Calculation	13
2.2 PRISM	13
2.3 Astrophysical Sites	14
2.3.1 Astrophysical Conditions	16
2.4 Nuclear Uncertainties	19
2.4.1 Self-Consistent Nuclear Data Input	19
Chapter 3: Observational <i>r</i> -Process Signatures	24
3.1 Metal-Poor Stars in the Galactic Halo	24
3.2 Chemical-Enhancement Signatures	25
3.3 Extra-Galactic <i>r</i> -II Stars	27
3.4 Universality of the <i>r</i> -Process Pattern	29
3.5 The <i>R</i> -Process Alliance	31
Chapter 4: The <i>R</i> -Process Alliance Observation and Analysis of Metal-Poor Stars	32
4.1 Identifying Metal-Poor Stars	32
4.2 The Spectroscopic Determination of Atmospheric Parameters	33

4.2.1	Equivalent Width and Line Formation	35
4.2.2	Key Atmospheric Parameters	37
4.3	Other Methods for Determining Atmospheric Parameters	39
4.3.1	Differential Analysis	39
4.3.2	Photometric Analysis	41
4.4	Atmospheric Parameters for RPA Targets	41
4.5	Neutron-Capture Abundances	43
4.6	Revisiting the [Eu/Fe] <i>r</i> -II Cutoff Value	47
4.6.1	Other Neutron-Capture Signatures	52
4.7	Radial-Velocity Variations	54
4.8	Summary and Discussion of RPA Efforts	61
Chapter 5: J09544277+5246414: The Most Actinide-Enhanced <i>r</i> -II Star Known		63
5.1	The Actinide Boost	63
5.2	Observations and Analysis	64
5.3	The <i>r</i> -Process Pattern	66
5.3.1	Light Neutron-Capture Elements	67
5.3.2	Heavy Neutron-Capture Elements	71
5.3.3	Thorium, Uranium, and the Actinide Boost	71
5.3.4	The Cosmochronometric Age of J0954+5246	73
5.4	Discussion and Conclusion	74
Chapter 6: Actinide Production in the Neutron-Rich Ejecta of a Neutron Star Merger		76
6.1	Actinide Formation and Cosmochronometry	76
6.2	Nucleosynthesis Calculations	78
6.3	Actinide Feeding	80
6.4	Production of Eu, Th, and U	84
6.4.1	Baseline Calculation: FRDM2012	84
6.4.2	Dependence on Fission Fragment Distribution: Kodama and Takahashi	88
6.4.3	Dependence on β -Decay Rates: Marketin	90
6.4.4	Dependence on Mass Model: Duflo-Zuker	94
6.5	Production Ratios	99
6.5.1	Comparison to Observations	99
6.5.2	The Actinide-Dilution Model	102
6.6	Conclusions	106
Chapter 7: An Astrophysical Solution to the Actinide Boost		108
7.1	Actinide Production as a Signature of NSM Nucleosynthesis	108
7.2	Observations of Metal-Poor Stars	109
7.2.1	Milky Way <i>r</i> -Process Enhanced Stars	110
7.2.2	Kinematically Linked Groups of <i>r</i> -Process Enhanced Stars	112
7.3	The Actinide-Dilution with Matching Model	114

7.4	ADM Model Results	119
7.4.1	The Low- Y_e Component	120
7.4.2	The Higher- Y_e Component	125
7.5	Model Variations	126
7.5.1	Astrophysical Sites	126
7.5.2	Nuclear Physics Inputs	129
7.5.3	The Low- Y_e Component	129
7.6	The GW170817 Associated Kilonova	131
7.7	Summary and Conclusions	132
Chapter 8: The First Neutron Star Mergers		136
8.1	Neutron Star Mergers in the Galaxy	136
8.2	Puzzle Pieces: Neutron Star Properties	138
8.2.1	NSM Ejecta	139
8.2.1.1	The Nuclear Equation of State	139
8.2.1.2	Disk Outflows	142
8.2.1.3	Dynamical Ejecta	144
8.2.1.4	Test on GW170817	147
8.2.2	Remnant Lifetime	149
8.3	Method: Assembling the Puzzle	151
8.3.1	Nucleosynthesis Calculations	152
8.3.2	Stellar Sample	154
8.3.3	ADMC: The MCMC Method	157
8.4	Results	160
8.5	Model Variations	166
8.5.1	No r -II Stars	167
8.5.2	Stellar Sample Distribution	168
8.5.3	The Ejecta Composition	170
8.5.4	No Prior	172
8.6	Summary and Discussion	174
Chapter 9: Conclusion and Future Outlook		178
Appendix A: Data from the Fourth Data Release of the RPA		181
A.1	Observation Log	181
A.2	Model Atmosphere Parameters	181
A.3	Neutron-Capture Abundances	181
Appendix B: Detailed MCMC Results for the First Neutron Star Mergers . . .		217
B.1	MCMC Results by EOS	217
B.2	Model Variations	226
Bibliography		235

FIGURES

1.1	Solar System elemental abundances showing the contribution from different nucleosynthetic processes	2
1.2	Typical <i>s</i> - and <i>r</i> -process equilibrium paths on the chart of nuclides .	3
1.3	[Eu/Fe] abundances of stars versus metallicity	9
2.1	Final <i>r</i> -process abundance patterns using various nuclear inputs . . .	21
2.2	Comparison of β -decay rates from Reaclib and up-to-date experimental β -decay rates from the NUBASE compilation	22
2.3	Final <i>r</i> -process abundance patterns comparing two nuclear networks and treatments of nuclear data	23
3.1	Spectrum snippet of an extremely metal-poor star with no <i>r</i> -process enrichment compared to an <i>r</i> -II star at a similar metallicity	26
3.2	Scaled abundance patterns of ten <i>r</i> -II stars	30
4.1	Schematic of a typical, continuum-normalized absorption feature and its equivalent width	36
4.2	Abundance trends of individual Fe I and Fe II lines for finding atmospheric parameters via the spectroscopic method	40
4.3	Surface gravity versus effective temperature and microturbulent velocities for RPA stars	43
4.4	Scaled spectrum snippets for an example <i>r</i> -I, <i>r</i> -II, and limited- <i>r</i> star identified by the RPA	45
4.5	Derived [Eu/Fe] abundances of RPA targets to date	48
4.6	Summaries of statistical methods used to redefine the <i>r</i> -I and <i>r</i> -II stellar classes	50
4.7	Metallicity histograms of <i>r</i> -process-enhanced stars identified by the RPA	51
4.8	Relative [Sr/Ba] and [Ba/Eu] abundance ratios for RPA stars as functions of [Fe/H], [Ba/Fe], and [Eu/Fe]	52
4.9	Comparison of radial velocity measurements by the RPA to Gaia DR2 .	55
5.1	The elemental abundance pattern of actinide-boost star, J0954+5246	67
5.2	Syntheses of important <i>r</i> -process elements present in J0954+5246 .	68

5.3	Th/Eu abundances vs. metallicity for known <i>r</i> -I and <i>r</i> -II stars	72
6.1	Isotopic abundance patterns of an <i>r</i> -process calculation at different times in the simulation	81
6.2	Integrated β -decay and α -decay flows of actinide elements in an <i>r</i> -process calculation	82
6.3	Europium, thorium, and uranium production as a function of initial Y_e using 50/50 fission fragment distributions and the FRDM2012 mass model	85
6.4	Average mass as a function of time for the baseline case, using symmetric fission fragment distributions and the FRDM2012 mass model	86
6.5	Final isotopic and elemental abundance patterns for the baseline case corresponding to the three initial Y_e values where lanthanides are maximized, actinides are maximized, and the nominal value	87
6.6	Europium, thorium, and uranium production as a function of initial Y_e using Kodama and Takahashi (1975) fission fragment distributions and the FRDM2012 mass model	89
6.7	Average mass as a function of time using Kodama and Takahashi (1975) fission fragment distributions and the FRDM2012 mass model	90
6.8	Final isotopic and elemental abundance patterns for the K&T case corresponding to the three initial Y_e values where lanthanides are maximized, actinides are maximized, and the nominal value	91
6.9	Europium, thorium, and uranium production as a function of initial Y_e using 50/50 fission fragment distributions, Marketin et al. (2016) β -decay rates, and the FRDM2012 mass model	92
6.10	Comparisons of β -decay rates between Marketin et al. (2016) and Möller et al. (2019), and the comparison of integrated neutron-induced fission flow when using these rates	93
6.11	Average mass as a function of time using 50/50 fission fragment distributions, Marketin et al. (2016) β -decay rates, and the FRDM2012 mass model	94
6.12	Final isotopic and elemental abundance patterns for the Marketin case corresponding to the three initial Y_e values where lanthanides are maximized, actinides are maximized, and the nominal value	95
6.13	Europium, thorium, and uranium production as a function of initial Y_e using 50/50 fission fragment distributions and the DZ mass model	96
6.14	Abundances at freezeout using FRDM2012 compared to the DZ mass model	97

6.15	Final isotopic and elemental abundance patterns for the DZ case corresponding to the three initial Y_e values where lanthanides are maximized, actinides are maximized, and the nominal value	98
6.16	Age of J0954+5246 as a function of Y_e using the baseline FRDM2012 mass model.	100
6.17	Predicted age of the actinide-boost star J0954+5246 based on the three chronometer pairs Th/Eu, U/Eu, and U/Th for each case discussed	101
6.18	Individual and combined abundance patterns that constitute the AD model applied to the baseline FRDM2012 case	103
6.19	Predicted age of actinide-boost star J0954+5246 based on the three chronometer pairs Th/Eu, U/Eu, and U/Th after applying the AD model to each case	105
7.1	Dy, Zr, and Th abundances of Galactic metal-poor halo stars	111
7.2	Abundance ranges of the three stellar groups considered in this work	115
7.3	Final Zy, Dy, and Th abundances as a function of Y_e for the disk wind using the FRDM2012 mass model	118
7.4	Ejecta distributions characterizing an r -process event predicted by the ADM model using the disk wind trajectory and the FRDM2012 mass model	119
7.5	Final combined abundance pattern results of the ADM model	121
7.6	Percentage of allowed very low Y_e (<0.18), actinide-rich mass to reproduce various $\log \epsilon(\text{Th}/\text{Dy})$ abundances at constant $\log \epsilon(\text{Zr}/\text{Dy})$ ratios	122
7.7	Ejecta distribution results for all three cases allowing no $Y_e < 0.18$	124
7.8	Percentage of allowed $Y_e > 0.3$, Zr-rich mass to reproduce various $\log \epsilon(\text{Zr}/\text{Dy})$ at constant $\log \epsilon(\text{Th}/\text{Dy})$ ratios	126
7.9	Ejecta distributions predicted by the ADM model under different astrophysical variations	128
7.10	ADM predictions using various nuclear mass models	130
7.11	Percentage of allowed very low Y_e (<0.18), actinide-rich mass to reproduce various $\log \epsilon(\text{Th}/\text{Dy})$ abundances using astrophysical and nuclear mass model variations	131
8.1	Mass-radius solutions for six different EOSs	141
8.2	Analytic form for the mass of the accretion disk compared to simulation data for different EOSs	143
8.3	Analytic form for the mass of the dynamical ejecta as a function of mass ratio (q) and total mass (M_{tot})	145
8.4	Predicted dynamical and wind ejecta masses from GW170817 compared to literature values	148

8.5	Lifetime of the HMNS remnant before it collapses into a black hole parameterized in terms of the total binary mass	150
8.6	Elemental abundances for merger remnants with different lifetimes	153
8.7	Corner plot showing a sample MCMC result for the most likely combination of M_1 and M_2	159
8.8	Individual neutron star mass results for each EOS choice compared to known neutron star binaries	161
8.9	Mass distributions for each EOS choice compared to fitted neutron star distributions	165
8.10	Neutron star mass distributions for DD2 when the original sample is varied	168
8.11	Neutron star mass distributions for DD2 when the ejecta composition is altered	171
8.12	Mass results for DD2 when using a flat prior	173
B.1	Scaled mass distributions for each EOS choice when r -II stars are removed	227
B.2	Scaled mass distributions for each EOS choice, re-weighted by the [Eu/Fe] distributions of RPA measurements	228
B.3	Mass results for each EOS choice when the Zr abundance of the dynamical ejecta is increased by 1.8 dex	229
B.4	Scaled mass distributions in arbitrary units for each EOS choice when the Zr abundance of the dynamical ejecta is increased by 1.8 dex	230
B.5	Mass results for each EOS choice when the Y_e of the disk wind is effectively shifted by 0.03	231
B.6	Scaled mass distributions when the Y_e of the disk wind is effectively shifted by 0.03	232
B.7	Mass results for each EOS choice when the prior is removed	233
B.8	Scaled mass distributions when the prior is removed	234

TABLES

2.1	Astrophysical Parameters for Leading Potential <i>r</i> -Process Sites	17
3.1	Classifications of Metal-Poor Stars	25
4.1	Abundances Uncertainties for Example Stars	46
4.2	Radial Velocities (in km s^{-1}) from Literature and this Data Release for Possible Binaries	57
5.1	Derived Atmospheric Parameters for J0954+5246	66
5.2	Derived Elemental Abundances of J0954+5246	69
7.1	Abundance Ratio Matching Conditions Used by the ADM Method .	116
8.1	Equations of State Used in this Work and Their Predictions on Neutron Star Properties	140
8.2	List of Stars Used for ADMC	155
A.1	Observation Log for the Fourth Data Release of the RPA	182
A.2	Model Atmospheric Parameters	198
A.3	Neutron-Capture Abundances and Subclass Assignments	208
B.1	Individual Results Using H4	217
B.2	Individual Results Using DD2	219
B.3	Individual Results Using ALF2	220
B.4	Individual Results Using LS220	222
B.5	Individual Results Using MPA1	223
B.6	Individual Results Using SFHo	225

ACKNOWLEDGMENTS

The past five years would not have been made possible without the wisdom, guidance, and—most of all—patience of my advisor, Rebecca Surman. Going above and beyond a mere thesis advisor, her encouragement and trust in my work—albeit sometimes tentative—continue to inspire and shape an increasingly confident and independent researcher. Half of this thesis would also not have been possible without the direction and support of Timothy Beers, who provided a nearly depthless reservoir of opportunities, resources, and sage anecdotes that improved both the quality and breadth of this research.

I am especially indebted to the many mentors and collaborators who have supported me both professionally and personally. Special thanks is dedicated (but not limited) to Vini Placco, Terese Hansen, Ian Roederer, and Chris Sneden, all of whom have offered guidance and help, even without needing to ask.

To my friends and officemates, namely Jared Coughlin, Chris Wotta, and Kevin Howard, who either kept me sane or gave me company in my moments of insanity. They were always there for support, whether it be Python help, finishing ABBA song lyrics, or late-night milkshake runs.

Lastly, to my two best friends: my sister, Kristin Holmbeck-Cannell, and my partner, Greg Horne. Their love, encouragement, and understanding kept me focused and stable through both the best and worst times.

SYMBOLS

k Boltzmann constant

h Planck constant

c speed of light

m_e electron mass

Z proton number

N neutron number

A atomic mass number

CHAPTER 1

INTRODUCTION

Why not other elements besides fire, air, earth and water? There are four of them, just four, those foster parents of beings! What a pity! Why aren't there forty elements instead, or four hundred, or four thousand?

— Guy de Maupassant

1.1 The Origin of the Heavy Elements

The origin and evolution of the elements in the Universe has long been a topic of discussion and debate between astronomers, physicists, and philosophers. The first non-terrestrial measurements of elemental abundances were made of the Sun via spectroscopy by [Russell \(1929\)](#) and in primordial meteorites by [Goldschmidt \(1929, 1938\)](#) in the late 1920's. From early on it was recognized that some elements are relatively more abundant than their neighbors, and studies were conducted to explain any periodicity in these features (see, e.g., [Clarke 1889](#)). In 1956 [Suess and Urey \(1956\)](#) found a nuclear physics explanation for the “peaks” that appear in the Solar System abundance pattern, shown in Figure 1.1. Since then, astrophysics and nuclear physics have been fundamentally intertwined in the search for the cosmic origin of the elements.

Simple nuclear physics principles can largely explain the production of the most abundant elements in the Solar System from He to Fe. These elements were formed by fusion in the successive burning stages of the stellar lifecycle. Energetic supernovae (SNe) can account for the iron-peak elements in which the relative abundances of

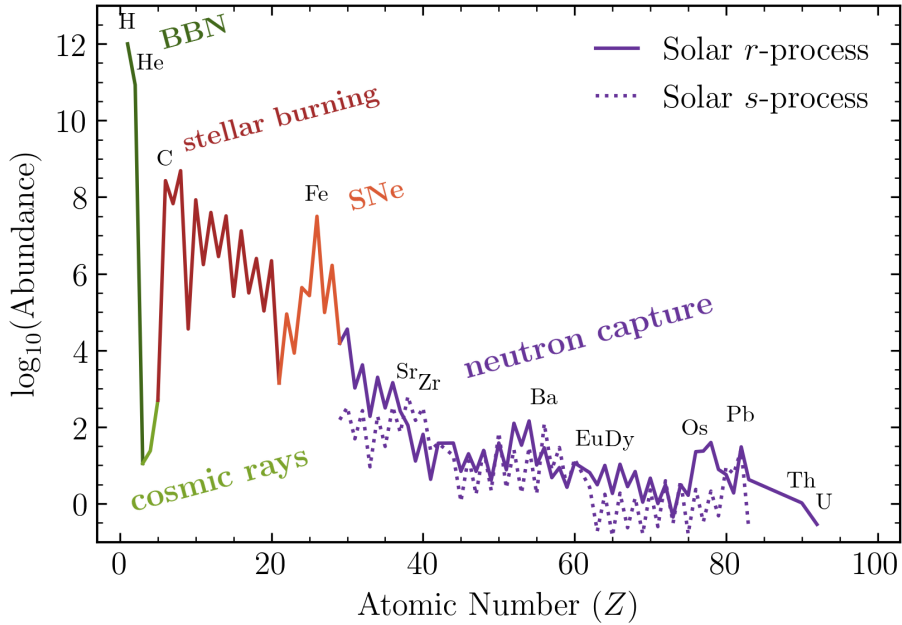


Figure 1.1. Solar System elemental abundances showing the contribution from different nucleosynthetic processes. The *s*- and *r*-processes are calculated from Arlandini et al. (1999) and Asplund et al. (2009).

elements in SN ejecta are determined by Nuclear Statistical Equilibrium (Truran et al. 1966). Beyond the iron peak, fusion processes in stars become energy-expensive and cannot explain the majority of heavy elements on the periodic table. Instead, another nuclear mechanism must be invoked: neutron capture.

1.2 Neutron-Capture Nucleosynthesis

In neutron-capture processes, a nucleus of charge and mass (Z, A) proceeds to the next isotope ($Z, A+1$) by capturing a free neutron. If this nucleus is unstable, it will β -decay into the isobar ($Z+1, A+1$) and access the next chain of isotopes. A sequence of neutron captures and β -decay thereby creates heavier and heavier elements. There are two main types of neutron-capture processes, both described in Burbidge et al. (1957) (hereafter “B²FH”) and Cameron (1957): slow and rapid neutron capture,

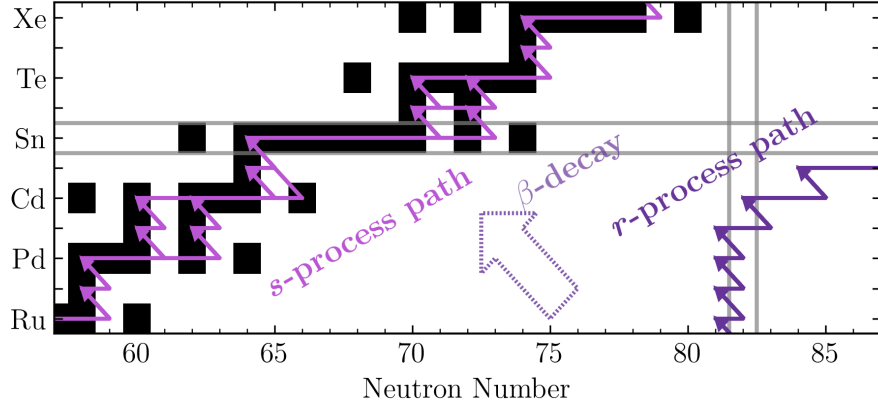


Figure 1.2. Typical *s*- and *r*-process equilibrium paths on the chart of nuclides.

each accounting for roughly half of the heavy elements found in the Solar System. The neutron-capture “peaks” in the Solar abundance pattern provide evidence that both the *s*-process and *r*-process have occurred in nature. Like the electron valence shells of atoms, nucleons also occupy energy shells. Nuclei with full neutron shells that are relevant to neutron-capture nucleosynthesis have neutron numbers $N = 50$, 82 , and 126 . In both the *s*- and *r*-processes, nuclei pile up and become abundant at these neutron numbers, producing “peaks” in the final abundance pattern. At the same shell closure, the *s*-process accesses nuclei at higher Z than the *r*-process, which leads to peaks that are shifted to heavier nuclei compared to the *r*-process peaks. The first, second, and third *r*-process peaks occur at (Z, A) of roughly $(36, 80)$, $(54, 130)$, and $(76, 195)$, respectively, while the *s*-process peaks are found at $(38, 88)$, $(56, 138)$, and $(82, 208)$. In addition, the observed *r*-process peaks tend to be broader than their *s*-process counterparts (due to the astrophysical conditions involved in each process).

In the *s*-process, the rate at which successive neutrons are captured is slower than the β -decay timescale, resulting in a neutron-capture path that proceeds along the valley of nuclear stability. Figure 1.2 illustrates typical *s*-process and *r*-process reaction pathways along the chart of nuclides. Astrophysically, hydrogen and helium-

burning ashes in asymptotic giant branch (AGB) stars provide a source of unstable neutrons and are therefore widely accepted sites for the *s*-process (Iben 1975; Truran and Iben 1977). On the other hand, nuclei in the *r*-process capture neutrons, on average, faster than the time it takes for the nucleus to decay, and thus the *r*-process accesses extremely neutron-rich, unstable nuclei. Although the rate at which free neutrons are generated in AGB stars may be sufficient for the *s*-process, the flux of free neutrons in these stars is not enough for the *r*-process. Due to the low neutron fluxes involved, the *s*-process terminates at $_{82}\text{Pb}$ and $_{83}\text{Bi}$. Beyond these elements, there are no long-lived nuclei able to capture neutrons until $_{90}\text{Th}$. On the other hand, the termination point of the *r*-process is unknown. At the very high neutron fluxes necessary for the *r*-process, extremely heavy nuclei can theoretically be produced. Since elements in the late actinide series decay quickly, the majority of actinide elements are unobservable in the Solar abundance pattern. Only two are found: the long-lived isotopes of Th and U. Since by definition the *s*-process does not have the neutron flux to cross the instability gap between Bi and Th, these nuclei must have a pure *r*-process origin.

1.2.1 The Equilibrium *r*-Process

The distinct signature of the *r*-process found in our Solar System is a testament that such a process must occur in nature. However, identifying an environment that may achieve such high neutron flux is not so obvious. To understand which astrophysical conditions—and therefore which cosmic site(s)—allow synthesis of the heavy elements via the *r*-process, we need to understand how those conditions influence the mechanics of neutron-capture nucleosynthesis. Early *r*-process formalisms employed equilibrium solutions in order to explain the elemental abundances with theory (see, e.g., Clayton et al. 1961; Clayton 1968). These “classical” *r*-process calculations assume $(n, \gamma) \rightleftharpoons (\gamma, n)$ equilibrium at a temperature T such that the

relative abundances along each isotopic chain are calculated with the nuclear Saha equation:

$$\frac{Y(Z, A + 1)}{Y(Z, A)} = \frac{n_n}{2} \frac{G(Z, A + 1)}{G(Z, A)} \left(\frac{h^2}{2\pi\mu kT} \right)^{3/2} e^{S_n/kT}, \quad (1.1)$$

where $Y(Z, A)$ is the number density of the nucleus (Z, A) , n_n is the neutron number density, $G(Z, A)$ is the statistical weight of nucleus (Z, A) , μ is the reduced mass of the compound nucleus $(Z, A + 1)$, and S_n is the energy necessary to separate one neutron from $(Z, A + 1)$. These types of equilibrium calculations are attractive since they do not require knowing the neutron-capture reaction cross-section for each nucleus. The equilibrium r -process path is found by solving for the maximum abundance along an isotopic chain with Equation 1.1 (Cameron et al. 1983; Cowan et al. 1991; Kratz et al. 1993). These points of maximum abundance are known as “waiting points,” since nuclei pile up at these isotopes and wait for β -decay to take nuclei up to the next $(Z + 1)$ isotopic chain. Then, Equation 1.1 can be solved again for $Z \rightarrow Z + 1$ to find the next waiting point. This series of waiting points constitutes the equilibrium r -process path, with the relative abundances along the path determined by how long nuclei occupy each waiting point via the steady β flow condition: $Y(Z, A)\lambda_\beta(Z, A) = \text{const.}$ For a waiting-point calculation, increasing the neutron number density or decreasing the temperature will decrease the ratio of $Y(Z, A)$ to $Y(Z, A + 1)$, and therefore shift the waiting points to heavier masses along each Z .

The waiting points can also be calculated from the one-neutron separation energy, S_n . Solving Equation 1.1 for the separation energy gives S_n as a function of temperature and neutron abundance:

$$S_n \propto -kT \ln \left\{ \frac{n_n}{2} \left(\frac{h^2}{2\pi\mu kT} \right)^{3/2} \right\}. \quad (1.2)$$

At a fixed temperature and density, the r -process path progresses along contours of constant S_n , setting the most abundant nuclei populated during the r -process. In this

form, it can be seen that increasing the temperature will shift the r -process waiting points along an isotopic chain to favor nuclei with higher one-neutron separation energies. After some set timescale, the r -process freezes out of equilibrium, and the nuclei undergo β -decay towards stability. Such waiting-point calculations have been used to explore possible astrophysical sites of the r -process through studying the role that temperature, density, and neutron fluence play in the extent and formation of r -process abundances. Many attempts were made to find the combination of temperature and neutron number density that fit the entire Solar r -process pattern, but these studies could not simultaneously fit all three of the observed abundance peaks (see, e.g., Kratz et al. 1993).

1.2.2 The Dynamic r -Process

In 1965, Seeger et al. (1965) recognized that no equilibrium solution or single freezeout time fit the Solar r -process pattern; rather, a superposition of r -process patterns at different freezeout times could better reproduce the Solar System abundances (Meyer 1994). This realization gave rise to the first dynamical calculations of the r -process, beginning with Delano and Cameron (1971); Sato et al. (1973), and Schramm (1973). Previously, non- r -process applications of nuclear reaction networks had been applied to silicon burning in the late evolutionary stages of massive stars, and included charged particle interactions such as (α, p) , (α, γ) , (p, n) , etc., along with their reverse reactions. (Truran et al. 1966). The most basic r -process network requires only neutron capture, photodissociation, and β -decay, the first two of which are related through detailed balance at a temperature T by:

$$\lambda_{\gamma}^{Z,A+1} = \frac{2}{n_n} \frac{G(Z, A)}{G(Z, A + 1)} \left(\frac{2\pi\mu kT}{h^2} \right)^{3/2} \lambda_n^{Z,A} e^{-S_n/kT}, \quad (1.3)$$

where $\lambda_i^{Z,A}$ is the rate of reaction i for a nucleus (Z, A) . These rates enter into a basic reaction network expressed in the following form:

$$\begin{aligned} \frac{dY(Z, A)}{dt} = & \rho n^{Z, A-1} Y_n \langle \sigma v \rangle_{n, \gamma} + Y(Z, A+1) \lambda_\gamma^{Z, A+1} \\ & + \sum_{i=0}^j Y(Z-1, A+i) \lambda_{\beta i}^{Z-1, A+i} \\ & - \rho n^{Z, A} Y_n \langle \sigma v \rangle_{n, \gamma} - Y(Z, A) \lambda_\gamma^{Z, A} \\ & - \sum_{i=0}^j Y(Z, A) \lambda_{\beta i}^{Z, A-i}. \end{aligned} \quad (1.4)$$

The first line describes flow into the nucleus (Z, A) by neutron capture from $(Z, A-1)$ and photodissociation of $(Z, A+1)$, where ρ is the density of the medium, $n^{Z,A}$ is the number density of nucleus (Z, A) , Y_n is the neutron abundance, and $\langle \sigma v \rangle_\lambda$ is the Maxwellian-averaged cross-section of reaction λ . The second line describes β flow into (Z, A) by β -decay and β -delayed neutron-emission, where the latter can emit from $i = 0$ to $i = j$ neutrons. The third line shows flow out of the nucleus (Z, A) by neutron capture into $(Z, A+1)$ and photodissociation into $(Z, A-1)$. Finally, the last line describes β -decay out of the nucleus into any nucleus $(Z, A-i)$ by β -delayed neutron emission. The upper limit j of how many neutrons can be emitted by β -delayed neutron-emission is unknown for r -process nuclei; at least one four-neutron emitter is known experimentally ([Dillmann et al. 2014](#)), and some theories predict up to $j = 10$ for the most neutron-rich nuclei ([Mumpower et al. 2016a](#)).

By the 1990's, r -process calculations became increasingly complex, from simple waiting-point methods nearly independent of nuclear reaction rates, to full network calculations that include experimentally measured and/or theoretically computed rates for each nucleus involved in the r -process. For an entire network of nuclei, Equation 1.4 is constructed as a system of coupled differential equations and computationally solved (by, e.g., implementing the Implicit Euler Method). With access

to full network calculations via computational methods, additional reactions can be included in Equation 1.4, such as proton-capture, α -decay, and fission. Increasingly complex r -process calculations, together with a new observational data, allows for deeper exploration of r -process sites to explain the observed elemental abundances.

1.3 The Observational r -Process

In the meantime, detailed comparisons to r -process models were limited to elemental abundances of the Solar System. The study of pre-Solar grains—condensed interstellar matter that preceded the formation of the Sun—from meteorites provided some *isotopic* abundance information for elements present in the Solar System and lent clues as to which stellar processes synthesized those isotopes. Further studies then used these grains to investigate the contribution of the s - and r -processes to each natural isotope (Clayton and Ward 1978; Bernatowicz and Zinner 1997; Zinner 1998). In turn, theoretical r -process models attempted to reproduce the Solar System r -process abundance pattern, assuming that some past astrophysical r -process event(s) synthesized those nuclei. Eventually, observations of elements outside the Solar System provided another basis for comparison to r -process models.

For over thirty years after the seminal B²FH and Cameron (1957) papers, it was generally assumed that iron and the r -process elements were synthesized in SNe. This theory was supported by observations of chemically simple, metal-poor stars that appeared to have uniform abundance patterns, including in the r -process elements (Spite and Spite 1978; Wheeler et al. 1989). Metal-poor stars have very low iron (Fe) content in their photospheres; by nature, either these stars are very old, or they formed from a gas that had not been enriched by many iron-producing events (e.g., by SNe). By the early 1990’s, studies of metal-poor stars revealed some scatter in the relative amount of neutron-capture elements to iron (Sneden and Parthasarathy 1983; Gilroy et al. 1988). To quantify this scatter, the relative abundances of elements are

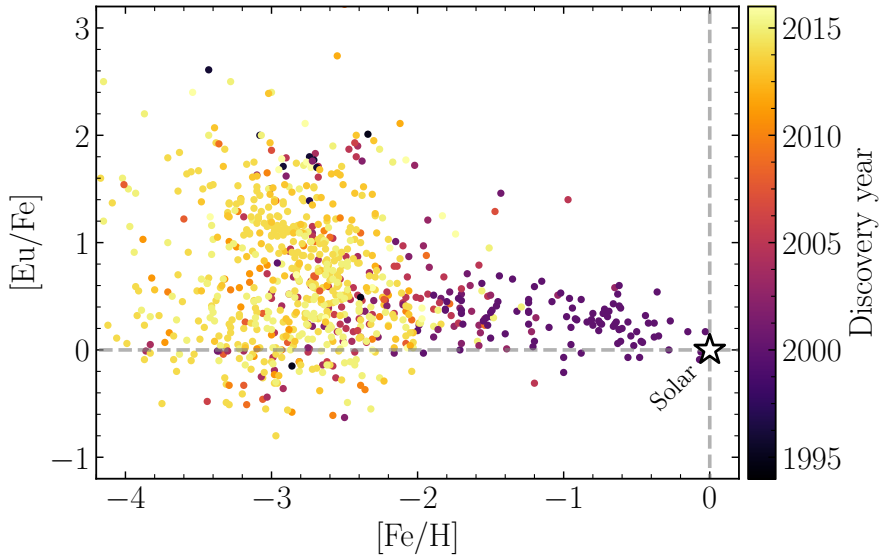


Figure 1.3. $[\text{Eu}/\text{Fe}]$ abundances of stars versus metallicity colored by their discovery dates (from data in [Abohalima and Frebel 2018](#)).

often reported in “bracket notation,” which scales the stellar $\log \epsilon$ abundance derived from measurements by the equivalent Solar values:

$$\log \epsilon(\text{A}) = \log_{10}(n_{\text{A}}/n_{\text{H}}), \quad (1.5)$$

$$[\text{A}/\text{B}] = \log_{10}(n_{\text{A}}/n_{\text{B}})_* - \log_{10}(n_{\text{A}}/n_{\text{B}})_{\odot}, \quad (1.6)$$

where A and B are two elements, and $n_{\text{A,B}}$ are the number densities of elements A and B in the star (*) and in the Sun (\odot). The hydrogen abundance is kept constant at $n_{\text{H}} = 10^{12}$ atoms. In this format, the bracket abundance describes the logarithm of the abundance ratio compared to the corresponding abundance in the Solar System. For example, $[\text{A}/\text{B}] = 0$ indicates that the measured A-to-B elemental abundance ratio is the same as that in the Sun, and $[\text{A}/\text{B}] = 1$ expresses that the abundance of element A is ten times greater than that of the Sun when scaled to the abundance of B. Figure 1.3 shows the bracket abundance of the r -process element Eu in metal-

poor stars, colored by their discovery year. The presence of *r*-process material in metal-poor stars at the time suggested that the *r*-process mechanism was universal, and assumed to be from CCSNe that could have contributed more significantly at earlier times (Wallerstein et al. 1997). There was no notion that other *r*-process production sites could be favored at lower metallicities, and therefore searches for the most metal-poor stars (i.e., the most pristine signatures of stellar events) hoped to uncover the *r*-process signature from first-generation Galactic SNe (Beers et al. 1985, 1992). Then, in the mid-1990’s, CS 22892–052 was discovered.

Although not the most metal-poor star known at the time, CS 22892–052 was recognized as unique in that the abundance of its neutron-capture elements far exceeded that of stars at extremely low metallicities ($[{\rm Fe}/{\rm H}] \leq -3$) (Sneden et al. 1994; McWilliam 1998). Its discovery begot a new classification of stars, “*r*-process-enhanced” stars, in which the abundance of elements with $Z > 35$ appear in patterns nearly duplicating the Solar System *r*-process abundance pattern, but, when scaled to iron, are over ten times the Solar abundance of heavy elements. The discovery of CS 22892–052 provided clear evidence that *r*-process production can occur independently of iron production, raising new questions about *r*-process sites and how SNe fit into *r*-process production. Gradually, more *r*-process-enhanced stars were identified, totaling about 30 as of 2005 (Barklem et al. 2005; Beers and Christlieb 2005). The universality of the *r*-process pattern, even at extremely low metallicites, argue that one site created the majority of the *r*-process elements early in the Galactic history. However, two-component models had better success at explaining both meteoritic data and abundances of metal-poor stars, indicating that the *r*-process originates from at least two sites Wasserburg et al. (1996); Qian and Wasserburg (2007).

1.4 Current Challenges

One of the main challenges facing nuclear astrophysics is identifying the cosmic site(s) of the *r*-process. Until 2017, no astrophysical *r*-process site had been definitively found observationally. Now, one astrophysical site has been confirmed: neutron star mergers (NSMs). With an answer to one question—whether NSMs are able to produce *r*-process elements—many more questions arise. For example, do NSMs produce the entire range of *r*-process elements, including the actinides, or is another site necessary? Are NSMs frequent and/or sufficiently prolific to account for the dominant fraction of *r*-process material in the Galaxy? Is the *r*-process abundance pattern from NSMs universal, or do different mergers leave their own distinct fingerprints on the abundance pattern?

The identification and differentiation between distinct *r*-process candidate sites is additionally obscured by uncertainties in nuclear physics. The *r*-process involves very unstable nuclei that have—at best—little available experimental data. Modern network calculations of the *r*-process rely on theoretical descriptions of neutron-rich nuclei, which can diverge broadly in their predicted observables, for example, in the nuclear masses they calculate. Using one theoretical description over another can leave an entirely different signature on the *r*-process abundance pattern, blurring the distinction between nuclear and astrophysical effects on the *r*-process abundances produced in an astrophysical site.

Understanding the *r*-process is as much a nuclear physics challenge as it is an astrophysical one. While modern *r*-process calculations encourage additional laboratory measurements of neutron-rich nuclei, the astrophysical laboratory in which such an *r*-process occurs plays an equally important role in determining the abundances that are produced. This thesis addresses several unanswered questions from both the nuclear and astrophysical perspective. First, we investigate different *r*-process sites in Chapter 2 and discuss the impact of nuclear physics uncertainties on differenti-

ating between sites. Next, we discuss in Chapter 3 the observable variations in the elemental-abundance patterns of metal-poor stars that may help distinguish between different *r*-process conditions. Chapter 4 outlines the observational effort to expand the catalog of known *r*-process-enhanced metal-poor stars in order to help characterize the observed variations in their elemental-abundance patterns. In Chapter 5, we discuss one of the largest variations in the *r*-process abundance pattern: the actinide boost. In order to investigate whether the source of this boost is nuclear or astrophysical in nature, we inspect the production of actinide elements in Chapter 6, specifically in NSM conditions. Finally, Chapter 7 presents a possible solution to the actinide boost signature in metal-poor stars, and Chapter 8 expands this solution in order to reconstruct the distribution of the earliest generation of *r*-process-producing neutron star binary systems.

ASTROPHYSICAL VARIATIONS AND NUCLEAR UNCERTAINTY

*Nature does not endure sudden mutations
without great violence.*

— François Rabelais

2.1 Ingredients for an *r*-Process Calculation

An *r*-process calculation requires two basic ingredients: nuclear reactions and astrophysical conditions. Astrophysical conditions describe the temperature and density (evolution) of an *r*-process site, which in turn determines what nuclear reactions may occur under those conditions (see, e.g., Arnould et al. 2007; Wiescher et al. 2012, for reviews). The astrophysical site of the *r*-process remains a mystery, and, consequently, so does a proper description of the dynamical evolution of *r*-process ejecta (e.g., Surman et al. 2008). Similarly, nuclei that are accessed in the *r*-process have little to no experimentally measured information (Mumpower et al. 2015, 2016b; Aprahamian et al. 2018). Accordingly, *r*-process calculations can be dominated as much by nuclear uncertainties as by astrophysical unknowns (Sprouse et al. 2020). Here we overview how nuclear uncertainties and differences in astrophysical sites can leave imprints on the *r*-process abundance pattern.

2.2 PRISM

Like any recipe, the right tools are required in order to properly combine ingredients. This work uses the nuclear network code Portable Routines for Integrated nu-

cleoSynthesis Modeling (PRISM; Mumpower et al. 2017; Côté et al. 2018; Mumpower et al. 2018; Vassh et al. 2019) to investigate the effects of nuclear uncertainties and astrophysical variations in *r*-process sites on the abundances that are produced. PRISM is built for complete flexibility in both the nuclear and astrophysical input, allowing individual reaction channels to be incorporated and studied. PRISM takes as input the astrophysical conditions in the form of a time-evolution of temperature and density, an initial seed distribution of nuclei with which to start the network, and a set of nuclear data. With this versatility, the complex interplay between astrophysical site and nuclear uncertainty is investigated in detail in order to study the origin of *r*-process elements in metal-poor stars.

2.3 Astrophysical Sites

Even before B²FH and Cameron (1957), core-collapse SNe (CCSNe) were thought to be natural sites for the *r*-process, due to their explosive nature and the perceived abundance of neutrons produced from photo-dissociation of the SN material (Hoyle 1946). For several decades, calculations of the high-entropy region outside a newly formed neutron star supported CCSNe as main *r*-process sources (Mathews et al. 1992; Meyer et al. 1992; Takahashi et al. 1994; Woosley et al. 1994; Qian and Woosley 1996). Later, hydrodynamical calculations that included neutrino effects on the shocked outflow showed that CCSNe cannot reach the conditions necessary to produce all of the *r*-process elements (Thompson et al. 2001; Arcones et al. 2007; Martínez-Pinedo et al. 2012; Roberts et al. 2012). Although several studies have shown that modern models of CCSNe cannot reproduce the heavy/main elemental *r*-process pattern of the Solar System, CCSNe may still be responsible for the light *r*-process elements (Thompson et al. 2001; Thielemann et al. 2011; Arcones and Thielemann 2013). Alternatively, rare types of SNe could contribute to Galactic *r*-process enrichment. The accretion disk around collapsars—the core collapse

of a massive rotating star—has been proposed as a possible site of robust r -process element production (Pruet et al. 2004; Surman and McLaughlin 2004; Miller et al. 2019). This idea has seen recent resurgence, and Siegel et al. (2019) argue that the electromagnetic signal from r -process production in these events could be veiled by the associated gamma-ray burst. Another possible site is within the jets of magneto-rotational instability-driven SNe (Cameron 2003; Winteler et al. 2012; Nishimura et al. 2015, but see also Mösta et al. 2018).

In 1974, Lattimer and Schramm proposed neutron star mergers (NSMs) as candidate r -process sites. Compact object mergers remained highly theoretical events with no definitive observation for over four decades. Some strong indirect evidence of compact object mergers were found in the unexplained short-duration γ -ray bursts (SGRBs), first detected over thirty years after Lattimer and Schramm (1974) (Berger et al. 2005). The combination of their extremely short duration, excess of near-infrared emission, and tendency to be located on the edges of elliptic galaxies point to an NSM origin for the SGRBs (Tanvir et al. 2013). Although there existed some evidence that NSMs were possible beyond theory, they were still not considered primary producers of r -process material at early times in the Galactic history. Mathews and Cowan (1990) concluded that the coalescence timescale for binary neutron stars is too long to explain the majority of r -process abundances at the lowest stellar metallicities (and therefore the earliest times) (Argast et al. 2004). NSMs remained unconfirmed until the first direct observation of an NSM event by the Laser Interferometer Gravitational-Wave Observatory (LIGO) (Abbott et al. 2017). This event, GW170817, occurred close enough to our galaxy to be observed in electromagnetic emission in addition to gravitational waves. Studies of the light curve (AT2017gfo or SSS17a; Kilpatrick et al. 2017; Cowperthwaite et al. 2017; Drout et al. 2017; Pian et al. 2017; Shappee et al. 2017) from this event showed that including lanthanides in the NSM ejecta could explain the long-lived red emission in the observations, thus

demonstrating that some extent of the r -process can occur in NSM sites (Kasen et al. 2017). However, it is still unknown whether GW170817 is characteristic of NSMs, whether NSMs occur often enough to account for the majority of r -process elements in our galaxy, or what astrophysical variations are allowed in NSM ejecta (Thielemann et al. 2017). Simulations suggest that one NSM event hosts several environments capable of undergoing an r -process. Of particular importance are the neutron-rich, low-entropy dynamical (tidal) ejecta, which escape at high velocities (Lattimer and Schramm 1974; Meyer 1989; Freiburghaus et al. 1999). On slightly longer timescales is the accretion disk wind, which is estimated to have slightly lower neutron-richness and higher entropy than the tidal ejecta (Surman et al. 2008; Metzger et al. 2008; Perego et al. 2014). Uncertainties in neutrino physics also carry over to NSM ejecta and their candidacy as r -process sites, since neutrino flavor transformation has the potential to make the disk wind significantly more (or less) neutron-rich than currently predicted by simulations (Malkus et al. 2016).

2.3.1 Astrophysical Conditions

The hydrodynamical evolution of astrophysical ejecta (a “trajectory”) can be sufficiently characterized by a small handful of parameters that are generally tracked in multi-dimensional simulations: temperature (T_9), density (ρ), specific entropy (s_k), expansion timescale (τ), and electron fraction (Y_e) or neutron-to-seed ratio. The specific entropy (s_k) measures the photon-to-baryon ratio of the r -process environment. Coupled with the density, the temperature dictates the specific rates of the nuclear reactions that occur at each timestep of a dynamic r -process calculation (see, e.g., Equation 1.3). In addition, the temperature and entropy generally affect how close to the neutron drip-line the r -process progresses, with “hotter” conditions pushing the r -process closer to stability. The expansion timescale describes how quickly the ejecta from an event expands, and thus, how rapidly the matter density drops. A short/fast

TABLE 2.1
 ASTROPHYSICAL PARAMETERS FOR LEADING POTENTIAL
 r -PROCESS SITES

Site	s_k	τ (ms)	Y_e	Extent	Yield (M_\odot)	R_{MW} (Myr $^{-1}$)
CCSN	50–200	20–80	0.3–0.5	$Z < 45$	10^{-6} – 10^{-4}	10^4
MHD	10–30	1–10	0.1–0.4	$Z > 30$	$\sim 10^{-3}$	10^3
Collapsar	10–100	20–50	0.1–0.4	$Z > 30$	$\sim 10^{-3}$	10^1
NSM wind	10–50	10–30	0.2–0.4	$Z > 35$	10^{-3} – 10^{-2}	10^2
NSM dyn.	1–10	0.1–1	< 0.2	$Z > 50$	10^{-3} – 10^{-2}	10^2

timescale typically leads to fewer seed nuclei being formed, and therefore allows more neutrons per seed to be captured and a more robust r -process. However, if the expansion timescale is too fast, the material may become too diffuse for neutrons to be captured onto seed nuclei, inhibiting the r -process. Lastly, the electron fraction describes the ratio of protons to total baryons at the onset of the r -process. A lower Y_e indicates a more neutron-rich composition, which generally produces a stronger r -process pattern. Table 2.1 summarizes typical values used for popular r -process sites as well as their r -process extent, mass yield, and (theoretical) occurrence rate in the Milky Way (Hotokezaka et al. 2018; Mösta et al. 2018; Horowitz et al. 2019, and references therein).

Historically, dynamical r -process calculations use parameterized descriptions of astrophysical ejecta. These parameterizations usually feature temperature and density decreasing exponentially, and a constant entropy until freezeout. For high-entropy sites like SNe, photons contribute a significant amount of external heat. In these “hot” r -process conditions where radiation dominates the entropy, the astrophysical parameters before freezeout can be related as follows (see Lattimer and

Swesty 1991, for a full derivation):

$$T_9 \propto \exp^{-t/\tau} \quad (2.1)$$

$$\rho \propto \frac{T_9^3}{s} \quad (2.2)$$

However, in “cold” r -process conditions where the $(n, \gamma) \rightleftharpoons (\gamma, n)$ equilibrium phase is short-lived (or non-existent), the density is not so cleanly related to the temperature, and parameterizations in the form of Equation 2.2 underestimate the entropy of the system. These simple parameterizations of hot r -process conditions allow systematic explorations of how these parameters affect the r -process abundances independent of specific astrophysical site (see, e.g., Seeger et al. 1965; Kodama and Takahashi 1975; Kratz et al. 1993; Freiburghaus et al. 1999; Otsuki et al. 2003; Surman and McLaughlin 2005; Panov and Janka 2009; Mumpower et al. 2012). Applications of parameterized trajectories can possibly assume all r -process ejecta follow the same, one-dimensional evolution, which is likely an oversimplification of real r -process events. On the other hand, hydrodynamical simulations can include tens of thousands of individual mass-element tracers, providing a range and distribution of astrophysical parameters within r -process sites, rather than a single set of parameters describing all ejecta. The temperature and density evolutions of individual tracers in hydrodynamical simulations may lead to entirely different r -process patterns, even within the same astrophysical site. These calculations are powerful in that they offer a more comprehensive nucleosynthetic treatment of distinct astrophysical sites. However, computing the detailed nucleosynthesis for tens of thousands of individual tracers can be computationally expensive. To balance the relative simplicity of single parameterized trajectories with the computational expense of using hydrodynamical simulations, sets of parameterized trajectories can be constructed from the range of astrophysical parameters predicted by more detailed simulations. Therefore, instead

of using one choice of parameters to represent the entirety of *r*-process ejecta, entire distributions of parameterized trajectories can also be used to replicate hydrodynamical results. This flexibility allows tests of astrophysical variations without the need to run additional full hydrodynamical simulations. This work employs both parameterized trajectories and those taken from hydrodynamical simulations.

2.4 Nuclear Uncertainties

The most basic nuclear reactions included in the *r*-process are neutron-capture, photo-dissociation, and (inverse) β -decay. Photo-dissociation can be calculated from Equation 1.3, with a set temperature, the neutron-capture rate at that temperature, and the one-neutron separation energy. Where possible, β -decay rates and nuclear masses are measured in a laboratory. With more complex *r*-process calculations, other reactions can be included, such as charge-transfer, proton and α -inducing, and fission reactions, as well as other decay mechanisms. However, these reactions are shrouded in uncertainty far from stability, along nuclei where the *r*-process occurs (Liddick et al. 2016).

2.4.1 Self-Consistent Nuclear Data Input

For the vast majority of nuclei involved in the *r*-process, theoretical calculations must be used to determine the nuclear reaction rates. Theoretical nuclear models range from fully microscopic, which attempt to describe the nucleus from its individual nucleons (e.g., the Hartree-Fock-Bogoliubov, “HFB,” approaches; Goriely et al. 2011, 2013), to macroscopic, which characterize the nucleus based on its collective behavior (e.g., Duflo-Zucker, “DZ;” Duflo and Zuker 1995; Kirson 2012). Regardless of theoretical approach, the tunable parameters of available nuclear models are in some way fit to experimental data. Macroscopic models tend to be more highly parameterized than microscopic models, and while they can reproduce known data

accurately, their reliability far from stability is unclear in the unknown regions of the nuclear chart. On the other hand, microscopic models potentially see more promise to be reliable away from stability since they attempt to fit the underlying interactions, but it is not clear with available data that this reliability has been realized (Lunney et al. 2003). Several models opt for a hybrid approach, such as starting with a macroscopic model and adding microscopic corrections (e.g., the Finite-Range Droplet Model, “FRDM,” Möller et al. 1995, 2012; the Weisäcker-Skyrme model, Liu et al. 2011; Zhang et al. 2014)

Due to the breadth of available nuclear models, the nuclear and astrophysical observables they predict also vary dramatically (see, e.g., Liddick et al. 2016; Mumpower et al. 2016b). The nuclear mass model enters into calculations for all reaction and decay rates, generally in some way through the mass difference between adjacent isotopes: the one-neutron separation energy (S_n). The dependence of photodissociation rates on S_n has already been shown in Equation 1.3. Similarly, the reaction Q -value determined by the mass difference between adjacent isobars affects the calculation of a nucleus’s β -decay half-life. Furthermore, the nuclear energy levels and Q -value also enter into β -delayed neutron emission probabilities. If the nucleus decays to an energy level above S_n , there is a probability that it will also emit one or more neutrons, shown schematically in Figure 1 of Mumpower et al. (2016a). Mumpower et al. (2016b) provides a detailed explanation of the influence of uncertainties in nuclear rates on the final r -process abundance pattern in dynamical r -process calculations. Among the most uncertain are the mass model, the β -decay rates, and the fission fragment distribution of very heavy nuclei. Figure 2.1 shows how changing these nuclear physics properties affects final the r -process abundances within the same astrophysical site.

Reaction and decay rates are intrinsically determined by the underlying nuclear interaction. Therefore, a self-consistent set of nuclear data is necessary to correlate

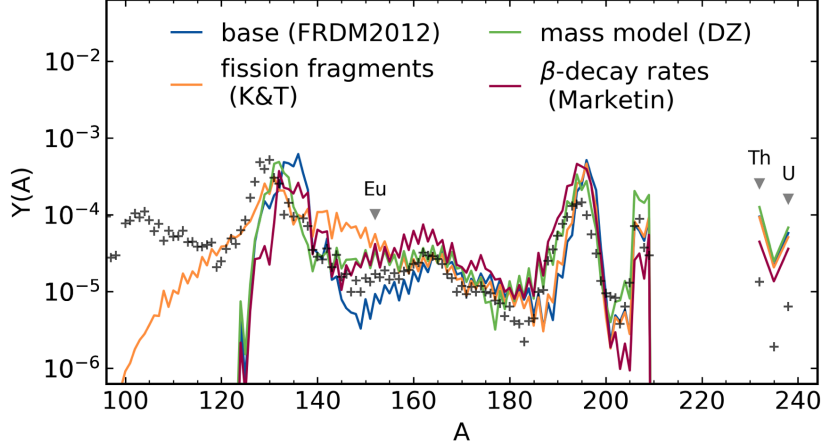


Figure 2.1. Final r -process abundance patterns using various nuclear inputs.

features of the r -process abundance pattern with fundamental nuclear properties. Without self-consistent nuclear data, features in the r -process abundance pattern may superficially be related to specific reaction rates, but the deeper connection to the properties determining those rates would remain inaccessible. For all the r -process calculations shown in this work, we employ nuclear reaction and decay rates that are calculated to be consistent with each nuclear mass model to the extent possible. Conclusions drawn from using nuclear data that are self-consistent with the masses help to clarify which nuclei involved in the r -process will benefit most from an experimental mass measurement. In turn, new mass measurements help to decouple the effect of nuclear masses on the r -process abundance pattern from astrophysical ones. The deeper link to fundamental properties beyond nuclear masses is a goal for nuclear theory moving forward. Our self-consistent approach rises above previous r -process networks that combine theoretical datasets from many different sources. In addition, other r -process reaction networks do not take care to incorporate experimental data. For the calculations in this work, we first start with theoretically calculated datasets, then incorporate laboratory measured data wherever possible and overruling theory values.

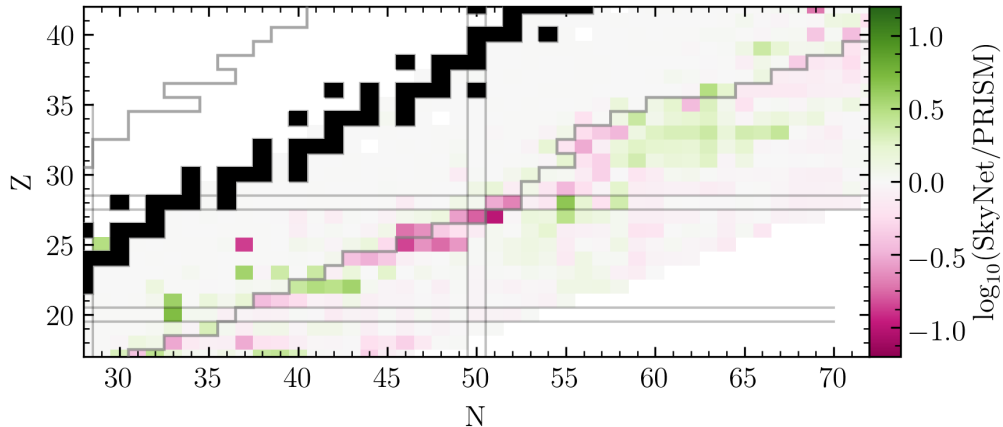


Figure 2.2. Comparison of β -decay rates from Reaclib employed by SkyNet and up-to-date experimental β -decay rates from the NUBASE compilation used by PRISM. The gray line shows the limit of experimentally measured β -decay rates.

Figure 2.2 shows a comparison between the β -decay rates employed by a similar reaction network, SkyNet (Lippuner and Roberts 2017), and those used by PRISM in the region around the first r -process peak. The β -decay rates used by SkyNet are drawn from the REACLIB database (Cyburt et al. 2010), which compiles theoretical data with experimental data where known. However, the experimental rates included are not always up to date, and theoretical datasets are drawn from many different sources, spanning decades of work. On the other hand, PRISM employs one theoretical, well-tested dataset (primarily from Möller et al. 2019 and consistent with the nuclear mass model) and experimental data from the NUBASE compilation (Audi et al. 2017). The gray line in Figure 2.2 shows the limit of nuclei in NUBASE where β -decay rates have been measured. There are several recently measured rates that influence the first r -process peak near $(Z, N)=(28,50)$ that are included in NUBASE but not updated in Reaclib. Notably, the measured rates in this region are faster than the theoretical rates in Reaclib. Additionally, the theoretical rates used by SkyNet near $(Z, N)=(32,60)$ are faster than those used by PRISM, which will leave an im-

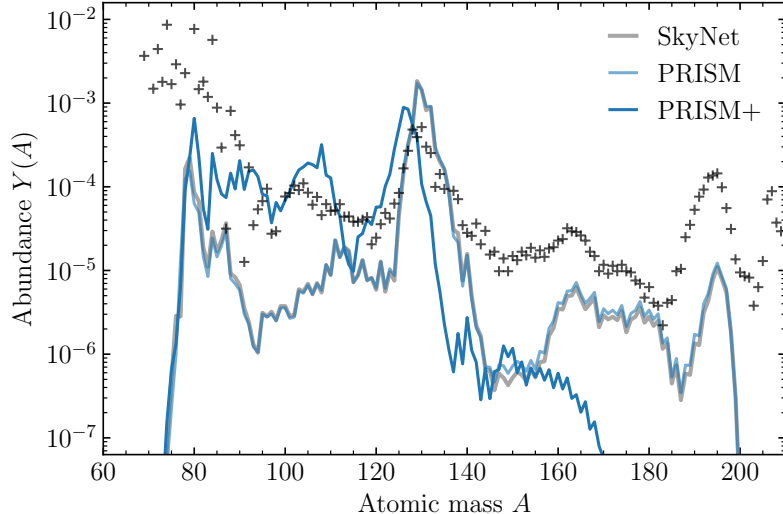


Figure 2.3. Final r -process abundance patterns comparing two nuclear networks and treatments of nuclear data, with the “PRISM+” simulation using self-consistent nuclear data.

print on the r -process abundance pattern by moderating the flow of abundance into heavier nuclei. Figure 2.3 illustrates the difference between the PRISM and SkyNet under the same astrophysical conditions. Using the same astrophysical input and nuclear data (from the REACLIB database), the two networks yield nearly identical results. When the PRISM network is supplemented with improved theoretical rates and recent laboratory measurements (“PRISM+” in Figure 2.3)—and still using the same astrophysical input—the final r -process abundances change dramatically, highlighting the importance of nuclear data calculated as self-consistently as possible.

An r -process calculation relies as much on astrophysics as on nuclear physics. Amongst the many uncertainties in astrophysical sites and nuclear interactions, it seems challenging to draw any robust conclusions about the r -process from nuclear network calculations. The next chapter discusses how data from metal-poor stars may be sufficiently robust to break through model uncertainties and alleviate the degeneracy between nuclear and astrophysical unknowns.

CHAPTER 3

OBSERVATIONAL *R*-PROCESS SIGNATURES

*If you wish to make an apple pie from scratch,
you must first invent the universe.*

— Carl Sagan

3.1 Metal-Poor Stars in the Galactic Halo

In the early 1800’s, [Wollaston \(1802\)](#) and [Fraunhofer \(1817\)](#) first noticed that certain wavelengths of light appeared much fainter or were missing altogether in the Solar spectrum. These dark bands were not identified as chemical in origin until 45 years later by [Kirchhoff \(1860\)](#), who found that they correspond to atomic transitions of elements present in the atmosphere of the Sun that absorb photons at specific wavelengths of light. At present, a whole range of elements on the periodic table has been identified throughout the Solar spectrum, offering a snapshot of the natal gas from which the Sun was created and the chemical evolution preceding its formation.

After a given stellar generation evolves, synthesizing elements via burning or explosive stages throughout its evolution, each subsequent generation enriches the primordial gas of the surrounding interstellar medium. As a new generation of stars form from this enriched material, the convection of a newly born star may fail to fully mix the outer layers where light finally escapes the stellar surface. Therefore, the photospheres of stars largely retain records of the natal gas of their birth environments, providing a signature of the chemical production of the preceding stellar generation(s). Accordingly, very metal-poor and extremely metal-poor stars (defined

TABLE 3.1
CLASSIFICATIONS OF METAL-POOR STARS[†]

Class	Definition
Metal-poor (MP)	$[\text{Fe}/\text{H}] < -1.0$
Very metal-poor (VMP)	$[\text{Fe}/\text{H}] < -2.0$
Extremely metal-poor (EMP)	$[\text{Fe}/\text{H}] < -3.0$
Ultra metal-poor (UMP)	$[\text{Fe}/\text{H}] < -4.0$
Hyper metal-poor (HMP)	$[\text{Fe}/\text{H}] < -5.0$
Mega metal-poor (MMP)	$[\text{Fe}/\text{H}] < -6.0$
CEMP	$[\text{Fe}/\text{H}] < -1.0$ and $[\text{C}/\text{Fe}] > +0.7$
limited- <i>r</i>	$[\text{Eu}/\text{Fe}] < +0.3$ and $[\text{Sr}/\text{Ba}] > +0.5$
<i>r</i> -I	$+0.3 < [\text{Eu}/\text{Fe}] \leq +1.0$ and $[\text{Ba}/\text{Eu}] < +0.0$
<i>r</i> -II	$[\text{Eu}/\text{Fe}] > +1.0$ and $[\text{Ba}/\text{Eu}] < +0.0$

[†]Adapted from Beers and Christlieb (2005) and Frebel (2018).

in Table 3.1) were created from gas that had not been enriched by many nucleosynthetic events before these stars formed. In the Milky Way, the highest fraction of metal-poor stars is found in the Galactic halo, revealing a location for where to begin dedicated searches, where to find the oldest stars in the Galaxy, and where to find the purest signatures of past nucleosynthetic events (Beers and Christlieb 2005; Beers et al. 2005; Carollo et al. 2018).

3.2 Chemical-Enhancement Signatures

A strong event enriching low-metallicity gas would leave a clear elemental signature in the photospheres of the metal-poor stars that form from that gas. Indeed, at low metallicities, distinct elemental signatures are found, including stars enhanced

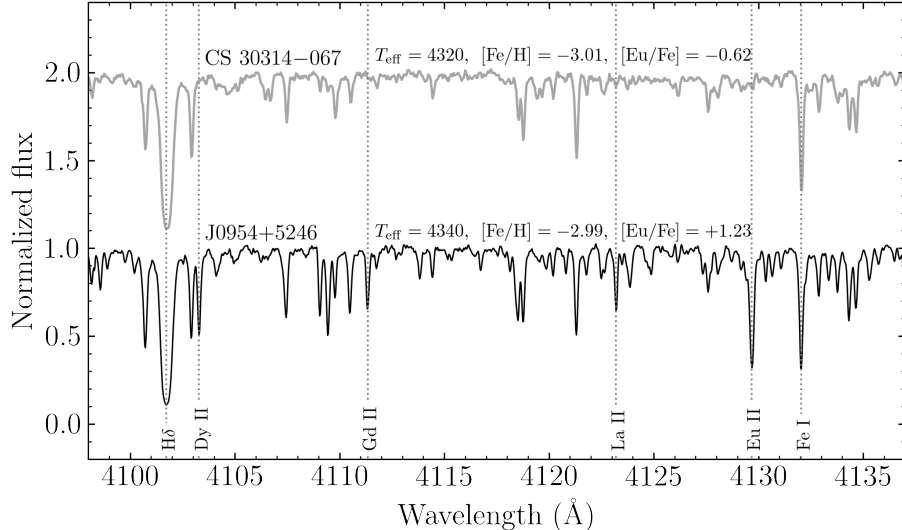


Figure 3.1. Spectrum snippet of an extremely metal-poor star with no *r*-process enrichment (top) compared to an *r*-II star at a similar metallicity (bottom). Key features of several lanthanide elements are labelled.

in neutron-capture elements appearing in relative abundances duplicating the Solar *s*-process and *r*-process abundance patterns (Sneden et al. 2008; Frebel and Norris 2013). Of particular importance are the *r*-process-enhanced stars, which show enhancement of the heavy *r*-process elements ($Z > 56$) in their photospheres. The level of enrichment by the *r*-process in metal-poor stars is quantified by europium ($Z = 63$) since this element is almost entirely produced by the *r*-process, and it is one of the easiest *r*-process elements to measure in optical wavelengths of stellar spectra. As an example, Figure 3.1 displays a snippet of spectrum comparing an *r*-II with a non-*r*-process-enhanced star of similar metallicity and effective temperature. Since these two stars have similar atmospheric parameters, which determine the absorption-line profiles, the difference in strengths of the absorption features is directly correlated to the difference in the elemental abundance forming each line. Currently, the *r*-process-enhanced stars are divided into two sub-classes characterizing their enhancement: “*r*-I” and “*r*-II,” as defined in Table 3.1.

The *r*-II stars display a strong relative enhancement of *r*-process elements in their photospheres compared to their iron content (Barklem et al. 2005; Beers and Christlieb 2005). About 3–5% of stars in the Milky Way halo with $[\text{Fe}/\text{H}] \lesssim -2$ are classified as *r*-II, totaling about 30 *r*-II stars identified as of 2015 (from data in Abohalima and Frebel 2018, “JINAbase”¹). The moderately enhanced *r*-I stars account for roughly 10–15% of very metal-poor stars. Owing to their low metallicity, the *r*-I and *r*-II stars record clear elemental signatures of single to a few *r*-process events, offering a window into *r*-process sources at low enrichment times, such as potential NSM events. The low metallicity of *r*-I and *r*-II stars was originally interpreted as indicating that an *r*-process source occurred at very early times in Galactic history, placing a timescale on *r*-process events (e.g., Argast et al. 2004). The short timescale required offered another argument for core-collapse supernovae (CCSNe) as natural *r*-process sources, while the long coalescence timescales for NSMs could not be accommodated by the inferred short formation history of the most metal-poor *r*-II stars.

3.3 Extra-Galactic *r*-II Stars

One way in which NSMs have again gained support as *r*-process sites is through the discovery of the ultra-faint dwarf galaxy (UFD) Reticulum II (Ret II). UFDs are low-luminosity, dark-matter-dominated satellites of the Milky Way. Their low mass inhibits the ability of the satellite to form new stars, since the first SNe occurring in these galaxies would be energetic enough to eject the remaining star-forming gas. Therefore, the surviving members of UFDs are the product of only a few enrichment events at most (Kirby et al. 2008; Brown et al. 2014). Surveys such as the Sloan Digital Sky Survey (SDSS) resulted in the identification of the first UFDs around the

¹<https://github.com/abduabohalima/JINAbase>

Milky Way (Willman et al. 2005b,a). Many additional UFDs have been discovered through new surveys (e.g., the Dark Energy Survey, “DES”; Bechtol et al. 2015), and investigations of their stellar members have overall found that these stars are indeed metal-poor (Koposov et al. 2015). Studies of their elements showed UFD stars have usually low neutron-capture abundances, consistent with the meager yields of SNe from massive stars. However, Ret II deviated from this perceived norm; of nine stars observed in Ret II, Ji et al. (2016b) and Roederer et al. (2016) identified seven as *r*-II members—a much higher *r*-II fraction than that found in the Milky Way, and much more enriched than any other UFD studied at the time (Frebel et al. 2014; François et al. 2016; Ji et al. 2016c). SNe alone cannot account for the extreme neutron-capture element enrichment of Ret II. Not only would SNe produce much more iron than what is observed in Ret II, but they would also have driven out the star-forming gas. Instead, one NSM is sufficient to reproduce the abundance of *r*-process material in Ret II.

In addition, many studies support a hierarchical merger origin of the Milky Way, where the Galactic metal-poor halo stars originally formed in small early galaxies such as analogs of the surviving UFDs (Searle and Zinn 1978; Prantzos 2008; Schlaufman et al. 2009; Tumlinson 2010). If the halo stars were accreted by the Milky Way from low-mass satellite galaxies, then strong *r*-process events like NSMs occurring in UFDs could explain the strong *r*-process enhancement in the present-day halo *r*-II stars. The somewhat less-enhanced *r*-I stars possibly formed in larger dwarf galaxies, such as Tucana III (Tuc III; Hansen et al. 2017), in which the yields of any prolific *r*-process event would be diluted more than in the case of the formation of *r*-II stars in smaller systems.

The discovery of UFDs like Ret II and Tuc III enhanced with *r*-process elements alleviates the tension with the metal-poor nature of the *r*-II stars and the long coalescence timescales of NSMs. Due to their low mass, UFDs could retain a metal-poor

nature long enough to accommodate an NSM event before the next (and possibly last) generation of star formation. Still, it is unclear whether NSMs alone can account for the range of metallicities and the level of *r*-process enrichment in the halo *r*-I and *r*-II stars, since *r*-process yields and the mass into which NSM ejecta is diluted are both uncertain. This idea finds theoretical support in galactic chemical-evolution studies; Côté et al. (2019) argue that it is likely that a separate site (or sites) could have contributed *r*-process material at early times in the Universe. In addition, cosmological zoom simulations of NSMs may be able to explain *r*-process enrichments of individual dwarf galaxies like Ret II and Tucana III, but cannot simultaneously reproduce Milky Way halo statistics of all *r*-process enhanced stars (Safarzadeh et al. 2019; Brauer et al. 2019).

3.4 Universality of the *r*-Process Pattern

When scaled, the main *r*-process elemental-abundance pattern (Ba to Hf) of *r*-I and *r*-II stars is strikingly similar and closely follows the *r*-process pattern observed in the Solar System for stars covering a wide range of metallicities (Sneden 2002; Siqueira Mello et al. 2014; Hansen et al. 2017). Figure 3.2 shows the abundance patterns of ten *r*-II stars, scaled to their average residual from the Solar pattern among the lanthanides. The universality of the main *r*-process pattern among Milky Way halo stars, UFDs, and classical dwarf galaxies suggests that either the *r*-process behaves uniformly regardless of its astrophysical site, or that the observed *r*-process material originates from one type of *r*-process-element production event that has to have operated in a consistent way throughout time.

Although the lanthanide patterns of the *r*-I and *r*-II stars show striking similarities, some variation exists in the actinide elements, Th and U, with about 30% showing an enhancement of Th relative to the lanthanides (Mashonkina et al. 2014), dubbed the “actinide-boost.” There is also a wider variation of the elemental abun-

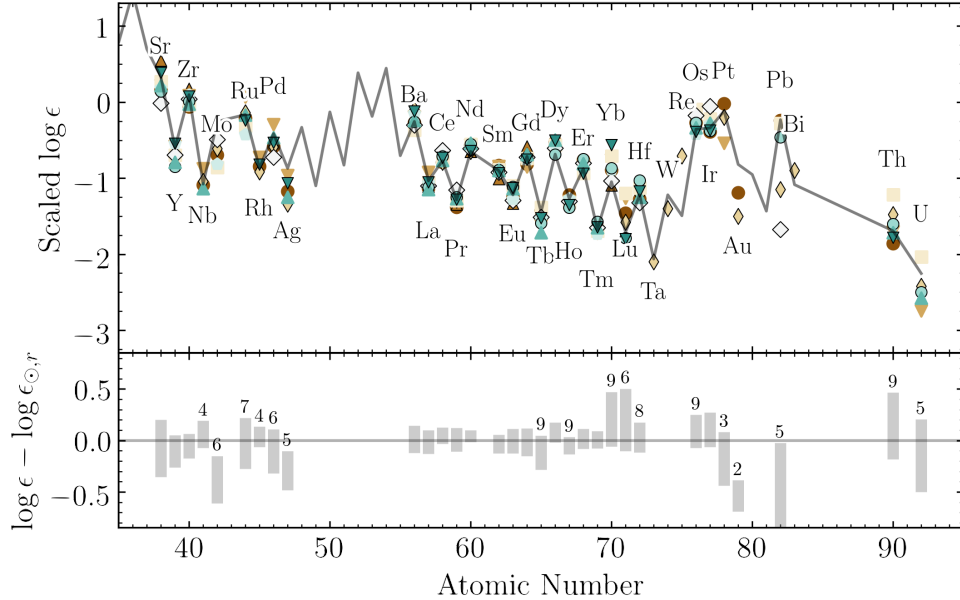


Figure 3.2. Scaled abundance patterns of ten r -II stars. The lower panel shows the spread of abundances from the Solar pattern, as well as how many stars have a reported measurement of each element.

dances that follow the first r -process peak—Sr, Y, and Zr—with respect to their scaled main r -process abundances (Siqueira Mello et al. 2014; Ji et al. 2016a). Due to these variations, it is thought that the Sr-Y-Zr group may originate from a different r -process environment than that which produces the lanthanides and actinides, such as the limited r -process, that primarily synthesizes the $Z < 56$ elements (Travaglio et al. 2004; Hansen et al. 2012; Arcones and Thielemann 2013; Wanajo 2013; Frebel 2018). Similarly, the actinide variation may indicate a separate r -process progenitor object or site that is responsible for the existence of actinide-boost stars (Schatz et al. 2002). The mechanism for producing this actinide boost is neither well-studied nor well-understood and suffers from low number statistics. Studying actinide-boost stars can provide clues to the different astrophysical conditions necessary to produce elements beyond the third r -process peak and help distinguish between suggested astrophysical sites for the r -process.

3.5 The *R*-Process Alliance

With only 30 *r*-II stars known in the Milky Way as of 2015—discovered in as many years—there is a clear need to discover additional “*r*-process relicts” in order to observationally constrain *r*-process production. A robust sample would allow the potential to differentiate between different sites, especially since SNe began to fall out of favor as primary *r*-process production sites. This necessity brought on the establishment of the *R*-Process Alliance (RPA) in 2016. Before the RPA, the *r*-II stars that were previously identified were drawn from a variety of observational efforts, each with different reduction and analysis techniques. The RPA was established not only to identify more *r*-II stars, but also to provide an homogeneously analyzed set of spectroscopic data. The next chapter discusses the RPA endeavor in detail, outlining our observing and analysis techniques used to identify *r*-process enhancement in metal-poor stars. Through only a few years of RPA efforts, an additional 30 *r*-II stars have been identified in the Galactic halo, already doubling the previous number (Sakari et al. 2018a; Hansen et al. 2018). Among the testaments to the success of RPA efforts, new significant discoveries have been made: two additional stars showing measurable amounts of uranium—only five of which were known previously—(Placco et al. 2017; Holmbeck et al. 2018), the highest-metallicity *r*-II star identified to-date (Sakari et al. 2018b), and a star with nearly Solar levels of absolute europium abundance (Roederer et al. 2018b). With a complete sample of *r*-process-enhanced stars in hand, we can begin to test the universality of the *r*-process pattern and quantify differences that arise, such as in the actinide elements.

CHAPTER 4

THE *R*-PROCESS ALLIANCE OBSERVATION AND ANALYSIS OF METAL-POOR STARS

The nitrogen in our DNA, the calcium in our teeth, the iron in our blood, the carbon in our apple pies were made in the interiors of collapsing stars. We are made of starstuff.

— Carl Sagan

4.1 Identifying Metal-Poor Stars

Spread across several “Phases,” the abstract goal of the RPA is to understand the *r*-process, which cannot be done effectively with the handful of *r*-II stars that were identified before the RPA was established. Phase I of the RPA is to first identify and confirm bright, low-metallicity candidates in the Milky Way using medium-resolution spectroscopy. Next, Phase II uses high-resolution spectroscopy to identify 75–100 new *r*-II stars among the confirmed metal-poor targets and build a robust catalog of observational *r*-process signatures with which to use in future analyses. This Phase II data release summarizes the work of Holmbeck et al. (2020), which provides an interim update on RPA efforts and progress towards identifying a robust, statistically significant sample of at least 100 new *r*-II stars.

To analyze metal-poor stars for *r*-process enhancement, a candidate list of metal-poor stars must first be compiled. Thanks to data from surveys such as the RAdial Velocity Experiment (RAVE; Steinmetz et al. 2006; Kordopatis et al. 2013; Matijević et al. 2017; Kunder et al. 2017), SkyMapper (Wolf et al. 2018; Yoon et al. 2018), Best

& Brightest (B&B; Schlaufman and Casey 2014), Hamburg/ESO (Christlieb et al. 2008), the Large Sky Area Multi-Object Fibre Spectroscopic Telescope (LAMOST; Deng et al. 2012), and stars selected based on the methods described in Meléndez et al. (2016), a first estimate of the stellar atmospheric parameters and metallicities of target stars can be found. These estimates are provided by the n-SSPP (Beers et al. 2014, 2017), a modified version of the SEGUE Stellar Parameter Pipeline (SSPP; Lee et al. 2008a,b, 2013). For this data release, target stars from RAVE were spectroscopically validated as metal-poor, and with effective temperatures useful for the identification of *r*-process elements (generally $4250 < T_{\text{eff}} < 5750$ K), using follow-up medium-resolution spectroscopy, e.g., as reported by Placco et al. (2018, 2019). After validating low-metallicity targets, moderately high signal-to-noise (S/N), moderately high-resolution ($R \sim 30,000$) “snapshot” spectra are taken of each target star. A S/N of ~ 30 at 4129 \AA is sufficient for the RPA Phase II snapshot determination of Eu abundances. Spectra in this data release were obtained with the Echelle spectrograph on the du Pont 2.5m telescope at the Las Campanas Observatory, using the $1'' \times 4''$ slit and 2×1 on-chip binning. The spectra cover a wavelength range from 3860 \AA to 9000 \AA for our 220 relatively bright stars ($10 \lesssim V \lesssim 13$) with low metallicities ($-3 \lesssim [\text{Fe}/\text{H}] \lesssim -1$). Data were reduced using the Carnegie Python Distribution¹ (Kelson 1998; Kelson et al. 2000; Kelson 2003). With spectra in hand we can determine the neutron-capture abundances of each target star and, therefore, identify potential *r*-process enhancement therein.

4.2 The Spectroscopic Determination of Atmospheric Parameters

Before determining the elemental abundances of each target star, something must be known of the structure of the stellar atmosphere that crucially shapes how the

¹<http://code.obs.carnegiescience.edu/>

elements are revealed in the spectrum. This analysis is accomplished by a careful evaluation of the atomic absorption features in the stellar spectrum. An absorption feature is formed when a photon entering an atom excites an electron to a different, discrete energy level. The wavelength (color) of the absorbed photon corresponds to the energy difference between these two energy levels. Since different elements have distinct energy separations of their electron orbitals, absorption features at particular wavelengths of light (give or take some quantum mechanical corrections) correspond to electronic transitions in specific elements.

In 1901, Annie Jump Cannon realized there was a relationship between the effective temperature of a star and the strength of its spectral lines. Now, the relationship between atomic absorption-line strength and stellar temperature can be calculated from statistical mechanics. Since the electrons of excited atoms occupy discrete energy levels, the ratio of ions populating a particular energy level versus the total number of ions in a gas at a temperature T is described by the Boltzmann equation:

$$\frac{n_i}{n} = \frac{g_i}{U} e^{-E_i/kT}, \quad (4.1)$$

where n_i is the number of ions in the i -th excitation level, g_i is the number of quantum states with the same energy (E_i), and U —the partition function—describes the statistical ensemble of the ion:

$$U = \sum_{i=1}^{\infty} g_i e^{-E_i/kT}. \quad (4.2)$$

Similarly, if the gas is hot enough, the ratio of atoms at a consecutive ionization levels is described by the Saha equation:

$$\frac{n_{i+1}}{n_i} = \frac{2U_{i+1}}{n_e U_i} \left(\frac{2\pi m_e k T}{h^2} \right)^{3/2} e^{-E/kT}, \quad (4.3)$$

where $n_{i,i+1}$ are the populations of adjacent ionization states i and $i + 1$, n_e is the number of free electrons, m_e is the electron mass, and here E is the ionization energy of the element. If the energy levels and degeneracies of a particular species are known, then for a certain density and temperature, the equilibrium population of ions can be determined from Equations 4.1–4.3. The process of determining the atmospheric abundances from stellar spectra employs this principle in reverse: measure the abundances of ions to find the temperature of a star. This process requires two basic ingredients: atomic data and an atmospheric model. The atomic data includes the excitation potentials and oscillator strengths for the electronic transitions of the elements, while the atmospheric model describes the structure of a stellar atmosphere with temperature, density, and stellar radius as a function of optical depth.

4.2.1 Equivalent Width and Line Formation

First, the abundances of the elements (n_i in Equations 4.1 and 4.3) must be calculated. One observable that can be measured from stellar spectra and related to the abundance is the equivalent width (W) of an absorption line, corresponding to a discrete atomic transition and occurring at a particular wavelength (energy) in the spectrum. In essence, W measures the area below the continuum: how much light is absorbed at a particular wavelength by an atomic transition. Since the stellar continuum flux is normalized to a height of 1, this area only needs to be expressed by the width of the rectangle that has the equivalent area to the flux absorbed by the entire feature, shown schematically in Figure 4.1. The strength of an absorption line for a particular atomic transition is related to its elemental abundance through W by

$$\log(W) = \log C + \log(N) + \log(gf \cdot \lambda) - \frac{5040}{T} \chi - \log(\kappa_\nu), \quad (4.4)$$

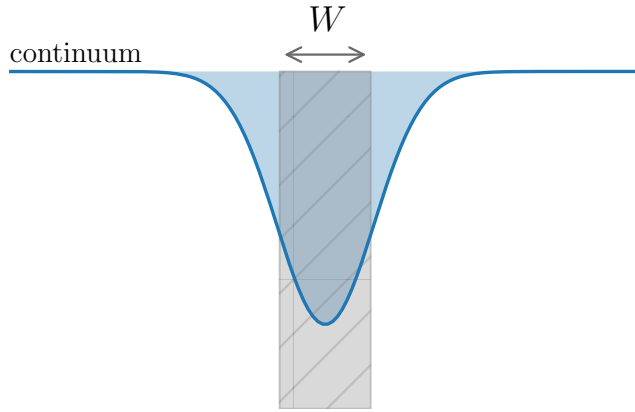


Figure 4.1. Schematic of a typical, continuum-normalized absorption feature and the equivalent width corresponding to that absorption.

where C is an empirical constant, N is the number of atoms of the element (the abundance), gf is the statistical oscillator strength of the transition, T is the temperature, χ is the excitation potential of the transition, and κ_ν is a continuum absorption coefficient. The absorption coefficient is related to the optical depth τ_ν , which determines the fraction of the intensity of light, I_ν , lost as it passes through the atmosphere by

$$\frac{d\tau_\nu}{ds} = \kappa_\nu, \quad (4.5)$$

where ds is the infinitesimal path travelled by the light at a frequency ν . Then the equivalent widths of transitions in particular elements, the atomic data describing those transitions (notably described by χ and gf), and a stellar atmospheric model are used to calculate the abundance of an element, given that the parameters supplied to the atmospheric model sufficiently describe the stellar photosphere.

4.2.2 Key Atmospheric Parameters

The key properties describing the structure of a stellar atmosphere and the strengths of the elemental absorption features are effective temperature (T_{eff}), surface gravity ($\log g$), and microturbulence (ξ). The impact of temperature is already shown in Equations 4.1–4.3. Generally, for stars targeted by the RPA, the higher the T_{eff} , the more ionization occurs, decreasing the strength of the absorption lines. Therefore, T_{eff} is sensitive to the ionization and excitation potentials of the absorbers. The surface gravity increases the density gradient of the atmosphere, thereby increasing the number density of available absorbers. For the same elemental abundance, an increase in $\log g$ will therefore cause more photons to be absorbed, and thus stronger-appearing absorption lines. Together with T_{eff} , the $\log g$ affects the ratio of adjacent ionization states (see Equation 4.3). The microturbulent velocity is added as a correction to the 1D stellar atmospheric models that are employed to describe the non-thermal, bulk motion of matter that is expected to occur in the real 3D atmosphere of a star. Changing the microturbulence causes electronic transitions to occur more or less red/blue-shifted from the central wavelength of the absorbed feature. However, this shift is not monotonic across all wavelengths, and instead affects transitions differently depending on their strength, i.e., their W .

These parameters are degenerate in their effects on individual lines. Therefore, the “spectroscopic” method for relating the microscopic spectral features to the macroscopic stellar parameters occurs iteratively. First, the equivalent widths of various elements are measured, and a line list describing the atomic properties of those electronic transitions is compiled. Then, some initial values of T_{eff} , $\log g$, and ξ are supplied to the model. All three of these components are used to solve Equations 4.1 and 4.3 and the radiative transfer equation, describing the loss of intensity at each

wavelength as it travels through the stellar atmosphere:

$$\frac{dI_\nu}{ds} = -\kappa_\nu I_\nu + \epsilon_\nu, \quad (4.6)$$

where κ_ν is the absorption coefficient as in Equation 4.4, and ϵ_ν is the corresponding emission coefficient. Integrating the intensity over the entire solid angle Ω yields the total flux of light at frequency ν , F_ν :

$$\pi F_\nu = \int I_\nu \cos \theta d\Omega, \quad (4.7)$$

Combining Equations 4.1–4.7 allows a solution for the flux of each wavelength of light through a stellar atmosphere, given a set of atomic data and atmospheric parameters. These equations are solved iteratively until the flux over all wavelengths agrees with the flux calculated from $F = \sigma T^4$ at every optical depth τ_ν . If convergence is reached, then the input atmospheric parameters are accepted as a good description of the star. If the flux has not converged, then the atmospheric parameters are adjusted, and the equations recalculated. Note that whenever the parameters are changed, the calculated abundance from a given equivalent width also changes. In this way, the atmospheric parameters are iteratively adjusted until convergence is reached.

This work uses the current version of the stellar line analysis code **MOOG**² to solve these equations (Sneden 1973). This version of MOOG includes an appropriate treatment of scattering (Sobeck et al. 2011) and assumes local thermodynamic equilibrium (LTE). Oscillator strengths and excitation potentials for all lines in this work were generated with `linemake`³, which compiles recent, accurate atomic transition data and includes hyperfine splitting. Isotopic ratios, employed when synthesizing features

²<https://github.com/alexji/moog17scat>

³<https://github.com/vmplacco/linemake>

with hyperfine-splitting and isotopic-shift effects, were taken from the Solar r -process ratios in [Sneden et al. \(2008\)](#). Since the majority of stars in this work are metal-poor, α -enhanced ($[\alpha/\text{Fe}] = +0.4$) ATLAS9 model atmospheres are used ([Castelli and Kurucz 2003](#)).

In `MOOG`, convergence of the atmospheric parameters can be visualized by the trends in line-by-line abundances, since the total abundance of an element in a stellar atmosphere should be independent of quantities like wavelength. A converged temperature will show no trend in the excitation potential, χ (refer to Equations 4.1–4.3), while a converged microturbulence shows no trend in the reduced equivalent width, $\log(W/\lambda)$. Based on Equation 4.3, the surface gravity, $\log g$, is found by balancing the abundance of an element in multiple ionization states. Since the abundance of a given element in an atmosphere should not be a function of χ , $\log(W/\lambda)$, or ionization state, the parameters must be adjusted until the total abundance of an element measured from one ionization state agrees with that measured from a different ionization state. Figure 4.2 summarizes the results of the spectroscopic method, displaying the trend of abundances derived from equivalent widths of individual Fe I and Fe II absorption features. The temperature, surface gravity, and microturbulence are iteratively adjusted until these trends are flattened.

4.3 Other Methods for Determining Atmospheric Parameters

Besides the spectroscopic method, there are other ways through which to infer the key properties of a stellar atmosphere.

4.3.1 Differential Analysis

Sometimes, the stellar parameters of a star are too extreme to be found spectroscopically. Requiring a flat trend in Fe I excitation potential pushes the $\log g$ to unphysical values if the grid of model atmospheres does not include giant stars with

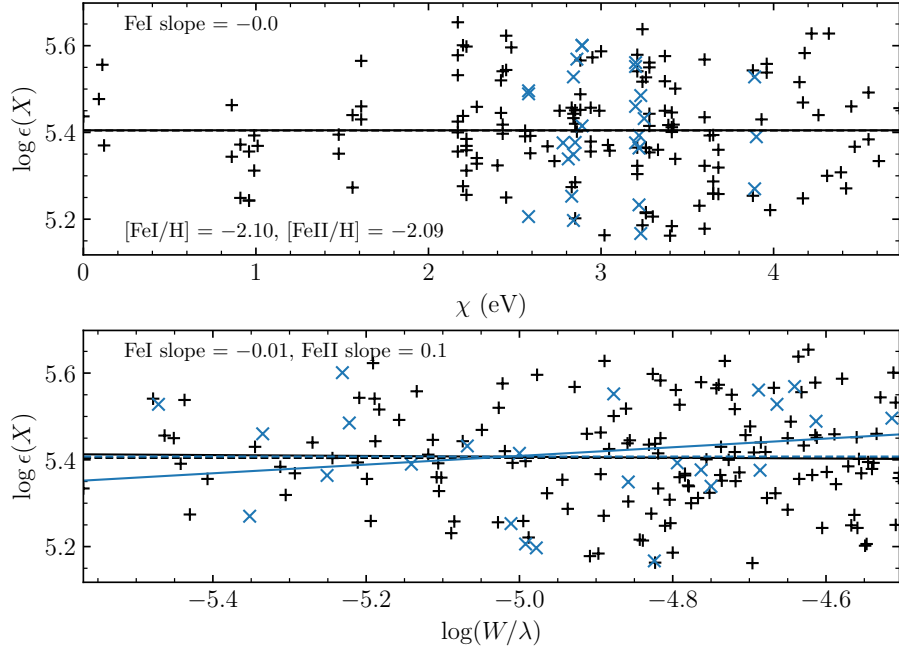


Figure 4.2. Abundance trends of individual Fe I and Fe II lines, indicated with black pluses and blue crosses, respectively, for finding atmospheric parameters via the spectroscopic method. Lines are a least-squares linear fit to each ionization state.

low effective temperatures ($T_{\text{eff}} \lesssim 4200$ K) and surface gravities. A differential analysis is a way to work around the direct spectroscopic method. This method involves selecting a star with well-known parameters relatively close to the star with unknown parameters. Using the incomplete grid of model atmospheres, the individual line-by-line Fe abundances may yield non-zero trends, even if the model atmosphere input parameters are well-known. For the star with unknown parameters, instead of requiring flattened trends in Fe abundance, the best-fit model atmosphere is when the trends (i.e., the slope of the line fitting the Fe abundances as a function of both excitation potential and reduced equivalent width) agree with those from the reference star.

4.3.2 Photometric Analysis

The atmospheric parameters of a star can also be determined photometrically. First, magnitudes and color indices supply the effective temperature of a star (e.g., Alonso et al. 1999; Casagrande et al. 2010). Next, if the star has a precisely measured parallax (for example, from Gaia Collaboration et al. 2016), then the surface gravity can be derived from its calculated distance, temperature, and apparent bolometric magnitude:

$$\log(g/g_{\odot}) = \log(M/M_{\odot}) + 4 \log(T_{\text{eff}}/T_{\text{eff},\odot}) + 0.4(M_{\text{bol}} - M_{\text{bol},\odot}), \quad (4.8)$$

where M is the mass of the star—assumed to be $0.8M_{\odot}$ for presumed old, low-metallicity giants—and M_{bol} is the absolute bolometric magnitude of the star, which can be calculated from the apparent bolometric magnitude through the distance modulus.

4.4 Atmospheric Parameters for RPA Targets

For this RPA data release, the spectroscopic method is employed to determine the atmospheric abundances of target stars, in which the equivalent-width measurements of Fe I and Fe II lines are used to derive the 1D LTE stellar parameters, based on ATLAS9 model atmospheres (Castelli and Kurucz 2003). First, the equivalent widths of a large number of Fe lines are measured (on average, 82 Fe I and 20 Fe II lines). Next, the MOOG code is used to derive an Fe abundance for each line and determine the atmospheric parameters as described in Section 4.2. Spectroscopically derived atmospheric parameters using 1D LTE models systematically disagree with photometric determinations. Therefore, the following relation from Frebel et al. (2013) to

correct the offset between the spectroscopic and photometric temperature scales:

$$T_{\text{eff,corrected}} = T_{\text{eff,initial}} - 0.1 \times T_{\text{eff,initial}} + 670. \quad (4.9)$$

As our sample is dominated by cool stars, this temperature shift is, on average, about 200 K, ranging from about 60 K for the warmest stars and up to about 400 K for the coolest stars.

Assuming LTE can often underestimate the iron abundance relative to non-LTE, and therefore affect the determination of stellar parameters, especially for increasingly metal-poor stars. Based on the low surface gravity and low temperature non-LTE Fe I abundance correction models in [Lind et al. \(2012\)](#), we find that the average non-LTE correction to the [Fe I/H] abundance is less than +0.2 dex for the stars in this sample that have $[\text{Fe}/\text{H}]_{\text{LTE}}$ between -3 and -2 . The correction decreases with both increasing metallicity and increasing surface gravity and becomes negligible at $[\text{Fe}/\text{H}] > -1$. This estimated correction is also supported by empirical fits to ultra-metal-poor stars in [Ezzeddine et al. \(2017\)](#), which show that for lower-metallicity stars, $[\text{Fe}/\text{H}]_{\text{LTE}}$ between -3 and -2 , the non-LTE correction to the iron abundance can range between 0.13 and 0.27 dex, and a star with $[\text{Fe}/\text{H}] \approx -1.0$ has a negligible -0.01 dex correction. However, for lower-metallicity stars with $[\text{Fe}/\text{H}] \approx -3.0$, this correction increases to nearly 0.3 dex, which dominates over the statistical line-by-line uncertainty. As most of the targets in this sample have metallicities between $-3 \leq [\text{Fe}/\text{H}]_{\text{LTE}} \leq -2$, the non-LTE effect to the iron abundance is at least on the order of the statistical line-by-line uncertainty and can significantly affect the derived atmospheric parameters. To be consistent with previous RPA data releases, we assume LTE in the current study. However, in future RPA data analyses, non-LTE effects will be homogeneously incorporated into the iron abundances and stellar parameter determinations. The (LTE) model atmospheric parameters for this RPA

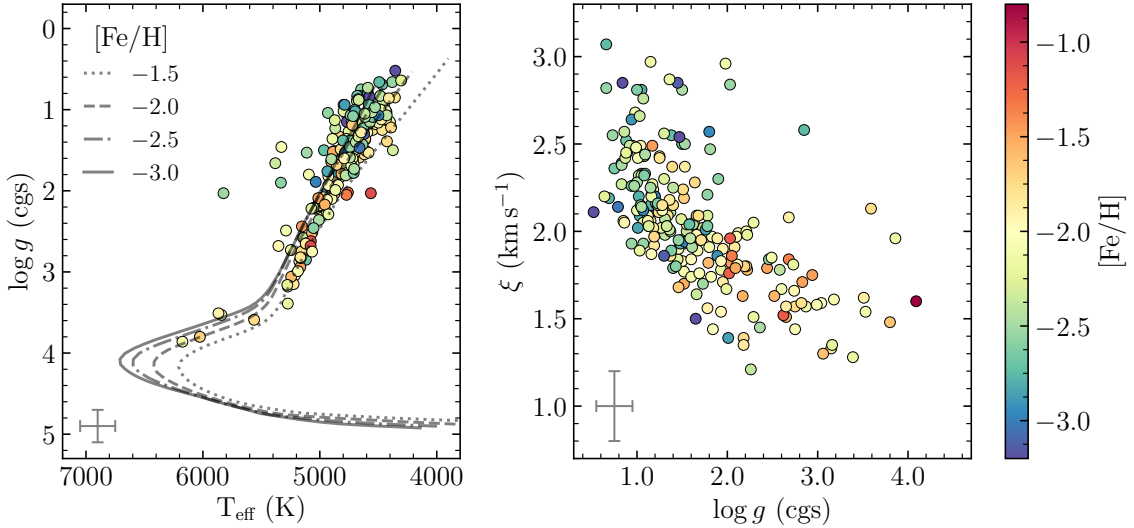


Figure 4.3. Left: surface gravity versus effective temperature measurements for the target stars. Solid, dot-dashed, dashed, and dotted lines are isochrones for $[\text{Fe}/\text{H}] = -3.0, -2.5, -2.0$, and -1.5 , respectively (Demarque et al. 2004). Right: microturbulent velocity versus surface gravity for our target stars. Both panels are color-coded by metallicity, and the error bars in the lower-left corners represent the standard uncertainties assumed on the atmospheric parameters (see text for details).

data release are listed in Table A.2 of the Appendix. Figure 4.3 shows the final derived surface gravities as a function of the derived effective temperature, after the applied correction and the microturbulent velocities used for the 1D LTE models as a function of the derived surface gravity. A few of the target stars were more metal-rich than previously estimated from the Phase I medium-resolution spectroscopic validation described in Placco et al. (2018), but overall the Phase I method proves effective for identifying metal-poor stars.

4.5 Neutron-Capture Abundances

MOOG is also used to derive abundances for C, Sr, Ba, and Eu from spectral synthesis in order to make an initial classification of each target into either r -I, r -II,

limited- r , CEMP, or no r -process enhancement (“non-RPE”). The C abundances were primarily derived by fitting the entire CH G -band at 4313 Å. For cooler CEMP stars ($\lesssim 4200$ K), where the G -band is likely saturated, abundances were derived from the C₂ Swan band at 5161 Å. The Sr abundances were derived from two strong lines, at $\lambda 4077$ Å and $\lambda 4215$ Å, which can be significantly blended with Fe (and ^{66}Dy , if present). We derive Ba abundances from lines at $\lambda 5853$ Å, $\lambda 6141$ Å, and $\lambda 6496$ Å. Eu abundances are mainly derived from the $\lambda 4129$ Å, $\lambda 4205$ Å, and $\lambda 4435$ Å features. Since the $\lambda 4435$ Å line is heavily blended by a neighboring Fe feature, and $\lambda 4205$ Å by C and Ca, the $\lambda 4129$ Å feature is primarily used to derive the Eu abundance. The $\lambda 4205$ Å feature may be significantly blended with C if the target is C-enhanced. However, since most of our targets do not have enhanced C, the $\lambda 4205$ Å line was minimally affected. Figure 4.4 shows key Sr, Ba, and Eu features in a limited- r , r -I, and r -II star along with their synthesized abundance.

To estimate the uncertainties on the derived abundances from constant stellar parameter uncertainties, we first assume a conservative typical uncertainty on effective temperature of 150 K, 0.2 dex on surface gravity, and 0.2 km s⁻¹ on microturbulence. We do not vary the metallicity, but instead use the random uncertainty associated with the line-by-line variation between iron abundances, i.e., $\sigma_{[\text{Fe}/\text{H}]}$ in Table A.2. Then, we choose spectra that represent the parameter ranges for our targets: a somewhat hot star (~ 5000 K) with $[\text{Fe}/\text{H}] \approx -2.0$, a cooler star (~ 4500 K) star with $[\text{Fe}/\text{H}] \approx -2.5$, and a moderate-temperature (~ 4800 K) star with $\log g \approx 1.0$. With these three representative targets, we vary each of the stellar parameters within the above uncertainties individually and rederive the best-fit abundances for C, Sr, Ba, and Eu.

Table 4.1 reports the abundance variations after changing the atmospheric parameters individually. We report both the systematic uncertainty (σ_{sys}) from the atmospheric parameters as well as the total uncertainty when the random error on

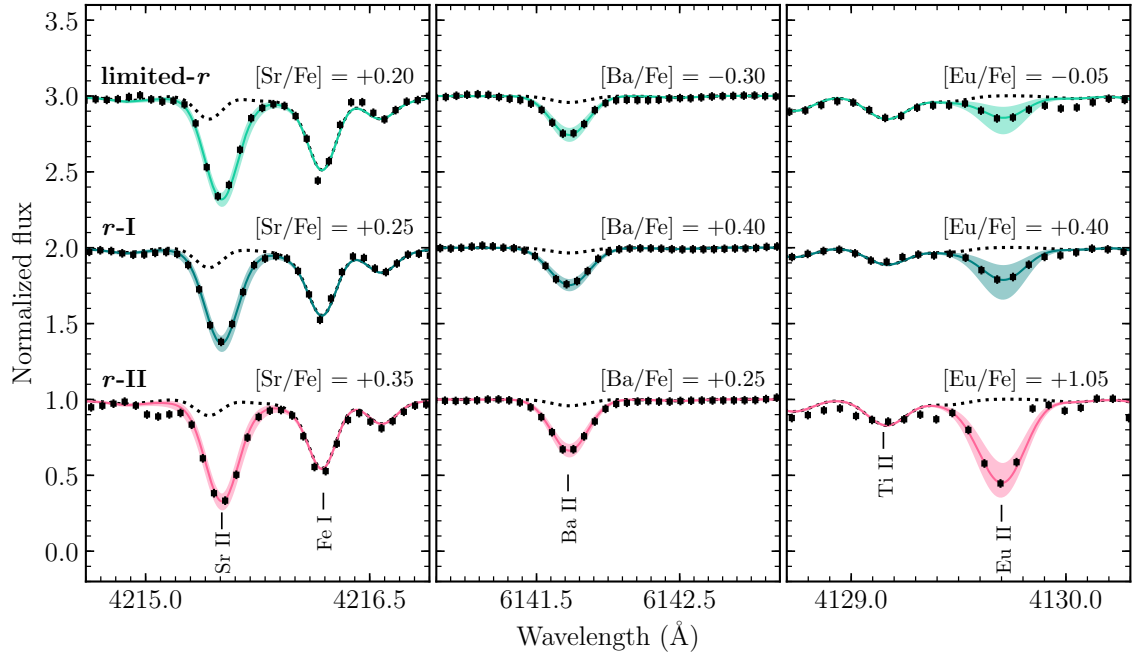


Figure 4.4. Scaled spectrum snippets in the regions of interest for an r -II star (bottom, J03422816–6500355), an r -I star (middle, J20194310–3158163), and a limited- r star (top, J10344785–4823544). The MOOG syntheses for Sr II (left), Ba II (middle), and Eu II (right) are shown for the best fit and with a ± 0.30 dex uncertainty, which more than accommodates the random uncertainty due to S/N and systematic uncertainties in the atmospheric parameters.

the metallicity is included (σ_{tot}). Note that it is more appropriate to use σ_{sys} when using the $\log \epsilon$ abundances and σ_{tot} for $[\text{X}/\text{Fe}]$ abundances. On average, the uncertainty on the $[\text{Sr}/\text{Fe}]$, $[\text{Ba}/\text{Fe}]$, and $[\text{Eu}/\text{Fe}]$ abundances round to 0.2 dex. The average random uncertainty from $[\text{Fe}/\text{H}]$ is 0.14 dex for stars in this data release. These average uncertainties are represented in Figures 4.5 and 4.8 by an error bar in the corner.

Final derived Fe, C, Sr, Ba, and Eu abundances for our 232 program stars are listed in Table A.3, along with their r -process classification. All $[\text{X}/\text{Y}]$ abundances use the Solar System measurements from Asplund et al. (2009). The neutron-capture elements—Sr, Ba, and Eu—indicate which neutron-capture processes dominated the

TABLE 4.1
ABUNDANCES UNCERTAINTIES FOR EXAMPLE STARS

	T _{eff} ± 150 K	log <i>g</i> ± 0.2 dex	ξ $\pm 0.2 \text{ km s}^{-1}$	[Fe/H] $\pm \sigma_{\text{[Fe/H]}}$	σ_{sys}	σ_{tot}
J16285613–1014576	5078	1.80	2.07	−1.93		
[C/Fe]	±0.23	±0.05	±0.05	±0.11	±0.24	±0.26
[Sr/Fe]	±0.11	±0.06	±0.04	±0.11	±0.13	±0.17
[Ba/Fe]	±0.11	±0.07	±0.12	±0.11	±0.18	±0.21
[Eu/Fe]	±0.07	±0.06	±0.03	±0.11	±0.10	±0.15
J20504869–3355289	4549	1.09	2.33	−2.63		
[C/Fe]	±0.32	±0.10	±0.03	±0.14	±0.34	±0.36
[Sr/Fe]	±0.15	±0.04	±0.11	±0.14	±0.19	±0.24
[Ba/Fe]	±0.08	±0.05	±0.08	±0.14	±0.12	±0.19
[Eu/Fe]	±0.10	±0.05	±0.01	±0.14	±0.11	±0.18
J04014897–3757533	4797	1.02	2.32	−2.28		
[C/Fe]	±0.33	±0.08	±0.05	±0.13	±0.34	±0.37
[Sr/Fe]	±0.10	±0.06	±0.14	±0.13	±0.18	±0.22
[Ba/Fe]	±0.08	±0.07	±0.08	±0.13	±0.13	±0.19
[Eu/Fe]	±0.08	±0.05	±0.02	±0.13	±0.10	±0.16

elemental production preceding the formation of these stars; the absorption features of these elements are among the strongest of all neutron-capture elements for stars with similar atmospheric parameters. Together, these five elements provide a comprehensive overview of the nucleosynthetic history of each star. This work focuses especially on characterizing the neutron-capture nucleosynthesis signatures in halo stars.

The Sr, Ba, and Eu abundances are used to both determine the dominant source of the neutron capture elements and also to quantify various regions of the *r*-process

pattern. In particular, Ba and Eu abundances can be used as a metric for whether the neutron-capture elements in each star were primarily synthesized through an *s*- or *r*-process (Frebel 2018, and references therein). In essence, if the *r*-process dominated the production of neutron-capture elements, the observed ratio of Ba to Eu will be less than the Solar value, or $[\text{Ba}/\text{Eu}] < 0$. Alternatively, the $[\text{Ba}/\text{Eu}]$ abundance is greater than Solar if the *s*-process dominated the production of neutron-capture elements. In the neutron-capture elemental abundance pattern, the “first *r*-process peak” is approximately indicated by the Sr abundance, while Ba is approximately representative of the second abundance peak. Current studies argue that the light *r*-process elements (i.e., the first *r*-process peak) could originate from a separate *r*-process source (the limited *r*-process) than that which synthesized the second and third *r*-process peaks (Truran et al. 2002; Honda et al. 2006; Wanajo and Ishimaru 2006). Thus, the ratio of Sr to Ba quantifies the amount of limited-*r* production. These considerations motivate using the relative abundances of Sr, Ba, and Eu to determine whether the elements in each originated primarily from a limited-*r*, *s*-process, or *r*-process production site.

4.6 Revisiting the $[\text{Eu}/\text{Fe}]$ *r*-II Cutoff Value

Figure 4.5 shows the $[\text{Eu}/\text{Fe}]$ abundances as a function of metallicity from this work and previous RPA data releases. The majority of the targets were identified as *r*-I stars, with eight as limited-*r* stars, under the current *r*-I and limited-*r* definitions. Using the value $[\text{Eu}/\text{Fe}] > +1.0$, as employed by the RPA up to now, only four new *r*-II stars were identified in the present data release. The four stars with $[\text{Eu}/\text{Fe}] > +1.0$ and $[\text{Ba}/\text{Eu}] < 0.0$ are J03422816–6500355, J05383296–5904280, J07103110–7121522, and J07202253–3358518. They are all of moderate temperature and together span about 1 dex in metallicity. This rate ($\sim 1.7\%$) indicates a decrease relative to the previous success rate of RPA efforts, which have either agreed with or exceeded the

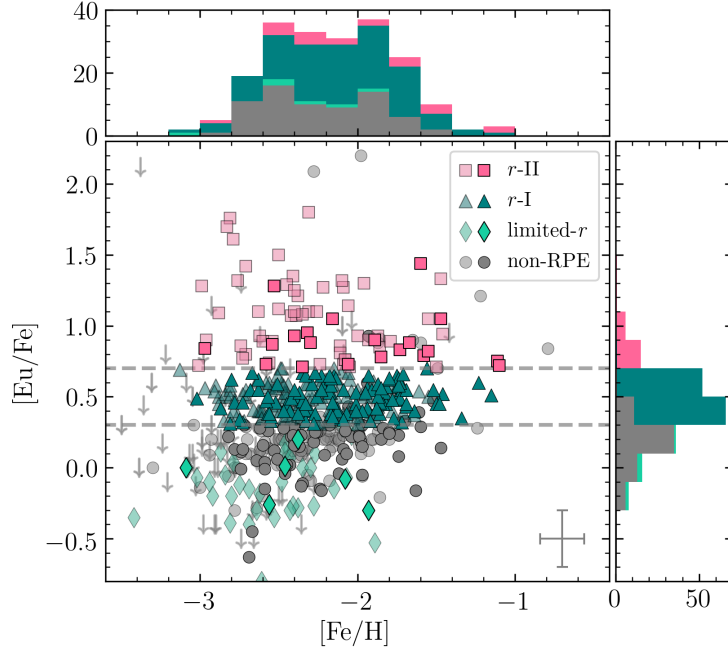


Figure 4.5. Derived $[\text{Eu}/\text{Fe}]$ abundances, as a function of metallicity, for the stars in this sample, labeled by r -process enhancement type: non-RPE (circles), r -II (squares), r -I (triangles), and limited- r (diamonds). Upper limits on Eu are indicated by a downward arrow. Also shown are the current RPA-identified r -process-enhanced stars (same labeling, lighter colors). Horizontal dashed lines indicate $[\text{Eu}/\text{Fe}] = +0.3$ and $+0.7$, showing the cutoff levels for r -I and r -II classification. See text for details.

expected r -II discovery rate among VMP stars of 3–5%, as estimated by Christlieb et al. (2004) and Barklem et al. (2005). This decrease is likely the result of the extension to higher metallicity of our present sample compared with previous RPA data releases.

The distribution of $[\text{Eu}/\text{Fe}]$ abundances found in metal-poor stars is likely to be a continuum, unless different classes of r -process progenitors contribute significantly different amounts of lanthanides, which remains uncertain at present. A simple Kolmogorov-Smirnov test fails to rule out the null hypothesis that r -I and r -II stars from the full RPA sample to date are drawn from the same parent distribution of $[\text{Fe}/\text{H}]$, as has been previously speculated based on smaller samples (e.g., Barklem

et al. 2005). Still, it is operationally useful to differentiate between moderately and extremely r -process-enhanced stellar signatures to investigate whether these stars have different r -process sources. With the availability of the now myriad amount of data from RPA efforts, we can reconsider where this split between r -I and r -II stars should lie, based on the data in hand.

Without appeal to any particular physical models, we agnostically consider the existence of two or three distinct populations within the entire [Eu/Fe] distribution (note that we include the limited- r stars for this exercise). To mitigate concerns of the sample size ($N = 471$) contributing to misinterpretation, we consider the r -I and r -II boundaries resulting from the robust partitioning technique known as k -medoids (Kaufman and Rousseeuw 1990). Similar to the k -means algorithm, this partitioning procedure seeks to minimize the distance between cluster members to determine cluster centers. We consider the cases $k=2$ and $k=3$ clusters separately, and evaluate the resulting [Eu/Fe] classifications. In the case of two clusters, the boundary is determined to occur at $[{\rm Eu}/{\rm Fe}] = +0.4 \pm 0.2$, whereas the three-cluster case results in the boundaries $[{\rm Eu}/{\rm Fe}] = +0.3 \pm 0.1$ and $+0.7 \pm 0.2$ for r -I and r -II classification, respectively. Increasing the number of clusters did not significantly reduce the information loss, so we do not consider $k > 3$ cases.

We evaluate the extent to which the [Eu/Fe] distribution is better represented by two or three components with a Gaussian mixture model via the Akaike information criterion (AIC; Akaike 1973). This criterion appropriately weights the goodness-of-fit with the simplicity of the model, mitigating the effects of overfitting when arbitrarily adding additional components to the model. Using a two-component Gaussian mixture model suggests a slightly higher degree of information loss (AIC = 284) than a three-component mixture (AIC = 278), from which we conclude that that sample [Eu/Fe] distribution is more appropriately represented by three distinct populations, given the assumption of normally distributed components. Note that

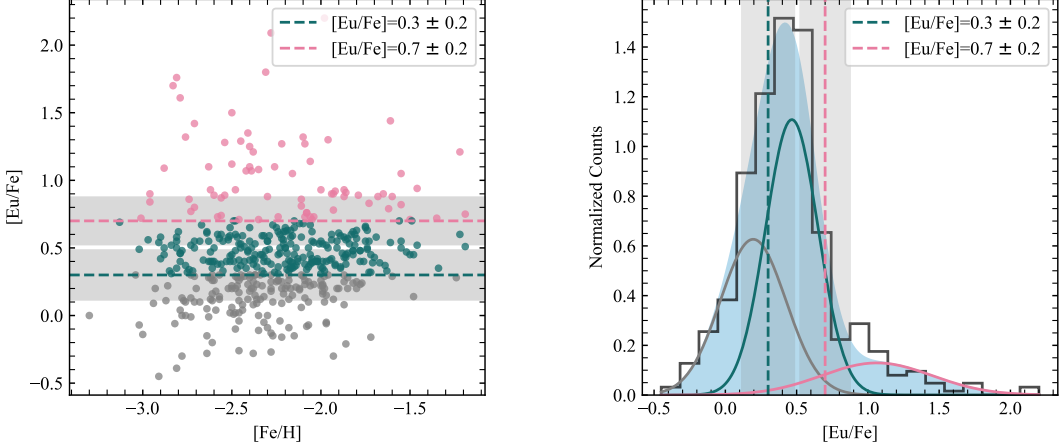


Figure 4.6. Left: scatter plot of [Eu/Fe] as a function of metallicity for RPA stars (excluding upper limits) colored by the average k -medoids grouping with $k=3$. Right: histogram of all RPA [Eu/Fe] abundances compared to Gaussian mixture model with three components. Teal and pink lines with gray shaded regions correspond to the average with their standard deviations of the k -medoids decision boundaries defining r -I and r -II.

the AIC for a four-component mixture increases to 290, reiterating that more than three populations will overfit the data in hand. Furthermore, the AIC presumes well-populated Gaussians, for which three components are sufficient to fit the current amount of data. This analysis does not preclude the possibility of four populations existing when more data are available in the future. Figure 4.6 depicts the resulting r -I and r -II classification boundaries, as well as the final three-component Gaussian mixture model.

Adopting the split at $[Eu/Fe] > +0.7$ to distinguish r -II stars from r -I stars, the new classifications of r -I and r -II are now:

$$r\text{-I: } 0.3 < [Eu/Fe] \leq +0.7, \quad [Ba/Eu] < 0$$

$$r\text{-II: } [Eu/Fe] > +0.7, \quad [Ba/Eu] < 0.$$

Note that Roederer et al. (2018a) also proposed a division at $[Eu/Fe] = +0.7$, based

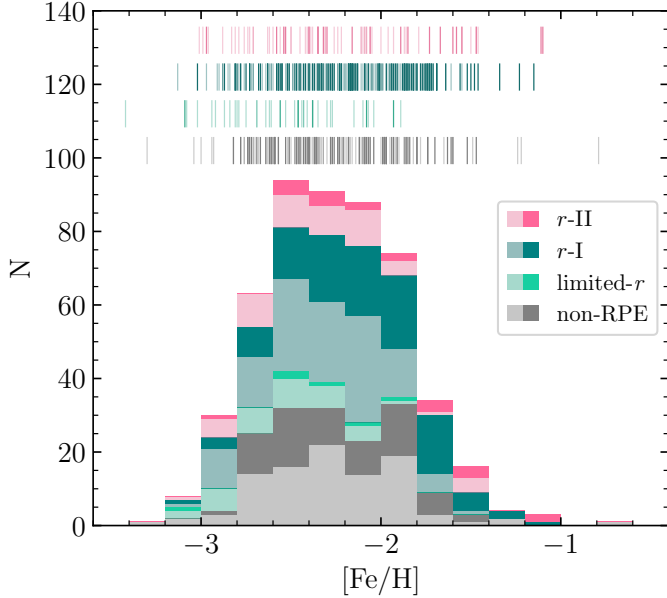


Figure 4.7. $[\text{Fe}/\text{H}]$ histograms of r -process-enhanced stars identified by the RPA. Darker colors represent this data release, and lighter colors are all previous RPA data releases (Hansen et al. 2018; Sakari et al. 2018a; Ezzeddine et al. 2020). At the top, stripe density plots of the individual classes are shown.

on the simple observation that this value effectively excluded most metal-poor stars in the globular cluster and disk populations from the r -II class. This redefinition does not affect the limited- r class, which are still defined as $[\text{Eu}/\text{Fe}] < +0.3$, $[\text{Sr}/\text{Ba}] > +0.5$, and $[\text{Sr}/\text{Eu}] > 0.0$ as in Frebel (2018). With this new classification of r -I and r -II, we identify a total of 21 new r -II, 111 new r -I, and 7 new limited- r stars in this data release. The number of previously identified r -I and r -II stars (before the RPA was established) changes from 136 and 28 to 99 and 65, respectively, using data in the JINAbase compilation. In the future, as we gather more data about the Milky Way halo, especially at higher metallicities ($[\text{Fe}/\text{H}] \gtrsim -2$), we might consider a metallicity-dependent separation, which may further help distinguish between r -process progenitors at different times throughout Galactic history.

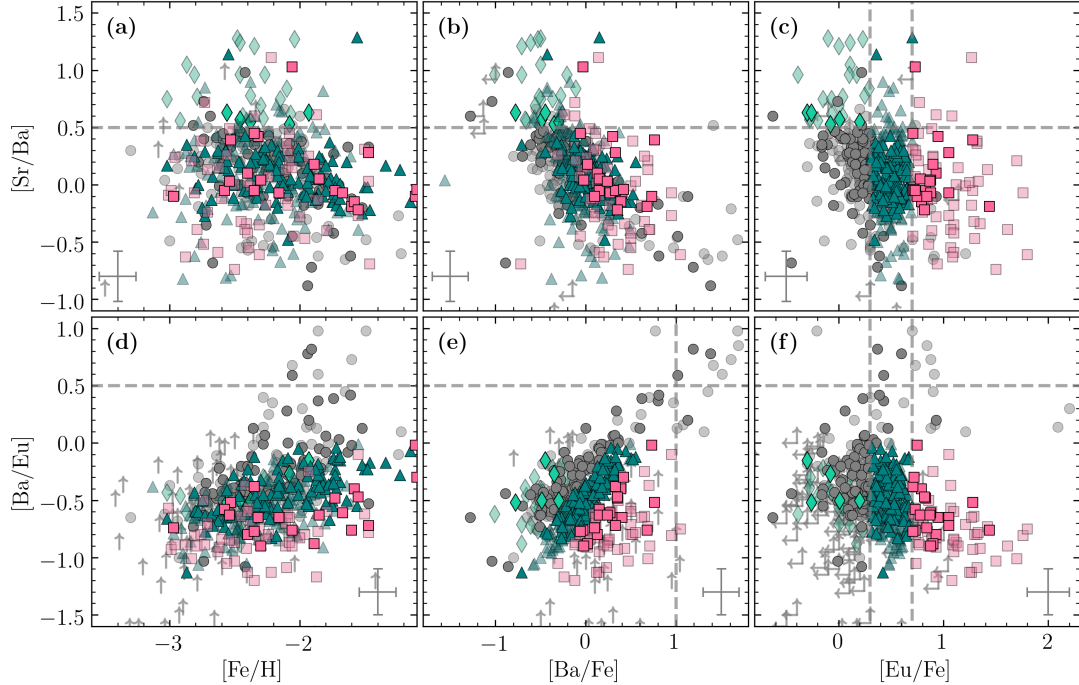


Figure 4.8. Abundance ratios versus $[Fe/H]$ (panels a and d), $[Ba/Fe]$ (panels b and e), and $[Eu/Fe]$ (panels c and f) for $[Sr/Ba]$ (panels a–c) and $[Ba/Eu]$ (panels d–f) for stars in this sample (dark colors) and previous RPA data releases (light colors). Dashed lines denote the adopted classification cutoffs for r -II, r -I, limited- r , and s -process signatures (see text for details).

Figure 4.7 is a summary of the classification of metal-poor stars based on the RPA data releases to date, using this new definition. Including this data release, RPA efforts now total 72 r -II, 232 r -I, and 42 limited- r stars among the 595 targets with snapshot and portrait spectra that have been analyzed to date in Hansen et al. (2018); Roederer et al. (2018b); Sakari et al. (2018a,b, 2019) and Ezzeddine et al. (2020).

4.6.1 Other Neutron-Capture Signatures

The $[Sr/Ba]$ and $[Ba/Eu]$ abundance ratios for RPA stars are plotted in Figure 4.8 as functions of $[Fe/H]$, $[Ba/Fe]$, and $[Eu/Fe]$. Stars classified as limited- r occupy the

high-[Sr/Ba], low-[Eu/Fe] end of the scatter (Figure 4.8c). There are no apparent correlations between the [Sr/Ba] and metallicities for *r*-I and *r*-II stars (Figure 4.8a). Instead, *r*-I and *r*-II stars are found in roughly equal proportions across a range of low metallicities, implying that the production sites of Sr and Ba are generally uncorrelated in metal-poor stars. However, we note that all identified limited-*r* stars thus far are VMP ($[\text{Fe}/\text{H}] \leq -2.0$). This lack of limited-*r* stars at higher metallicities can also be seen in Figure 4.5, in which the spread of [Eu/Fe] abundances dramatically decreases at higher metallicity. Côté et al. (2019) discuss this narrowing in detail, and investigate which *r*-process sites might be responsible for this behavior. For example, a limited-*r* mechanism could have dominated at early times, then became more rare as metallicity increased.

Interestingly, there is a downward trend of high [Sr/Ba] with increasing [Eu/Fe] abundance (Figure 4.8c). At $[\text{Sr}/\text{Ba}] > +0.5$, most stars have somewhat low [Eu/Fe] and are thus classified as limited-*r* stars. Fewer stars have both high [Sr/Ba] and an *r*-I signature, and even fewer stars with high [Sr/Ba] are considered *r*-II. This apparent upper limit could suggest a possible constraint on limited-*r* production by prolific main *r*-process sources. The *r*-II stars with high [Sr/Eu], by definition, show evidence for at least one robust *r*-process source, but also for a potential secondary limited-*r* production site, since they exhibit an over-abundance of both Sr and Eu, but a relative under-abundance of Ba. Our ability to refine and interpret these apparent behaviors will only increase as the size of the RPA sample continues to expand.

We also identify some stars with high [Ba/Eu] and high [Ba/Fe] (Figure 4.8e); the neutron-capture elements in these stars are dominated by *s*-process production. We identify three new *s*-process-enhanced stars based on these high Ba ratios, and label them as such in Table A.3. Slightly lower on the [Ba/Eu] scale are stars with a more mixed neutron-capture element signature showing an apparent combination of an *r*-process and *s*-process pattern, notably with $0.0 < [\text{Ba}/\text{Eu}] \leq +0.5$ (Frebel 2018).

Based on this criterion only, we identify 10 new stars with moderately high [Ba/Eu] abundance ratios. It is currently unclear how the neutron-capture element abundance pattern in these stars is formed. For one star it has been identified to be a combination of enrichment by first an *r*-process and then an *s*-process, earning the label of “*r+s*” (RAVE J094921.8–161722; see [Gull et al. \(2018\)](#) for details) For the majority of these stars, this two-component enrichment cannot be invoked to explain their abundance patterns, and it has been speculated to be the signature of the *i*-process ([Dardelet et al. 2015](#); [Hampel et al. 2016](#)). Higher resolution, higher S/N spectroscopic follow-up (“portrait” RPA spectra) on the ten candidate *r+s* stars could provide a distinct definition for this new classification of stars, as well as distinguish them from the *r/s* and *i*-process classes.

4.7 Radial-Velocity Variations

Monitoring any variation in the radial velocity (RV) of stars can reveal whether these stars are in binary systems. Binarity may affect the derived stellar abundances by allowing, e.g., mass transfer between stars. Therefore, we measure the RV of our target stars to identify potentially interesting systems. RVs were measured with the *fxcor* task in the Image Reduction and Analysis Facility ([IRAF](#)⁴), using order-by-order cross-correlation between the target and select RV standards: HD 14412 (7.46 km s^{−1}), HD 96700 (12.84 km s^{−1}), HD 146775 (−30.15 km s^{−1}), HD 22879 (120.40 km s^{−1}), and HD 189625 (−28.13 km s^{−1}), from [Soubiran et al. \(2013\)](#). For each target, the RV is found by taking the weighted average of each order’s individual radial-velocity measurements, following the iterative removal of 2- σ outliers. On average, 15 orders with strong, unsaturated features were used for cross-correlation

⁴IRAF is distributed by the National Optical Astronomy Observatory, which is operated by the Association of Universities for Research in Astronomy, Inc., under cooperative agreement with the NSF.

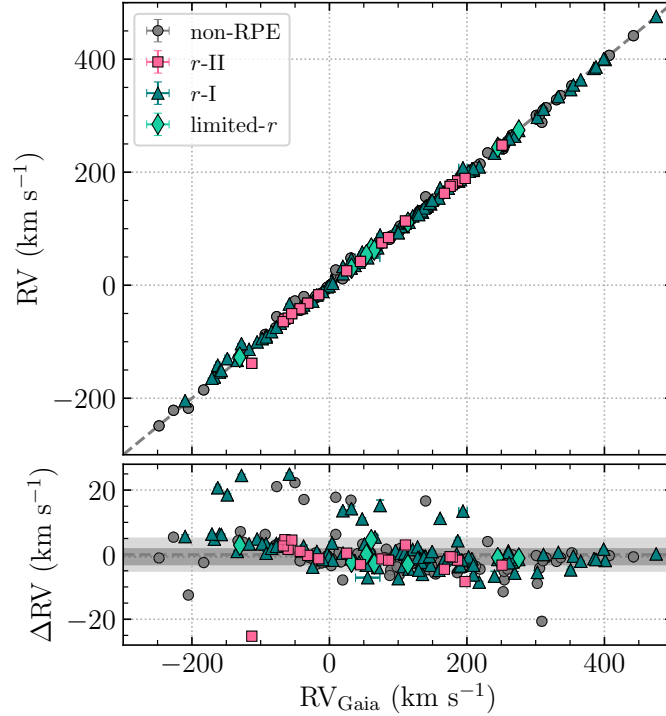


Figure 4.9. Radial velocities reported by Gaia DR2 of our target stars compared to radial velocities measured by this work. Stars with radial velocities different by greater than 5 km s^{-1} are reported in Table 4.2.

of each spectrum. The uncertainties on our measured RVs are calculated from the standard error of the mean of the individual order-by-order cross-correlation results from *fxcor*. The computed heliocentric RVs and S/N for each target are listed in Table A.1, along with the RA, DEC, *V* magnitude, MJD of the observation, and the exposure times.

The heliocentric RVs measured from our high-resolution spectra are displayed in Figure 4.9, compared with the Gaia DR2 reported values (Gaia Collaboration et al. 2016, 2018). We find that 47 of our targets (20%) have a measured RV that differs by more than 5 km s^{-1} from the Gaia DR2 measurement, indicating potential for binarity; these stars are listed in Table 4.2. In addition to a measurement by *Gaia*, many of these stars are found in RAVE DR5 (Kunder et al. 2017), which provides

another RV measurement for comparison. The spread of all RV differences between RAVE and *Gaia* can be fit by two gaussian functions, where the broader gaussian has a standard deviation of 2.6 km s^{-1} (Steinmetz et al. 2020). Interestingly, the average RV difference between our high-resolution RV measurements and the *Gaia* measurements of non-possible-binary stars is $-0.65 \pm 2.35 \text{ km s}^{-1}$. Other spectroscopic surveys also find a negative offset of RVs compared to *Gaia* (-0.3 for RAVE and -0.2 for APOGEE; see Steinmetz et al. 2018, 2020). A few other sources of RV estimates for our program stars are available as well and are provided in Table 4.2. Note that most spectroscopic surveys that report an RV (including Gaia DR2 and RAVE) do not include gravitational redshift or stellar atmosphere corrections, which are expected to be $-0.3 \pm 0.2 \text{ km s}^{-1}$ for giants (Zwitter et al. 2018). For consistent comparison, such corrections are also omitted from our RV measurements.

Some of the program stars in Table 4.2 suffer from low S/N spectra (for example, J10540994–1347522 and J14165685+1215598), increasing the uncertainty in the cross-correlation routine; for completeness, we retain these stars in the list of possible binaries. Although low S/N effects may lead to a few false positives, the most promising binary candidates are those where the previous literature measurements differ and where the reported *Gaia* uncertainty is large ($>1.0 \text{ km s}^{-1}$). Note that the *Gaia* uncertainty is based on deviations from an average over multiple epochs. Therefore, a higher uncertainty can indicate possible binarity by reflecting a spread in the individual RV measurements. On average, the RVs of stars in this RPA data release had eight transits used by Gaia DR2 for their RV measurements.

J04411241–6518438 (HD 30229) is a known Pop II field binary with a very low eccentricity and orbital period of about 140 days (Pasquini and Lindgren 1994). J05381700–7516207 has several RV measurements, all of which differ from each other outside of their uncertainty. This star is also an *r*-II star, with an extreme [Eu/Fe] enhancement (+1.28), designating it an interesting target for high-resolution follow-

TABLE 4.2
 RADIAL VELOCITIES (IN KMS⁻¹) FROM LITERATURE AND THIS
 DATA RELEASE FOR POSSIBLE BINARIES

Stellar ID	RV	RV _{err}	RV _{other} [†]	RV _{err}	ΔRV
J00374325–1204391	−27.84	0.41	−50.14 ^a	0.48	+22.30
			−48.60 ^b	1.74	+20.76
			−51.2 ^c	...	+23.4
J01213447–2528002	+33.17	0.26	+19.57 ^a	2.26	+13.60
			+23.62 ^b	0.60	+9.55
J01265856+0135153	−221.38	0.92	−226.79 ^a	1.70	+5.41
			−211.4 ^d	...	+10.0
J01311599–4016510	−33.31	0.38	−58.21 ^a	0.28	+24.90
J01371888–1729037	−204.31	0.55	−209.90 ^a	0.77	+5.59
			−210.1 ^e	0.3	+5.9
			−209.90 ^f	0.30	+5.65
J03142084–1035112	+241.24	0.10	+252.71 ^a	4.46	−11.47
			+239.3 ^d	...	+1.9
J03190629–0819306	+293.47	0.61	+302.39 ^a	0.21	−8.92
			+304.99 ^b	2.70	−10.81
J03425812–3047217	+296.96	0.62	+302.48 ^a	0.31	−5.52
			+323.8 ^d	...	−26.8
			+302.13 ^b	0.70	−5.17
J04014897–3757533	+156.55	0.17	+139.92 ^a	0.51	+16.63
			+139.77 ^b	0.80	+16.78
			+139.1 ^c	...	+17.5
J04315411–0632100	+209.37	0.27	+217.89 ^a	0.43	−8.52

TABLE 4.2 (CONTINUED)

Stellar ID	RV	RV _{err}	RV _{other} [†]	RV _{err}	ΔRV
			+211.64 ^b	2.20	-2.27
J04411241-6518438	+288.28	1.27	+308.93 ^a	1.95	-20.65
			+292.18 ^b	1.28	-3.47
J05311779-5810048	+129.19	0.31	+135.32 ^a	1.04	-6.13
			+133.38 ^b	1.56	-4.19
J05381700-7516207	+58.73	0.34	+47.66 ^a	1.05	+11.07
			+52.91 ^b	0.68	+12.15
			+43.0 ^c	...	+22.1
J05383296-5904280	+189.02	0.37	+197.35 ^a	0.41	-8.33
			+196.65 ^b	0.54	-7.63
J06014757-5951510	+246.53	0.22	+254.34 ^a	0.31	-7.81
			+253.64 ^b	0.56	-7.11
J06420823-5116448	+15.43	0.27	+9.16 ^a	0.80	+6.27
			+8.57 ^b	0.87	+6.86
J07265723-5647500	+71.75	0.62	+66.31 ^a	3.33	+5.44
			+63.29 ^b	1.11	+9.75
J09255655-3450373	+203.06	0.39	+209.35 ^a	0.27	-6.29
			+210.11 ^b	0.59	-7.05
J10025125-4331098	+233.46	1.53	+240.13 ^a	1.93	-6.67
J10251539-3554026	+248.87	0.45	+254.10 ^a	0.59	-5.23
			+254.68 ^b	3.62	-5.81
J10302845-7543299	+263.78	0.54	+269.53 ^a	0.31	-5.75
			+270.29 ^b	0.86	-6.51
J10540994-1347522	+180.23	0.77	+185.81 ^a	1.76	-5.58
			+188.7 ^d	...	-8.5

TABLE 4.2 (CONTINUED)

Stellar ID	RV	RV _{err}	RV _{other} [†]	RV _{err}	ΔRV
J11404726–0833030	+172.22	0.10	+161.00 ^a +160.33 ^b	1.63 0.84	+11.22 +11.89
J14165685+1215598	-87.15	0.82	-93.43 ^a	2.10	+6.28
J15141994–4359554	+148.50	0.97	+154.50 ^a	0.98	-6.00
J15360493+0247300	-20.03	0.23	-37.11 ^a	2.56	+17.08
J19050116–1949280	+95.31	0.35	+101.60 ^a +99.51 ^b	0.57 1.38	-6.29 -4.20
J19175585–5440147	+48.08	0.54	+31.22 ^a +25.51 ^b	0.68 3.94	+16.86 +22.47
J19445483–4039459	+92.74	0.30	+100.17 ^a +99.52 ^b	0.53 0.58	-7.43 -6.78
J19451414–1729269	+46.23	0.80	+32.00 ^a +35.45 ^b +30.4 ^g +30.60 ^f	1.66 0.54 ... 0.20	+14.23 +10.78 +15.8 +15.63
J20194310–3158163	-130.00	0.30	-148.51 ^a -153.43 ^b	3.34 0.56	+18.51 +23.43
J20233743–1659533	-141.72	0.23	-162.43 ^a -157.44 ^b	3.05 1.34	+20.71 +15.72
J20504869–3355289	-153.72	0.22	-160.02 ^a -158.76 ^b	0.39 0.56	+6.30 +5.04
J20554594–3155159	-151.07	0.19	-157.29 ^a -155.06 ^b	0.25 0.65	+6.22 +3.99
J21055865–4919336	+207.72	0.19	+194.24 ^a +169.90 ^b	6.10 1.71	+13.48 +37.82

TABLE 4.2 (CONTINUED)

Stellar ID	RV	RV _{err}	RV _{other} [†]	RV _{err}	ΔRV
J21080151–6555366	+81.27	0.27	+87.72 ^a	0.39	-6.45
			+88.44 ^b	0.38	-7.17
J21103411–6331354	-122.35	0.23	-129.48 ^a	0.44	+7.13
			-130.56 ^b	1.54	+8.21
J21314253–1459110	+11.39	0.30	+19.24 ^a	2.87	-7.85
			+17.79 ^b	0.91	-6.40
J22125424–0235414	-103.40	0.40	-127.91 ^a	0.95	+24.51
			-127.05 ^b	1.29	+23.65
			-145.8 ⁱ	...	+42.4
J22161170–5319492	+88.90	1.71	+73.70 ^a	0.44	+15.20
			+73.39 ^b	1.69	+15.51
J22223324–1314488	+26.96	0.25	+9.19 ^a	0.55	+17.77
			+11.07 ^b	0.73	+15.89
J22233596–5301145	+146.88	0.26	+152.56 ^a	0.29	-5.68
			+153.6 ^h	1.4	-6.7
J22372037–4741375	-138.25	0.26	-112.98 ^a	4.45	-25.27
			-107.5 ^d	...	-30.8
J22585069–3923437	-55.60	0.40	-76.68 ^a	1.63	+21.08
J23425814–4327352	+48.53	0.22	+55.66 ^a	17.69	-7.13
J23490902–2447176	-164.58	0.22	-170.94 ^a	0.68	+6.36
			-167.46 ^b	0.90	+2.88
J23552837+0421179	-217.70	0.41	-205.18 ^a	3.38	-12.52

[†]Sources are defined as follows: *a*: Gaia DR2 [Gaia Collaboration et al. \(2018\)](#); *b*: RAVE DR5 [Kunder et al. \(2017\)](#); *c*: [Ruchti et al. \(2011\)](#); *d*: [Beers et al. \(2017\)](#); *e*: [Ishigaki et al. \(2012\)](#); *f*: [Gontcharov \(2006\)](#); *g*: [Roederer et al. \(2014b\)](#); *h*: RAVE DR3 [Siebert et al. \(2011\)](#); and *i*: [Schlaufman and Casey \(2014\)](#).

up and RV monitoring. Only one of the possible binaries listed in Table 4.2 exhibits a high level of carbon enhancement: J03142084–1035112, with $[C/Fe] = +0.76$. For this star, only upper limits on the Ba and Eu abundances could be determined from our existing spectra. Detailed follow-up, both with higher-resolution spectroscopy and RV monitoring, can reveal how the observed elemental abundances are affected by mixing and binary interactions, especially for CEMP stars (Choplin 2018), to further understand the evolution of the elements.

4.8 Summary and Discussion of RPA Efforts

This data set constitutes the fourth data release of the RPA search for *r*-process-enhanced stars, culminating in a current total of 595 metal-poor stars with Phase II (snapshot) spectroscopy in the total published sample (Hansen et al. 2018; Roederer et al. 2018b; Sakari et al. 2018a,b, 2019; Ezzeddine et al. 2020). Another \sim 1000 snapshot spectra of candidates have already been taken with a number of telescopes in the Northern and Southern Hemispheres and will be released in due course.

Quantified chemical identifications provide clues as to the formation history of the Milky Way, since stars with similar metallicities and levels of *r*-process enrichment have also been found to be dynamically linked in small associations (see, e.g., Roederer et al. 2018a; Yuan et al. 2020). Current and future RPA efforts will help to refine the mapping of *r*-process-enhanced stars into their parent dynamical groups, so that we may learn more about the natal environment in which the *r*-process occurred in each of these now-disrupted systems. By identifying entire systems of *r*-process-enhanced stars that likely shared a common birthplace and star-formation history, we can test the dilution hypothesis of nucleosynthetic events, i.e., whether the heavy-element material in *r*-I and *r*-II stars came from similar sources, but the *r*-I stars have simply been diluted by larger masses of baryons in their natal mini-halos, leading to

smaller enhancements. [Tarumi et al. \(2020\)](#) suggest other alternatives to account for the different levels of *r*-process enhancements in the UFDs Ret II and Tuc III (and by extension to the *r*-I and *r*-II stars in the halo field) based on the locations of their progenitor NSMs.

Future data releases by the RPA will continue to increase the number of stars with identified *r*-process signatures, and perhaps reveal new ones for investigations of the various proposed nucleosynthetic sites. Fresh investigations of actinide production, for example, are being used to distinguish between specific *r*-process sites and the conditions that produce these heavy elements ([Eichler et al. 2019](#); [Holmbeck et al. 2019a](#)). Furthermore, the identification of dynamical groups that include *r*-process-enhanced stars are useful to constrain theoretical models of *r*-process production; see, e.g., [Holmbeck et al. \(2019b\)](#) and Gudin et al. (in prep.).

CHAPTER 5

J09544277+5246414: THE MOST ACTINIDE-ENHANCED *R*-II STAR KNOWN

We have a hunger of the mind which asks for knowledge of all around us, and the more we gain, the more is our desire; the more we see, the more we are capable of seeing.

— Maria Mitchell

5.1 The Actinide Boost

With the increase in *r*-process-enhanced stellar signatures discovered through RPA efforts, it is clear that the *r*-process pattern isn't quite universal. One of the largest areas of elemental abundance variation can be found in the heaviest observable elements: the actinides, thorium and uranium. Although the elemental-abundance patterns of *r*-process-enriched stars are relatively homogeneous among the lanthanides, about 30% of *r*-process-enhanced stars exhibit Th/Eu abundance ratios a factor of 2–3 higher than the majority of other *r*-process-enriched stars (see Hill et al. 2002; Mashonkina et al. 2014). At the highest values of $\log \epsilon(\text{Th}/\text{Eu})$ are the “actinide-boost” stars, so-named for their overabundance of actinides compared to the rest of their *r*-process elements (quantified by Eu). This chapter reports the discovery of a new actinide-boost star, 2MASS J09544277+5246414 (hereafter J0954+5246), originally identified as a very bright ($V = 10.1$), extremely metal-poor ($[\text{Fe}/\text{H}] = -2.99$) K giant in the LAMOST survey, and found to be an *r*-II star ($[\text{Eu}/\text{Fe}] = +1.28$), during the snapshot phase of the RPA. Based on a high S/N, high-resolution spectrum obtained with the Harlan J. Smith 2.7-m telescope, this star is

the first confirmed actinide-boost star found by RPA efforts. With an enhancement of $[\text{Th}/\text{Eu}] = +0.37$, J0954+5246 is also the most actinide-enhanced r -II star yet discovered, and only the sixth metal-poor star with a measured uranium abundance ($[\text{U}/\text{Fe}] = +1.40$). Using the Th/U chronometer, we estimate an age of 13.0 ± 4.7 Gyr for this star. The unambiguous actinide-boost signature of this extremely metal-poor star, combined with additional r -process-enhanced and actinide-boost stars identified by the RPA, will provide strong constraints on the nature and origin of the r -process at early times.

5.2 Observations and Analysis

J0954+5246 was first identified as a candidate very metal-poor K giant in the LAMOST (DR4) Survey (Liu et al. 2014). The SEGUE Stellar Parameter Pipeline (SSPP; Lee et al. 2008a,b) was used to estimate the atmospheric parameters (T_{eff} , $\log g$, and $[\text{Fe}/\text{H}]$)—as well as its carbon-to-iron ratio ($[\text{C}/\text{Fe}]$, as described in Lee et al. 2013)—from the LAMOST medium-resolution data. The metallicity and $[\text{C}/\text{Fe}]$ estimated by the SSPP revealed J0954+5246 to be extremely metal-poor, non-carbon-enhanced, and with a low effective temperature, suitable for inclusion in the RPA search for r -process-enhanced stars. We carried out high-resolution (“portrait”) spectroscopic observations during 2018A using the Harlan J. Smith 107-in (2.7-m) telescope and the TS23 echelle spectrograph (Tull et al. 1995) at McDonald Observatory. The high-resolution setup uses a $1''2$ slit and 1×1 binning, yielding a resolving power of $R \sim 60,000$, with full wavelength coverage of $3600\text{--}5800\text{\AA}$ and partial wavelength coverage up to $10,000\text{\AA}$. From co-addition of nine spectra (total exposure time 15,600 s), a final S/N of 90 per resolution element at 4100\AA was achieved. The data were reduced using standard `IRAF` packages (Tody 1993).

Equivalent widths (W_s) of 125 Fe I and 27 Fe II lines were measured using the *splot* task in `IRAF`, fitting a Gaussian profile to each line, and deblending where necessary.

Individual Fe I and Fe II abundances were derived from their W s using the current version of the LTE stellar line analysis code `MOOG`, using the spectroscopic method described in Section 4.2. All other elemental abundances were derived from spectral synthesis of features in the portrait spectrum using `MOOG`. Oscillator strengths and excitation potentials for all lines in this work were generated with `linemake`. Isotopic ratios, employed when synthesizing features with hyperfine-splitting and isotopic shift effects, were taken from the Solar r -process ratios in Sneden et al. (2008).

J0954+5246 is a cool, extremely metal-poor giant; at such extremes, it becomes difficult to determine atmospheric parameters based on spectroscopy alone. Over a large range of excitation potentials, the spectroscopically-derived Fe I abundances equilibrate at 4100 K. However, with the spectroscopic method Fe I and Fe II abundance equilibration fails at these low effective temperatures, disagreeing by about 0.3 dex. Instead of a pure spectroscopic approach, we first use the temperature scaling for giant stars from Alonso et al. (1999), applied to 2MASS photometry (Skrutskie et al. 2006), to obtain a T_{eff} estimate of 4340 K, based on the $(J - K)$ color of 0.716.¹ After applying the correction from Frebel et al. (2013) to the 4100 K found previously, we find a spectroscopic temperature of 4360 K, which agrees with the photometric estimate and validates the spectroscopic method, despite the differences that arise between Fe I and Fe II abundances at low temperatures. The reddening is sufficiently low ($E(B - V) = 0.007$; Schlafly and Finkbeiner 2011) that it does not significantly affect the $(J - K)$ color. After fixing the temperature to the photometric estimate of 4340 K, ionization equilibration was carried out to find the surface gravity and metallicity. Microturbulence was determined by minimizing the Fe I and Fe II abundance trends in reduced equivalent width. Carbon abundance was measured based on high-resolution spectral synthesis of the 4300 Å CH G -band. Table 5.1 summarizes the

¹This photometric temperature matches that obtained from the SSPP, based on the medium-resolution spectrum.

TABLE 5.1

DERIVED ATMOSPHERIC PARAMETERS FOR J0954+5246

Parameter	LAMOST	SSPP	TS-23 ^a
T_{eff} (K)	4462 ± 110	4340 ± 150	4340 ± 125
$\log g$ (cgs)	0.91 ± 0.19	0.6 ± 0.30	0.41 ± 0.20
[Fe/H]	-2.46 ± 0.11	-3.16 ± 0.15	-2.99 ± 0.10
ξ (km s $^{-1}$)	2.28 ± 0.20
[C/Fe]	...	-0.34	-0.50 ± 0.20
MJD	57030	57030	58128
RV (km s $^{-1}$)	-71 ± 5	-71.9 ± 1.8	-67.7 ± 0.1

^a Final parameters adopted for this work.

derived atmospheric parameters (and their estimated errors) for this star from the medium- and high-resolution spectra. Measured radial velocities are also reported in Table 5.1; based on the similarity between radial velocity measurements, there is no indication of binarity for J0954+5246.

5.3 The r -Process Pattern

Derived neutron-capture-element abundances of J0954+5246 are shown in Figure 5.1. The abundances unequivocally match a scaled-Solar pure r -process pattern, with no apparent contribution from the s -process. Also shown in Figure 5.1 is a comparison to the elemental-abundance pattern of the canonical actinide-boost star, CS 31082–001 (Hill et al. 2002). Table 5.2 lists the derived abundances for all elements identified in J0954+5246, their comparison to Asplund et al. (2009) Solar abundances, the uncertainty of the abundance, and the number of lines measured.

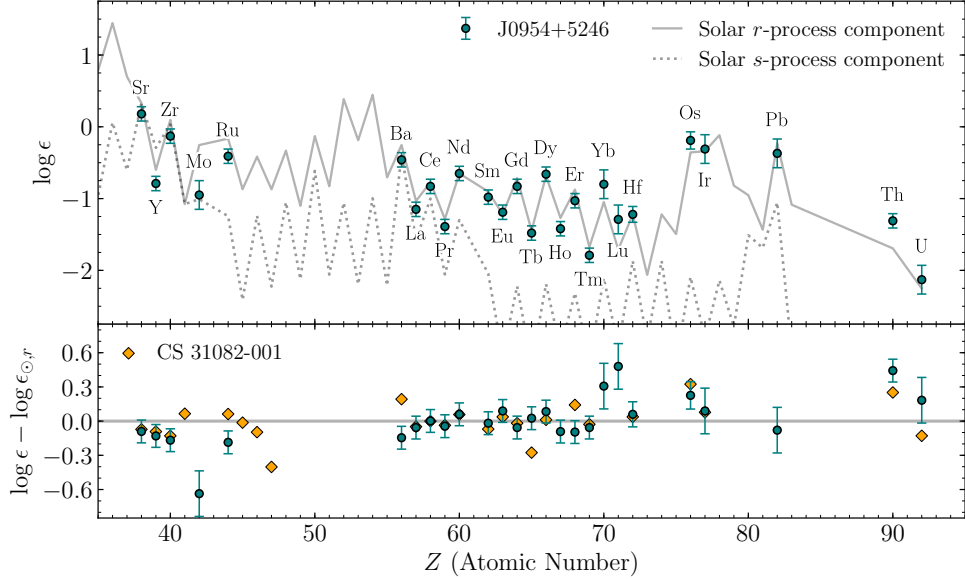


Figure 5.1. Top panel: full r -process elemental-abundance pattern of J0954+5246 compared to the scaled-Solar s -process (dotted line) and r -process (solid line) components, normalized to Sr. Bottom panel: difference between the observed abundances and the Solar r -process component for J0954+5246 and observations of the canonical actinide-boost star CS 31082–001, as reported by Hill et al. (2002). The residuals in the bottom panel are normalized to the average residual between Ba and Tm.

We adopt a minimum uncertainty of 0.10 dex. For elements with only one feature, a 0.2 dex uncertainty is assumed. Important spectral features, including Sr, Ba, and Eu—used to classify r -process-enhancement in metal-poor stars—are shown in Figure 5.2. Abundances of the elements from C to Ga in J0954+5246 resemble those of normal metal-poor halo stars. In the following, we focus on the neutron-capture element abundances.

5.3.1 Light Neutron-Capture Elements

The elements Sr, Y, Zr, Mo, and Ru were measured in this star; atomic transitions of Rh, Pd, and Ag occur at wavelengths bluer than the instrumental system limit for efficient throughput, preventing measurement of their abundances. It has been

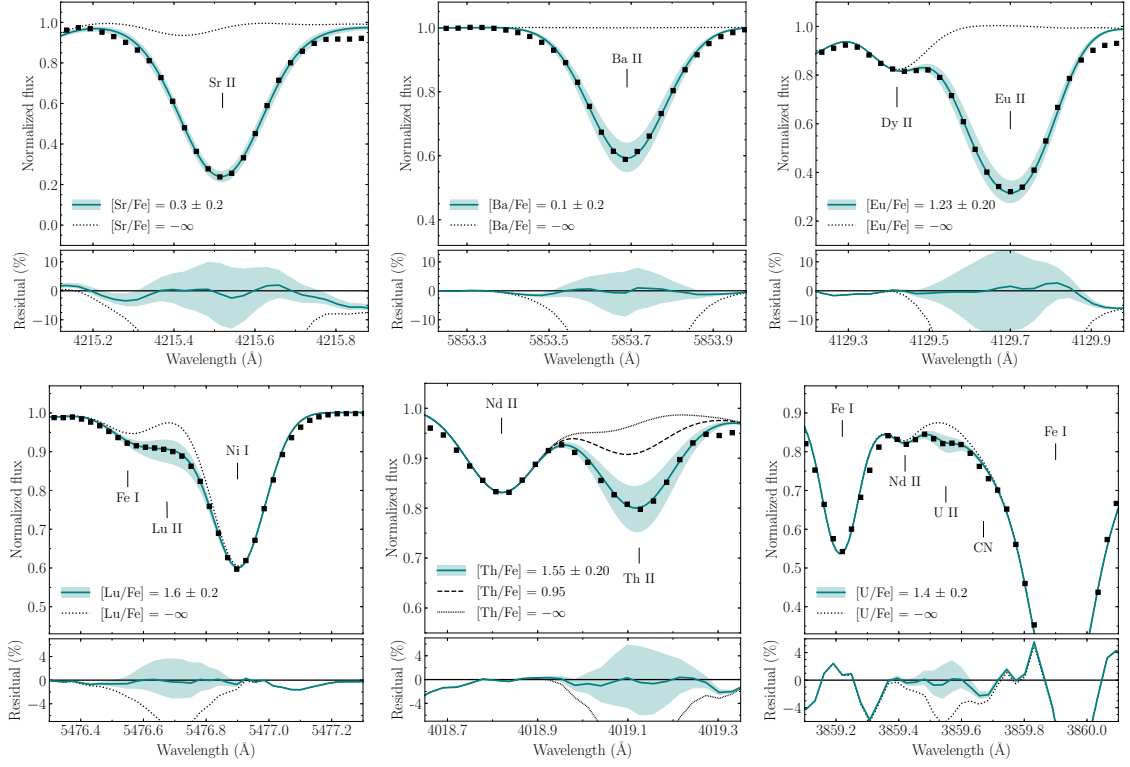


Figure 5.2. Relevant syntheses and derived abundances for important r -process elements present in J0954+5246. Top panels of each plot show the best-fit syntheses (solid lines) and 0.2 dex uncertainties (shaded regions) compared to the observed spectrum (points). Key features are labeled. Bottom panels show the residuals between the observed spectrum and the synthetic fits. Derived abundances corresponding to the plotted syntheses are indicated in each legend. The $[Th/Fe] = 0.95$ synthesis corresponds to a typical non-actinide-enhanced Th II line profile.

previously noted that a significant spread in the light neutron-capture elements exists in r -process-enhanced stars, with r -I stars generally exhibiting stronger relative first-peak enhancement (Siqueira Mello et al. 2014). This spread is often attributed to a separate r -process, which is referred to as a limited, or weak, r -process (Wanajo and Ishimaru 2006; Hansen et al. 2012; Frebel 2018), and is distinct from that responsible for the production of second- and third-peak elements. Compared to the scaled-Solar pattern, the light r -process elements in J0954+5246 are indeed slightly lower,

TABLE 5.2

DERIVED ELEMENTAL ABUNDANCES OF J0954+5246

Species	$\log \epsilon_{\odot}$	$\log \epsilon$	[X/H]	[X/Fe]	$\sigma_{\log \epsilon}$	N
C (CH)	8.43	4.94	-3.49	-0.50 ^a	0.20	1
Na I	6.24	3.53	-2.72	0.28	0.10	2
Mg I	7.60	5.25	-2.35	0.64	0.10	4
Al I	6.45	3.06	-3.39	-0.40	0.20	1
Ca I	6.34	3.60	-2.74	0.25	0.10	14
Sc II	3.15	-0.02	-3.17	-0.18	0.10	7
Ti I	4.95	1.97	-2.98	0.01	0.10	9
Ti II	4.95	2.17	-2.78	0.21	0.10	11
V II	3.93	0.94	-2.99	0.00	0.10	2
Cr I	5.64	2.34	-3.30	-0.31	0.10	7
Cr II	5.64	2.81	-2.84	0.16	0.10	2
Mn I	5.43	1.64	-3.79	-0.80	0.14	3
Fe I	7.50	4.51	-2.99	0.00	0.12	27
Fe II	7.50	4.51	-2.99	0.00	0.12	125
Co I	4.99	1.98	-3.02	-0.02	0.10	2
Ni I	6.22	3.26	-2.96	0.03	0.10	3
Cu I	4.19	< 0.15	< -4.04	< -1.05	...	1
Zn I	4.56	1.72	-2.84	0.15	0.20	1
Ga I	3.04	< 0.05	< -2.99	< 0.00	...	1
Sr I	2.87	0.88	-1.99	1.00	0.20	1
Sr II	2.87	0.18	-2.69	0.30	0.10	3
Y II	2.21	-0.79	-3.00	-0.01	0.10	12
Zr II	2.58	-0.13	-2.71	0.28	0.10	4

TABLE 5.2 (CONTINUED)

Species	$\log \epsilon_{\odot}$	$\log \epsilon$	[X/H]	[X/Fe]	$\sigma_{\log \epsilon}$	N
Mo I	1.88	-0.95	-2.83	0.16	0.20	1
Ru I	1.75	-0.41	-2.16	0.84	0.10	2
Ba II	2.18	-0.46	-2.64	0.35	0.10	3
La II	1.10	-1.15	-2.25	0.74	0.10	16
Ce II	1.58	-0.83	-2.41	0.58	0.10	13
Pr II	0.72	-1.39	-2.11	0.88	0.10	7
Nd II	1.42	-0.65	-2.07	0.92	0.10	14
Sm II	0.96	-0.98	-1.94	1.05	0.10	11
Eu II	0.52	-1.19	-1.71	1.28	0.10	4
Gd II	1.07	-0.83	-1.90	1.09	0.10	7
Tb II	0.30	-1.48	-1.78	1.21	0.10	4
Dy II	1.10	-0.66	-1.76	1.23	0.10	6
Ho II	0.48	-1.42	-1.90	1.10	0.10	4
Er II	0.92	-1.03	-1.95	1.04	0.10	4
Tm II	0.10	-1.79	-1.89	1.10	0.10	4
Yb II	0.84	-0.80	-1.64	1.35	0.20	1
Lu II	0.10	-1.29	-1.39	1.60	0.20	1
Hf II	0.85	-1.22	-2.07	0.92	0.11	2
Os I	1.40	-0.19	-1.59	1.40	0.12	3
Ir I	1.38	-0.31	-1.69	1.30	0.20	1
Pb I	1.75	-0.37	-2.12	0.87	0.20	1
Th II	0.02	-1.31	-1.36	1.63	0.10	3
U II	-0.54	-2.13	-1.59	1.40	0.20	1

^aNatal [C/Fe]=+0.24, based on corrections from [Placco et al. \(2014\)](#).

indicating little limited- r contribution. It should be noted that Mo has a significant p -process component, which is not accounted for in the Solar r -process residual, likely causing its apparent under-abundance (Meyer 1994).

5.3.2 Heavy Neutron-Capture Elements

We were able to derive abundances for all stable elements between Ba and Hf, as well as Os, Ir, and Pb. Like most r -II stars, the abundance pattern of J0954+5246 in this region agrees well with scaled-Solar r -process values, with some deviations. Intriguingly, the abundance of Yb II is much higher than the scaled-Solar r -process value in J0954+5246; this over-abundance is also observed in CS 29497–004 (Hill et al. 2017) and CS 22892–052 (Sneden et al. 2008), neither of which display an actinide boost. However, it should be noted that the Yb abundance is derived from only one feature, and is affected by hyperfine splitting, which is included in this synthesis. Similarly, Lu and Ir appear over-abundant relative to the Solar r -process pattern, but these elements each have just one optical feature suitable for abundance derivations. Figure 5.2 shows the synthesis of the lutetium feature from which we derived the Lu II abundance.

5.3.3 Thorium, Uranium, and the Actinide Boost

As with all r -II stars, the heavy-element abundance pattern of J0954+5246 reproduces the observed scaled-Solar lanthanide abundances, with deviations greater than the formal uncertainties for only a few elements. However, the most striking difference between J0954+5246 and other r -II stars is its actinide signature. Uranium is among the most difficult elements to measure in a star. Being able to measure uranium—together with thorium—provides clues to the nature and possible site of the r -process that synthesized the actinides. Three lines of Th II were measured in

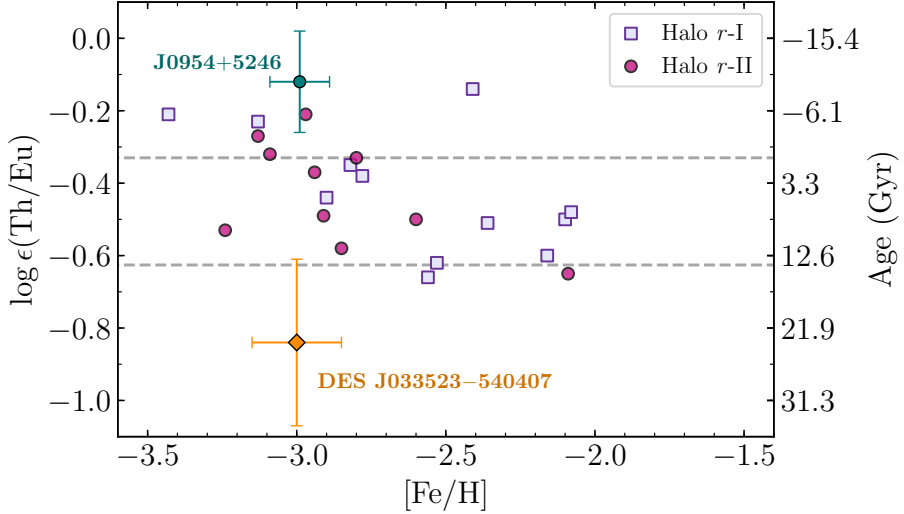


Figure 5.3. Th/Eu abundances vs. metallicity for known *r*-I and *r*-II stars where a Th measurement is provided. Also shown is the Reticulum II member, DES J033523–540407, as reported by Ji and Frebel (2018). The right axis shows the Th/Eu age calculated based on Schatz et al. (2002) production ratios. Horizontal lines indicate physical limits on the age (i.e., 0 and 13.8 Gyr). Data were generated using JINAbase, supplemented by measurements from Mashonkina et al. (2014), Roederer et al. (2014b), Hill et al. (2017), Placco et al. (2017), and Sakari et al. (2018b).

this star, spanning an abundance range of 0.23 dex. Only one line of U II is available for measurement in the spectrum; syntheses for key actinide features are shown in Figure 5.2.

The actinide-to-lanthanide ratio of $[\text{Th}/\text{Eu}] = +0.37$ demonstrates the actinide-boost designation of J0954+5246. Figure 5.3 shows the $\log \epsilon(\text{Th}/\text{Eu})$ abundances of halo *r*-I and *r*-II stars; non-actinide-boost stars typically have $\log \epsilon(\text{Th}/\text{Eu})$ values near -0.5 . Even allowing for a 0.15 dex uncertainty, the $\log \epsilon(\text{Th}/\text{Eu})$ abundance of J0954+5246 is larger than its non-actinide-boost cousins by a factor of ~ 2 , making it the most actinide-enhanced *r*-II star currently known. The actinide enhancement of J0954+5246 is even larger than that of the canonical actinide-boost star CS 31082–001 with $[\text{Th}/\text{Eu}] = +0.20$ (Hill et al. 2002).

5.3.4 The Cosmochronometric Age of J0954+5246

The presence of long-lived radioactive actinides allows an approximate age determination by radioactive decay dating, as described in [Placco et al. \(2017\)](#) and expanded upon in detail in Chapter 6. In the absence of a uranium measurement, the Th/Eu chronometer is used to derive ages by comparing to a set of initial production ratios from *r*-process simulations, e.g., from [Schatz et al. \(2002\)](#). However, in actinide-boost stars, using the Th/Eu ratio leads to unphysical values, since the measured Th/Eu ratio may be higher than the theoretical initial production ratio. For example, Figure 5.3 specifies some radioactive decay ages corresponding to different Th enhancements. Note that—using a certain set of production ratios—only a narrow range of $\log \epsilon(\text{Th}/\text{Eu})$ gives radioactive decay ages within the physical limits of the Universe: 0 to 13.7 Gyr. To our knowledge, none of the existing *r*-process nucleosynthesis models can account for the abundance pattern observed in actinide-boost stars. Notwithstanding this shortcoming, the Th/U chronometer can still be used to estimate stellar ages since the actinide boost affects thorium and uranium proportionally. The Th/U chronometer is insensitive to variations in the relative production of actinides and lanthanides and thus leads to more realistic ages of actinide-boost stars than the Th/Eu chronometer.

Using the production ratios from [Schatz et al. \(2002\)](#), the Th/U age is 13.0 ± 4.7 Gyr, commensurate with its low metallicity. Uncertainties on the age contain only the measured abundance uncertainty and do not include those on the production ratios. The Th/Eu and U/Eu ages are -9.5 Gyr and 5.8 Gyr, respectively. These ages can be made to agree with the Th/U age of 13.0 Gyr by boosting the initial production ratios of thorium and uranium by a factor of 3.1. In a similar analysis, [Schatz et al. \(2002\)](#) found a “boost factor” of 2.5 for CS 31082–001. Values for this boost factor vary, as Th/Eu abundances are not found at discrete enhancement levels, but rather, cover a range.

5.4 Discussion and Conclusion

The scatter of the Sr-Y-Zr-group abundances among *r*-process-enhanced stars may be attributed to different levels of production by the limited *r*-process, and thus the production of the first *r*-process peak can be decoupled from the second and third peaks. However, it seems unlikely that the actinides can be similarly decoupled from the main *r*-process, or attributed to a separate *r*-process entirely, since some main *r*-process contribution is nearly always produced in nucleosynthesis simulations when the actinides are synthesized. The presence of the actinide boost demonstrates that a real variation exists among the actinide abundances. Therefore, measuring Th (and U) abundances for a larger number of *r*-process-enhanced stars is essential to distinguish between possible astrophysical *r*-process sites and to determine what conditions enable strong actinide production. Specifically, actinide enhancement could indicate fission cycling in *r*-process nucleosynthesis, which may only occur under certain astrophysical conditions. Other studies explore the effect of fission cycling in the low-entropy dynamical ejecta of a neutron star merger as one possibility for the origin of the actinide-boost phenomenon (Eichler et al. 2019; Holmbeck et al. 2019b).

On the other hand, there may exist evidence for *weak* actinide production. Ji and Frebel (2018) measured thorium for the brightest *r*-II star in the UFD galaxy Reticulum II: DES J033523–540407. This star exhibits an *under*-abundance of thorium, relative to europium, even though the rest of the main *r*-process is consistent with and other *r*-process-enhanced stars. The $\log \epsilon(\text{Th}/\text{Eu})$ abundance of DES J033523–540407 is shown relative to its Milky Way counterparts in Figure 5.3. Such a low thorium abundance has not yet been observed in Milky Way halo stars, which brings into question the type of *r*-process that could under-produce the actinides. With refined stellar main *r*-process abundances—particularly for Th, U, and the third *r*-process-peak elements where few features exist from which to derive abundances—as well as species that can only be measured from UV data, we may

find clues that are unique to and correlated with actinide production, and thereby characterize the actinide boost and better understand its origin.

CHAPTER 6

ACTINIDE PRODUCTION IN THE NEUTRON-RICH EJECTA OF A NEUTRON STAR MERGER

No one really thought of fission before its discovery.

— Lise Meitner

6.1 Actinide Formation and Cosmochronometry

The origin of the actinide-boost in *r*-process-enhanced stars is as of yet unexplained. Notably, their apparent unphysical radioactive decay ages call for a better theoretical description of actinide production in *r*-process events. This chapter is based on the work of Holmbeck et al. (2019b), in which we study the production of the actinide elements in NSMs to investigate whether these sites are uniquely responsible for the actinide-boost signature. Specifically, this work takes the theoretical steps of applying nucleosynthesis calculations to NSM conditions, studying the effects of nuclear variations on *r*-process production, and using the principles of radioactive decay to estimate whether actinide production in NSMs is consistent with observations of Th and U.

The actinides ^{232}Th and ^{238}U are produced exclusively via the *r*-process, and their long half-lives—14.0 Gyr and 4.468 Gyr, respectively—allow for their potential use as cosmochronometers, providing an estimate on the age of the *r*-process material in metal-poor stars (Cowan et al. 1991). The ages of *r*-process events can be extracted from the observed abundance ratios of actinides to co-produced stable species, given some estimate of their initial production. Although the comparison can be to any

stable r -process element, it is common to use Eu because of its role in quantifying r -process enrichment of metal-poor stars. Observed thorium-to-europium abundance ratios in most cases result in inferred ages of $\sim 2\text{--}14$ Gyr (see Figure 5.3). By contrast, actinide-boost stars are overabundant in thorium (and uranium, for the few stars for which measurements are available) with respect to the lanthanides, resulting in apparently contradictory negative ages when standard cosmochronometry is applied, even outside of large abundance uncertainties.

Key quantities in cosmochronometry are the theoretical production ratios of elements produced by r -process events: Th/Eu and U/Eu. Over time, radioactive decay decreases these ratios to what is observed today in r -process-enhanced stars. The extracted ages depend on these ratios as follows:

$$t = 46.67 \text{ Gyr} [\log \epsilon(\text{Th}/\text{Eu})_0 - \log \epsilon(\text{Th}/\text{Eu})_{\text{obs}}] \quad (6.1)$$

$$t = 14.84 \text{ Gyr} [\log \epsilon(\text{U}/\text{Eu})_0 - \log \epsilon(\text{U}/\text{Eu})_{\text{obs}}] \quad (6.2)$$

$$t = 21.80 \text{ Gyr} [\log \epsilon(\text{U}/\text{Th})_0 - \log \epsilon(\text{U}/\text{Th})_{\text{obs}}], \quad (6.3)$$

where $\log \epsilon(X/\text{Eu})_0$ is the initial production ratio corresponding to the formation of europium and element X at $t = 0$, and $\log \epsilon(X/\text{Eu})_{\text{obs}}$ is the observed ratio after the radioactive element X has decayed for a time t . The Th/Eu and U/Eu production ratios that have so far been applied to metal-poor stars are largely derived from supernova models (e.g., Wanajo et al. 2002; Farouqi et al. 2010) and fail to account for actinide-boost stars. Notably, only the thorium-to-uranium (U/Th) ratios produce realistic age estimates in both actinide-boost and non-actinide-boost stars.

This work investigates the production of actinides and lanthanides in the low-entropy dynamical ejecta of a NSM. Abundance predictions for this environment depend on the astrophysical conditions assumed, as well as microphysics inputs for the thousands of nuclear species between the valley of stability and the neutron drip

line. The astrophysical parameters that determine the robustness of the *r*-process are most importantly entropy, dynamical timescale, and electron fraction (Y_e), which manifest as temperature and density profiles as a function of time and the initial composition of the nuclear seed material. The electron fraction is set in part by weak interactions; neutrino emission from the accretion disk (and possibly the hypermassive neutron star) produced in the merger event can shape the initial composition of accretion disk (Surman and McLaughlin 2004; Perego et al. 2014; Malkus et al. 2016) and dynamical outflows (Wanajo et al. 2014; Goriely et al. 2015; Martin et al. 2018). Here we focus on the impact of Y_e and select nuclear physics inputs on actinide and lanthanide production.

Section 6.2 describes the nucleosynthesis calculations used to determine initial production ratios and discuss actinide feeding, including recent calculations of nuclear input that has so far not been used in the context of actinide production. Section 6.3 presents a fresh exploration of the production of europium, thorium, and uranium in NSM outflows as a function of neutron excess and investigates the impact of variations in nuclear physics inputs (fission distributions, β -decay rates, and nuclear masses) on simulated actinide and lanthanide production. Section 6.5 applies the resulting initial production ratios of the cosmochronometer pairs Th/Eu, U/Eu, and U/Th to calculate the age of a recently-discovered actinide-boost star and introduce a new method to explain the actinide-boost phenomenon. Lastly, these age calculations are used to explore a possible source of the actinide boost.

6.2 Nucleosynthesis Calculations

In the present work, PRISM is used to study *r*-process nucleosynthesis in a NSM trajectory, allowing a thorough exploration of the influence of different nuclear physics properties on simulated actinide and lanthanide production. We adopt the JINA Reaclib nuclear reaction database (Cyburt et al. 2010) for charged-particle and light-

nuclei reactions. All relevant r -process data are replaced with datasets we construct as self-consistently as possible. Our calculations start with nuclear masses from the Finite Range Droplet Model (FRDM2012; Möller et al. 2012, 2016). We calculate the rates for neutron capture and neutron-induced fission self-consistently with the FRDM2012 masses using the Los Alamos National Laboratory statistical Hauser-Feshbach code (Kawano et al. 2016). Photodissociation rates are calculated using detailed balance. The β -decay strength functions are from Möller et al. (2019), and the relative probabilities for β -decay, β -delayed neutron emission, and β -delayed fission are calculated using the QRPA+HF framework (Mumpower et al. 2016a). All theoretical fission rates use fission barriers from Möller et al. (2015), including the spontaneous fission channel, which is calculated from the relation in Zagrebaev et al. (2011). All fission distributions are assumed to follow a simple symmetric split in which the fissioning nucleus (Z, A), with Z protons, N neutrons, and mass number A , splits into two product nuclei $(Z/2, A/2) + (Z/2, A/2)$; no neutron emission is included in this simple treatment. Theoretical α -decay rates are found from a Viola-Seaborg relation using Q_α values calculated from FRDM2012 masses and parameters fit to known data. All calculations presented here include evaluated masses and decay rates where known, based on the Atomic Mass Evaluation and NUBASE2016 (Audi et al. 2017). We take care to ensure no theoretical decay rates supplant experimentally established decay data.

For astrophysical conditions, we implement NSM trajectories from a variety of sources and dynamically calculate nuclear reheating, adjusting the temperature of the trajectory accordingly (as in, e.g., Lippuner and Roberts 2017). We find that Y_e and nuclear physics inputs affect the simulated abundances more than the details of reheating (Mendoza-Temis et al. 2015). Therefore, in this study, we focus on exploring the effects of varying the initial neutron abundance and choices of nuclear physics inputs on the production of the actinides and chronometer pairs. We choose a

trajectory from the 1.4-1.4 M_{\odot} NSM simulations of S. Rosswog (Rosswog et al. 2013; Piran et al. 2013), as in Korobkin et al. (2012), with the nominal electron fraction of $Y_e = 0.035$. We begin calculations at a temperature of 10 GK with seed distributions in nuclear statistical equilibrium (NSE) calculated with the SFHo/FRDM model from Steiner et al. (2013a). All final abundances shown are at 1 Gyr after the start of the r -process event.

6.3 Actinide Feeding

Metal-poor, r -process-enhanced stars are sufficiently old that the only isotopes contributing to the total actinide abundance are ^{232}Th and ^{238}U . These two nuclei are primarily populated by β -decay and through α -decay chains of heavier nuclei. Here we investigate their population in the FRDM2012 (“baseline”) simulation with starting electron fraction of $Y_e = 0.035$. The net amount of material available to eventually feed ^{232}Th and ^{238}U is determined by the nuclear flow of material into the actinide region of the N - Z plane. The $N = 126$ shell closure, in particular, moderates the flow into this region. The flow of material out of this region is determined by fission and, eventually, α decay. The evolution of the abundances as material populates the actinide region is shown in Figure 6.1 at key times in the r -process for the baseline simulation.

At early times, sufficient nuclear reheating occurs such that the nuclear flow proceeds largely in (n, γ) - (γ, n) equilibrium; nuclear masses therefore set the location of the r -process path, and the flow through the $N = 82$, 126, and 184 closed shells is regulated by the β -decay lifetimes of the waiting points at each shell closure. Here the r -process path is terminated in A by neutron-induced fission just above the predicted $N = 184$ shell closure. At these early stages of the r -process, the abundances in the actinide region and above are shaped by the strengths of the predicted $N = 126$ and 184 shell closures, the β -decay lifetimes in the $N = 126$ region and above, and by the

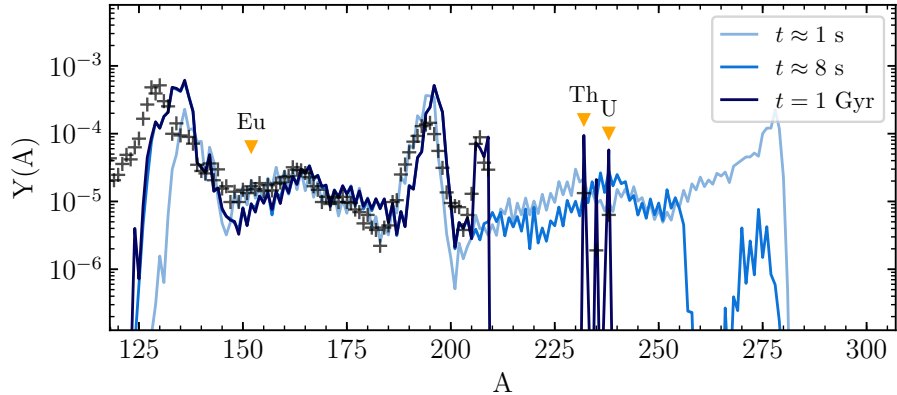


Figure 6.1. Isotopic abundance patterns for the baseline simulation at r -process freezeout ($t \approx 1$ s), when the β -delayed fission dominates over neutron-induced fission ($t \approx 8$ s), and the final time ($t = 1$ Gyr). The isotopes ^{232}Th , ^{238}U , and the region of Eu ($A = 151, 153$) are indicated.

fission barrier heights that determine where the r -process path terminates in A .

As the neutron flux decreases significantly, the system falls out of (n, γ) - (γ, n) equilibrium. The abundance pattern for the baseline simulation at this “freezeout time” is shown by the light blue line (labeled “ $t = 1$ s”) in Figure 6.1. At this time, a $N = 184$ closed shell peak is evident at $A \sim 275$, and the abundances drop sharply at higher A due to the onset of neutron-induced fission above the closed shell.

As the neutron abundance continues to drop precipitously, the rates for neutron-induced fission also decline, and eventually β -delayed fission takes over as the dominant fission channel (Thielemann et al. 1983; Panov and Thielemann 2004; Petermann et al. 2012; Mumpower et al. 2018). The abundances at this time are indicated by the medium blue line in Figure 6.1 (labeled “ $t \approx 8$ s”). Between the first two times in Figure 6.1, about 78% of the mass above $A = 230$ leaves the heavy region as fission transfers material to lower mass numbers. By the end of the simulation, at $t = 1$ Gyr, approximately 10% of the original $A > 230$ mass finds its way into either ^{232}Th or ^{238}U . The remaining $A > 230$ mass (1) populates other short-lived actinides, (2) con-

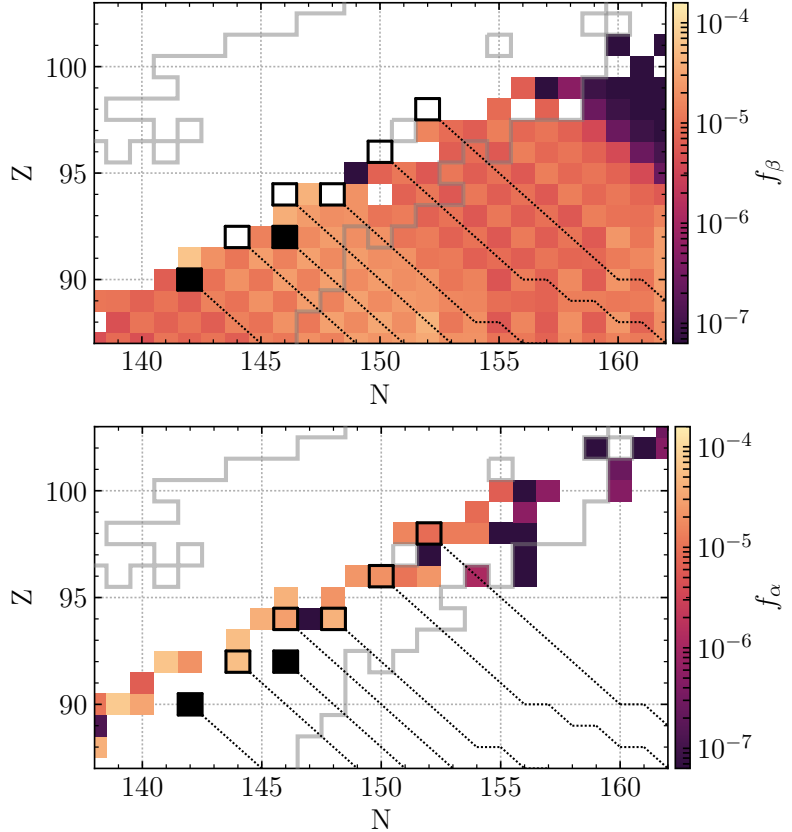


Figure 6.2. Integrated flows for the base calculation at $Y_e = 0.035$ for β -decay (top) and α -decay (bottom). Filled boxes indicate ^{232}Th and ^{238}U . Bold outlined boxes denote nuclei that α -decay into ^{232}Th or ^{238}U , and dashed diagonal lines are the most probable β -decay paths feeding those nuclei. The region outlined in gray denotes nuclei which are included in NUBASE2016.

tinues α -decay to populate lead and bismuth, or (3) simply fissions. The abundance pattern at this final time is shown by the dark blue line in Figure 6.1.

The late-time population of the actinides can be followed in detail using integrated reaction flows. Figure 6.2 shows the integrated β - and α -decay flows for the baseline calculation. For discrete timesteps, the integrated reaction flow $f_x(Z, A)$ of nucleus (Z, A) is expressed as

$$f_x(Z, A) = \sum_i \lambda_{x,i}(Z, A) Y_i(Z, A) (t_{i+1} - t_i), \quad (6.4)$$

where i is the timestep, t_i the time at timestep i , $\lambda_{x,i}(Z, A)$ the rate for reaction x for nucleus (Z, A) at time t_i , and $Y_i(Z, A)$ the abundance of nucleus (Z, A) at time t_i . The reaction flow at time t_i is $\lambda_{x,i}(Z, A) Y_i(Z, A)$. Five nuclei are primarily responsible for the population of observable thorium and uranium by direct α -decay chains; these actinide “feeders” are indicated by bold boxes in Figure 6.2. The primary α -decay feeders of ^{232}Th are ^{236}U and ^{240}Pu . Population of nuclei higher up this α chain, ^{244}Cm and ^{248}Cf , are effectively blocked by long-lived α -emitters ^{244}Pu and ^{248}Cm (80 and 0.35 Myr, respectively). ^{238}U is fed via the α decays of ^{242}Pu , ^{246}Cm , and ^{250}Cf . The β -feeding of the next-higher nucleus on this α chain, ^{254}Fm , is blocked by the spontaneous fission of ^{254}Cf (Zhu et al. 2018), and its α -feeding is prevented by the spontaneous fission of ^{258}No .

These α -chain feeders are populated by β decay. Close to stability, β -feeders can be traced directly to their parent nuclei. However, farther from stability, the probability of β -delayed neutron-emission increases, and many parent isotopes may decay to the same daughter nucleus. Consequently, many nuclei far from stability contribute to the total abundance of the α -feeders through complex β -decay pathways. The β -feeding pathways following the highest β -delayed neutron-emission flows are indicated by the dotted lines in Figure 6.2. The solid gray line in Figure 6.2 indicates the extent of evaluated decay data from NUBASE2016. Included in this database are the half-lives of all of the primary α -feeders, as well as the spontaneous fission branchings that directly impact the ^{232}Th and ^{238}U feedings. Thus the theoretical α -decay and spontaneous fission rates we implement outside of this region have no substantive quantitative impact on the final simulated abundances of ^{232}Th and ^{238}U , since many nuclei surrounding ^{232}Th and ^{238}U are well-studied experimentally. We confirmed this negligible effect by rerunning the baseline calculation with a variety of choices for theoretical α -decay and spontaneous fission rates found in literature (e.g., Zagrebaev et al. 2011; Swiatecki 1955; Petermann et al. 2012), including removing

them completely from the calculation. We find that the sensitivity of the final abundances to these choices of theoretical spontaneous fission and α -decay rates is less than 0.1%.

Instead, the major theoretical nuclear data sets that affect our calculations of actinide feeding include fission fragment distributions, β -decay rates and branchings, and nuclear masses. In the next section we describe the production of thorium and uranium relative to europium as a function of the neutron richness of the astrophysical conditions for distinct choices of the nuclear physics.

6.4 Production of Eu, Th, and U

6.4.1 Baseline Calculation: FRDM2012

For our baseline calculation set, we take FRDM2012 nuclear masses and nuclear data as described in Section 6.2 and vary the initial electron fraction (Y_e) of the baseline astrophysical trajectory between 0.005 and 0.250 in equal intervals of 0.005. We run a full r -process nucleosynthesis calculation for each starting Y_e . Figure 6.3 shows the production of total europium¹, ^{232}Th , and ^{238}U as a function of initial Y_e for the 50 r -process simulations. We hereafter refer to the abundances of these nuclei as generally “thorium” (or “Th”) and “uranium” (or “U”). For this analysis, we focus on three values of Y_e in particular:

- Y_e^L : When Eu (a Lanthanide) reaches the first local maximum as Y_e decreases
- Y_e^A : When Th (an Actinide) is maximized
- Y_e^N : The Nominal value of 0.035 from Korobkin et al. (2012)

These critical Y_e values for the FRDM2012 (baseline) case are denoted in Figure 6.3 and analyzed in detail in Figures 6.4 and 6.5. Figure 6.4 shows the average mass number (\bar{A}) as a function of time for simulations with starting Y_e values of Y_e^L ,

¹Only ^{151}Eu and ^{153}Eu are produced by the r -process and are stable on these timescales.

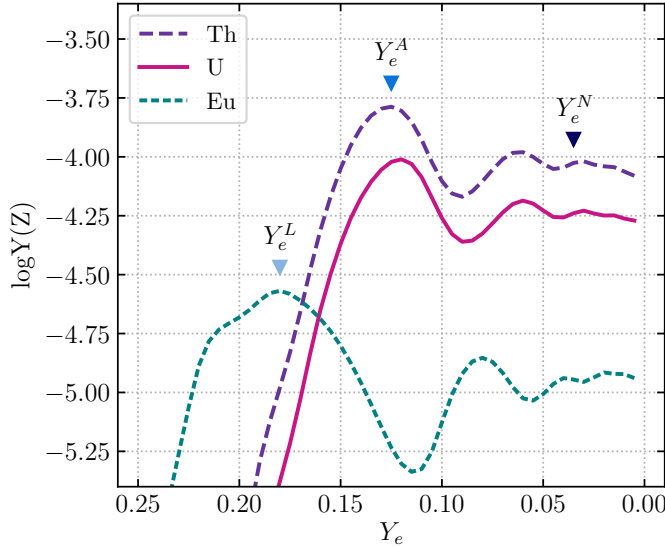


Figure 6.3. Europium, thorium, and uranium production as a function of initial Y_e using 50/50 fission fragment distributions and the FRDM2012 mass model. The Y_e is shown on a reversed scale to reflect increasing neutron richness.

Y_e^A , and Y_e^N , and Figure 6.5 presents their final isotopic and elemental abundance patterns.

As can be seen in Figure 6.3 at the highest Y_e considered (0.25), the *r*-process is insufficiently neutron-rich to proceed past the $N = 82$ shell closure, and $A > 140$ nuclei are not significantly populated. Simulations with increasing neutron-richness, $0.185 < Y_e < 0.25$, produce increasing amounts of the lanthanides, with Eu production reaching a maximum at $Y_e = 0.185 = Y_e^L$. The Y_e^L simulation is sufficiently neutron-rich to produce the $N = 126$ closed-shell peak but not neutron-rich enough to move much material beyond it. As a result, the majority of mass in the network is within and between the $N = 82$ and $N = 126$ closed-shell peaks. The evolution of average mass number \bar{A} for this simulation is indicated by the light blue line of Figure 6.4. \bar{A} initially increases as the *r*-process path is populated and the nuclear flow proceeds to higher mass numbers. Once the free neutrons are exhausted and the

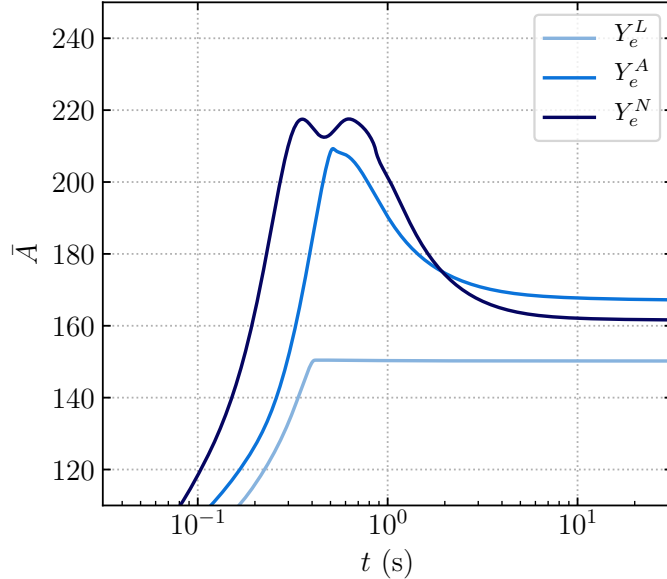


Figure 6.4. Average mass as a function of time for Y_e^L , Y_e^A , and Y_e^N for the baseline case, using symmetric fission fragment distributions and the FRDM2012 mass model.

material begins to decay toward stability, at around $t \sim 0.4$ s, \bar{A} flattens out to its final value of $\bar{A} \sim 150$. The final abundance pattern in Figure 6.5 includes robust $A \sim 130$ and rare-earth ($A \sim 160$) peaks, with a deficit of material beyond $A \sim 200$.

In simulations with $Y_e < Y_e^L$, neutron capture continues past the $N = 126$ closed-shell peak and populates the actinides more effectively. As the material moves up to higher A , the lanthanides are correspondingly depopulated. At $Y_e = 0.125 = Y_e^A$, as indicated in Figure 6.3, the Th abundance reaches a maximum and Eu a local minimum. The evolution of \bar{A} for the simulation with Y_e^A is indicated by the medium blue line of Figure 6.4. Here most of the mass of the simulation moves beyond the $N = 82$ peak and \bar{A} exceeds 200 at freezeout, which occurs around $t \sim 0.5$ s in this case. After freezeout, the drop in \bar{A} is due to the depopulation of the $A > 230$ region by fission and α decay, as described in Section 6.3. The fission products are deposited in the $A \sim 130$ region, and insufficient neutrons remain for the products

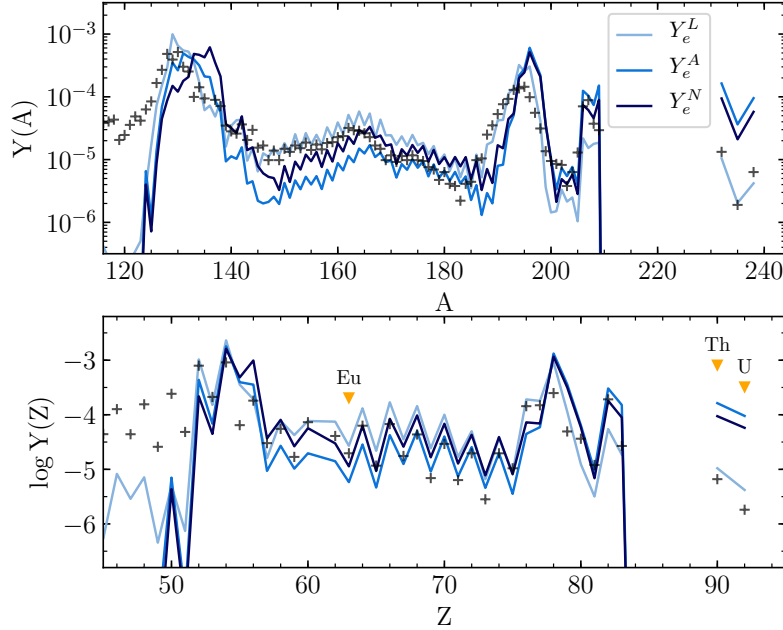


Figure 6.5. Final isotopic (top) and elemental (bottom) abundance patterns for the baseline case corresponding to the three initial Y_e values where lanthanides are maximized (Y_e^L), actinides are maximized (Y_e^A), and the nominal value (Y_e^N). Scaled-Solar r -process abundances (“+”) are from [Sneden et al. \(2008\)](#). The elements Eu, Th, and U are indicated in the bottom panel for clarity.

to capture out of this region. This effect produces a final abundance pattern with strong closed-shell peaks and under-abundant lanthanides, as shown by the medium blue line of Figure 6.5.

Simulations with $Y_e < Y_e^A$ have increased availability of neutrons to both induce fission—removing material from the actinides—and to allow fission products to capture into the rare-earth region. Correspondingly, in simulations with $0.08 < Y_e < 0.125$, the europium abundance again increases and the actinides decrease with decreasing Y_e , as seen in Figure 6.3. A second local europium-minimum/actinide-maximum is found at $Y_e = 0.06$, which occurs when sufficient neutrons are present for fission products to capture past the $N = 126$ shell closure and back into the ac-

tinide region. At this point the integrated fission flow summed over the nuclear chart, $\sum_{Z,A} f_x(Z, A)$, roughly equals the total abundance of the network $\sum_{Z,A} Y(Z, A)$, suggesting the onset of fission recycling.

Fission recycling becomes increasingly robust for simulations with decreasing $Y_e < 0.06$. At Y_e^N , the evolution of \bar{A} shows evidence of multiple fission cycles, shown by the oscillatory pattern in Figure 6.4 at $\bar{A} > 200$, which ends at freeze-out ($t \sim 0.8$ s). Material is deposited into the second peak and recycled several times, allowing the abundance patterns in Figure 6.5—in particular the europium abundance—to stabilize between the two extremes of the Y_e^L and Y_e^A cases (Beun et al. 2008; Mendoza-Temis et al. 2015).

6.4.2 Dependence on Fission Fragment Distribution: Kodama and Takahashi

At low Y_e , the shape of the r -process pattern is dominated by fission recycling and is therefore dependent on the fission properties of neutron-rich nuclei. The fission barriers, rates, and product distributions of these nuclei are poorly known; little experimental data are available, and theoretical estimates vary widely, leading to significant differences in the r -process pattern (Eichler et al. 2015; Côté et al. 2018). Here we examine the impact of fission product yields on lanthanide and actinide production by repeating the simulations of Section 6.4.1 while replacing the 50/50 simple split fission fragment distributions with the double-Gaussian fission distributions of Kodama and Takahashi (1975) (hereafter “K&T”).

Figure 6.6 shows the effect of using the K&T fission fragment distribution on the europium and actinide abundances compared to the simple 50/50 split. As expected, Th and U production is similar in both cases. The small differences that do arise between the abundances of these nuclei are due to the width of the K&T fission distribution, which allows more material to neutron capture up into the fissioning region. This width results in slightly more neutron-induced fission than the baseline

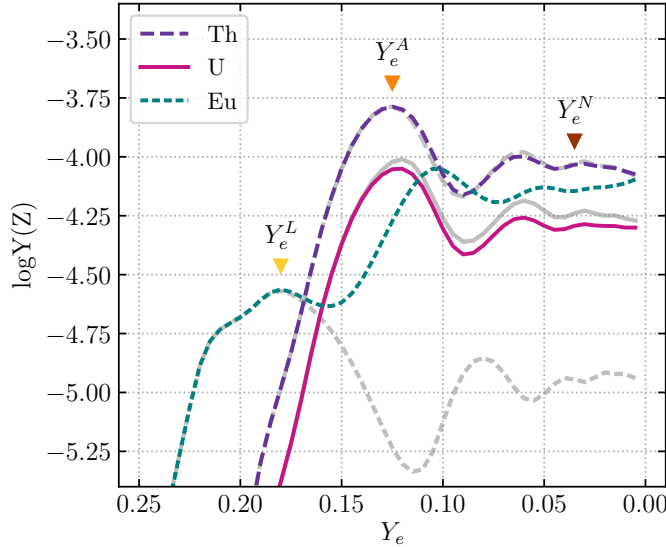


Figure 6.6. Europium, thorium, and uranium production as a function of initial Y_e using [Kodama and Takahashi \(1975\)](#) fission distributions and the FRDM2012 mass model. The baseline case abundances of Figure 6.3 are plotted in gray for comparison.

case, leading to slightly smaller \bar{A} during fission recycling, as shown in Figure 6.7 for the Y_e^N simulation, and slightly lower actinide production for $Y_e < Y_e^A$ as indicated in Figure 6.6.

In contrast to thorium and uranium, europium exists at an atomic mass that can be significantly affected by fission fragment distribution. The K&T fission distribution probabilities are modeled by very broad Gaussians, and our simulations using these yields show fission product deposition in a wide region around the $A \sim 130$ peak, including in the lanthanide region. The additional direct deposition of fission products significantly increases the final Eu abundances for all simulations with an appreciable amount of fission, as shown in Figure 6.6. The resulting final abundance patterns at Y_e^L , Y_e^A , and Y_e^N are shown in Figure 6.8. Even after a single episode of fission cycling (Y_e^A), the $A \sim 145$ region is completely reshaped by the distribution of fission products. Although the actinides are relatively unaffected, fission fragment

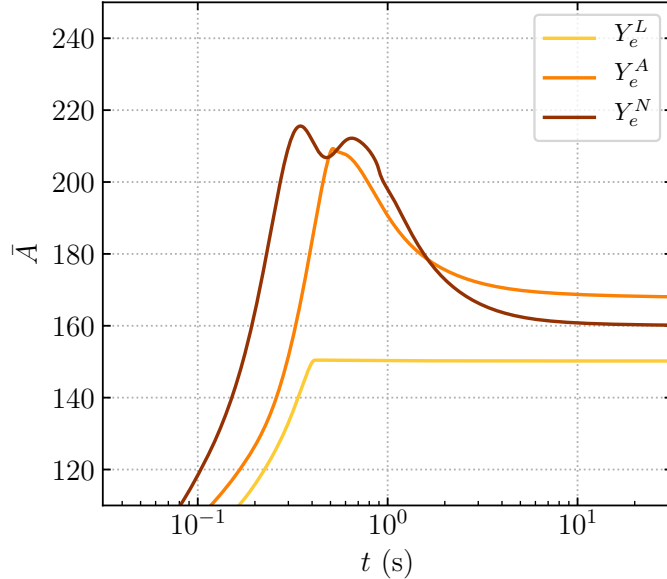


Figure 6.7. Average mass as a function of time for Y_e^L , Y_e^A , and Y_e^N for the K&T case.

distributions may impact the lanthanides directly, reshaping the Th/Eu and U/Eu production ratios.

6.4.3 Dependence on β -Decay Rates: Marketin

The β -decay half-lives of neutron-rich nuclei influence all phases of the r -process. At early times they set the timescale for nuclear flow to high A , the rate of nuclear reheating, and the relative abundances along the r -process path. During freezeout, the final abundances are determined from a competition between β -decay and all other available reaction channels. To study the impact of theoretical β -decay rates on lanthanide and actinide production, we start with our baseline case and use β -decay rates from [Marketin et al. \(2016\)](#) in place of [Möller et al. \(2019\)](#). Reheating is recalculated self-consistently with the updated rates.

Figure 6.9 shows the resulting abundance evolution as a function of Y_e . The same cyclic pattern as the baseline case can still be identified, however, with the [Marketin](#)

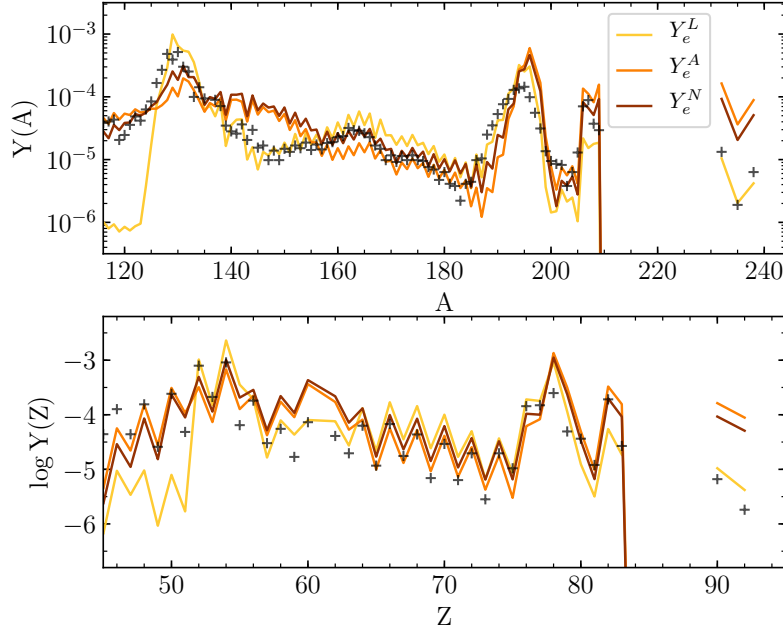


Figure 6.8. Final isotopic (top) and elemental (bottom) abundance patterns for the K&T case corresponding to the three initial Y_e values where lanthanides are locally maximized (Y_e^L), actinides are maximized (Y_e^A), and the nominal value (Y_e^N). Scaled-Solar r -process abundances (“+”) are from Sneden et al. (2008).

et al. (2016) rates the Eu production is larger, the U and Th abundances are lower, and the ratio of U to Th is higher. These differences are driven by two distinct regions of disparity between the Marketin et al. (2016) and the baseline Möller et al. (2019) β -decay rates.

The first relevant difference is in the $A = 130$ peak region. In particular, the Möller et al. (2019) β -decay rates along the $Z = 48$ isotopic chain near the doubly-magic shell closure are approximately four times slower than the Marketin et al. (2016) rates. Differences greater than a factor of two are also present for the $Z = 44$ and $Z = 46$ isotopic chains. When applied to r -process simulations, the faster Marketin et al. (2016) rates of these isotopic chains result in less material piling up in the $A = 130$ region and more material filling the rare-earth region, producing the

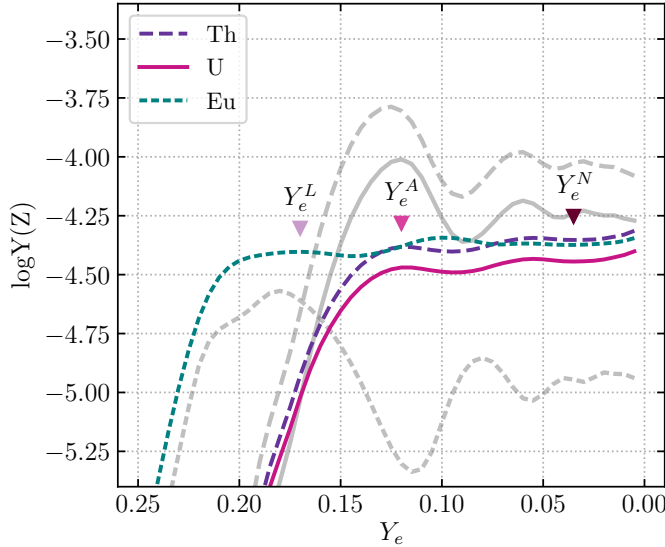


Figure 6.9. Europium, thorium, and uranium production as a function of initial Y_e using 50/50 fission fragment distributions, Marketin et al. (2016) β -decay rates, and the FRDM2012 mass model. The baseline case abundances of Figure 6.3 are plotted in gray for comparison.

increased amount of Eu in Figure 6.9 relative to the baseline.

The second and larger region of disparity is at high A . The Marketin et al. (2016) β -decay rates range between two and several thousand times faster than the Möller et al. (2019) rates above $A \sim 190$, as shown in Figure 6.10. The faster β -decay rates of Marketin et al. (2016) beyond the third r -process peak allow material to pass through the predicted $N = 184$ shell closure and the entire fissioning region faster than in the baseline simulations. As can be seen from Figure 6.10, the neutron-induced fission flow increases due to the high flow of material above the third peak. This effect is also noted and discussed in Eichler et al. (2015). With less material accumulating in this region, particularly at $N = 184$, the late-stage feeding of the actinides is significantly reduced. The lack of material at high A is further illustrated in Figure 6.11, which shows the average mass number of the r -process material over time. Compared to the baseline case (Figure 6.4), the average A is lower for the Y_e^A and Y_e^N simulations,

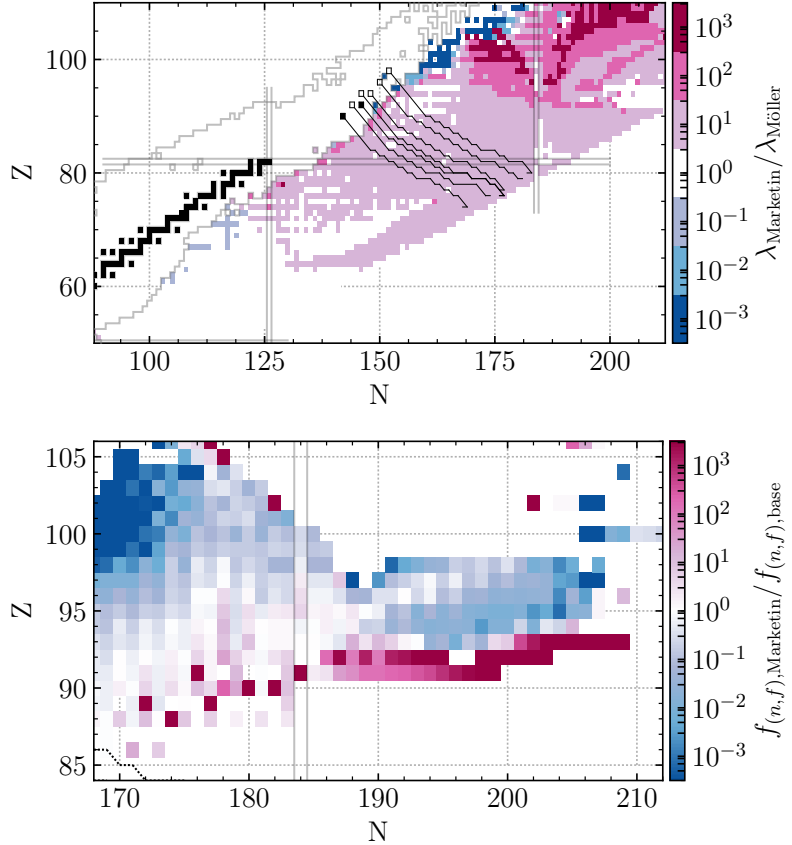


Figure 6.10. Top: comparison of the β -decay rates between QRPA+HF and [Markentin et al. \(2016\)](#). Bottom: integrated neutron-induced fission flow comparison of the [Markentin et al. \(2016\)](#) case and the baseline at $Y_e = 0.035$.

most markedly at the robust fission recycling case, Y_e^N . Although fission cycles can still be identified in the patterns of Figures 6.9 and 6.11, the high fission flows result in diminished variations relative to the baseline case. Similarly, the abundance patterns at different values of Y_e (Figure 6.12) show little variation once fission begins to take place.

The faster [Markentin et al. \(2016\)](#) β -decay rates near $A = 130$ and above $A = 190$ result in simulations that produce more europium and fewer actinides, and thus the predicted Th/Eu and U/Eu initial production ratios are significantly lower than for the baseline case. The impact of these ratios on the ages of r -process material in

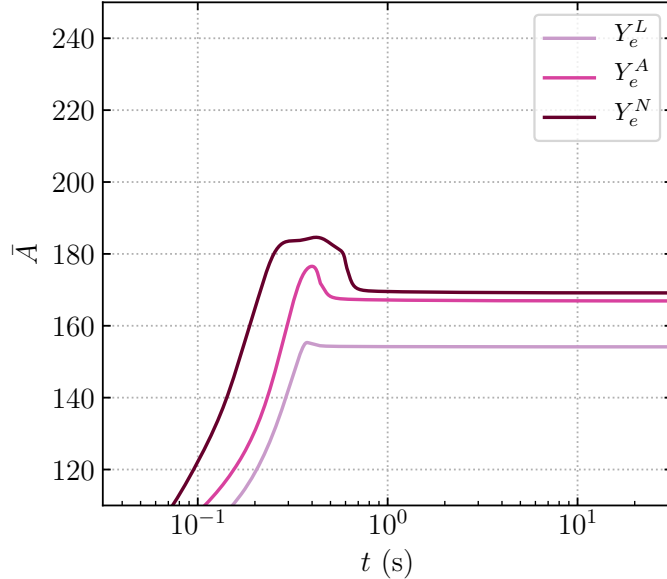


Figure 6.11. Average mass as a function of time for Y_e^L , Y_e^A , and Y_e^N for the Marketin case.

metal-poor stars is discussed in Section 6.5.

6.4.4 Dependence on Mass Model: Duflo-Zuker

The r -process takes place far from stability where we must rely on nuclear mass models to estimate nuclear data. Nuclear masses set the reaction rate and decay Q -values required for calculations of all unknown reaction and decay properties. To study the effect of the mass model choice on predicted actinide production, we implement the Duflo-Zuker mass model with 33 terms (DZ; [Duflo and Zuker 1995](#)). We re-calculate all neutron-capture rates, photodissociation rates, β -decay half-lives, and β -delayed neutron emission probabilities using DZ masses as described in Section 6.2 and [Mumpower et al. \(2015\)](#). We continue to use [Möller et al. \(2015\)](#) fission barrier heights, [Möller et al. \(2019\)](#) β -decay strength functions, and all experimental data. Fission distributions and initial seed nuclei distributions also remain the same as in the baseline case.

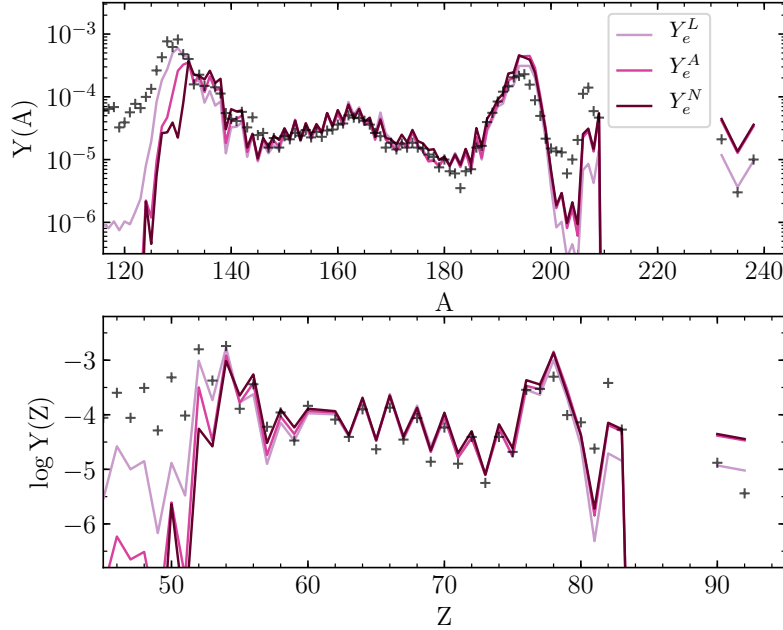


Figure 6.12. Final isotopic (top) and elemental (bottom) abundance patterns for the Marketin case corresponding to the three initial Y_e values where lanthanides are locally maximized (Y_e^L), actinides are locally maximized (Y_e^A), and the nominal value (Y_e^N). Scaled-Solar r -process abundances (“+”) are from [Sneden et al. \(2008\)](#).

Figure 6.13 shows the effect of varying initial Y_e on Th, U, and Eu production in simulations using the DZ mass model. Although the patterns of actinide and lanthanide production as a function of Y_e remain similar to the baseline (FRDM2012) case, there are several features worthy of discussion. Of particular note is the strong amount of Eu that is produced compared to the baseline calculations.

The one-neutron separation energies of DZ are generally lower than FRDM2012; the strength of the second r -process peak in FRDM2012 combined with the 50/50 fission distribution set leads to a characteristic deficiency just beyond the second peak, near $A = 145$ ([Kratz et al. 2014](#)). DZ predicts somewhat weaker closed shells than FRDM2012, and as a result r -process simulations with DZ masses do not produce this deficiency. Instead, material flows smoothly and quickly to heavier masses,

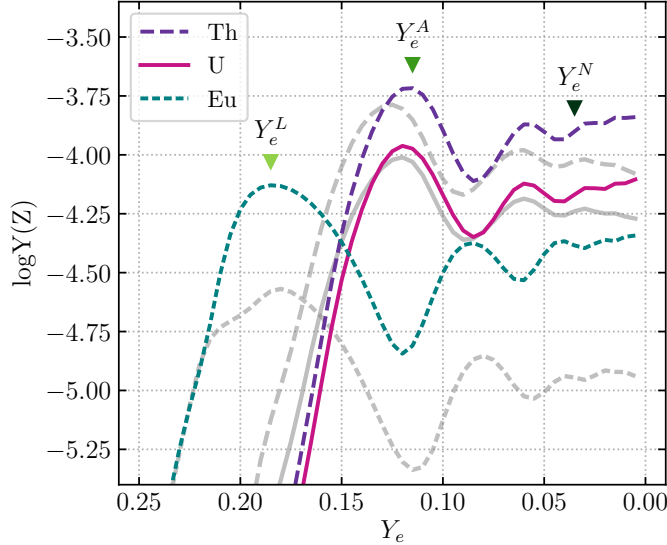


Figure 6.13. Europium, thorium, and uranium production as a function of initial Y_e using 50/50 fission fragment distributions and the DZ mass model. The baseline case abundances of Figure 6.3 are plotted in gray for comparison.

spending less time at the neutron shell closures. Figure 6.14 shows the r -process path just before freezeout for both the baseline and DZ cases, using $Y_e = Y_e^N = 0.035$. Note that while overall the DZ r -process path sits slightly closer to stability, the “kinks” in the path at the neutron shell closures are less pronounced than with the FRDM2012 masses. The r -process waiting points at the top of each closed shell are therefore a bit farther from stability in the DZ simulation and have shorter half-lives, leading to a reduced pile-up of material at the closed shells. This produces a final abundance pattern with a lower $A \sim 130$ peak and higher rare-earth region compared to simulations with FRDM2012, as shown in Figure 6.15.

The second notable feature is that actinide production requires lower Y_e with DZ masses than with FRDM2012, as seen by the shifted rise in Th and U abundances in Figure 6.13 to lower Y_e . This shift indicates that more neutrons are required to initiate actinide production. This is again because of the weaker shell structure of

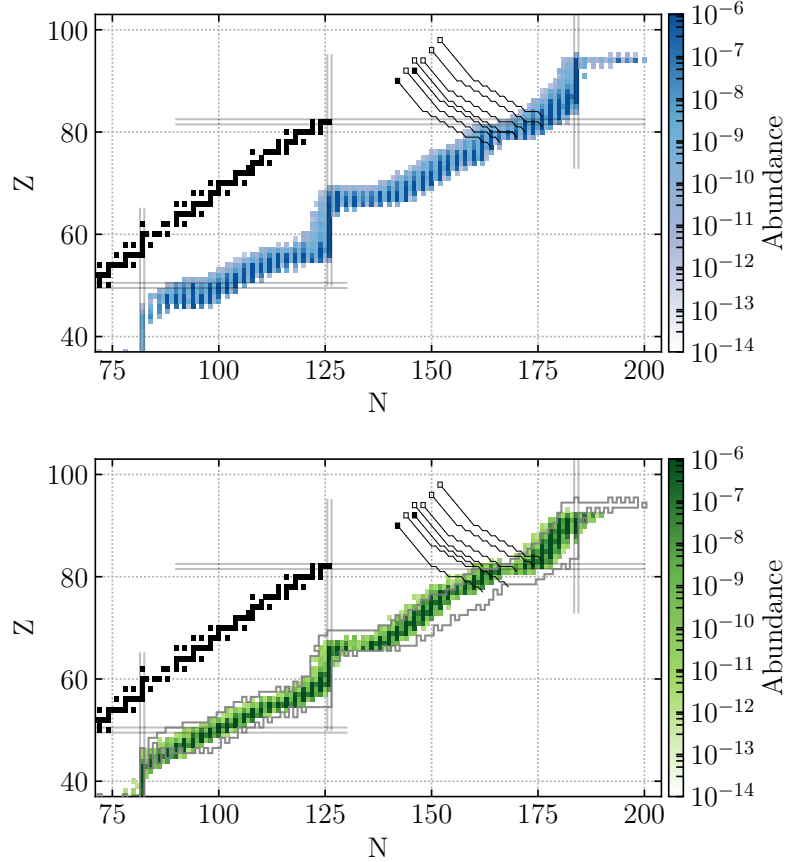


Figure 6.14. Abundances at freezeout using the baseline model (top) and the DZ mass model (bottom) at $Y_e = 0.035$. The baseline FRDM2012 abundances are outlined in gray in the bottom panel for direct comparison.

DZ compared to FRDM2012. With DZ, less material is held up at the $N = 82$ closed shell, so more $N > 82$ material is able to capture neutrons and reach heavier masses. With more material involved in capturing neutrons, a smaller fraction of those neutrons is available to populate the actinides.

For simulations sufficiently neutron-rich for actinide production and fission cycling, the actinide abundances shown in Figure 6.13 follow roughly the same trend with Y_e as the baseline case. One notable difference is that, at the extremely low Y_e end, Th and U production steadily increase with decreasing Y_e , whereas they decrease in the baseline case. At low Y_e , there is more neutron-induced fission when

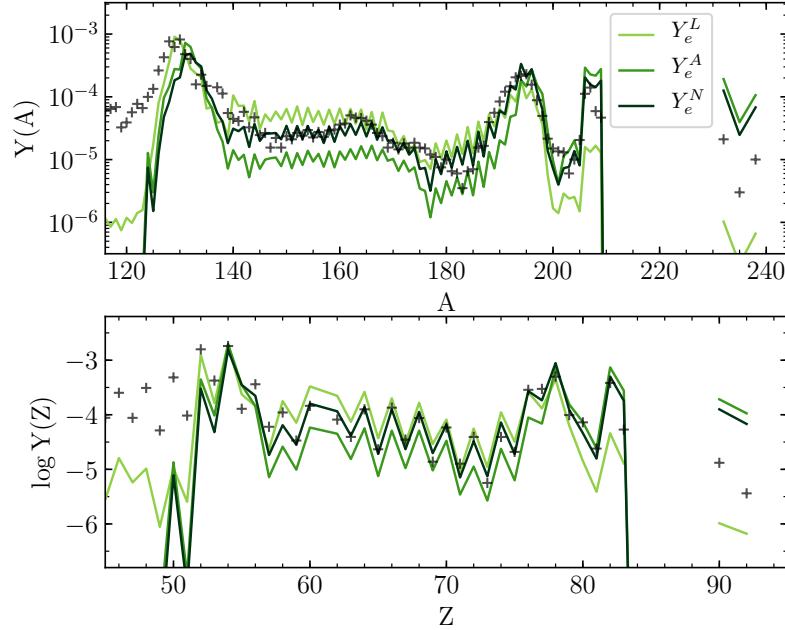


Figure 6.15. Final isotopic (top) and elemental (bottom) abundance patterns for the DZ case corresponding to the three initial Y_e values where lanthanides are maximized (Y_e^L), actinides are maximized (Y_e^A), and the nominal value (Y_e^N). Scaled-Solar r -process abundances (“+”) are from [Sneden et al. \(2008\)](#).

using FRDM2012 masses, which causes the divergence of the actinide abundances between the two models. The higher separation energies of FRDM2012 compared to the incident neutron energy result in an increased likelihood to fission rather than neutron capture.

Simulations with the DZ mass model differ from the baseline most markedly in the production of europium. Consequently, the Th/Eu and U/Eu production ratios are lower than the baseline at every Y_e considered in this work. The impact of these chronometers to the ages of r -process material is discussed in Section 6.5.

6.5 Production Ratios

6.5.1 Comparison to Observations

We now apply the production ratios from Section 6.4 to calculate the age of an *r*-process-enhanced, metal-poor star exhibiting an actinide boost, in order to examine whether the low-entropy dynamical ejecta from NSM could be the source of this signature. We choose to consider the recently discovered *r*-II star J0954+5246 (Holmbeck et al. 2018), which exhibits the strongest actinide boost of any metal-poor star studied to date.

Figure 6.16 shows the derived ages of J0954+5246 using the baseline Th, U, and Eu final abundances from Figure 6.3. These ages are calculated by applying the Th/Eu, U/Eu, and U/Th abundance ratios to Equations 6.1–6.3. At sufficiently low Y_e , the U/Th production ratio stabilizes to a roughly constant value, and the age is estimated to be between 12 and 13 Gyr. However the Th/Eu and U/Eu ages are inconsistent with the U/Th age. This inconsistency at every $Y_e < 0.17$ suggests that if *r*-process conditions are very neutron-rich, the actinides are always over-produced, predicting a Th/Eu age that is far too high compared to observations of actinide-boost stars.

As illustrated in Section 6.4, the predicted production ratios exhibit strong sensitivity to unknown nuclear physics properties of neutron-rich nuclei, and in particular Eu appears to be underproduced relative to Solar in the low- Y_e baseline simulations. We therefore repeat the age estimates for J0954+5246 using production ratios calculated using each set of nuclear physics considered in Section 6.4. Figure 6.17 shows the ages resulting from the $Y_e^N = 0.035$ production ratios using all four cases studied in Section 6.4. For the model to successfully describe the observed ratios of *r*-process material present in the star, all three ages must agree (i.e., lie on a flat line). However, neither literature nor any case presented in Section 6.4 succeeds in describing the

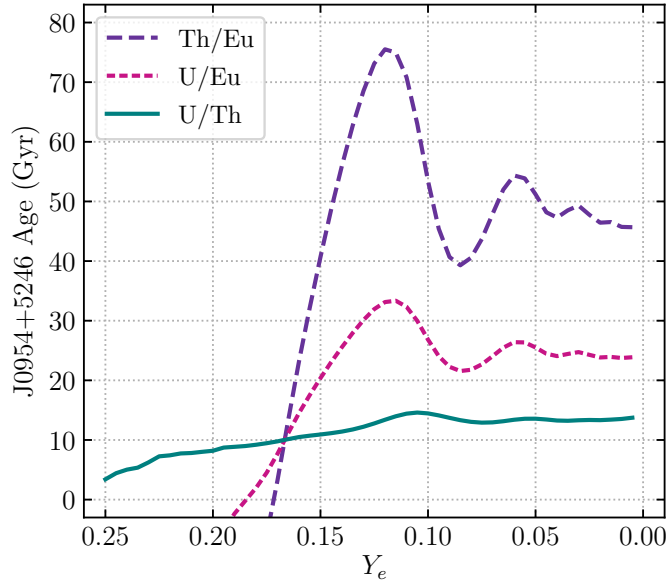


Figure 6.16. Age of J0954+5246 as a function of Y_e using the baseline FRDM2012 mass model.

actinide-boost star, J0954+5246. The cases range from underproducing the actinides (e.g., literature and Marketin) to overproducing them (e.g., base and DZ).

A variety of literature (SNe) production ratios (e.g., [Schatz et al. 2002](#); [Wanajo et al. 2002](#); [Farouqi et al. 2010](#)) all underproduce the actinides in J0954+5246, as shown in Figure 6.17 by the extremely low (often negative) derived Th/Eu and U/Eu ages. Negative ages result from simulation abundances that are less than observed abundances, implying negative (unphysical) actinide decay. In contrast, the baseline and DZ models both overproduce the actinides, resulting in calculated Th/Eu and U/Eu ages that are much larger than the age of the Universe (13.8 Gyr; [Planck Collaboration et al. 2014](#)). The simulation using the [Marketin et al. \(2016\)](#) β -decay rates results in Th/Eu and U/Eu ages that follow a similar trend to those of the literature values. However, the U/Th ratio in this case is quite high and also suggests an age longer than the age of the Universe for both actinide-boost and non-actinide-boost stars. The most consistent ages are obtained from the simulation with the

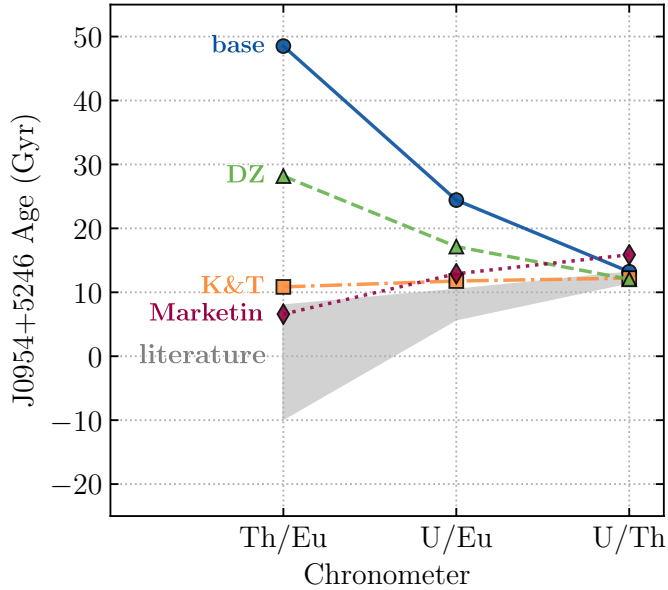


Figure 6.17. Predicted age of the actinide-boost star J0954+5246 based on the three chronometer pairs Th/Eu, U/Eu, and U/Th for each case discussed. Production ratios are taken at Y_e^N .

K&T fission distributions. This result is misleading since both the actinides and europium are overproduced relative to the rest of the pattern, generating a smaller Th/Eu ratio. The actinides are still overproduced compared to lanthanides higher in A , which are less sensitive to fission fragment distribution than europium (e.g., Dy, $Z = 66$, for which the Th/Dy age is ~ 30 Gyr). All but the Marketin case produce roughly similar U/Th ratios, which agree with published production ratios. No model, however, sufficiently describes the actinide-boost star J0954+5246.

It may be possible to produce both a match to the Solar elemental abundance pattern and consistent stellar ages with one fission-cycling trajectory through variations of the nuclear physics inputs beyond those considered here. As described in the previous section, actinide production relative to the rest of the main r -process is shaped by the nuclear masses, fission properties, and β -decay rates, while the europium abundance is particularly sensitive to the fission fragment distribution. Thus,

consistent ages could be obtained by, for example, some combination of a different choice of fission fragment distribution, along with changes to the β -decay or fission rates above $N = 126$. More systematic studies of nuclear properties of heavy nuclei, particularly above $N = 126$, by both theorists and experimentalists are clearly needed. Given the nuclear inputs as chosen, we turn our attention to whether an astrophysical solution can be found to yield consistency between the implied ages.

6.5.2 The Actinide-Dilution Model

Across a variety of nuclear physics inputs, actinides are generally predicted to be overproduced in the low-entropy dynamical ejecta with fission recycling, and none of the models succeed in providing both realistic production ratios and abundance pattern-matching for actinide-boost stars. The low-entropy dynamical ejecta, however, are only one component in NSMs capable of harboring r -process nucleosynthesis. Nucleosynthesis may also occur in the wind of a NSM (e.g., from the accretion disk), which is typically characterized by higher Y_e and higher entropy than the astrophysical trajectory considered here. If the disk wind produces a sufficiently robust r -process pattern (i.e., up to Eu) without synthesizing the actinides, then Th and U abundances can be diluted by the material from the NSM disk wind, lowering the total Th/Eu and U/Eu abundance ratios from the NSM event.

To estimate how combinations of NSM disk and dynamical nucleosynthesis can provide an explanation for the actinide boost, we present a simple actinide-dilution (“AD”) model. In this model, we start with mass distributions as a function of Y_e from the literature: the low-entropy H000 model of Lippuner et al. (2017) for the disk wind and the SFHO model of Bovard et al. (2017) for the dynamical ejecta. We fit Gaussian functions to these two distributions and obtain fits with centroids at $Y_e = 0.16$ and 0.22 and one-sigma spreads of 0.042 and 0.037 for the dynamical ejecta and disk wind, respectively. Next, we normalize the Gaussian fits to the ratio of the

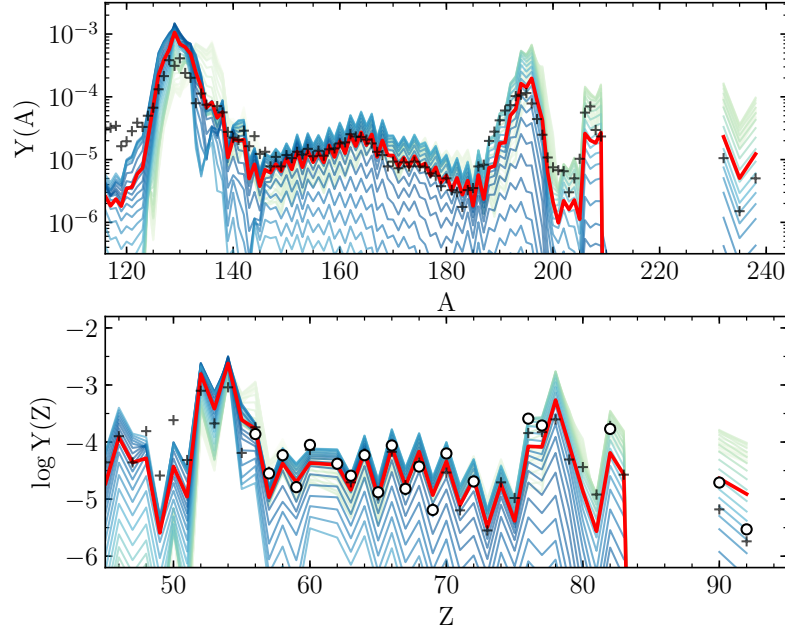


Figure 6.18. The individual (green/blue) and combined (red) abundance patterns that constitute the AD model applied to our baseline FRDM2012 case. Each individual pattern corresponding to different initial Y_e is colored by their mass contribution with light green being the lowest and blue the highest. Scaled-Solar r -process abundances (“+”) from [Sneden et al. \(2008\)](#) and J0954+5246 (circles) are shown for comparison.

mass distributions of the dynamical ejecta (m_{dyn}) and disk wind (m_w). We adopt $m_w/m_{\text{dyn}} = 3$, which both [Rosswog et al. \(2018\)](#) and [Tanaka et al. \(2017\)](#) estimate as the ejected mass distribution ratio for GW170817. This method leaves us with a double-Gaussian approximation for the mass distribution as a function of Y_e . Finally, we multiply the final abundances of each Y_e case by the mass fraction modeled by our fitted double-Gaussian distribution of ejecta. Combining the adjusted abundances by this weighting scheme results in the abundance pattern of Figure 6.18 using the baseline abundances. Figure 6.19 shows the predicted age of J0952+5246 using this weighting scheme applied to all cases considered in Section 6.4. It is important to note that we have used neither the abundances of J0954+5246 nor the abundances

calculated in Section 6.4 to inform the choice of mass distribution. Rather, the same fitted mass distribution is applied to all four cases.

The specific mass distribution assumed by the AD model are such that material which has undergone little to no fission cycling constitutes a majority of the ejecta mass. Therefore, the baseline case—which produced the most unrealistic X/Eu stellar ages when applied to one fission-cycling trajectory as in Figure 6.17—is more successful with AD. The overproduction of actinides and underproduction of europium characteristic of the baseline fission-cycling abundances are moderated by contributions at higher Y_e that fill in the europium and dilute the actinides, resulting in abundance patterns that are a good match to Solar and J0954+5246, as shown in Figure 6.18.

The DZ and Marketin cases are less successful with AD. Simulations using Marketin β -decay rates do not tend to overproduce actinides, even in fission-cycling conditions, and dilution results in extreme negative ages. The unrealistic U/Th age for the Marketin case in Figure 6.17 is not influenced by actinide dilution, and this case is still ruled out under AD. On the other hand, the DZ case shows similar, if not as extreme, X/Eu age overestimates as the baseline case in Figure 6.17. The X/Eu ages become negative, however, under the specific choice of mass distribution and ratio of dynamical-to-wind mass ejecta mass used with the AD model in Figure 6.19. A slight modification to the mass distribution choice used by the AD model could produce a consistent age for the DZ case.

The K&T case appears to be the most successful when applying AD. The reduction of fission-cycling material included in the chosen mass distributions mitigates the overproduction of both europium and actinides, leading to similar actinide-to-europium production ratios before and after AD. The different fission fragment distributions used by the baseline and K&T cases could perhaps represent extreme variations of fission yield asymmetry. Seeing as perfect consistency between the Th/Eu,

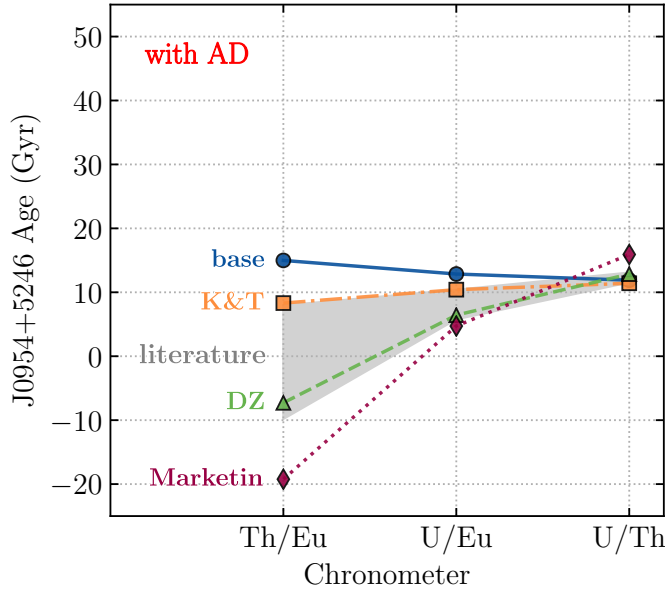


Figure 6.19. Predicted age of actinide-boost star J0954+5246 based on the three chronometer pairs Th/Eu, U/Eu, and U/Th after applying the AD model to each case.

U/Eu, and U/Th ages lies between the baseline and K&T cases with the AD model, modern treatments of fission fragment distributions (e.g., [Goriely et al. 2013](#); [Eichler et al. 2015](#)) could further improve our ability to reproduce observational data.

By simulating a wind component that adds a significant high- Y_e contribution as suggested by the literature, the estimated actinide production in the low-entropy dynamical ejecta is sufficiently diluted to better account for the observations of J0954+5246. We postulate that the r -process event that produced the material observable in J0952+5246 could have been produced by a NSM event occurring 12.9 billion years ago.

Although Y_e is not the only astrophysical parameter describing NSM ejecta, we are able to reproduce the observations of an actinide-boost star by adjusting relative contributions based only on the Y_e . The actinide-boost phenomenon is observed over a range of enhancement levels in different r -process-enhanced stars; if the low- Y_e dy-

nodynamical ejecta of NSMs produce this actinide boost, different mixing ratios between the wind and dynamical ejecta components could account for the observed variation in Th/Eu levels in metal-poor stars. Since actinides are grossly overproduced once fission cycling begins, the actinide-boost variation cannot be explained by the presence of fission cycling alone. Instead, we propose that the observed actinide variation results from the mixing ratio between *r*-processes with slightly different astrophysical conditions, namely Y_e . Since J0954+5246 is presently the highest actinide-boost *r*-II star, the ratio we assume of $m_w/m_{dyn} \approx 3$ is simply a lower limit; more disk mass would be required to account for *r*-process-enhanced stars with lower Th/Eu ratios, as these observed ratios would require more dilution of the actinides. Metal-poor stars with observed ratios of Th/Eu lower than that of J0954+5246 would require a higher mass ratio of disk wind to dynamical ejecta according to our actinide-dilution model.

6.6 Conclusions

The NSM dynamical ejecta are attractive environments for the production of lanthanides and actinides via *r*-process nucleosynthesis. We consider wide variations in the initial neutron richness of the ejected material and distinct choices for the nuclear physics: fission fragment distributions, β -decay rates, and nuclear mass models. We find that the ratio of europium to uranium or thorium is quite sensitive to the electron fraction of the outflow, unless the Y_e is sufficiently low to result in fission recycling, where roughly constant production ratios are achieved. These constant ratios almost uniformly predict an overproduction of actinides relative to lanthanides.

While the predicted overproduction of actinides points to a possible avenue to explain the phenomenon of actinide-boost stars, we find our NSM dynamical ejecta production ratios do not result in realistic age estimates for even the most actinide-boosted star discovered so far, J0952+5246. This may suggest that a significant disk

wind component which synthesizes lanthanides but fewer actinides is required. We construct a simple model, combining low- Y_e dynamical ejecta with higher- Y_e disk material according to modeled Y_e distributions from the literature. We find that a ratio of disk to dynamical ejecta mass of ~ 3 produces realistic Th/Eu and U/Eu ages that are consistent with the U/Th age of an actinide-boost star.

The range in actinide ratios observed thus far in *r*-process-enhanced metal-poor stars can possibly be explained as coming from neutron star mergers with varying ratios of disk to dynamical ejecta. In future work we will explore this possibility by extending our actinide-dilution (AD) model to include the full variety of disk and dynamical outflow trajectories from modern NSM simulations. As part of the RPA efforts, much larger numbers of *r*-process-enhanced stars are currently being discovered in the Galactic halo (e.g., Hansen et al. 2018; Sakari et al. 2018a; Ezzedine et al. 2020), including additional stars with both U and Th measurements, enabling a refined estimate of the fraction of actinide-boost stars and better constraints on the observed variation in the range of derived Th/Eu, U/Eu, and U/Th ratios among *r*-process-enhanced stars. The precision to which we can reliably quantify the disk/dynamical mass ratio necessary to explain observational data will still be limited by uncertainties in the nuclear physics, neutrino physics, and stellar astrophysics. In future work, we will aim to quantify the impact of these uncertainties as we look forward to experimental, observational, and theoretical progress in these areas.

CHAPTER 7

AN ASTROPHYSICAL SOLUTION TO THE ACTINIDE BOOST

*Reserve your right to think, for even to think
wrongly is better than not to think at all.*

— Hypatia

7.1 Actinide Production as a Signature of NSM Nucleosynthesis

The previous chapter showed how the neutron-rich ejecta (e.g., the tidally ejected material) of NSMs may be responsible for the actinide-boost that is observed in a fraction of metal-poor stars. However, this actinide-rich ejecta must be diluted by a lanthanide-poor, actinide-rich component—from possibly the accretion disk wind—in order to match observed actinide abundances. In this work, we quantify the contribution by both of these components and shows that NSMs can produce both an actinide-boost and an actinide-deficient stellar signature, depending on how much wind and tidal material is ejected.

Incorporating heavy element signatures of metal-poor, *r*-process enhanced stars into theoretical studies of *r*-process production can offer crucial constraints on the origin of heavy elements. In this chapter, we introduce and apply the “Actinide-Dilution with Matching” model to a variety of stellar groups ranging from actinide-deficient to actinide-enhanced to empirically characterize *r*-process ejecta mass as a function of electron fraction. We use this methodology to speculate whether the actinide variation may indicate a separate *r*-process progenitor object or site that is responsible for the existence of actinide-boost stars (Schatz et al. 2002), or, alternatively, whether

it may be possible that the variations in the actinides and limited-*r* elements in the *r*-I and *r*-II stars can be fully accounted for by variations of astrophysical conditions (e.g., the electron fraction, Y_e) within the same *r*-process source (i.e., type of site). We find that actinide-boost stars do not indicate the need for a unique and separate *r*-process progenitor. Rather, small variations of neutron richness within the same type of *r*-process event can account for all observed levels of actinide enhancements. The very low- Y_e , fission-cycling ejecta of an *r*-process event need only constitute 10–30% of the total ejecta mass to accommodate most actinide abundances of metal-poor stars. With this analysis in hand, we are able to weigh in on the implications of the observations of limited-*r* and actinide elements, and further, to use observations of low-metallicity stars to provide a consistency check on the amount of lanthanide-rich material inferred from recent “kilonova” observations. We find that our empirical Y_e distributions of ejecta are similar to those inferred from studies of GW170817 mass ejecta ratios, which is consistent with neutron-star mergers being a source of the heavy elements in metal-poor, *r*-process enhanced stars.

7.2 Observations of Metal-Poor Stars

In this section, we discuss observations of metal-poor stars in the context of actinide and limited-*r* production. To study the full range of the elemental *r*-process pattern at early times, we choose Zr, Dy, and Th as representative of the limited-*r* process, main *r*-process, and actinides, respectively. Although $_{38}\text{Sr}$ and $_{63}\text{Eu}$ are traditionally used to quantify the limited-*r* and main *r*-process contributions, we instead use $_{40}\text{Zr}$ and $_{66}\text{Dy}$ to probe these two regions. More and unsaturated absorption lines of Zr II are available over the few of Sr II from which to derive an abundance, leading to Zr abundances with higher precision. In addition, Sr II suffers larger systematic abundance corrections from assuming LTE over non-LTE, while the Zr II corrections are lower and the abundances more robust under LTE (Andrievsky et al. 2011).

In the lanthanide region, the production of Eu by the *r*-process may be sensitive to fission yields, especially to broad and asymmetric fission distributions that place material above the second *r*-process peak (e.g., [Kodama and Takahashi 1975](#); [Eichler et al. 2015](#); [Côté et al. 2018](#); [Vassh et al. 2019](#)). Moreover, the fission fragment distributions of nuclei that may participate in the *r*-process at high nuclear masses are far from known. To avoid fission-dependent results, we use Dy instead of Eu. At a slightly higher mass, Dy is less sensitive to (but not entirely free from) the direct effects of fission fragment distributions.

7.2.1 Milky Way *r*-Process Enhanced Stars

We first consider all metal-poor Milky Way stars that have both Zr and Dy abundance measurements included in JINAbase and individual additions from the recent discoveries in [Placco et al. \(2017\)](#); [Ji and Frebel \(2018\)](#); [Sakari et al. \(2018b\)](#), and [Holmbeck et al. \(2018\)](#). This data set is displayed in the left panel of Figure 7.1. The absence of stars with both low Zr and high Dy abundances (i.e., upper-left of the left panel of Figure 7.1) may suggest that some minimum Zr is made in the same event that created Dy. This trend was also noted in [Roederer \(2013\)](#) who analogously used Sr and Ba abundances.

The light and dark blue dashed lines in Figure 7.1 indicate $\log \epsilon(\text{Zr}/\text{Dy}) = 0.95$ and $\log \epsilon(\text{Zr}/\text{Dy}) = 0.46$, respectively, for reference and guidance on the abundance trend. Stars with $\log \epsilon(\text{Zr}/\text{Dy}) > 0.95$ are mostly those with no *r*-process enhancement (i.e., $[\text{Eu}/\text{Fe}] \leq +0.3$) and/or with enhancement in other elements, such as carbon and *s*-process elements (e.g., $[\text{Ba}/\text{Eu}] \geq 0$). The line at $\log \epsilon(\text{Zr}/\text{Dy}) = 0.46$ reflects that of the scaled, average $\log \epsilon(\text{Zr}/\text{Dy})$ abundance for *r*-process stars in Ret II. We note that all stars with a Th measurement have a $\log \epsilon(\text{Zr}/\text{Dy})$ abundance of at least this value. The right panel of Figure 7.1 shows the subset of stars from the left panel that, in addition, have a Th measurement. The wide range of

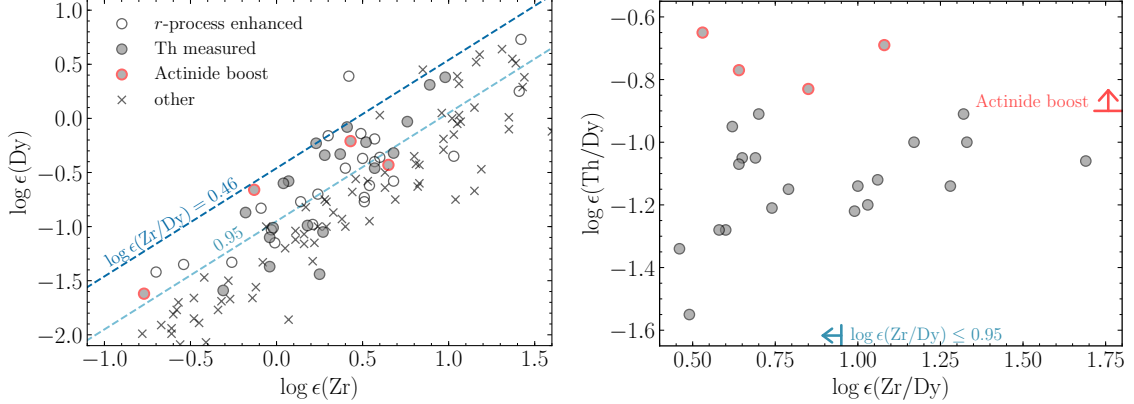


Figure 7.1. Left: Dy versus Zr abundances for metal-poor Milky Way stars with an *r*-process signature (circles), a measurement of Th (filled circles), an actinide-boost signature (red outlines), or other enrichment (e.g., *s*-process, *i*-process, and/or carbon enhancement; crosses). The dashed lines are constant values of $\log \epsilon(\text{Zr}/\text{Dy})$ of 0.46 and 0.95. Right: scatter of $\log \epsilon(\text{Th}/\text{Dy})$ as a function of $\log \epsilon(\text{Zr}/\text{Dy})$ for those stars with a measurement of Th. Data were selected from Abohalima and Frebel (2018); Placco et al. (2017); Ji and Frebel (2018); Sakari et al. (2018b); Holmbeck et al. (2018).

$\log \epsilon(\text{Th}/\text{Dy})$ abundances is entirely represented by stars with $\log \epsilon(\text{Zr}/\text{Dy}) \leq 0.95$. At higher values of $\log \epsilon(\text{Zr}/\text{Dy})$, the $\log \epsilon(\text{Th}/\text{Dy})$ appears to converge towards a constant value of $\log \epsilon(\text{Th}/\text{Dy}) \approx -1.0$.

Most of the confirmed *r*-process enhanced stars lie in the range $0.46 \leq \log \epsilon(\text{Zr}/\text{Dy}) \leq 0.95$. These stars also show the broadest range of $\log \epsilon(\text{Th}/\text{Dy})$. For this work, we posit that these *r*-process stars display a pure *r*-process signature that has come from just one event. For *r*-process stars with $\log \epsilon(\text{Zr}/\text{Dy}) > 0.95$, while it is possible that their *r*-process signatures may have also come from a single event, it is also possible that their *r*-process material has been diluted or altered by additional types of nucleosynthesis (i.e., other than a main *r*-process) or strong contributions from limited-*r* process events. Therefore, to study the widest range of actinide production by a single *r*-process site, we focus on *r*-process stars with $\log \epsilon(\text{Zr}/\text{Dy}) \leq 0.95$.

7.2.2 Kinematically Linked Groups of *r*-Process Enhanced Stars

Given the presumed accretion of stars that now reside in the Milky Way’s halo, the *r*-process enhanced halo stars have essentially unknown origins. Specifically, it has been suggested that the *r*-process enhanced halo stars originated in dwarf galaxies that were eventually accreted by the Milky Way as part of its hierarchical growth. If a prolific *r*-process event enriched the original, low-mass host galaxy, such as that in Ret II, the imprints on these stars offer a window into the element production by (presumably) single *r*-process events.

[Roederer et al. \(2018a\)](#) recently found kinematic grouping among spatially unrelated *r*-process enhanced halo stars. These kinematic groups are further evidence that *r*-process enhanced halo stars were once members of satellite galaxies which became accreted by the Milky Way. The progenitor dwarf galaxies of these kinematic groups could resemble Ret II, where all stars belonging to each of these progenitor systems would have formed from gas enriched by single, respective *r*-process events. Therefore, we assume that the elemental abundances of stars in the kinematic groups now reflect the range of element production by single events. Abundance pattern differences among members of each group could then point to different astrophysical *r*-process conditions within the same type of event or even entirely different *r*-process sources. In this regard, the seven *r*-II stars in Ret II can be treated as an additional such group as it is highly likely that only one *r*-process event took place prior to their formation. Hence, stellar abundance variations within these groups could provide insight into the range of *r*-process element production by a single event.

In the following, we expand on the principal idea of assigning groups of *r*-process stars. Specifically, we focus on elemental abundance variations between these groups in the actinide and limited-*r* elements. Here, we choose to define “actinide-deficient” as $\log \epsilon(\text{Th}/\text{Dy}) < -1.20$, “actinide-normal” as $-1.20 \leq \log \epsilon(\text{Th}/\text{Dy}) \leq -0.90$, and “actinide-boost” as $\log \epsilon(\text{Th}/\text{Dy}) > -0.90$.

Ret II — Although the scaled, heavy-element (between Ba and the third r -process peak) abundance patterns of seven Ret II stars closely resemble those of r -II halo stars, the only Ret II member for which a Th measurement is available (DES J033523–540407; [Ji and Frebel 2018](#)) displays a strikingly low actinide abundance compared to its lanthanides ($[Th/Eu] = -0.34$). The seven r -II stars of Ret II might reflect an event with low actinide production, or possibly one with a significant range. Without a complete set of Th abundances for each of the r -II stars in Ret II, we assume, for simplicity, that this low actinide level reflects low actinide production in the r -process event that enriched the Ret II gas. Thus we assume Ret II has $\log \epsilon(Th/Dy) = -1.49$.

Group F — The kinematic “Group F” in [Roederer et al. \(2018a\)](#) consists of three stars: CS 29529–054 ([Roederer et al. 2014a,b](#)), HE 2224+0143 ([Barklem et al. 2005](#); [Ren et al. 2012](#)), and HD115444 ([Westin et al. 2000](#)), the latter two of which have “normal” actinide abundances: $[Th/Eu] = 0.05$ and $[Th/Eu] = -0.21$, respectively, and $\log \epsilon(Th/Dy) = -1.19$ on average.

J0954+5246 — Just a single star, but representing extreme levels of actinide production by an r -process. 2MASS J09544277+5246414 (“J0954+5246”; [Holmbeck et al. 2018](#)) is currently the most actinide-enhanced r -II star known, with $[Th/Eu] = 0.38$ and $\log \epsilon(Th/Dy) = -0.65$.

We treat these three levels of relative actinide enhancement as three distinct “groups” and assume that each group’s members formed from gas enriched by a individual r -process event. Together, the stellar abundances of the stars in Ret II, Group F, and J0954+5246 reflect a range of actinide enhancement, which may indicate either separate r -process actinide sources or a variation within one type of r -process source.

Between the three groups, the abundances of the limited- r elements (Sr, Y, and Zr) also vary with respect to the lanthanide abundances. Whereas it has been

suggested that these light neutron-capture elements may originate from a separate r -process site, we assume in this analysis that for r -process enhanced stars with $\log \epsilon(\text{Zr}/\text{Dy}) \leq 0.95$, these elements come from the same event that also synthesized the actinides. Thus, within each group, we consider the relative variations among the limited- r elements as well as the actinides as intrinsic to the progenitor r -process event.

For this study, we combine the abundances of stars within Ret II and Group F by scaling the individual abundance patterns to the respective average residual obtained from comparison with the Solar r -process pattern between $_{56}\text{Ba}$ and $_{71}\text{Lu}$. After scaling the Solar pattern such that the average deviation of the stellar pattern from Solar pattern between Ba to Lu is minimized, we find the range of scaled abundances derived for each element over all stars in Ret II and Group F separately. For J0954+5246, and in the cases where an element was only measured in one star in the group (e.g., Th in Ret II), we use the reported uncertainty in its derived abundance as representative of the “range” for the group. These ranges/uncertainty bands are displayed in Figure 7.2 for the three enrichment cases. In Section 7.3, we adopt these scaled and combined abundance values as model input, in order to reconstruct possible distributions of r -process material ejected by each of the putative progenitor r -process events.

7.3 The Actinide-Dilution with Matching Model

The electron fraction (Y_e) is a major factor governing the ultimate extent of element production by an r -process event. Variations of how r -process ejecta mass is distributed in Y_e may explain the abundance variations within and between stellar groups of r -process enhanced stars, as those described in Section 7.2. Holmbeck et al. (2019b) introduces an Actinide-Dilution (“AD”) model in which a systematic study of Y_e is applied to a mass distribution motivated by literature in order to

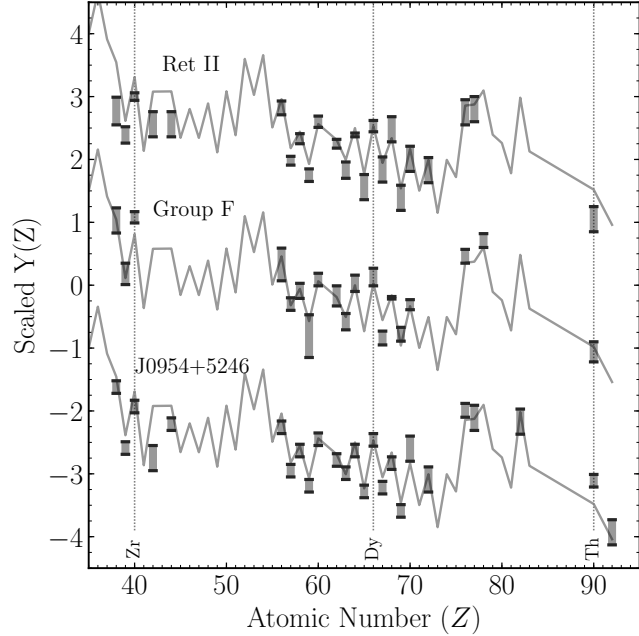


Figure 7.2. Abundance ranges (arbitrary scaling) of the three stellar groups considered in this work. Solid gray lines show the scaled Solar r -process pattern.

match scaled actinide-boost stellar abundances. In this section, we build empirical r -process ejecta distributions as a function of Y_e by employing a Monte-Carlo method as an extension to the AD model, which we call the Actinide-Dilution with Matching (“ADM”) model. Rather than start with literature mass distributions, this model constructs mass distributions using stellar abundances as input. To constrain the model by matching results to stellar abundances, we use three particular regions of the observed r -process elemental abundance patterns: the limited- r group, the lanthanides, and the actinides, represented by Zr, Dy, and Th, respectively. These abundance constraints and their allowed tolerances for the ADM model results are listed in Table 7.1 for the three groups described in Section 7.2.2.

Since Th could only be measured in one or two stars per group, the allowed abundance ratios listed in Table 7.1 come from a single star with the assumption

TABLE 7.1
ABUNDANCE RATIO MATCHING CONDITIONS USED BY THE ADM
METHOD

Group	#	$\log \epsilon(\text{Zr}/\text{Dy})$	$\log \epsilon(\text{Th}/\text{Dy})$	$\log \epsilon(\text{U}/\text{Th})$
Ret II	7	0.46 ± 0.20	-1.49 ± 0.30	-0.25 ± 0.10
Group F	3	0.95 ± 0.20	-1.19 ± 0.30	-0.25 ± 0.10
J0954+5246	1	0.53 ± 0.20	-0.65 ± 0.30	-0.25 ± 0.10

that all other stars within the group have $\log \epsilon(\text{Th}/\text{Dy})$ ratios lying with a broad 0.3 dex of that single measurement. Furthermore, we add 0.2 dex to the adopted $\log \epsilon(\text{Th}/\text{Dy})$ matching-constraint listed in Table 7.1. This addition accounts for radioactive Th decay over roughly 10 Gyr from the final abundances of our *r*-process calculations to the present.

Of the three groups in Figure 7.2, only one star has a reliable uranium measurement, which is unsurprising given that overall, fewer than ten *r*-process enhanced stars have a reliable detection of uranium. For stars with both Th and U measurements available, studies applying radioactive decay dating have shown the U/Th production ratio agrees with a roughly constant value, $\log \epsilon(\text{U}/\text{Th}) \approx -0.25$, even for the actinide-boost stars which show absolute enhancement in these elements (e.g., Cowan et al. 1999; Schatz et al. 2002; Wanajo et al. 2002; Farouqi et al. 2010). Hence, for this analysis, we assume that the *r*-process material in all stars with Th was produced with the same U/Th ratio, and supply this ratio as an additional constraint to the ADM model. The *production* ratio rather than the observed ratio is used since Th and U are radioactive, and their abundances change over time.

After establishing the observational constraints, we first ran several *r*-process

simulations using a medium-entropy parameterized trajectory (evolution of an ejecta mass element, here with initial entropy $s/k \approx 40$ and dynamical timescale $\tau_{\text{dyn}} = 20$ ms) as in Zhu et al. (2018). This trajectory is consistent with an accretion disk wind around a proto-neutron star (e.g., a collapsar or NSM remnant; Surman and McLaughlin 2004). We vary the Y_e as in Holmbeck et al. (2019b) to allow for multiple levels of neutron-richness within the same environment, changing the initial Y_e from 0.005 to 0.450 in equal steps of 0.005. The r -process calculations are run using the nuclear network code Portable Routines for Integrated nucleoSynthesis Modeling (PRISM; Mumpower et al. 2017; Côté et al. 2018; Mumpower et al. 2018; Vassh et al. 2019). Reaction and decay rates relevant to the r -process are constructed as self-consistently as possible. Starting with nuclear masses from the Finite Range Droplet Model (FRDM2012; Möller et al. 2012, 2016), we adopt the neutron-capture and neutron-induced fission rates calculated self-consistently with FRDM2012 masses using the Los Alamos National Laboratory statistical Hauser-Feshbach code (Kawano et al. 2016). The QRPA+HF framework (Mumpower et al. 2016b) is used to calculate the relative probabilities of β -decay, β -delayed fission, and β -delayed neutron emission for each nucleus, using Möller et al. (2019) β -decay strength functions. Fission barrier heights from Möller et al. (2015) are used to calculate fission rates, employing the Zagrebaev et al. (2011) relation for the spontaneous fission channel and adopting symmetric fission fragment distributions for all fission channels.

Figure 7.3 shows the final calculated Zr, Dy, and Th abundances as functions of Y_e . At the highest values of Y_e considered, a large amount of limited- r material around the first r -process peak (here, Zr) is synthesized, yet material does not move much beyond the second r -process peak ($A \approx 130$, $Z \approx 54$) until $Y_e < 0.30$. With decreasing Y_e , the lanthanides (Dy) are produced, and actinide (Th) production begins at $Y_e < 0.23$. The oscillatory behavior of the lanthanide and actinide abundances at very low Y_e are due to fission cycles that occur in very neutron-rich environments (as discussed

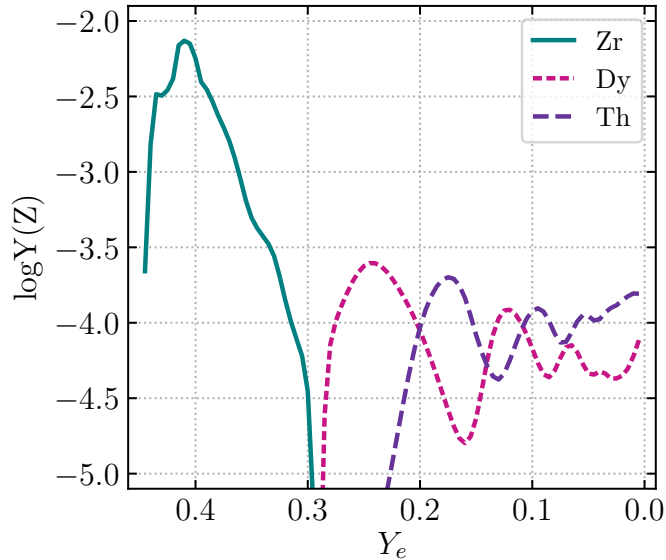


Figure 7.3. Final Zy, Dy, and Th abundances as a function of Y_e for the disk wind using the FRDM2012 mass model.

in detail in Holmbeck et al. 2019b).

With final abundances generated as functions of Y_e , we randomly select N number of Y_e 's between 0.005 and 0.450 and the corresponding final Zr, Dy, Th, and U abundances. We choose $N = 15$ to minimize computational time, allow the results to converge, and robustly probe the entire Y_e range. Results generally converge with $N \geq 8$. Next we add the total Zr, Dy, Th, and U abundances over the N randomly selected values. If the total $\log \epsilon(\text{Zr}/\text{Dy})$, $\log \epsilon(\text{Th}/\text{Dy})$, and $\log \epsilon(\text{U}/\text{Th})$ abundances are within the specified constraints of Table 7.1, we keep all N Y_e 's. We repeat this sampling until we accumulate 100 successes, summing a total of $100N$ individual abundance patterns. When combined, the summed abundances pattern matches the relative observational Zr, Dy, Th, and U abundances for a given kinematic group within the listed tolerances.

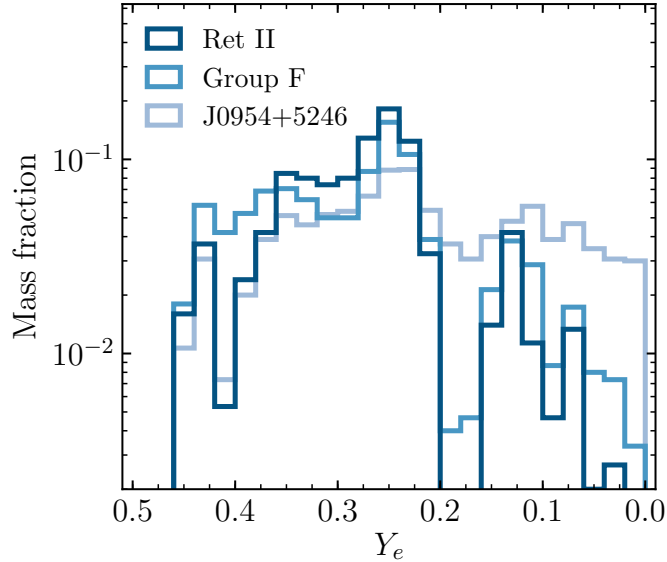


Figure 7.4. Ejecta distributions characterizing an r -process event predicted by the ADM model when matching Ret II, Group F, and J0954+5246 abundances using the disk wind trajectory and the FRDM2012 mass model.

7.4 ADM Model Results

Figure 7.4 shows the empirical r -process ejecta distribution results of the ADM model applied to the three stellar cases discussed in Section 7.2.2. The empirical mass ejecta distributions that characterize the observed abundance ratios of Ret II, Group F, and J0954+5246 mainly differ in the very low- Y_e tail ($Y_e < 0.18$ in this trajectory) where robust fission cycling and actinide production occurs. The low actinide abundance constraints of the Ret II group allows less mass in this very low- Y_e tail to be ejected, while the actinide-normal Group F and actinide-boost J0954+5246 allow increasing amounts of this fission-cycled material.

The bulk of the mass of material ($Y_e \geq 0.18$) maintains a similar shape in all three cases, including a strong preference for $Y_e \approx 0.25$ and a dip in ejecta production at $Y_e \approx 0.18$. The peak occurs because the $\log \epsilon(\text{Th}/\text{Dy})$ ratio is satisfied near $Y_e \approx 0.25$ for all three cases. On the other hand, the dip at $Y_e \approx 0.18$ coincides with

maximal actinide production and (locally) minimal lanthanide production when using this trajectory (see Figure 7.3), producing a $\log \epsilon(\text{Th}/\text{Dy})$ ratio that is much higher than what observations suggest.

Figure 7.5 shows the final abundance patterns for the ejecta distributions shown in Figure 7.4. Every individual abundance pattern (blue) represents a successful set of the N random Y_e choices made in the ADM method. Each combined abundance pattern (red) succeeds in reproducing the scaled abundances of the limited- r elements and many of the lanthanide elements. The common dip surrounding $Z = 60$ (Nd) is mostly due to the strong shell closures of FRDM2012, and partially due to the pure symmetric fission fragment yields we employ. However, this underproduction does not have any influence over the results we present here. We finally note that for all three stellar groups, we have only supplied three abundance constraints to the ADM model. Hence, with few constraints, relatively good agreements across the entire r -process patterns are produced.

7.4.1 The Low- Y_e Component

The largest difference in the empirical Y_e distributions of ejecta with varying levels of actinide enhancement lies in the allowed mass produced in very low- Y_e environments. To investigate this difference in detail, we systematically vary the ADM model input $\log \epsilon(\text{Th}/\text{Dy})$ constraint while holding the $\log \epsilon(\text{Zr}/\text{Dy})$ constraint constant. This way, we can quantify the amount of very low- Y_e material that the progenitor r -process event may eject. We repeat this process twice, once holding the $\log \epsilon(\text{Zr}/\text{Dy})$ constraint at 0.46 and again at 0.95, following the labeled bounds in Figure 7.1 (left panel). Recall that these bounds contain r -process enhanced stars in which the r -process material likely originated from one r -process event. These systematic results are also compared to ADM results using both the $\log \epsilon(\text{Th}/\text{Dy})$ and $\log \epsilon(\text{Zr}/\text{Dy})$ observational abundance ratios from single r -process enhanced stars in

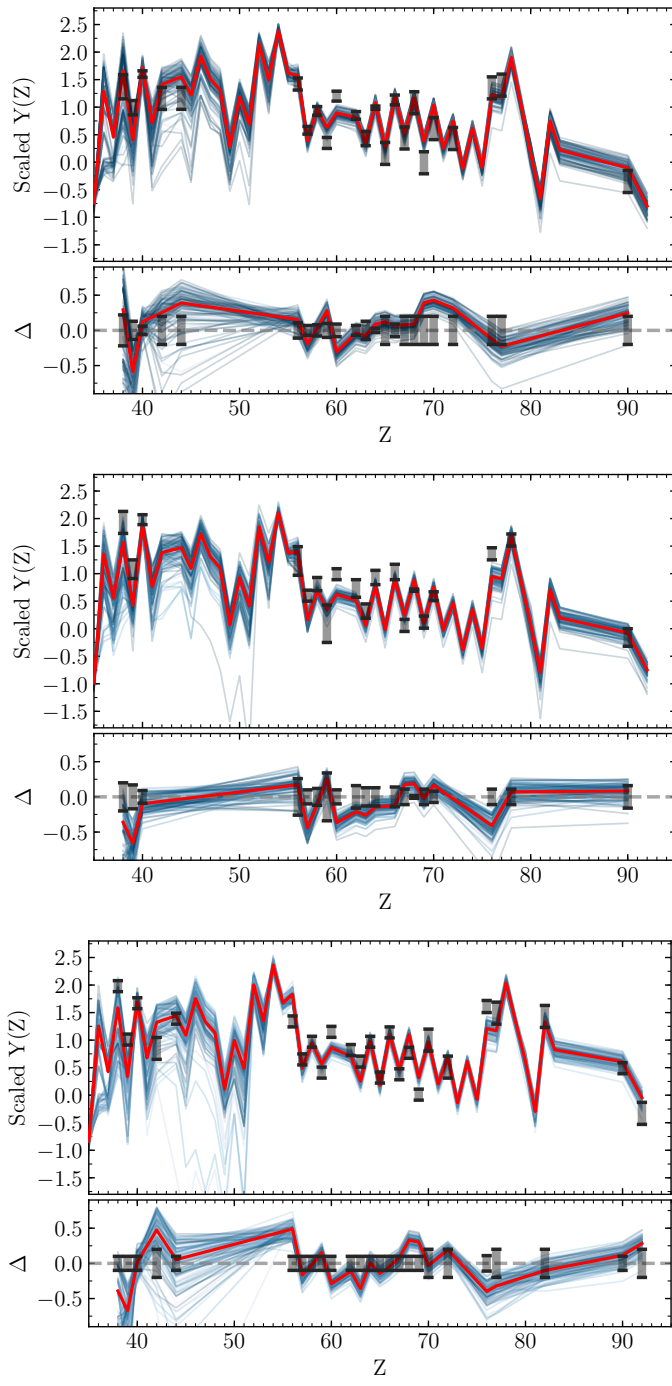


Figure 7.5. Final combined abundance pattern results (red lines) of the ADM model when matching Ret II (top), Group F (middle), and J0954+5246 (bottom) abundances. Successes of individual runs are shown in blue.

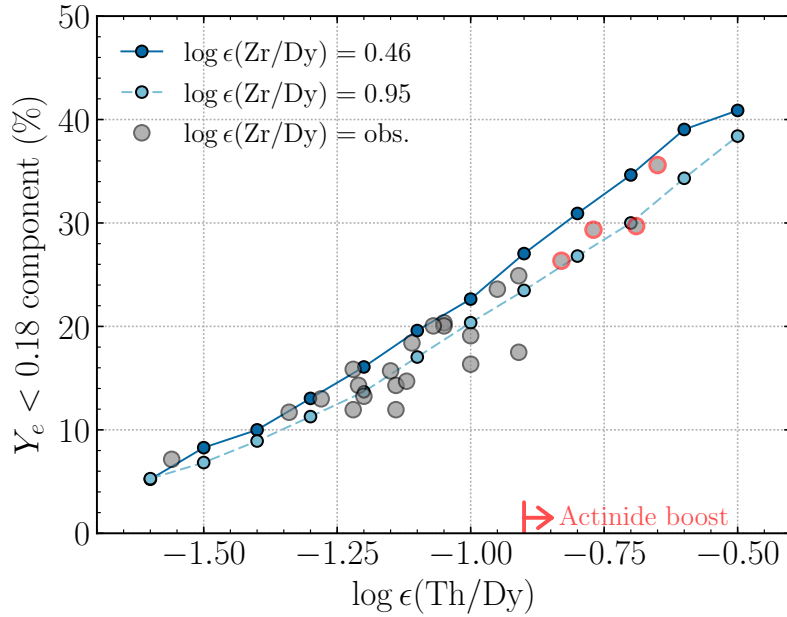


Figure 7.6. Percentage of allowed very low Y_e (<0.18), actinide-rich mass to reproduce various $\log \epsilon(\text{Th}/\text{Dy})$ abundances, while requiring the specified $\log \epsilon(\text{Zr}/\text{Dy})$ ratio. Gray dots show the ADM model applied to select r -process stars with observed $\log \epsilon(\text{Zr}/\text{Dy})$ and $\log \epsilon(\text{Th}/\text{Dy})$ ratios as input constraints (Abohalima and Frebel 2018; Placco et al. 2017; Sakari et al. 2018b; Holmbeck et al. 2018).

the right panel of Figure 7.1.

Systematically varying the $\log \epsilon(\text{Th}/\text{Dy})$ input constraint shows a smoothly increasing fraction of allowed ejecta masses at very low- Y_e . The r -process enhanced stars with likely single r -process progenitors fall between the two calculated curves (blue solid and dashed lines) in Figure 7.6, by definition. Most of these stars thus allow about 10% to 25% of their progenitor’s r -process ejecta mass to be at $Y_e < 0.18$. The actinide-boost stars found at $\log \epsilon(\text{Th}/\text{Dy}) > -0.90$ allow roughly 25% to 35% of this very low- Y_e material. This enhancement accounts for increased actinide abundances. Stars falling below the lower curve are those with higher $\log \epsilon(\text{Zr}/\text{Dy})$ ratios, which formed from gas that was likely polluted by multiple events. Assuming the r -process signature in stars with higher $\log \epsilon(\text{Zr}/\text{Dy})$ originated from a single event,

the ADM model can then account for their observed r -process element distributions using a mass ejecta distribution that is shifted to higher- Y_e values.

Our ADM model results do not indicate a clear separation between the actinide-boost stars and their non-actinide-enhanced counterparts. This agrees with the observed actinide abundances which suggest a smooth distribution of actinide enhancements, with the actinide-boost stars populating a low-probability tail of this distribution. This indicates that the same r -process source can produce all levels of actinide enrichment seen in r -process enhanced stars. Different levels of actinide enhancement would then reflect a slightly different distribution in the mass ejecta properties within the r -process progenitor. In all cases, the amount of fission-cycled (in this trajectory, $Y_e < 0.18$) material required to reproduce our r -process abundance observations may be a significant—but not dominant—fraction of the entire r -process mass ejecta since it sensitively affects the actinide contribution.

Interestingly, the abundance ratios can still be reproduced by the ADM model when the very low- Y_e component is omitted entirely. We investigate this effect by repeating the ADM calculation, only allowing the model to sample at $0.18 \leq Y_e \leq 0.45$. These results are shown in Figure 7.7. Disallowing Y_e below 0.18 produces a somewhat bimodal distribution driven by the $\log \epsilon(\text{Zr}/\text{Dy})$ and $\log \epsilon(\text{Th}/\text{Dy})$ requirements. For Ret II and Group F, a peak forms at $Y_e \approx 0.25$, coinciding with the single Y_e that satisfies the input $\log \epsilon(\text{Th}/\text{Dy})$ ratio. Since now no Th can come from $Y_e < 0.18$, all the Th contribution is concentrated around this Y_e . However, for the actinide-boost case, not enough Th is produced at $Y_e \approx 0.25$, and the ejecta mass builds up near the cutoff at $Y_e = 0.18$ where actinides are still able to be synthesized at levels necessary to eventually reproduce observed stellar abundances, within the allowed ranges of Table 7.1. With the total amount of Dy constrained mostly by contributions from the $Y_e = 0.25$ region, the Zr abundance primarily comes from higher values of Y_e . This restraint produces the broad peak around $Y_e = 0.37$. Although these precise

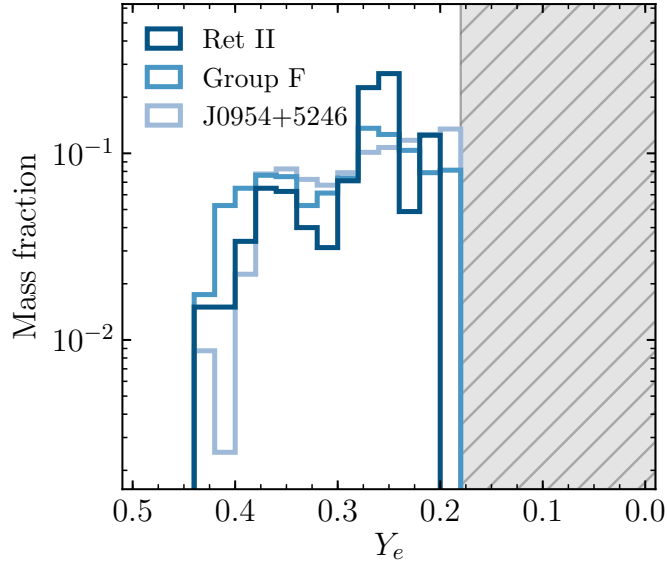


Figure 7.7. Ejecta distribution results for all three cases allowing no $Y_e < 0.18$.

Y_e constraints are mildly dependent on other astrophysical parameters (discussed in Section 7.5), we conclude that it is possible to reproduce the abundance patterns seen in r -process enhanced stars without fission cycling (for the conditions considered here, meaning without $Y_e \lesssim 0.25$ material), but such a cutoff places stricter and more finely tuned requirements on the distribution of Y_e in the ejecta.

The ADM model would fail for Ret II if a Y_e cutoff of 0.23 or greater was applied because there is simply not enough actinide material produced. Similarly, applying a cutoff at $Y_e \geq 0.21$ would prevent the ADM model from reproducing actinide-boost abundance ratios. As seen in Figure 7.3, the Th abundance rises rapidly as Y_e decreases from 0.24 to 0.17, covering over four dex—and thus all observed levels—of actinide abundance. It is therefore unsurprising that the ADM model consistently favors this range. Next, we turn to the higher Y_e component which contributes the bulk of the ejected Zr (i.e., limited- r) material.

7.4.2 The Higher- Y_e Component

In analogy to Figure 7.6 of the very low- Y_e component fraction, Figure 7.8 shows the allowed fraction of material ejected at $Y_e > 0.30$ as a function of the input $\log \epsilon(\text{Zr}/\text{Dy})$ constraint to characterize the limited- r contribution from single r -process events. The ADM model is run multiple times varying the input $\log \epsilon(\text{Zr}/\text{Dy})$ while holding the $\log \epsilon(\text{Th}/\text{Dy})$ constant, first at the actinide-boost cutoff (-0.90) and then at the very actinide-poor value following Ret II (-1.49). The ejecta mass fraction with $Y_e > 0.30$ is also shown for individual stars using their observational $\log \epsilon(\text{Zr}/\text{Dy})$ and $\log \epsilon(\text{Th}/\text{Dy})$ abundance ratios as constraints.

Figure 7.8 suggests that in order for the r -process event to synthesize all the required limited- r material as well as the main r -process material, a minimum of roughly 25% of the mass must be ejected at $0.30 < Y_e \leq 0.45$. For stars with $\log \epsilon(\text{Zr}/\text{Dy}) \leq 0.95$ —which likely received their r -process material from only one progenitor—between roughly 25% and 35% of the progenitor ejecta mass has $0.30 < Y_e \leq 0.45$. Furthermore, because there is an observational minimum of $\log \epsilon(\text{Zr}/\text{Dy}) \approx 0.46$, our ADM model results imply that at least $\sim 25\%$ of the r -process ejecta mass must be ejected at these higher values of Y_e .

If the material in stars with $\log \epsilon(\text{Zr}/\text{Dy}) > 0.95$ were to originate from a single r -process progenitor, then more than 40% of the r -process ejecta must be at $Y_e > 0.30$. However, as previously noted, the main r -process material found in stars moderately enhanced in r -process elements with $\log \epsilon(\text{Zr}/\text{Dy}) > 0.95$ could have been diluted by limited- r -only events such as CCSN neutrino-driven winds that primarily produce the limited r -process elements (Arcones and Thielemann 2013; Wanajo 2013).

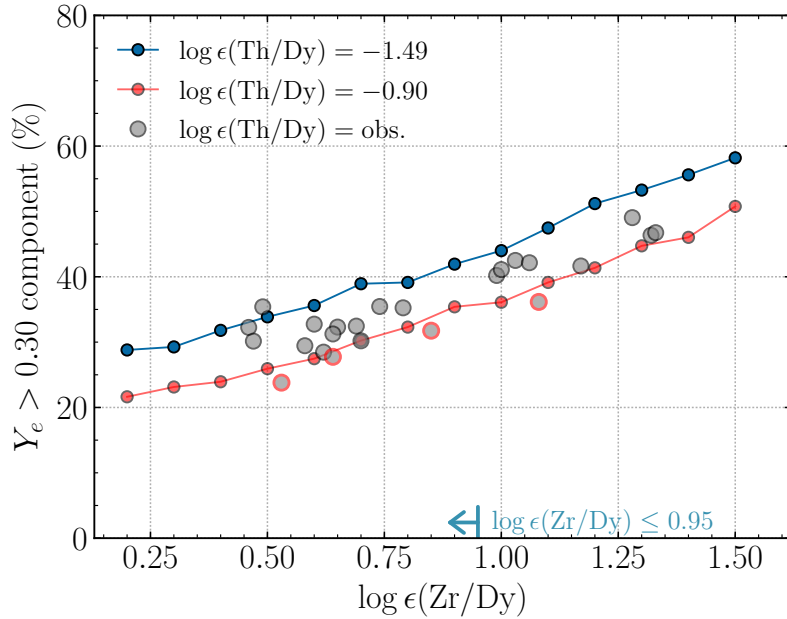


Figure 7.8. Percentage of allowed $Y_e > 0.3$, Zr-rich mass to reproduce various $\log \epsilon(\text{Zr/Dy})$ abundances with constant $\log \epsilon(\text{Th/Dy})$ ratio constraints. Gray dots show the ADM model applied to select *r*-process stars with their observed $\log \epsilon(\text{Zr/Dy})$ and $\log \epsilon(\text{Th/Dy})$ ratios as input constraints (Abohalima and Frebel 2018; Placco et al. 2017; Sakari et al. 2018b; Holmbeck et al. 2018), with red circles denoting the actinide-boost stars.

7.5 Model Variations

In this section, we investigate the impact that both astrophysical and nuclear physics variations have on the results of our ADM model to test the robustness of these empirically built mass ejecta distributions.

7.5.1 Astrophysical Sites

The previous calculations only consider the *r*-process originating from a single site: an accretion disk wind. Two situations that might occur in “realistic” astrophysical *r*-process events are a mix of ejecta types and a mix of different entropies. One promising *r*-process production site is the very low- Y_e tidal ejecta of an NSM. We

choose a low-entropy ($s/k \approx 10$) trajectory from the 1.4-1.4 M_⦿ NSM simulations by S. Rosswog as in [Korobkin et al. \(2012\)](#) for the tidal ejecta. Next, we vary the initial Y_e between 0.005 and 0.180 and run full *r*-process calculations for this tidal ejecta trajectory. Then we used the ADM model to randomly sample from only the tidal ejecta component at $Y_e < 0.13$, and from only the wind component at $Y_e \geq 0.18$. For the region at $0.13 \leq Y_e < 0.18$, the ADM model samples from both the tidal and wind ejecta with equal probability, producing a mixed-ejecta distribution. This combination may be one representation of total NSM ejecta undergoing an *r*-process. Figure 7.9 shows the empirical Y_e distribution obtained by using a combination of wind and tidal ejecta which match the Ret II abundances (“ejecta mix”). Although the $Y_e < 0.18$ component is distributed differently in the mixed ejecta case than the wind-only counterpart, the amount of necessary $Y_e < 0.18$ mass from the tidal ejecta is similar to that of the wind.

The *r*-process can also feasibly occur in an environment that supports a range of entropies. We investigate the effect of entropy on the Y_e distribution by repeating the simulations with a high entropy ($s/k \approx 85$) trajectory for the entire range of $0.005 \leq Y_e \leq 0.450$ in equal steps, and extended the very low entropy tidal trajectory to $Y_e \leq 0.250$. Next, the ADM model was run, randomly sampling between the original disk wind trajectory and the high entropy trajectory for $0.250 < Y_e \leq 0.450$, and between the low, medium, and high entropy trajectories for $0.005 \leq Y_e \leq 0.250$. The ejecta distribution results from the ADM model using a random combination of entropies are shown in Figure 7.9 (“entropy mix”).

The previously mentioned dip at $Y_e \approx 0.18$ disappears when combining trajectories with different astrophysical properties. This is because the value $Y_e = 0.18$ does not universally signify robust actinide production for all *r*-process trajectories. In the lowest entropy (tidal ejecta) trajectory, the Th abundance peaks at the lower Y_e of 0.125. At $Y_e = 0.18$, instead of a peak in Th production occurring—as that

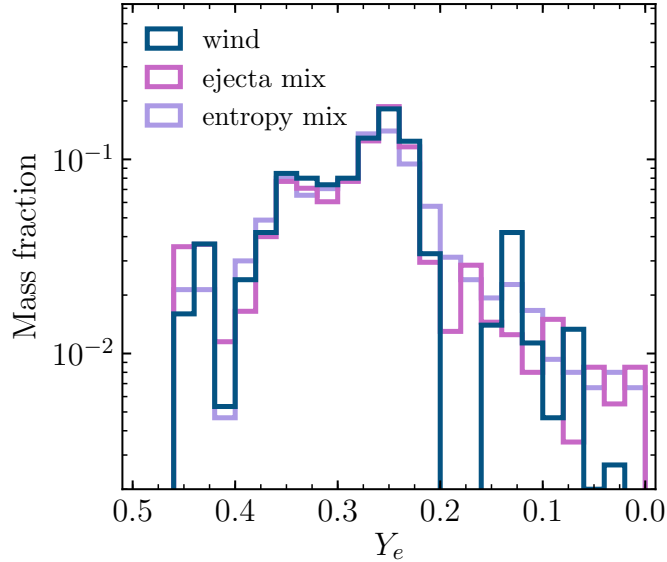


Figure 7.9. Ejecta distribution predicted by the ADM model matching Ret II abundances using the disk wind trajectory only (“wind”), an NSM represented by a combination of wind and tidal ejecta (“ejecta mix”), and a combination of different entropies (“entropy mix”). All simulations use the FRDM2012 mass model.

produced by the high and medium entropy (wind) trajectories—the very low-entropy tidal ejecta trajectory produces a Dy peak, allowing the mass at $Y_e \approx 0.18$ to satisfy the input abundance ratio constraints and wash out the apparent two-component Y_e distribution.

In summary, considering variations in the astrophysical site slightly affects the details of the predicted ejecta mass distribution. However, qualitatively, the ADM model robustly suggests that if there is any low- Y_e fission cycling ejecta component, it must be small compared to the r -process material ejected by the disk wind at higher Y_e .

7.5.2 Nuclear Physics Inputs

Nucleosynthesis calculations of the r -process rely heavily on theoretical data to attempt estimates of reaction rates for very unstable (and as of yet unmeasured) nuclei along the r -process path. Using different prescriptions of nuclear data far from stability can lead to dramatic differences in both the extent of the r -process and the final shape of the abundance pattern (e.g., Kratz et al. 1993, 1998; Wanajo et al. 2004; Mumpower et al. 2016b). We test the robustness of the ADM model results by repeating our calculations using nuclear data informed by the Duflo-Zuker (DZ; Duflo and Zuker 1995) and the Hartree-Fock-Bogoliubov (HFB; Goriely et al. 2009) mass models. We use theoretical reaction and decay rates recalculated to be consistent with each mass model and use HFB barrier heights for fission rates within this mass model as in Vassh et al. (2019). Figure 7.10 shows the results using the disk wind trajectory and three different nuclear mass models, using the Ret II abundance constraints. Although using DZ and HFB mass models results in ADM distributions with more low- Y_e mass, the relative shape and magnitude of higher- Y_e material reflects our results found when using the FRDM2012 mass model.

7.5.3 The Low- Y_e Component

As seen in Figure 7.10, the amount of predicted very low- Y_e ejecta mass varies with mass model. In contrast, Figure 7.9 displays little variation when using a mix of ejecta types or entropies. In Figure 7.11, we quantify the fraction of very low- Y_e mass that the ADM model predicts is ejected when applying nuclear and astrophysical variations across a range of actinide abundances. The DZ mass model tends to allow $\sim 5\%$ more very low Y_e material than FRDM2012 since simulations using the DZ mass model does not produce the actinides as robustly as with FRDM2012 (Holmbeck et al. 2019b). Similarly, material leaves the actinide region due to higher neutron-induced reaction flows at later times with the HFB mass model compared to when using

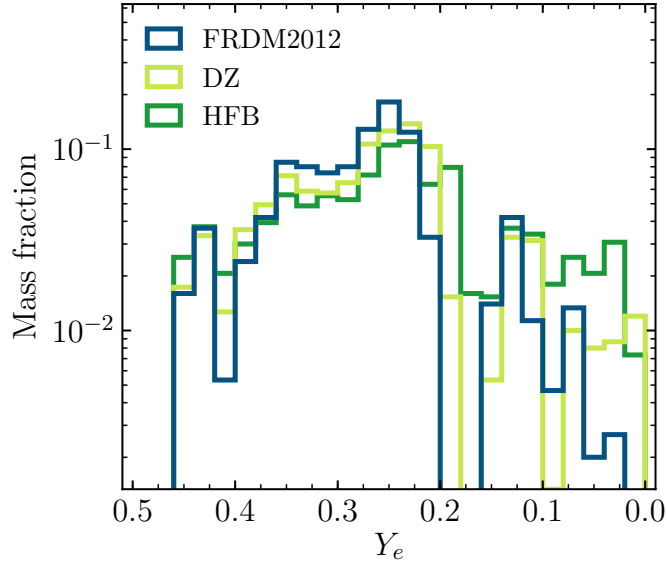


Figure 7.10. ADM predictions for Ret II using a disk wind trajectory and the FRDM2012 (blue), DZ (light green), and HFB (dark green) mass models.

FRDM2012, also producing a lower final actinide abundance. As a result, using HFB masses allows for $\leq 10\%$ more low- Y_e mass than when employing FRDM2012. Using a combination of tidal and wind ejecta or a combination of entropies slightly boosts the allowed very low Y_e mass; however, the astrophysical variations lie comfortably within uncertainties in the nuclear masses.

In summary, accounting for nuclear mass model variations, the very low Y_e ejected mass fractions may be as high as 40% to account for most observations of actinides in *r*-process enhanced metal-poor stars. Our results are robust under changes to the nuclear physics, with a variation of the allowed low- Y_e component of $\sim 10\%$ of the total mass when considering variations to nuclear mass models or astrophysical environments.

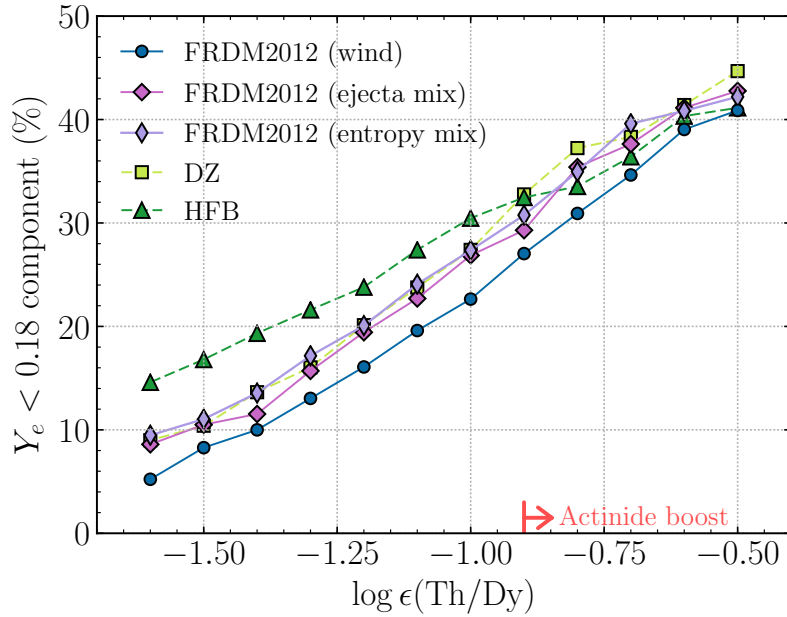


Figure 7.11. Percentage of allowed very low Y_e (<0.18), actinide-rich mass to reproduce various $\log \epsilon(\text{Th}/\text{Dy})$ abundances constraining the $\log \epsilon(\text{Zr}/\text{Dy})$ to be the Ret II value for each mass model specified.

7.6 The GW170817 Associated Kilonova

A parameterized accretion disk trajectory—and the conclusions drawn from using this trajectory—is consistent with one possible description of NSM ejecta environments. However, these conclusions are not necessarily unique and could still be applicable to other astrophysical sites, such as collapsars. Here we test if the ADM model results agree with what has been inferred from the GW170817 associated kilonova (“SSS17a” or “AT 2017gfo”). This could offer another hint for NSMs as primary r -process sources of material in early, small emerging dwarf galaxies that gave rise to the r -process enhanced stars.

Cowperthwaite et al. (2017) proposed that the light curve AT 2017gfo could only be explained by multiple components: a lanthanide-poor (“blue”) and lanthanide-rich (“red”) component. Inspired by this two-component model, we split our ADM

model Y_e distributions for Ret II into a blue and a red component. We define the blue component as primarily producing limited- r elements, extending over a range of $0.29 < Y_e \leq 0.45$ (recall Figure 7.3), and the red component consisting of the remaining material at $Y_e \geq 0.29$. Using these ranges, we find lanthanide mass fractions of $X_{\text{lan}} = 10^{-0.8}$ for the red and $X_{\text{lan}} = 10^{-3.8}$ for the blue components when using our ADM model. The mass ratio between these components is $m_{\text{red}}/m_{\text{blue}} = 1.7$.

[Kasen et al. \(2017\)](#) also invoke a two-component model to resemble AT 2017gfo, based on the high opacity of lanthanide elements that would produce an extended emission spectrum. For their models to agree with AT 2017gfo, a lanthanide-rich red kilonova would need to have a lanthanide mass fraction of $X_{\text{lan}} \sim 10^{-1.5}$, and the lanthanide-poor blue kilonova would need to have $X_{\text{lan}} \sim 10^{-4}$. The ejecta mass ratio they estimate between these components is $m_{\text{red}}/m_{\text{blue}} = 1.6$.

The lanthanide mass fractions extracted from our model are slightly larger than those found by [Kasen et al. \(2017\)](#). Our ADM simulations do not extend to iron-peak elements, which could be produced in higher- Y_e regions during a NSM event. Adding a contribution from iron-peak ejecta could bring our lanthanide mass fractions into further agreement with results by [Kasen et al. \(2017\)](#). Overall, our results agree, despite our inherently different approaches.

7.7 Summary and Conclusions

Using elemental abundances of r -process enhanced metal-poor stars, we have constructed empirical Y_e distributions describing the ejecta of r -process events through the ADM model. We find that the r -process abundance signatures of actinide-boost and actinide-deficient stars can likely originate from variations in Y_e distribution of ejecta from the same type of astrophysical r -process event. Both observationally and in the ADM model results, there is no clear point or distinct set of conditions at which the actinide-boost activates. Rather, the smoothness of the distribution of observed

actinide abundances correlates well with the smooth growth of the allowed very low Y_e tail of our ADM ejecta mass distributions, as seen in Figures 7.6 and 7.11.

Most actinide enrichments of metal-poor r -process enhanced stars can be explained by an r -process source with a very neutron-rich, fission-cycling component. We estimate this fission-cycling ejecta to be a non-dominant (10–30%) constituent of the r -process ejecta mass. All levels of limited- r abundance with respect to the lanthanides in stars with $\log \epsilon(\text{Zr}/\text{Dy}) \leq 0.95$ can be straightforwardly accommodated within the same r -process source. For these stars, the lanthanide-poor component, which is rich in limited- r elements, constitutes about 25–40% of the ejecta mass. This suggests that the r -process material in these stars need only come from one site that can produce the entire observed relative r -process abundance range from Sr to U.

The r -process signatures of very metal-poor stars allow the study of single r -process events, which we have characterized through the ADM model. We compared our empirically found progenitor Y_e distributions of ejecta to the results of an independent study of the currently favored r -process site, an NSM. We found that both the lanthanide mass fraction and the red-to-blue mass ejecta ratio derived from the ADM model are consistent with results matching the light curve of the GW170817 associated kilonova, AT 2017gfo. The shape of our empirical Y_e distributions also resemble those extracted from available hydrodynamical NSM simulations (Fernández et al. 2015; Radice et al. 2018b). However, the accretion disk wind used in this work may be theoretically similar to—or perhaps even observationally indistinguishable from—other astrophysical sites, e.g., the accretion disk wind from a collapsar remnant. Explicitly calculating the lanthanide mass fraction from stellar abundances, Ji et al. (2019) also find larger lanthanide mass fractions than studies of the AT2017gfo kilonova. These authors argue that if NSMs are the dominant source of r -process material, future kilonovae observations should find much higher lanthanide mass frac-

tions than for GW170817. If future follow-up of LIGO/aLIGO detections do not find high lanthanide mass fractions of material ejected by NSM events, then another site must be invoked to account for *r*-process production in the early Universe. Upcoming LIGO/aLIGO detections of NSMs and follow-up observations of their electromagnetic counterparts will be helpful to further characterize the progenitor site(s) of *r*-process enhanced stars and determine whether NSMs are the dominant source of *r*-process material in the early Universe.

In addition to investigations of NSMs and other *r*-process events, a comprehensive study of the *r*-process calls for more observations of metal-poor stars enhanced in these elements. Further identifications of *r*-II stars and their elemental abundances can be used to progress several areas of *r*-process studies. For example, more measurements of Th can test if DES J033523–540407 in Ret II and J0954+5246 in the halo represent limits on Th/Dy production, or if an even broader range exists. Large actinide variations at higher metallicities could indicate activity by other *r*-process sources as a function of chemical evolution, which can be identified and characterized through theoretical tools such as the ADM. Although Th abundances have not been determined in all *r*-process enhanced stars, many upper limits on stellar Th abundances are available. Results derived through an adapted ADM model from those upper limits on Th could set meaningful constraints on, e.g., the maximum allowed very low- Y_e material for *r*-process events if all *r*-process enhanced stars share a progenitor site. Detailed spectroscopy of more *r*-II stars will also allow further measurements of U. Due to the observed spread in abundance ratios, there is currently no unifying set of actinide-to-lanthanide production ratios that can be unilaterally applied to carry out cosmochronometry. However, the U/Th ratio principally remains a robust and reliable tool for radioactive decay dating if ejecta distributions built from observed elemental patterns could be used to refine the required type of production ratios that accurately reflect the relevant progenitor site(s).

Overall, larger numbers of known *r*-II stars would increase and/or refine identifications of kinematic groups in the Galactic halo as well as enable additional Th and U measurements. Hence, a main objective of the RPA ([Hansen et al. 2018](#); [Sakari et al. 2018b](#); [Ezzeddine et al. 2020](#)) is to increase the number of known *r*-II stars from \sim 30 to \sim 100. Applying information from additional statistically significant kinematic groupings to the ADM model could then be used to investigate whether NSMs are main sources of *r*-process material, or if the ADM suggests that other *r*-process sources are predominantly needed.

The wealth of stellar abundance data—from surveys such as that being conducted by the RPA—together with theoretical *r*-process studies, future NSM detections, and nuclear physics constraints from next-generation rare-isotope beam facilities (e.g., FRIB) will allow thorough investigations of the origins of all *r*-process elements.

CHAPTER 8

THE FIRST NEUTRON STAR MERGERS

She tried to fancy what the flame of a candle is like after the candle is blown out, for she could not remember ever having seen such a thing.

— Lewis Carroll, Alice’s Adventures in Wonderland

8.1 Neutron Star Mergers in the Galaxy

The observation of a neutron star merger (NSM) in gravitational wave (GW) emission (GW170817 Abbott et al. 2017) and electromagnetic radiation (Cowperthwaite et al. 2017; Drout et al. 2017; Kilpatrick et al. 2017; Shappee et al. 2017, AT 2017gfo or SSS17a) confirmed that the *r*-process occurs in the Universe and that NSMs are one astrophysical site that plays host to the *r*-process mechanism. What remains unclear is whether NSMs are sufficiently frequent or high-yield to account for the majority of *r*-process material in the Galaxy (Côté et al. 2019). Presently only one NSM has been so thoroughly observed, limiting our ability to answer this question through direct observations of NSMs.

Fortunately, additional observational evidence on the nature of *r*-process source(s) can be found in lieu of direct NSM detections—in the abundance signatures of metal-poor stars. Due to their chemical simplicity, metal-poor stars retain in their photospheres detectable imprints of individual nucleosynthetic events that occurred prior to their formation, at a time when the ISM had not yet been enriched by the fusion products of subsequent eras of star formation and stellar evolution (Barklem et al. 2005; Beers and Christlieb 2005; Frebel 2018). The elemental abundance patterns in

metal-poor stars are therefore direct clues as to the lives and deaths of previous stellar generations and their remnants. Stars with large amounts of *r*-process elements in their atmospheres are particularly helpful in this regard. Many of these “*r*-process-enhanced” stars indeed provide a nearly pure record of a single (to at most a few) prior astrophysical event that synthesized the ultimately observed heavy elements.

Investigations into potential, specific *r*-process conditions may manifest themselves in yield or relative abundance differences, that in turn, might be detectable within tangible star-to-star abundance variations. For example, several recent studies have investigated actinide production in NSMs in order to explain the subset of *r*-process-enhanced stars with high thorium and uranium abundances (Eichler et al. 2019; Holmbeck et al. 2019a,b). By comparing theoretical *r*-process yields to observed stellar abundances, studies like these help to constrain the hydrodynamic and thermodynamic nature of the conditions under which the *r*-process occurs. Such constraints can then be used to explore particular sites for the *r*-process.

This study aims at taking such comparisons a step further by using observed abundances of *r*-process-enhanced stars together with results of recent simulations, to infer properties of the erstwhile neutron stars themselves. We assume that the *r*-process abundances in metal poor stars stem from single, prior mergers of two neutron stars, and that recent simulations are qualitatively good predictors of key quantities regarding element production. Yields of elements produced by the NSMs are then compared to the elemental signatures of the *r*-process-enhanced stars to calculate the masses of the progenitor double neutron star system (DNS) that merged and synthesized the heavy elements observed in the *r*-process-enhanced stars. We note that since the nuclear equation of state (EOS) is a known uncertainty in the outcome of hydrodynamic simulations, we include EOS effects in our investigation of whether NSMs (and which ones) were responsible for the majority of *r*-process production in the Galaxy. This innovative utilizing of observational abundances has the potential

to forge new connections between the body of observed metal-poor stars, theoretical NSM studies, and upcoming results from the LIGO collaboration.

First, we discuss in Section 8.2 how NSM outflows are fundamentally related to the masses of the coalescing neutron stars and the nuclear EOS. Section 8.3 then describes how we will connect the merger outflow to stellar abundances of metal-poor stars in order to reconstruct the progenitor merging neutron star pair. Section 8.4 presents the results of this new method in terms of individual masses and mass distributions of the merging DNSs for six different EOSs. Lastly, Section 8.5 explores variations on the model that can potentially support or oppose the theory that NSMs synthesized the majority of *r*-process material found in Galactic metal-poor stars.

8.2 Puzzle Pieces: Neutron Star Properties

Hydrodynamical simulations of NSMs predict the mass of the accretion disk around the merger remnant, the amount of dynamically ejected material, and the lifetime of the now-massive neutron star before it collapses into a black hole (if at all). These quantities bear directly on the global *r*-process abundances that may be ejected from individual NSMs and consequently enrich the star-forming ISM. The wealth of NSM simulation data—and, with it, analytical descriptions of NSM ejecta—presents an opportunity to connect stellar *r*-process abundance signatures to progenitor NSM events. With *r*-process abundances in hand from stellar signatures, we investigate the implication of assuming an NSM origin for the majority of *r*-process abundance in the Galaxy. In the following sections, we review relevant parameterizations of hydrodynamical output and how we will use these analytic forms to find the individual masses of binary neutron star members.

8.2.1 NSM Ejecta

Material that may undergo nucleosynthesis and escape from an NSM is typically grouped into two main categories: the dynamical ejecta, which escapes promptly from the merger, and the wind outflows, which emanate from the accretion disk around the newly formed merger remnant. Within the dynamical ejecta category, there exist multiple physical mechanisms that drive the ejection. First, as the neutron stars coalesce, they become tidally deformed, and the tidal tails of the deformed star(s) are expelled from the system. Additionally, as the neutron stars make contact, a contact-interface ejecta can be produced. There are also different physical mechanisms driving the wind outflows. On longer timescales, an accretion disk/torus forms around the merger remnant, and material can be lost from the disk due to either viscously heated or neutrino-driven winds. A critical ingredient in our study is how much mass is ejected by each mechanism, which is largely determined by the masses of the colliding neutron stars.

8.2.1.1 The Nuclear Equation of State

Hydrostatic equilibrium, the balance between the gravitational weight of a star's mass and the radiation pressure emanating from nuclear fusion in its core, offers a sufficient description of stellar structure throughout the majority of a star's lifecycle. After a massive star has evolved, however, and ejected its outer layers in an energetic supernova, its now-exposed core is no longer supported by radiation pressure, but by the degeneracy pressure of cold, compact matter. The structure of exotic states of matter such as that found in these stellar remnants, neutron stars, is characterized theoretically by the nuclear EOS. The nuclear EOS is a fundamental thermodynamic description of the energy per nucleon as a function of nucleon density at various temperatures and pressures. For a neutron star, solving these theoretical models maps into a relationship between the masses and radii of neutron stars. Colloquially,

TABLE 8.1
 EQUATIONS OF STATE USED IN THIS WORK AND THEIR
 PREDICTIONS ON NEUTRON STAR PROPERTIES

EOS	Reference	M_{TOV} (M_{\odot})	$R_{1.4 M_{\odot}}$ (km)	$R_{1.6 M_{\odot}}$ (km)
H4	Lackey et al. (2006)	2.02	13.75	13.63
DD2	Typel et al. (2010)	2.42	13.26	13.30
ALF2	Alford et al. (2005)	2.06	13.16	13.19
LS220	Lattimer and Swesty (1991)	2.05	12.66	12.48
MPA1	Müther et al. (1987)	2.46	12.47	12.51
SFHo	Steiner et al. (2013a)	2.06	11.92	11.79

EOSs can often be described as “soft” or “stiff,” which are related to the predicted compressibility of neutron star matter. At the same neutron star mass, a soft EOS generally predicts more compressible matter—a smaller neutron star radius—than a stiff EOS. For this study we choose six EOSs, listed in Table 8.1 along with their predictions for the maximum, non-rotating neutron star mass (M_{TOV}) and predicted radii at $M = 1.4$ and $1.6 M_{\odot}$.

The EOS of dense nuclear matter remains unknown; however, both experimental and astrophysical studies place some constraints on the nuclear EOS (e.g., Piekarewicz and Centelles 2009; Lattimer 2012; Mathews et al. 2013; Steiner et al. 2013b). Recently, the gravitational wave signal GW170817 and its corresponding kilonova AT2017gfo provide additional information from the astrophysical perspective. For example, Radice et al. (2018b) applied observations of the NSM event and ruled out many EOSs; H4 and SFHo are ruled out at 90% confidence on the stiff and soft side, respectively, since such extreme EOSs theoretically cannot eject enough luminous

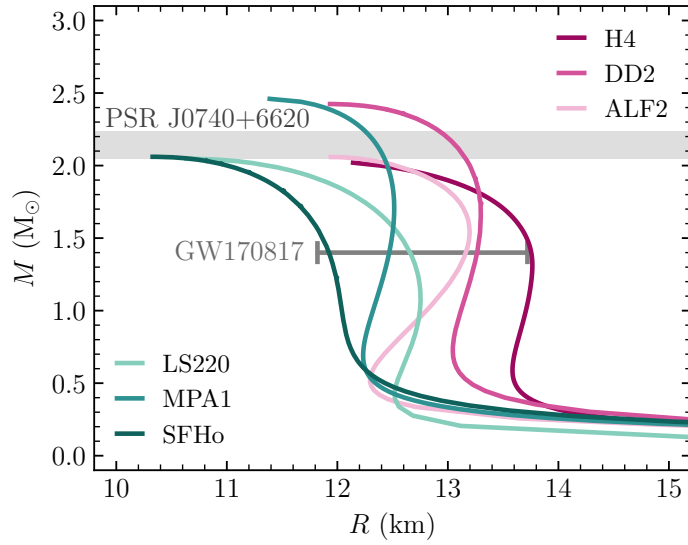


Figure 8.1. Mass-radius solutions for the six EOSs listed in Table 8.1 compared to pulsar (Antoniadis et al. 2013) and GW constraints (Malik et al. 2018).

material to reproduce the AT2017gfo kilonova. Comfortably within the constraints are, for example, LS220 and ALF2, which both allow a maximum neutron star mass of $\sim 2.1 M_{\odot}$. Figure 8.1 shows the mass-radius curves for six EOSs which we will consider in this work, including the “ruled out” EOSs, H4 and SFHo for comparison. Also displayed in Figure 8.1 are some astrophysical constraints on the EOS: the radius of a $1.4 M_{\odot}$ star inferred from GW170817 ($11.82 \leq R_{1.4 M_{\odot}} \leq 13.72$ km; Malik et al. 2018), and the allowed maximum neutron star mass currently set from observations of PSR J0348+0432 ($2.01 \pm 0.04 M_{\odot}$; Antoniadis et al. 2013).

Not only does the EOS determine the mass-radius relationship of neutron stars, but the EOS also affects the predicted nucleosynthesis of material ejected by merging neutron star binaries (e.g., Goriely et al. 2011; Radice et al. 2018a). For example, a stiff EOS will allow significant tidal deformations earlier in a merger event compared to a soft EOS. The material in this tidally deformed ejecta tends to be very

neutron-rich and capable of fission-cycling. On the other hand, a “soft” EOS describes more compact neutron stars, causing less tidal deformation in a merger, and therefore ejecting less neutron-rich material. Consequently, a stiff EOS predicts more dynamical ejecta from an NSM event than a soft EOS, and therefore more actinide production from this neutron-rich ejecta. Additionally, the lifetime of the remnant massive object before it may collapse into a black hole also depends on the EOS. A stiff EOS generally resists collapse, leading to a longer-lived supra/hyper-massive neutron star remnant (for details, see [Dai and Lu 1998](#); [Dai et al. 2006](#); [Hotokezaka et al. 2013](#); [Dietrich et al. 2015](#); [Radice et al. 2018a](#), among others) In the next sections, we discuss the models of the disk outflows and dynamical ejecta in detail and how these two quantities can be parameterized in terms of the neutron star masses and the EOS.

8.2.1.2 Disk Outflows

The total mass lost through disk wind outflows depends on the mass of the accretion disk/torus that is created around the merger remnant. Currently, only a few analytic fits of the disk mass to simulation data are available: Equation 25 in [Radice et al. \(2018a\)](#), Equation 1 in [Coughlin et al. \(2019\)](#), and Equation 4 in [Krüger and Foucart \(2020\)](#). Both [Radice et al.](#) and [Coughlin et al.](#) use the same set of numerical relativity simulation data, but the latter finds that their fitting formula shows a lower fractional error compared to simulation data than the fit by [Radice et al.](#) The fit by [Krüger and Foucart](#) behaves similarly to the fit by [Coughlin et al.](#), but we find the latter produces slightly better agreement with simulation data compared to simulation data for EOSs considered in this work. The fit from [Coughlin et al.](#) that we adopt approximates the disk mass as a function of the total mass, $M_{\text{tot}} = M_1 + M_2$:

$$\log_{10}(m_{\text{disk}}) = \max \left\{ -3, a \left(1 + b \tanh \left[\frac{c - M_{\text{tot}}/M_{\text{thr}}}{d} \right] \right) \right\}, \quad (8.1)$$

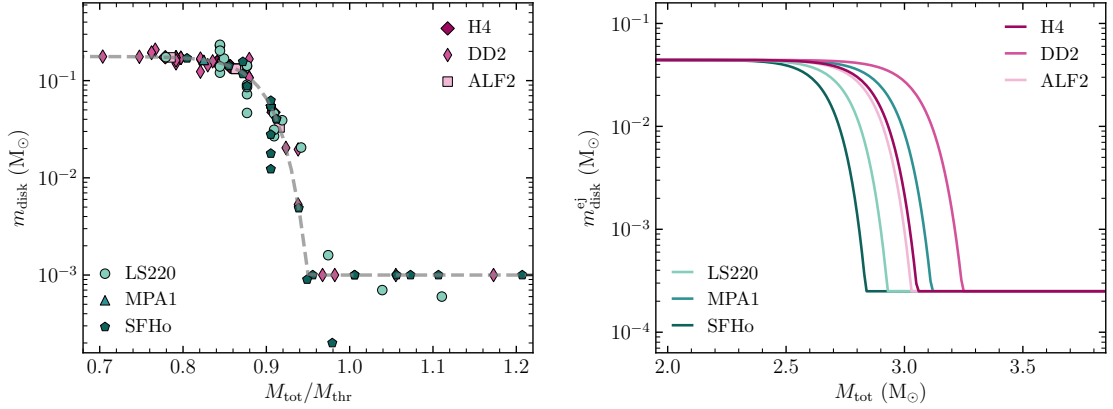


Figure 8.2. Left: analytic form for the mass of the accretion disk (gray, dashed) from Equation 8.1 compared to simulation data compiled in Dietrich and Ujevic (2017) and Radice et al. (2018a). Right: the same analytic form as a function of only M_{tot} for each EOS choice.

with fitting parameters $a = -31.335$, $b = -0.9760$, $c = 1.0474$, and $d = 0.05957$, and M_{thr} given by

$$M_{\text{thr}} = M_{\text{TOV}} \left(2.38 - 3.606 \frac{GM_{\text{TOV}}}{c^2 R_{1.6 M_{\odot}}} \right), \quad (8.2)$$

where M_{TOV} is the maximum mass of a non-rotating neutron star (the Tolman-Oppenheimer-Volkoff limit), and $R_{1.6 M_{\odot}}$ is the radius of a $1.6 M_{\odot}$ neutron star for a given EOS. The left panel of Figure 8.2 shows Equation 8.1 in gray compared to simulation data for many choices of EOS. A similar plot can also be found in Coughlin et al. For binary systems with larger total masses, the resulting accretion disk will be less massive than for binaries with smaller total masses. This effect arises since a larger remnant mass will collapse into a black hole faster, and thus disallow the formation of a more massive accretion disk. Assuming a softer EOS will generally predict the remnant to collapse faster, also leading to a less massive disk that is formed.

In a merger, roughly 10–40% of the torus mass lost will be ejected (Fernández

et al. 2018; Coughlin et al. 2019). For this study, we assume a constant of 25% for the disk ejecta, which is supported by simulations, e.g., by (Just et al. 2015). The right panel of Figure 8.2 shows the same analytic fit scaled by 25%, and now as a function of only M_{tot} to show the dependence on EOS. This representation shows that at the same total binary mass, the softest EOSs have the least massive accretion disks. The two EOSs that apparently break this trend are DD2 and MPA1. Their apparent shift to more massive disks is a direct result of the allowed maximum neutron star mass M_{TOV} in Equations 8.1 and 8.2. In this way, a simple analytic estimate of the amount of ejecta an NSM event produces from the disk outflows can be estimated from the total mass of the merging neutron stars, under a certain choice of EOS.

8.2.1.3 Dynamical Ejecta

The mass ratio of the binary system ($q \equiv M_2/M_1 \leq 1$) in part determines how much mass is lost to dynamical ejecta. Generally, a more extreme mass ratio ($q < 1$) leads to more tidal deformation, and thus more dynamical ejecta. The first phenomenological fit to simulation data for the ejecta mass as a function of M_1 and M_2 was proposed by Dietrich and Ujevic (2017). Radice et al. (2018a) fit new coefficients to the analytic form in Dietrich and Ujevic for an improved fit to simulation data; however, both fits rely on the baryonic masses of the coalescing neutrons stars in addition to the gravitational masses, which would add a new step of complexity to our model. Coughlin et al. (2019) introduced a new fit, independent of the baryonic mass. However, this fit belies the fundamental nature of tidally deformed NSM ejecta, predicting that neutron stars with the highest compactness eject the most material. While this behavior may hold true in a narrow mass range ($1.2\text{--}1.4 M_{\odot}$), neutron stars that are even more massive are expected to collapse quicker than their less-massive counterparts, allowing little time for material to be ejected dynamically. Therefore, Krüger and Foucart (2020) introduced an improved functional form taking

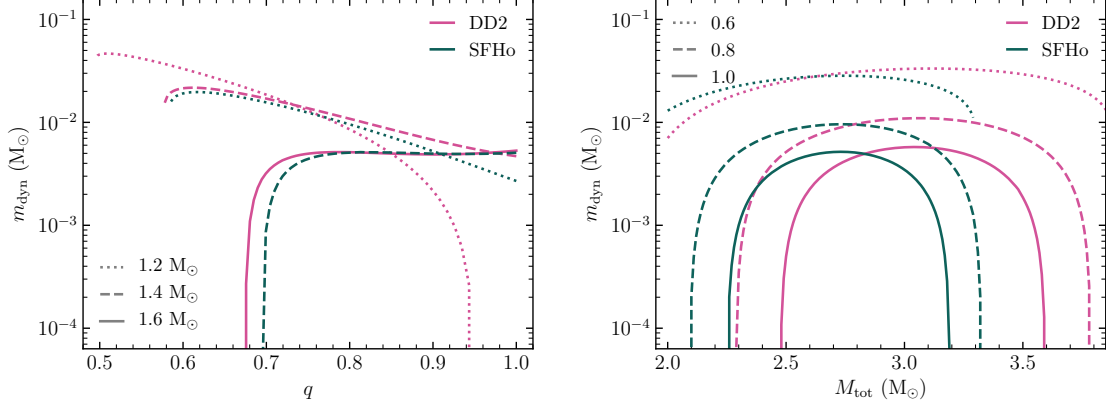


Figure 8.3: Analytic form for the mass of the dynamical ejecta from Equation 8.3 as a function of mass ratio, $q = M_2/M_1$, for a stiff EOS (DD2, pink) and a soft EOS (MPA1, teal). Each curve shows the calculation for a different value of the primary mass, M_1 : $1.2 M_\odot$ (dotted), $1.4 M_\odot$ (dashed), and $1.6 M_\odot$ (solid).

into account the expected behavior at high neutron star masses:

$$\frac{m_{\text{dyn}}}{10^{-3}M_\odot} = \left[\frac{a}{\mathcal{C}_1} + b \left(\frac{M_2}{M_1} \right)^n + c\mathcal{C}_1 \right] M_1 + (1 \leftrightarrow 2), \quad (8.3)$$

where M_i is the gravitational mass of the neutron star, and \mathcal{C}_i is the compactness parameter defined as

$$\mathcal{C}_i = \frac{GM_i}{c^2R_i}, \quad (8.4)$$

where R_i is the radius of the neutron star with mass M_i , which can be obtained from the mass-radius relationship as in Figure 8.1 for each EOS. With this formulation, Krüger and Foucart find best-fit values to simulation data of $a = -9.3335$, $b = 114.17$, $c = -337.56$, and $n = 1.5465$. Figure 8.3 shows this analytic form both as a function of the mass ratio q (left) and total binary mass M_{tot} (right) for a relatively stiff (DD2) and very soft (SFHo) EOS. With this analytic fit, Figure 8.3 reveals complex behavior of dynamical ejecta as a function of the neutron star masses and their compactness.

The effect of compactness on the dynamical ejecta can be seen by comparing the pink and teal curves in Figure 8.3, which represent EOSs with comparatively low and

high \mathcal{C} , respectively. As described above, neutron stars with a higher compactness should eject less dynamical mass. This effect can be seen directly in the left panel of Figure 8.3 by comparing two EOS curves with the same primary mass. For example, compare dashed pink (DD2) and teal (SFHo) curves, both representing DNS systems with $M_1 = 1.4 M_\odot$, and the mass of the secondary determined by $M_2 = 1.4 q (M_\odot)$. For nearly all values of q , the dashed teal curve (high \mathcal{C}) predicts a lower dynamical mass than the corresponding pink curve (low \mathcal{C}). For even higher neutron star masses ($M_1 = 1.6 M_\odot$), the high-compactness EOS predicts no dynamical ejecta at all, as seen by the lack of a solid teal line in the left panel of Figure 8.3.

The right panel of Figure 8.3 shows similar curves, this time for constant q with varying M_{tot} . Similar to the above description, notice that lines of similar q for different EOSs may overlap with a shift to M_{tot} . In other words, assuming a stiff EOS for systems with, e.g., $q = 1.0$ will eject roughly the same amount of dynamical material as a system with a smaller total mass and a higher compactness (softer EOS). Therefore, binary neutron stars with higher compactness (i.e., higher mass) eject less dynamical material than binaries of smaller compactness. In general, note that the dynamically ejected mass stays relatively constant for a wide range of M_{tot} , only dropping precipitously at very high and very binary masses. On the other hand, the dynamical ejecta is much more sensitive to the mass ratio q .

The delicate interplay between the neutron star masses, their mass ratio, and EOS determines the amount of r -process material that may be ejected into the ISM and make its way into the primordial gas that formed metal-poor stars. Next, we turn to the composition of the outflowing ejecta and how the neutron star masses may effect the extent of the r -process pattern in addition to the abundance of r -process elements.

The delicate interplay between the neutron star masses, their mass ratio, and EOS determines the amount of r -process material that may be ejected into the ISM

and make its way into the primordial gas that formed metal-poor stars. Next, we can apply these outflow equations to GW170817 to test if they agree with kilonova observables.

8.2.1.4 Test on GW170817

After GW170817 and its associated kilonova, several studies placed estimates on the NSM ejecta, e.g., on the masses of the wind and dynamical components and on the lanthanide mass fractions thereof (see, e.g., Cowperthwaite et al. 2017; Chornock et al. 2017; Evans et al. 2017; Kasen et al. 2017; Perego et al. 2017; Rosswog et al. 2018; Smartt et al. 2017; Tanaka et al. 2017; Tanvir et al. 2017; Troja et al. 2017, and also Côté et al. 2018). In this section, we test whether Equations 8.1 and 8.3 hold for GW170817 using observational constraints on M_1 and M_2 . While precise estimates on the individual neutron star masses cannot be attained from present GW data, the chirp mass offers a tight constraint on the *combination* of M_1 and M_2 . Therefore, we take all M_1 - M_2 combinations satisfying the chirp mass of GW170817 ($\mathcal{M} = 1.188^{+0.004}_{-0.002} M_\odot$)—as well as other, broad limits on the maximum and minimum neutron star masses—and apply Equations 8.1 and 8.3. The curves in Figure 8.4 show the calculated wind and dynamical masses from an NSM with GW170817’s chirp mass for each of the six EOSs we use in this work. In addition, these curves can be compared to similar evaluations from the GW170817 observation itself.

Many studies have estimated the GW170817 dynamical and wind masses by comparing their models to the lightcurve data; a useful handful are tabulated in Côté et al. (2018), and these values are displayed in Figure 8.4 as gray boxes. Several of these studies place direct estimates on the wind and dynamical masses (Evans et al. 2017; Perego et al. 2017; Rosswog et al. 2018; Tanaka et al. 2017; Tanvir et al. 2017; Troja et al. 2017), whereas others employ kilonova models to estimate the amount of mass contributing to the apparent red and blue components of the lightcurve (Cow-

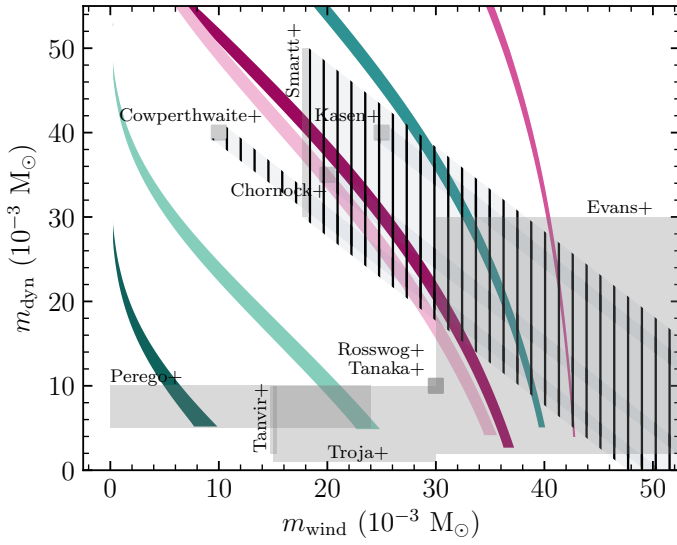


Figure 8.4. Predicted dynamical and wind ejecta masses from GW170817 for each EOS considered in this work (colored curves, from left to right: SFHo, LS220, ALF2, H4, MPA1, and DD2) compared to literature values (gray boxes). The hatched boxes show how results from kilonovae models can vary based on the mapping strength between red kilonova and dynamical mass.

perthwaite et al. 2017; Chornock et al. 2017; Kasen et al. 2017; Smartt et al. 2017).

The models that estimate more dynamical than wind ejecta in Figure 8.4 and Côté et al. (2018) all use a method that fits red and blue components, rather than dynamical and wind. The transformation of red and blue kilonova mass to dynamical and wind mass, respectively, has been assumed as a one-to-one mapping in works such as Côté et al. (2018). This simple mapping may account for the disparity between the kilonova-based models and the rest, since the entirety of the red kilonova component need not be purely dynamical in origin. A significantly neutron-rich wind could contribute some red component to the produced lightcurve, which is accommodated in this work by the short-lived hypermassive neutron star (HMNS) remnants that immediately (or very quickly) collapse into a black hole (as discussed next in Section 8.2.2). If the one-to-one mapping between the red kilonova and dynamical mass

is relaxed, then the red-and-blue-based analyses of GW170817 would predict simultaneously higher wind masses and lower dynamical masses. These possibilities are represented in Figure 8.4 by the hatched boxes extending from the reported values. Without varying the total mass predicted by these models, the hatched regions simply show how the wind and dynamical mass estimates change when the origin of the red kilonova is varied between dynamical-only and wind-only. Therefore, although the GW170817 mass estimates from kilonova-based models appear to be discrepant with other models, there is a clear need to understand how much the wind outflow can contribute to a red NSM afterglow.

Especially considering the broad uncertainties from literature studies of the GW170817 lightcurve, all EOSs can find some agreement with literature. This agreement, while providing little constraint on the GW170817 merger and EOS properties, at least verifies that Equations 8.1 and 8.3 reasonably reproduce values derived from NSM observations. Next, we turn to the composition of the outflowing ejecta and how the neutron star masses may effect the extent of the *r*-process pattern in addition to the abundance of *r*-process elements.

8.2.2 Remnant Lifetime

In the previous sections, we have summarized the dependence of ejecta mass on the initial neutron star masses and the EOS. Not only do these quantities directly affect the amount of mass ejected, but they also determine the nuclear composition of the wind ejecta. Lippuner et al. (2017) showed that the lifetime of the HMNS remnant affects the nucleosynthesis in the accretion disk outflows from the merger, with a longer lifetime leading to a less robust *r*-process pattern, i.e., lower lanthanide and actinide abundances. The remnant lifetime affects the nucleosynthesis in this way due to the extent of allowed neutrino interactions that alter the composition of the ejecta (e.g., Metzger and Fernández 2014). The lifetime of the remnant before its

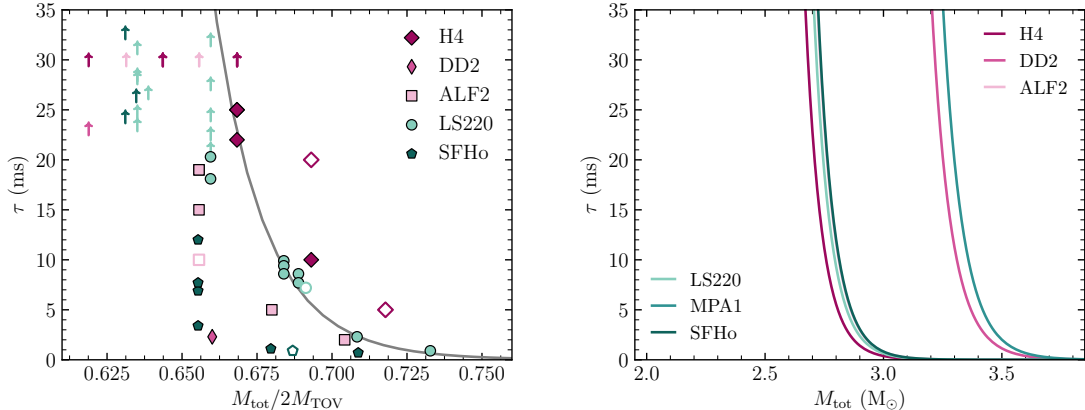


Figure 8.5. Lifetime of the HMNS remnant before it collapses into a black hole (if at all) as a function of $M_{\text{tot}}/2M_{\text{TOV}}$. Up arrows indicate the HMNS survived longer than 30 ms, generally meaning it is indefinitely lived.

collapse into a black hole sets a neutrino irradiation time, which can drive down the initial neutron-richness of the r -process composition (i.e., a higher electron fraction, Y_e), thus producing a less robust r -process pattern.

The lifetime of the merger remnant also depends on the EOS and the total binary mass, as investigated in [Hotokezaka et al. \(2013\)](#). [Lucca and Sagunski \(2020\)](#) compiled many investigations to fit a simple analytical form describing the collapse time from the mass and radius of the HMNS remnant.

$$\log_{10}(\tau) = e_0 + e_1 \log_{10} \left(\frac{M_{\text{NS}}}{M_{\text{TOV}}} \right), \quad (8.5)$$

with best-fit parameters $e_0 = -5.45 \pm 0.40$ and $e_1 = -38.9 \pm 1.7$. Recall that M_{TOV} is EOS-dependent. These authors use only symmetric ($q = 1$) mergers such that $M_{\text{NS}} = M_1 = M_2$. To utilize this description of the HMNS remnant lifetime, we take M_{NS} to be the average mass between M_1 and M_2 . Figure 8.5 shows a variety of simulation data (from [Hotokezaka et al. 2013](#); [Dietrich et al. 2015](#); [Kastaun and Galeazzi 2015](#); [Radice et al. 2018b](#)) plotted against Equation 8.5. Simulation

data from asymmetric ($q < 1$) mergers are also included in this plot in white-filled points. Also notice the EOS-dependence in the right panel of Figure 8.5, which plots Equation 8.5 as a function of only total binary mass. EOSs with very high values of M_{TOV} such as DD2 and MPA1 are estimated to lead to longer-lived remnants than EOSs with lower M_{TOV} at the same total mass. By definition, DD2 and MPA1 allow a more massive remnant, which can then survive collapse for much longer.

With Equations 8.1, 8.3, and 8.5, it is now possible to estimate the mass ratio of ejecta from the dynamical mechanism and disk outflows using the masses of the neutron stars and a given EOS. In summary, the total mass, mass ratio between the neutron stars, and the EOS affect the amount of ejected mass and remnant lifetime as follows:

- M_{tot} : the mass of the accretion disk and the remnant lifetime are generally anti-correlated with the total mass, and the correlation with m_{dyn} is mostly flat except for very high or very low total masses (see Figure 8.3).
- q : under Equations 8.1 and 8.5, the disk mass and remnant lifetime have no clear dependence on the mass ratio; however, the dynamical mass is generally anti-correlated with q , except for very high masses.
- EOS: both the ejecta masses as well as the remnant lifetime are anti-correlated with compactness, or, equivalently, positively correlated with tidal deformability.

Next, we review the method by which we place estimates on the progenitor DNS systems that merged to create the observed *r*-process enhancement of metal-poor stars in the Galactic halo.

8.3 Method: Assembling the Puzzle

As described in Section 8.2, a choice of neutron star masses and EOS will affect the amount of mass ejected by the merger. In addition, the neutron star masses also determine the *r*-process extent of the ejecta, in particular of the disk wind outflows. The mass of ejected disk and dynamical material then sets the amount by which

to scale the respective abundance patterns of the ejected material. Therefore, given a choice of (independent variables) M_1 , M_2 , and EOS, we can quantify the total r -process ejecta from a merger event.

Here we describe this concept in reverse: how to go from observed r -process abundances to the original neutron star masses of the progenitor merger. First, we describe the nucleosynthesis simulations used for the disk and dynamical ejecta. Next, we detail the MCMC method we use to explore the M_1 - M_2 parameter space to build a bridge between observationally derived r -process abundances and NSM properties.

8.3.1 Nucleosynthesis Calculations

For the r -process extent of the disk wind, we start with the same set of models used in Lippuner et al. (2017): from Metzger and Fernández (2014) for a HMNS remnant with lifetimes 0 ms, 10 ms, 100 ms, and infinitely lived. Of roughly 10,000 tracer particles, only a fraction will be ejected in the disk outflows, depending on the lifetime of the remnant. The tracers are each evolved with the nuclear reaction network code Portable Routines for Integrated nucleoSynthesis Modeling (PRISM; Sproue et al. 2020). We start with all reactions from the JINA ReacliB database, then supply to PRISM theoretically computed (from the FRDM nuclear model; Möller et al. 2012), experimentally evaluated, and laboratory measured data to supplement and/or overrule ReacliB input, following the same procedure as in, e.g., Mumpower et al. (2018); Holmbeck et al. (2019a,b); Vassh et al. (2019). Astrophysically, the temperature and density evolution initially follow the simulation data. Once the temperature of the tracer drops below 5 GK, nuclear reheating is computed by PRISM at 50% efficiency, and the increase in entropy due to reheating is used to dynamically recalculate the temperature. Initial compositions of the ejecta for each tracer particle are computed in nuclear statistical equilibrium (NSE) using the Y_e and density from the simulation

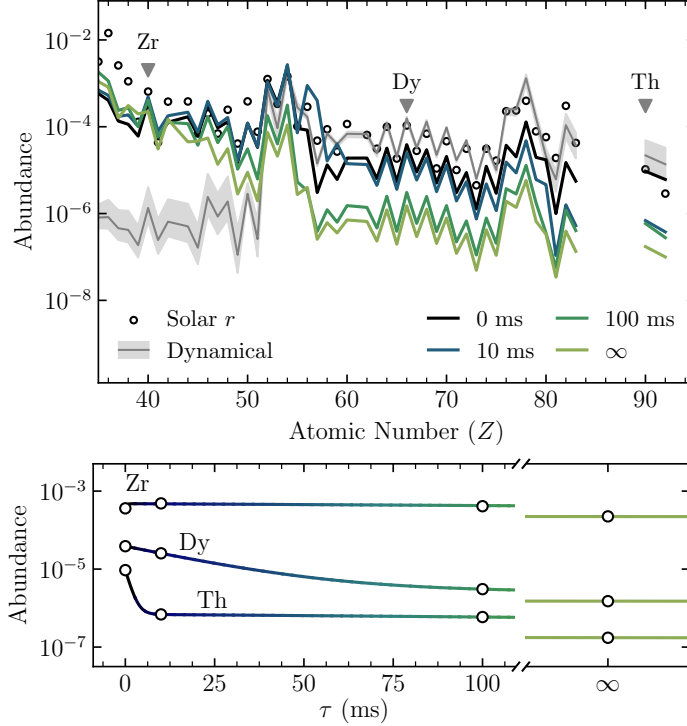


Figure 8.6. Top: elemental abundance patterns for the dynamical ejecta (gray) and disk outflows from DNS merger remnants with different lifetimes (colored lines) in milliseconds. Bottom: exponential fits to the Zr, Dy, and Th abundances versus remnant lifetime for the disk outflows.

data at 10 GK. Figure 8.6 shows the final, combined abundance patterns produced by a massive remnant with different lifetimes.

The \log_{10} Zr, Dy, and Th abundances for remnants with lifetimes 0 ms, 10 ms, 100 ms, and ∞ are well described by exponential functions with a linear background. Note that linear-with-exponential functional forms also fit the abundance data in Lippuner et al. (2017) (see values in Table 2 therein). Therefore, to obtain the abundances at any given lifetime, linear-exponential functions are fit to each element so that the abundances can be found for any given value of τ , shown in the bottom panel of Figure 8.6. Since the abundances change very little between 100 ms and the infinite case, winds from remnants with lifetimes $\tau \geq 300$ ms are assumed to obey

the abundances of the infinite case.

For the dynamical ejecta, we choose a trajectory from the NSM simulations of S. Rosswog ([Piran et al. 2013](#); [Rosswog et al. 2013](#)), as in [Korobkin et al. \(2012\)](#). Some representative abundance patterns for the dynamical ejecta with Y_e between 0.16 and 0.18 are shown Figure 8.6 compared to the wind abundance patterns (see Section 8.3). Whereas the abundance patterns of the disk outflow depend on M_1 and M_2 , the relative composition of the dynamical ejecta is roughly constant for any choice of neutron star masses.

8.3.2 Stellar Sample

The aim of this study is to explore how observed stellar r -process signatures can be explained with theoretical descriptions of NSM ejecta. We choose a subset of metal-poor stars and hypothesize that their entire r -process abundance patterns—from the limited- r elements to the actinides—were produced by individual NSM events. We choose the Th/Dy abundance ratio to represent the relative production of actinide-to-main r -process material and the Zr/Dy ratio to represent limited-to-main r -process production. These three elements and their ratios capture the relevant regions of the abundance pattern to provide a sense of r -process extent in an astrophysical environment. We select all metal-poor stars in JINAbase that have reported measurements of Zr, Th, and Dy (30 in total), listed in Table 8.2. These stars vary from non-enhanced (r -0), to slightly enhanced (r -I), to very enhanced (r -II), based on the definitions in [Frebel \(2018\)](#).

Next, we describe how we use the observational Zr, Th, and Dy abundances of these 30 metal-poor stars as input to the MCMC method to derive progenitor neutron star binary masses. For this study, we work under the assumption that the majority of r -process material—especially second-peak elements and beyond—originated from one r -process event, and therefore that each star can be traced to individual NSMs.

TABLE 8.2
LIST OF STARS USED FOR ADMC

ID	Star	Class	[Fe/H]	[Eu/Fe]	[Zr/Dy]	[Th/Dy]	Reference
1	HD 110184	<i>r</i> -0	−2.51	0.10	0.21	0.02	Honda et al. (2004)
2	BD +10°2495	<i>r</i> -0	−2.31	0.12	−0.16	0.17	Roederer et al. (2010)
3	BD −15°5781	<i>r</i> -0	−2.92	0.14	−0.20	−0.06	Roederer et al. (2014b)
4	J08580584−0809174	<i>r</i> -0	−3.16	0.25	−0.20	−0.16	Cain et al. (2018)
5	HD 186478	<i>r</i> -0	−2.75	0.25	−0.15	0.08	Roederer et al. (2014b)
6	HD 108577	<i>r</i> -I	−2.36	0.38	−0.31	0.08	Johnson (2002)
7	BD+08°2856	<i>r</i> -I	−2.10	0.44	−0.45	−0.12	Johnson (2002)
8	HD 6268	<i>r</i> -I	−2.82	0.45	−0.42	−0.04	Roederer et al. (2014b)
9	HD 108317	<i>r</i> -I	−2.53	0.64	−0.28	−0.16	Roederer et al. (2012)
10	CS 30315-029	<i>r</i> -I	−3.43	0.69	−0.63	0.25	Siqueira Mello et al. (2014)
11	HD 221170	<i>r</i> -I	−2.16	0.80	−0.48	−0.06	Ivans et al. (2006)
12	HD 115444	<i>r</i> -I	−2.96	0.83	−0.49	−0.14	Westin et al. (2000)
13	BD +17°3248	<i>r</i> -I	−2.06	0.89	−0.69	−0.07	Cowan et al. (2002)
14	CS 30306-132	<i>r</i> -I	−2.41	0.89	−0.40	0.39	Honda et al. (2004)

TABLE 8.2 (CONTINUED)

ID	Star	Class	[Fe/H]	[Eu/Fe]	[Zr/Dy]	[Th/Dy]	Reference
15	CS 22953-003	<i>r</i> -I	-3.13	0.94	-0.79	0.03	Roederer et al. (2014b)
16	J20050670–3057445	<i>r</i> -I	-3.03	0.96	-0.76	-0.18	Cain et al. (2018)
17	HE 2327-5642	<i>r</i> -I	-2.78	0.99	-0.84	0.01	Mashonkina et al. (2010)
18	CS 29491-069	<i>r</i> -II	-2.60	1.07	-0.74	-0.13	Hayek et al. (2009)
19	HE 2252–4225	<i>r</i> -II	-2.94	1.14	-0.83	0.03	Mashonkina et al. (2014)
20	J15383085–1804242	<i>r</i> -II	-2.09	1.27	-0.90	-0.20	Sakari et al. (2018b)
21	COS82	<i>r</i> -II	-1.47	1.29	-0.79	-0.30	Aoki et al. (2007)
22	J09544277+5246414	<i>r</i> -II	-2.99	1.30	-0.95	0.43	Holmbeck et al. (2018)
23	HE 1219–0312	<i>r</i> -II	-2.97	1.41	-0.86	0.13	Hayek et al. (2009)
24	J14325334–4125494	<i>r</i> -II	-2.97	1.46	-0.96	0.00	Cain et al. (2018)
25	CS 31082-001	<i>r</i> -II	-2.90	1.62	-0.84	0.31	Hill et al. (2002)
26	CS 22892-052	<i>r</i> -II	-3.10	1.65	-1.02	-0.26	Sneden et al. (2003)
27	J20384318–0023327	<i>r</i> -II	-2.91	1.66	-0.78	0.17	Placco et al. (2017)
28	BD –16°251	<i>r</i> -II	-2.80	1.69	-0.96	0.16	Honda et al. (2004)
29	CS 29497-004	<i>r</i> -II	-2.68	1.73	-0.88	-0.20	Christlieb et al. (2004)
30	J033523–540407	<i>r</i> -II	-3.05	1.78	-0.99	-0.47	Ji and Frebel (2018)

8.3.3 ADMC: The MCMC Method

To reconstruct the merger properties of the systems that could have produced the *r*-process-enhanced stars, we use the `emcee` Python package (Foreman-Mackey et al. 2013), a Markov chain Monte Carlo (MCMC) algorithm, to explore M_1 and M_2 combinations of the progenitor neutron star binary. The way in which we apply this method takes observational abundance ratios as input and generates distributions of predicted M_1 and M_2 as output. First, for each EOS, the MCMC randomly samples M_1 and M_2 from a prior distribution. Then, with this random choice of M_1 and M_2 , we apply Equations 8.1 and 8.3 to determine how much mass is lost due to the wind outflow and dynamical ejecta mechanisms, yielding m_{wind} and m_{dyn} , respectively.

The same M_1 and M_2 values also provide a unique estimate of the lifetime of the NSM remnant from Equation 8.5, which in turn sets a characteristic abundance pattern of the ejecta (see Figure 8.6). We take the model Zr, Dy, and Th abundances obtained from the fitted wind outflow patterns for any remnant lifetime, then scale the abundances by m_{wind} found previously. Lastly, these abundances are multiplied by 25% to account for only a fraction of the total disk mass being ejected. After these steps, we obtain the predicted total Zr, Dy, and Th ejected by the disk outflows using M_1 , M_2 , and EOS as input.

The computed abundance pattern of the dynamical ejecta is similarly scaled by m_{dyn} . The relative abundances produced in the dynamical ejecta is mostly insensitive to the NSM properties; still, the initial Y_e of dynamical ejecta is unknown. We let the MCMC algorithm also sample Y_e and find that the range 0.16–0.18 can account for almost all input stellar abundances. Therefore, for a particular choice of M_1 and M_2 , a total ejected Zr, Dy, and Th abundance from two ejecta mechanisms within the merger are obtained by first finding m_{wind} and m_{dyn} , then multiplying representative abundance patterns of the wind and dynamical ejecta by the corresponding ejecta masses.

The MCMC algorithm computes output abundances from M_1 and M_2 for each EOS as it explores the M_1 - M_2 parameter space, preferring solutions whose computed abundance ratios are within certain tolerances on the input observed Zr/Dy and Th/Dy abundances. To find the posterior distribution of likely neutron star binaries, our MCMC algorithm uses 50 “walkers” distributed across the M_1 - M_2 parameter space within theoretical and observational limits of neutron star masses (i.e., $M_2 \leq M_1 \leq M_{\text{TOV}}$). The walkers are sampled from a prior that is fitted to the binary neutron star distribution: essentially a Gaussian with a peak near $1.35 M_{\odot}$ and a standard deviation of $\sim 0.1 M_{\odot}$, obtained from fitting to data in [Tauris et al. \(2017\)](#). Using Equations 8.1–8.5, the ratios of the combined Zr/Dy and Th/Dy model abundances are compared to the observationally derived values to find the likelihood that a particular M_1 - M_2 combination reproduces the input abundance ratios. We use a likelihood function of the form:

$$\ln P(\vec{x}|\vec{\theta}) = -\frac{1}{2} \sum_i \left(\frac{\theta_i - x_i}{\sigma_i} \right)^2, \quad (8.6)$$

where $\vec{\theta}$ are the model Zr/Dy and Th/Dy abundances, and \vec{x} are the corresponding observed abundances. The tolerances ($\vec{\sigma}$) supplied to the likelihood function are such that the fitted Zr/Dy be at most 0.1 dex greater than the input Zr/Dy abundance, but can allow the Zr/Dy to be significantly lower. We choose a relaxed tolerance on Zr/Dy since some amount of Zr could come from SNe sites that also created the Fe-peak elements present in the star. However, we require that the Th/Dy is at maximum ± 0.1 dex from the input value, since we presume that the majority of main r -process-element abundances in each star were created by a merger event. As a result, the MCMC algorithm—which we now name ADMC (Actinide-Dilution with Monte Carlo)—finds the most probable combination of M_1 and M_2 of the original NS binary that merged to produce nearly all the Zr, Dy, and Th abundances present

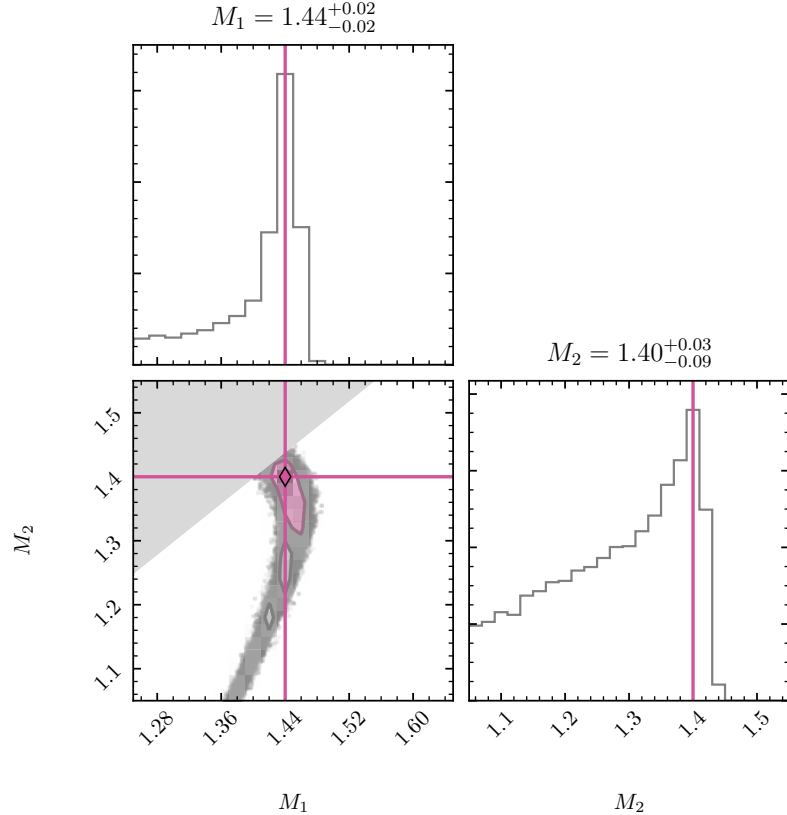


Figure 8.7. Corner plot showing the most likely combination of M_1 and M_2 for CS30306-132 (Star ID 14) using the DD2 EOS. The contour of $1-\sigma$ solutions is shaded in pink.

in each stellar atmosphere.

Figure 8.7 shows an example of the mass results of ADMC for CS30306-132 (Star ID 13) using the DD2 EOS. Due to the small parameter space, we found that 2000 steps with a burn-in stage of 500 is more than sufficient for the walkers to thoroughly explore the parameter space. On average, the MCMC algorithm takes a step size in the M_1 - M_2 parameter space of $\sim 0.1 \text{ M}_\odot$; very rarely ($< 0.02\%$) does the step size exceed 1 M_\odot . The gray shaded region in the upper-left corner of the M_1 - M_2 plot shows one of the limits supplied as a prior: M_2 should always be less than or equal to M_1 . Without this constraint, ADMC would simply find superfluous solutions

reflected about the $M_1 = M_2$ axis, which are equivalent to $M_{1\leftrightarrow 2}$. The long tail visible in the M_1 - M_2 plot offers a view into the complexity of the parameter space. Under the constraints we use with ADMC, only delicate combinations of NS masses can reproduce the input abundances within the supplied tolerances. The pink colored region denotes $1-\sigma$ edges of the solutions in the two-dimensional parameter space. The $1-\sigma$ uncertainties on M_1 and M_2 are taken from the contour edges.

8.4 Results

The ADMC results provide for each input star (i.e., pair of observationally derived Zr/Dy and Th/Dy abundances) a distribution of the primary (M_1) and secondary (M_2) neutron star masses whose computed merger outflow composition reproduces the observed (input) stellar abundances. Output abundances are computed according to the lifetime of the merger remnant that sets the composition of the wind and the preferred Y_e of the dynamical ejecta. Figure 8.8 shows ADMC results as a plot of the most likely M_1 - M_2 pairs that would have merged to account for the r -process abundances of each star in Table 8.2 for each EOS. These results are also tabulated in Tables B.1–B.6. The ADMC-predicted binary progenitors are colored by their r -process enhancement signature that their outflows produce: r -II (dark-filled symbols), r -I (lightly filled symbols), or non-enhanced (white-filled). The gray stars in Figure 8.8 show M_1 and M_2 for existing DNS systems in the Galaxy. Lines of constant q are shown for guidance, and the diagonal thin gray band displays the range of M_1 - M_2 solutions satisfying the chirp mass of GW170817: $\mathcal{M} = 1.188^{+0.004}_{-0.002} \text{ M}_\odot$. Since MCMC produces a posterior *distribution* of solutions, the (asymmetric) error bars on each M_1 - M_2 pair represent the limits of the two-dimensional $1-\sigma$ contours from the ADMC output (see Figure 8.7). These uncertainties correspond directly to the provided tolerance on how far the computed abundances are allowed to deviate from the input abundances and still consider the M_1 - M_2 pair producing those abundances a successful match.

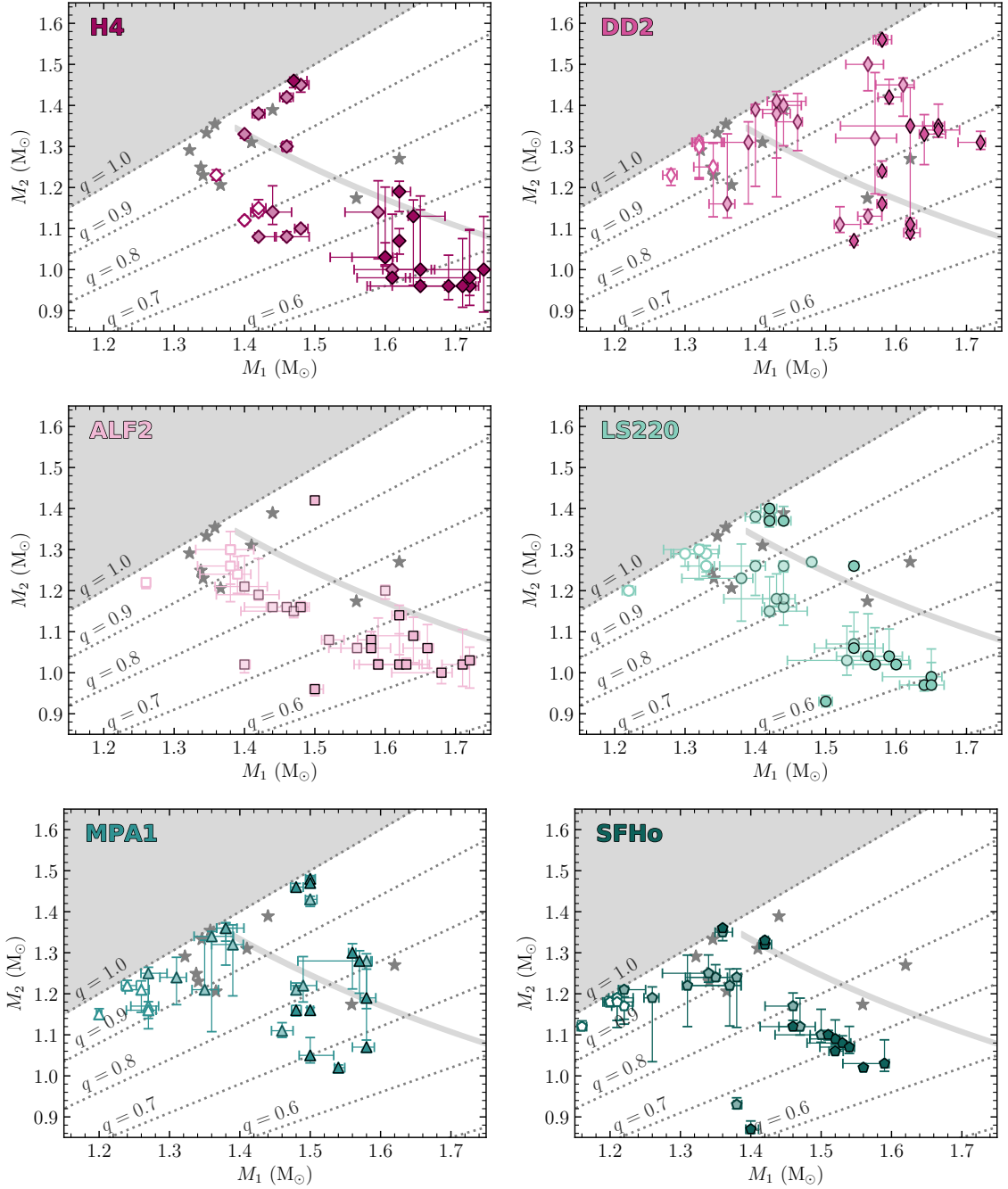


Figure 8.8. Mass results for each EOS choice compared to known neutron star binaries (stars). Lines of constant q are shown for comparison. Dark-filled symbols with black outlines denote r -II stars, light-filled symbols denote the r -I stars, and white-filled symbols with colored outlines show r -0 stars.

We will start by taking these results at face-value with the caveat that ADMC output and its interpretation rely on several underlying assumptions:

1. The majority of r -process material in the Galaxy (observed in metal-poor stars) was made by NSMs, and that each star had only one major NSM progenitor. Furthermore, the elemental production by each of these sites extends over the entire r -process pattern from the limited- r elements (Zr) all the way to the actinides (Th).
2. The 30 stars we pick are a representative subset of r -process-enhanced stars in the Galaxy, and thus our conclusions can be extended to a larger population of metal-poor stars.
3. The dynamical ejecta is extremely neutron-rich and contributes nearly no Zr abundance to the combined abundances of the total ejecta. Similarly, the composition of the disk wind is determined by simulations with no additional neutrino effects altering their composition.
4. DNS systems, their mass distributions, and chirp masses are roughly constant, so that the present-day distribution of DNSs in the Galaxy reflects earlier distributions.

The first noticeable effect in the ADMC results is the apparent trend with stellar r -process enhancement type. As can be seen in Figure 8.8, NSM progenitors of the r -II stars are most likely asymmetric neutron star binary systems, given all of the above underlying assumptions. ADMC predicts slightly more symmetric progenitor binary systems for stars with r -I signatures. Finally, the abundances of r -0 stars are well reproduced by nearly symmetric—and quite low-mass—neutron star binaries, similar to existing neutron star binaries in the Galaxy. These results are unsurprising considering the observational trends of first r -process peak abundances with main r -process abundances in metal-poor stars; the r -II stars generally display the lowest Zr/Dy ratios and r -I stars slightly higher Zr/Dy abundances. With low Zr/Dy abundances, this MCMC method will favor systems that dilute the strong Zr production of the disk outflows. This dilution can be achieved by producing more Dy in the dynamical ejecta, therefore requiring a more asymmetric binary system to produce a low total Zr/Dy abundance ratio.

Next, we can evaluate the results based on applied EOS. The dependence on the EOS manifests mainly through M_{TOV} and how the maximum neutron star mass plays into the total disk ejecta. For EOSs with a lower M_{TOV} (i.e., H4, ALF2, LS220, and SFHo), the results in Figure 8.8 tend to gather along lines of constant total binary mass. Recall that the total binary mass, M_{tot} , directly influences the total mass of the disk outflows as well as the lifetime of the remnant before collapse into a black hole. Both the disk mass and the remnant lifetime then determine the majority of Zr production in the NSM ejecta. Therefore, the grouping of our results along certain values of M_{tot} reflects the matching condition for the Zr/Dy constraint. Many of the r -II and highly enhanced r -I stars have similar Zr/Dy abundance ratios, and therefore favor similar values of M_{tot} . Since their relative Th/Dy abundances differ much more broadly, the optimal solution is found at different values of q along comparable M_{tot} values. Similarly, notice in Tables B.1–B.6 that, for many cases, the amount of mass ejected by the disk wind outflows is roughly constant for many EOSs, while the amount of dynamical ejecta varies widely. This simple observation itself reveals that the Th/Dy abundance can act as a sensitive test of r -process conditions, such as in merger environments, and emphasizes the importance of measuring actinide abundances in metal-poor stars.

EOSs with a larger M_{TOV} , MPA1 and DD2, produce the longest-lived merger remnants (and widest variations in lifetimes). The effect of M_{TOV} on remnant lifetime is shown explicitly in Equation 8.5; for systems with the same total mass, assuming an EOS with a larger M_{TOV} will produce a shorter-lived remnant. Therefore, to achieve the same result as an EOS with a smaller M_{TOV} , the remnant must survive collapse for *longer* to compensate for the same level of total limited- r (Zr) production. However, a longer-lived remnant produces an increasingly weak main r -process component, so the majority of main r -process material (Dy) must come from the dynamical ejecta. Consequently, many of the solutions assuming an EOS with a large M_{TOV} are grouped

around narrow values of q that is primarily responsible for Th/Dy production. Then, to account for the Zr/Dy abundance, these solutions are spread across a wide range of M_{tot} . Figure 8.8 shows that the results for DD2 and MPA1 do not tend to follow lines of constant M_{tot} like the EOSs with smaller M_{TOVs} , but rather favor narrow ranges of q . Clearly, the EOS-dependence is more sensitive to M_{TOV} than the detailed mass-radius relationship (i.e., compactness).

The ADMC results can also be compared to the observed distributions of individual neutron star masses. Figure 8.9 shows the distribution of optimal neutron star masses computed by ADMC compared to parameterized fits to observations of neutron stars. The “MSP” distribution comes from the fit presented in [Antoniadis et al. \(2016\)](#) from millisecond pulsar measurements. The “DNS” distribution is the same as the prior given to the MCMC (a Gaussian with $\mu \approx 1.35 \text{ M}_\odot$ and $\sigma \approx 0.1 \text{ M}_\odot$). Overall, our results do not well reproduce current Galactic neutron star distributions in binary systems. Instead, across most EOSs, our results tend to favor somewhat lower neutron star masses in more asymmetric binary systems than are what observed today, with one peak of the neutron star mass distribution at $\sim 1.25 \text{ M}_\odot$ and the other at $\sim 1.45 \text{ M}_\odot$. Additionally, several of our results—especially for $r=0$ —favor lower chirp mass systems than that inferred from GW170817. The dominance of low-mass systems in our results may be a consequence of the wide variation in the mass of dynamical ejecta for systems with a low-mass primary ($M \sim 1.2 \text{ M}_\odot$). As shown in Figure 8.3, very low-mass systems with $q \approx 1$ produce the least amount of dynamical ejecta, which in turn implies a lower actinide abundance in the ejecta. However, a low primary mass with an even lower-mass companion (e.g., $M_1 = 1.2 \text{ M}_\odot$ and $q = 0.5$) produces the highest amount of dynamically ejected material. The wide variation in the dynamical ejecta mass translates directly into wide variations in the produced actinide abundances in our model. In summary, assuming a low-mass primary can sufficiently account for many of these abundance differences, so the MCMC model

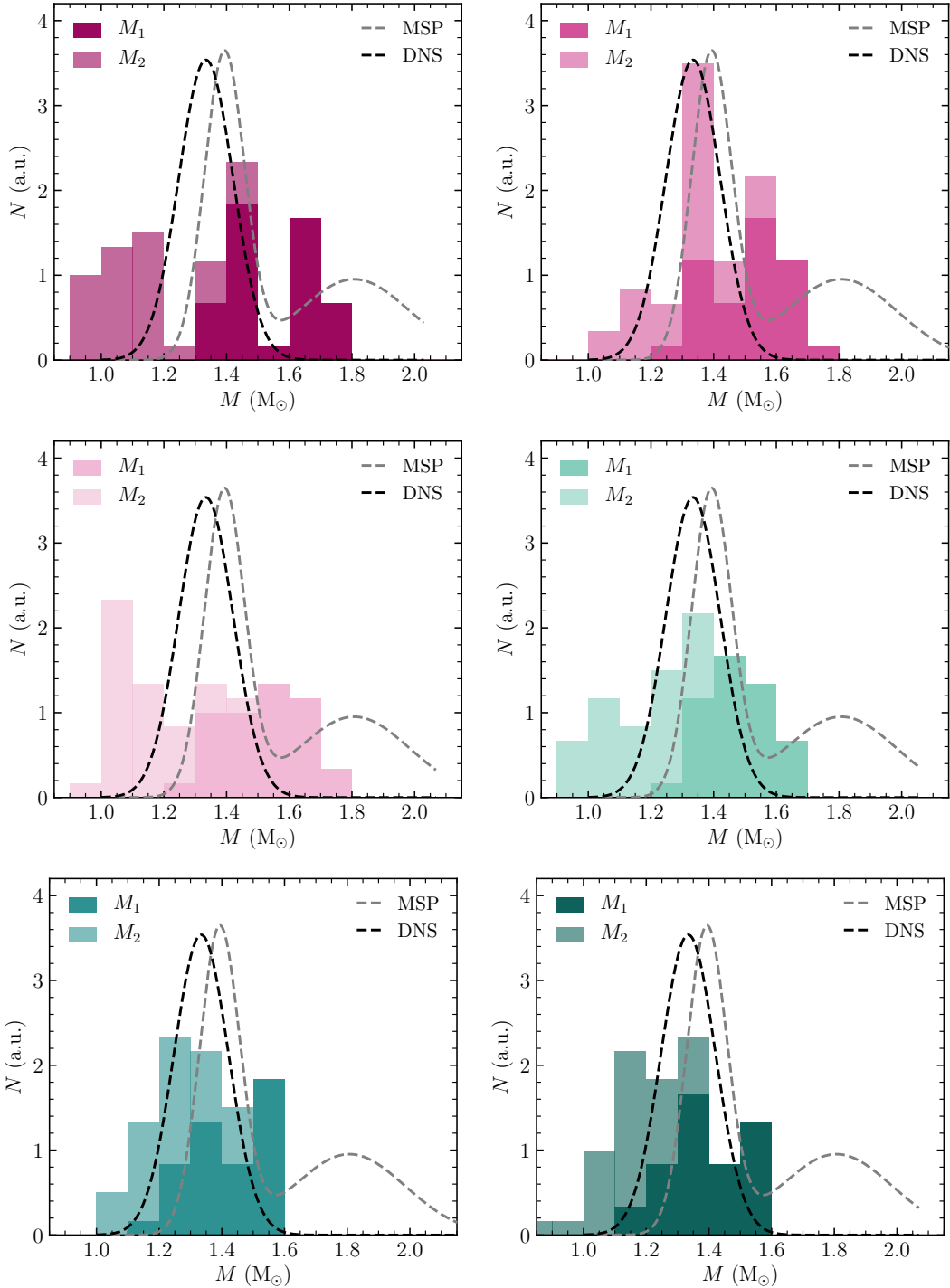


Figure 8.9. Mass distributions for each EOS choice compared to fitted neutron star distributions.

gravitates to these low-mass solutions.

Supposing that all of our initial assumptions hold, and that the first NSMs were distributed the same way as present-day neutron star binary systems, the literal interpretation of our results imply that NSMs could not have been the progenitors of very metal-poor *r*-process-enhanced stars since these systems are much too asymmetric. This conclusion could either arise from an observational bias, or have a physical explanation. Observationally, Th in metal-poor stars is straightforward to identify and measure in high-resolution spectra if the star is already enhanced in *r*-process elements. Our sample does not include upper limits on Th or account for Th that may be below the observational limit. If our stars already represent extreme examples, then it naturally follows that we would predict similar extremes on the DNS masses in order to create high Th abundances. Symmetric NSMs perhaps produce Th below the observational limit at these moderately low metallicities. On the other hand, the literal interpretation of our results in the context of the initial assumptions suggests that the first neutron star binary systems producing observational levels of Th were asymmetric, and perhaps that low-*q* systems were more common at low metallicities (or that these systems simply merged earlier). With this interpretation, there is no need for the first NSMs to resemble present-day binary systems.

8.5 Model Variations

Under the assumptions outlined in Section 8.4, our ADMC results point to very asymmetric neutron star binary systems as the progenitors of the material in *r*-process-enhanced stars, if these asymmetric systems are allowed at early times in Galactic history. Otherwise, if historical neutron star binary systems were only (or near enough to) symmetric, then NSM could not have been the progenitors of the highly enriched *r*-II stars. Within our model, NSMs may still be responsible for the metal-poor stars with very low *r*-process abundances, pointing to typically more

symmetric—but lower total mass—systems. In this section, we relax each of our initial assumptions in turn to study the impact on the neutron star distribution and reveal under what conditions NSMs can be reconciled as main r -process production sites. The individual results for all variations are included in Appendix B.

8.5.1 No r -II Stars

Let us start by addressing the first assumption: that NSMs contributed a majority of r -process elements found in metal-poor stars in the Galaxy, especially those with actinide measurements. If we keep the basic speculation that the distribution of binary neutron star systems is roughly constant throughout time—i.e., that our reconstructed binaries should match present-day ones—then perhaps NSMs are responsible for only certain stellar signatures? Figure 8.8 shows some correlation between enhancement level (i.e., r -I, r -II, or none) and the masses of the neutron stars, as discussed in Section 8.4. Specifically, the r -II stars often favor highly asymmetric binary systems, while the non-enhanced stars frequently imply more symmetric, but lower-mass binaries. When the highly enriched r -II stars are removed from the neutron star mass distributions—equivalent to saying that their r -process material would not have a (single) NSM origin—then the mass distributions overall are closer to resembling present-day neutron star systems. For example, the left panel of Figure 8.10 shows the distribution using the DD2 EOS when the r -II stars are removed. Eliminating the results for the most highly r -process enhanced stars removes both the very-high and very-low neutron star masses from the distribution, bringing the total distribution closer in agreement with present-day DNS systems in the Galaxy. Therefore, if the present-day mass distribution of binary neutron stars represents a constant distribution throughout time, then NSMs can explain all but the very- r -process-enriched metal-poor stars, since those stars require very asymmetric systems that are inconsistent with the present-day DNS distribution. In this case, a separate

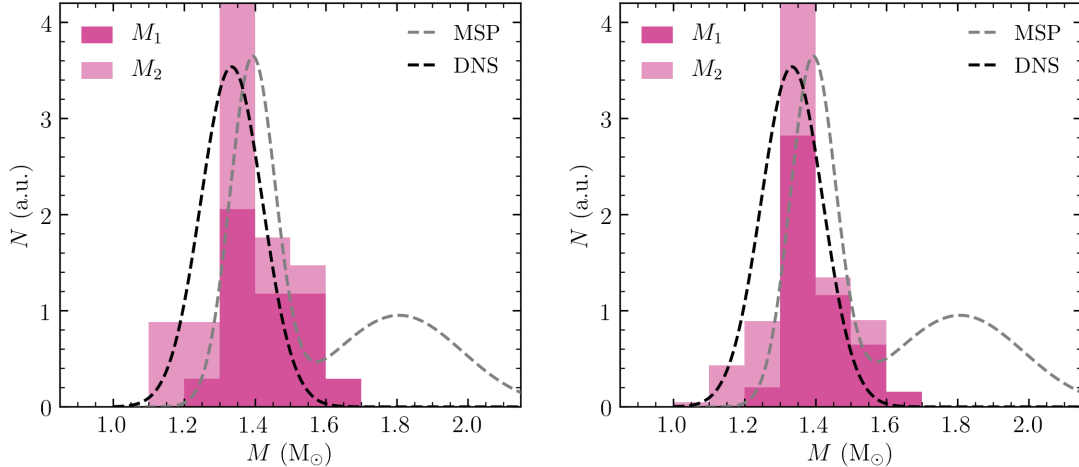


Figure 8.10. Neutron star mass distributions for DD2 when r -II stars are removed from the distribution (left), and when the results are weighted by the [Eu/Fe] distributions of very metal-poor stars (right).

astrophysical progenitor would be required to explain the most r -process-enriched metal-poor stars, assuming that only one r -process progenitor is needed.

8.5.2 Stellar Sample Distribution

The next assumption implicitly folded in to the interpretation of our results—in particular, the mass distributions in Figure 8.9—is that the elemental signatures of our 30 stars are representative of the majority of r -process material found in metal-poor stars in the Galaxy. However, these 30 stars are clearly not representative of all metal-poor stars in the Galactic halo that have so far been studied. For instance, our sample consists of primarily ($\sim 83\%$) r -I and r -II stars (by observational and selection bias on requiring measurements of all three of Zr, Dy, and Th), whereas these stars are estimated to be only a fraction ($\sim 20\%$) of all metal-poor halo stars. Recently, efforts by the RPA have quantified r -process abundances of a large sample of metal-poor halo stars, using primarily Sr, Ba, and Eu. Here we rescale our results to the large sample of RPA stars in an effort to make our 30 stars representative of a broader stellar

population. We select all RPA stars with definite measurements on Ba and Eu (i.e., no upper limits), metallicities below -2.06 (the maximum metallicity of our 30 stars), and $[\text{Ba/Eu}] < -0.22$ (the maximum $[\text{Ba/Eu}]$ ratio of our 30 stars). Of 585 RPA stars, these cuts leave 285 stars, still a more sizable sample than the 30 with reported Zr, Dy, and Th measurements. Next, we bin the $[\text{Eu/Fe}]$ abundances of the 285 RPA stars and our 30 in increments of 0.2 dex and determine by how much each bin of our 30-star sample must be rescaled in order to match the corresponding $[\text{Eu/Fe}]$ bin of the RPA sample. Then, based on these adjustments, we weigh each MCMC result by the rescaled amount, depending on the $[\text{Eu/Fe}]$ bin in which each star lies. In this way, contribution to the ADMC results by the $r\text{-II}$ stars are attenuated, while the $r\text{-I}$ and non-enhanced stars are given more weight, reflective of a larger sample of metal-poor stars.

The right panel of Figure 8.10 shows the neutron star mass distribution for DD2 after applying this rescaling. Rather than simply removing the results for $r\text{-II}$ stars, rescaling the results accomplishes a similar effect by mitigating the contribution of the highly r -process-enriched stars to the total mass distribution, producing a similar distribution as that in which the $r\text{-II}$ stars were removed entirely. Similar results are achieved for the other EOSs, with low- and high-mass tails reduced and a stronger peak near 1.3 M_\odot . It is worth noting, however, than the H4 case cannot be reconciled with the present-day DNS distribution either by this rescaling or removal of $r\text{-II}$ results, which could provided additional, indirect support of ruling out this EOS. Overall, if the present-day mass distribution of binary neutron star systems is time-invariant, then NSMs could still produce the r -process material found metal-poor stars by assuming that NSMs were responsible for the r -process elements found in *all* Galactic metal-poor stars, not just the highly enhanced $r\text{-I}$ and $r\text{-II}$ stars. It is important to note that neither removing $r\text{-II}$ stars from the distribution nor rescaling our 30-star sample completely removes the need for at least some highly asymmetric

mergers. The contribution by highly mass-asymmetric NSMs can only be *attenuated* by either of the above considerations if NSMs are to be the predominant source of *r*-process material in metal-poor stars. However, there are other variations on the model to consider, which may contradict or further support this conclusion.

8.5.3 The Ejecta Composition

Here we address the second assumption: what if the composition of the dynamical ejecta and disk wind is more (or less) neutron-rich? As modern calculations take increasing care to include neutrino effects on the composition of astrophysical ejecta, future simulations might predict higher (or lower) Y_e values for NSM outflows. These effects could potentially alter the ADMC results by requiring different values of m_{wind} and/or m_{dyn} and therefore different progenitor neutron star masses since the overall contribution to the *r*-process abundances by each ejecta component would change.

We start with the dynamical ejecta: what if this material contributes some significant amount of Zr to the final abundances? Since we assume that the dynamical ejecta is composed largely of main *r*-process material, we might expect that increasing the amount of Zr that is produced by these outflows decreases the necessary relative contribution by the disk wind. As a result, slightly total binary masses may be required to decrease the contribution from the disk outflows. As a straightforward test case, we artificially increase the Zr abundance of the dynamical ejecta by 1.8 dex, which increases the $\log \epsilon(\text{Zr/Dy})$ abundance from about -2.05 to -0.25 . This addition is still a very weak limited-*r* contribution, but it is much greater than the original ratio and could potentially be achieved in dynamical outflows (see, e.g., Radice et al. 2018a). In general after this abundance increase, the mass distributions for each EOS become slightly broader, shifting some solutions to lower or higher neutron star masses. The increase of Zr in the dynamical ejecta brings DD2 into the best agreement with current neutron star binary mass distributions, as shown in the

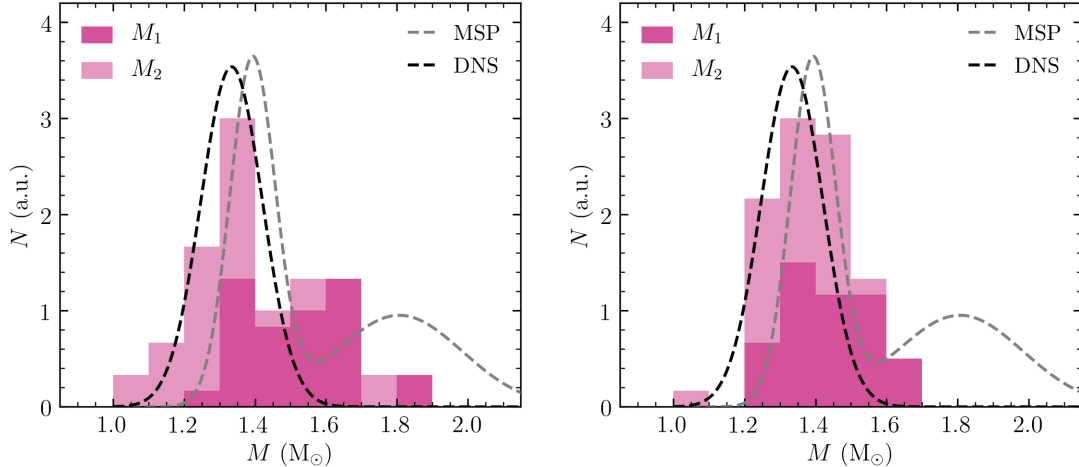


Figure 8.11. Neutron star mass distributions for DD2 when the dynamical component contributes some Zr abundance to the total outflow mass (left) and when the composition of the disk is increased by $Y_e + 0.03$ (right).

left panel of Figure 8.11.

Next, we simulate the effect of added neutrino interactions in the disk wind outflows by adjusting the relative contribution of each tracer based on their initial Y_e . By reweighing the contribution by each tracer, we effectively increase the Y_e of the disk outflows by 0.03 (roughly 10%). Since the abundances of main r -process elements—especially the actinides—are sensitive to variations in the low- Y_e ejecta, the Zr abundance is nearly unaffected when the Y_e is slightly increased. On the other hand, the Dy and Th abundances show an appreciable decrease when the Y_e is increased even slightly, especially for longer lived merger remnants. After slightly altering the nucleosynthesis yields from the disk outflows, we run ADMC again to see if different solutions are found.

The right panel of Figure 8.11 shows the neutron star mass distribution after a slight increase to the disk Y_e . For many EOSs, the Y_e increase produces *more symmetric* systems. It may seem unintuitive that an increase in Y_e of the disk wind would lead to more symmetric cases, but a careful interpretation of Figure 8.3 in

particular can elucidate the cause of this apparent contradiction. A binary neutron star system with a primary mass of $1.4 M_{\odot}$ will produce more dynamical ejecta at low q than a system with a $1.2 M_{\odot}$ primary. Not only do these higher-mass systems provide enough dynamical ejecta to produce all the Th and Dy missing from the now relatively neutron-poor disk, but they also produce neutron stars with masses that are more consistent with observations of existing DNS systems. In addition, higher-mass systems are predicted to form smaller-mass disks around the massive remnant, and thus eject less Zr-rich material (see Figure 8.2). Therefore, the increase in Zr due to the shift in Y_e of +0.03 is mitigated by preferring higher-mass systems that contribute less Zr in general from the disk wind component. With Y_e shifted to slightly greater values, the total Zr contribution from the disk outflows is effectively decreased, allowing a less massive dynamical component to make up for the loss of light- r production by the disk.

8.5.4 No Prior

Enforcing a prior is useful in that expectations or physical limitations can be imposed on the otherwise knowledge-agnostic Monte-Carlo algorithm. However, using a prior can restrict the MCMC walkers from exploring a parameter space that may find a statically more likely solution. In this section, we relax our third assumption and apply a flat prior rather than a Gaussian one to test if other, more or equally likely solutions are found in the parameter space.

While many of the stars still predict similar DNS systems as using a Gaussian prior, using a flat prior sometimes yields very high-mass results. For example, Figure 8.12 shows the M_1 and M_2 neutron star masses using the DD2 EOS and a flat prior. A handful of input finds solutions around $M_{1,2} \approx 1.8 M_{\odot}$. When both M_1 and M_2 are at these high masses, two effects occur according to Equations 8.1–8.5. First, at very high total masses, the merger remnant collapses immediately into a

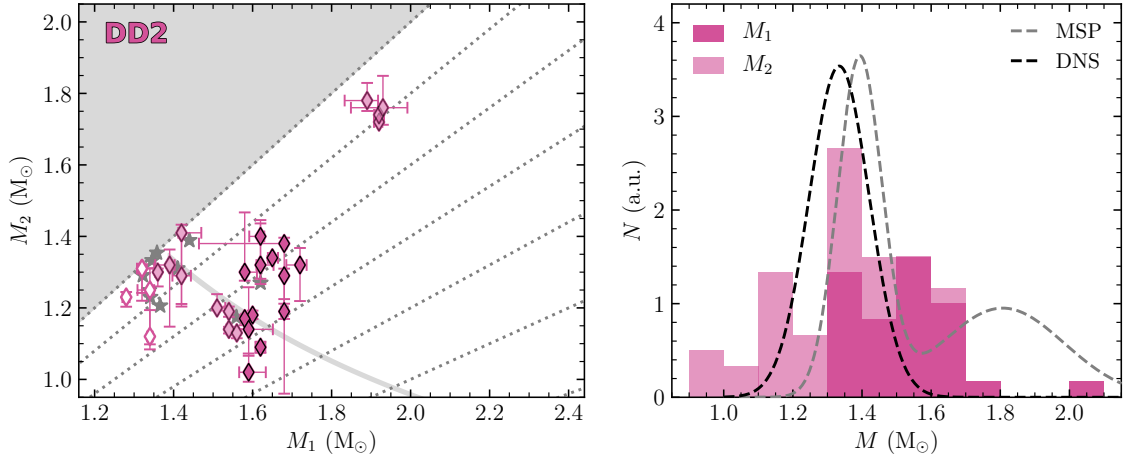


Figure 8.12. Individual (left) and total (right) neutron star mass results for DD2 when using a flat prior. Note the axes on the left figure are on a different scale from Figure 8.8.

black hole, i.e., $\tau = 0$ ms. In prompt-collapse cases, there is theoretically no time for neutrino irradiation by the disk to change the composition of the ejecta, so the disk outflows stay extremely neutron rich. Secondly, the high neutron star masses prevent dynamical ejecta from escaping the merger. Since the disk wind can now be neutron-rich enough to produce all three regions of interest in the abundance pattern—the limited- r elements, the main r -process, and the actinides—no dynamical ejecta is required at all.

While the high-mass solutions are statistically as or more likely than the previous solutions using a prior, this high-mass region of the parameter space pushes into analytical limits of the model. Both the dynamical and wind ejecta masses are at a minimum allowed by Equations 8.1 and 8.3, and every more massive M_1 - M_2 combination produces the exact same abundances. This high-mass corner of the parameter space represents, for certain stellar inputs, a likelihood plateau where the success of one solution cannot be discerned from any another. These are real solutions from the MCMC, but with the limits on the analytic forms in hand, they

cannot be disentangled from computational artifacts. In the absence of the high-mass solutions the MCMC algorithm still finds similar solutions as before (within uncertainty), demonstrating that our method has little sensitivity to details of the prior distribution.

With different variations on both the implicit and explicit assumptions in our model, the outflow composition indicates the largest area for improvement. Furthermore, the variations on ejecta composition reveal that the ratio of weak to main *r*-process production—or Zr/Dy, as we represent that ratio—is absolutely critical. In the same vein, one model variation that we have not addressed is the possibility of additional, subdominant sites that contribute significantly to the observed *r*-process patterns in metal-poor stars. For example, a second site might pollute star-forming gas with an abundance of Zr, and hence, a higher weak-to-main *r*-process ratio, than an NSM event enriching the same gas. In this case, the particular NSM contributing the majority of main *r*-process material would require less Zr to be produced in its outflows. As described in the interpretation of our fiducial results, a lower weak-to-main matching constraint would likely push the MCMC solutions to higher mass asymmetries. This important variation on the outflow ejecta can either have theoretical or astrophysical origins; i.e., is the ejecta less (or more) neutron-rich than predicted by simulations, and/or does more than one site contribute to each stellar *r*-process signature? These are important questions in which further investigation that can strength this model and its results.

8.6 Summary and Discussion

This work demonstrates an innovative technique in which stellar abundances work hand-in-hand with simulation data in order to uncover histories of past astrophysical phenomena in a way that has thus far not been attempted in literature. We achieve this by applying the best current fits to hydrodynamical simulation data describing

the total wind and dynamical ejecta from NSMs as a function of the individual NS masses. Next we use state-of-the-art nucleosynthesis network solvers to find the composition—and therefore the total r -process yields—of the two ejecta components. Then, we input observed stellar r -process abundances through the ratios of limited- r -to-main-to-actinide elements and postulate that unique NSMs were responsible for the observed r -process abundances. Working backwards from the observed stellar abundance ratios, this method uses an MCMC algorithm to find the optimal masses of the NSs that would have merged to produce those r -process abundances. Combining current theoretical and observational results, we make the best possible predictions given the data in hand and strive for self-consistency wherever possible, both in the nuclear data and in the EOS that sensitively affects NSM ejecta.

Based on the current best simulation and observational data, our main results are

- If mergers are responsible for the majority of main r -process material observed in Galactic metal-poor halo stars, then many of the progenitor NS binary systems were primarily mass-asymmetric.
- The asymmetry increases with level of r -process enhancement; the r -II stars favor higher asymmetries, while stars with low r -process abundance ratios can be reproduced by mergers between somewhat equal-mass NSs.
- If our 30 stars are a representative sample of metal-poor stars, then this asymmetry implies that either the past distributions of DNSs were distinctly different from the present-day distribution in the Galaxy, or NSMs could not have been the main r -process source to explain the r -I and r -II stars.
- Our results using EOSs with larger values of M_{TOV} predict slightly more symmetric binaries, indicating that the effect of EOS on the MCMC results manifests from the maximum NS mass rather than the compactness (\mathcal{C}).

We have also explored some variations to the model that could be expected given future descriptions of the NSM ejecta, identifying some aspects and assumptions of our model that currently have significant leverage on our results. For example, we have mitigated the inconsistency between our predicted DNSs and those in the Galaxy by rescaling our limited sample (30) to a larger sample set (298). Under this

rescaling, we found that a smaller percentage of high-asymmetry systems are needed to reproduce the majority of Galactic r -process abundances, yet the need for some asymmetric mergers is not completely eliminated. Whether such high-asymmetry systems could physically form—and how frequently, if so—is beyond the scope of this work. Another sensitive aspect of our model is the composition of the ejecta. For example, if the disk wind is slightly more proton-rich than current simulations estimate, then more massive—and more symmetric—NS binary systems could explain the r -process abundances of metal-poor stars.

The variations we explore reflect potential for our model to be adapted and updated as more experimental, theoretical, and observational data are gathered. Population synthesis studies can elucidate whether high mass-asymmetry DNS systems are more likely to form from low-metallicity gas, or if enough can form for NSMs to be the primary producers of r -process material in the metal-poor halo stars. Detailed treatment of neutrino interactions in NSM ejecta are essential to understanding the outflow composition and can reveal whether the disk wind can reach significant levels of neutron-richness. NSMs simulations and ejecta mass characterizations from hydrodynamical simulation data at extreme NS mass-asymmetries can explore the lower ejecta limit for NSMs and whether the alternative, high-mass solutions are viable. Complete, self-consistent stellar abundances of the entire r -process pattern (limited- r elements to the actinides) as well as measurements of second-peak elements (e.g., tellurium) could be used as additional constraints on the predicted DNS systems.

This work nonetheless demonstrates a unique and adaptable route by which the elemental signatures of metal-poor stars can place predictions on the first generation(s) of stellar evolution in the Universe and, potentially, on the nuclear EOS. We look forward to how future predictions by hydrodynamical simulations of NSM disk outflows may alter our results, how additional stellar measurement (for example, by the RPA) can supplement our reconstructed DNS distributions, and how future

LIGO observations—and any electromagnetic counterparts—can offer further constraints on the likelihood that NSMs produced a majority of *r*-process elements in metal-poor stars.

CHAPTER 9

CONCLUSION AND FUTURE OUTLOOK

My comprehension can only be an infinitesimal fraction of all I want to understand.

— Ada Lovelace

The astrophysical site of the production of *r*-process elements—and thus the origin of the *r*-process-enhanced stars—remains one of the most significant unknowns in the field of nuclear astrophysics. With the observation of GW170817 and its associated kilonova, NSMs are currently favored as *r*-process sites. To further investigate the potential of NSMs as the dominant source of *r*-process material in the Galaxy, the RPA was established with one of its goals to increase by a factor of four the number of identified highly *r*-process-enhanced *r*-II stars. Through dedicated RPA efforts, the work in this thesis has helped to increase the number of identified *r*-II stars by over twofold from thirty to more than seventy.

Along the way, we have uncovered new clues useful for the study of the *r*-process mechanism and its astrophysical location. For example, using RPA data, it has recently been discovered that stars with similar chemical enrichments and metallicities also share kinematic properties. Consequently, stars with similar dynamics in the Galactic halo could have once been independent satellite galaxies that were eventually disrupted and accreted by the Milky Way, effectively analogs of present *r*-process enhanced dwarf galaxies like Reticulum II and Tucana III. Then, halo stars with similar kinematics also share a chemistry in which each member of the kinematic group retains some record of the galaxy’s history of nucleosynthetic events. Using

nucleosynthesis network calculations, this thesis has shown that the distinct actinide signatures of these chemo-dynamically related systems implies that NSMs not only may be responsible for the actinide-boost stars, but also can explain nearly all levels of actinide-to-lanthanide abundances in metal-poor stars by considering astrophysical variations in merger ejecta.

Such analysis can be pushed even further to paint an entire picture of the nucleosynthetic history of a past-disrupted host system. First, full chemical analyses must be conducted for members of chemo-dynamically related groups. If the chemical enrichment patterns of stars from the same dynamically linked group differ, then at least two possibilities exist: either (1) these different patterns indicate separate events, or (2) the ejecta from one event was mixed non-homogeneously into the primordial gas of the ISM. (Alternatively, some complex combination of these two cases is perhaps more realistic.) By studying and comparing stars that likely originated from the same enriched gas, details on separate *r*-process events and/or the mixing properties of event ejecta can be studied by placing estimates on (1) the frequency of certain *r*-process sites (i.e., how often does elemental pattern “X” appear in each group of stars compared to pattern “Y”?) and (2) the yield of material from those sites (i.e., how often and in what abundance does elemental pattern “X” appear compared to all members of the group?) The methods presented in this thesis allows such work to be done by first obtaining high-resolution spectra of metal-poor stars, then by comparing the abundance patterns of those stars to abundances from *r*-process nucleosynthesis network calculations.

This thesis also emphasizes the power of combining nuclear effects into astrophysical observables. By pushing self-consistency from the nuclear regime to the astrophysical domain, an entire suite of observables can be fundamentally correlated. For example, propagating nuclear physics effects into all aspects of NSM simulations—from the birth of NS binary systems to their eventual merging—can reveal what

specific combination of nuclear masses, nuclear EOS, NSM rates, and NSM nucleosynthesis yields can reproduce observations of gravitational waves (in frequency, shape, and intensity), kilonovae signatures, and the occurrence rates and elemental abundances of metal-poor stars both inside and outside the Galaxy. Future work will combine population synthesis models, stellar evolution codes, hydrodynamical simulations, and nuclear network calculations to track the evolution and observation of explosive astrophysical events that are responsible for creating the heaviest elements in the Universe.

APPENDIX A

DATA FROM THE FOURTH DATA RELEASE OF THE RPA

A.1 Observation Log

Table A.1 lists the right ascension (RA), declination (Dec), V magnitude, the modified julian date of the observation (MJD), the exposure time (in seconds), the signal-to-noise ratio (S/N) at 4129Å, and the computed heliocentric RVs for all stars in the fourth data release of the RPA (Holmbeck et al. 2020).

A.2 Model Atmosphere Parameters

Table A.2 lists the model atmospheres computed via the spectroscopic method for all stars in the fourth data release of the RPA. These parameters include the correction to the temperature from Equation 4.9 and are used in the spectral synthesis routine to find the neutron-capture abundances.

A.3 Neutron-Capture Abundances

Table A.3 lists the carbon, strontium, barium, and europium abundances compared to iron for all stars in the fourth data release of the RPA. Also shown are carbon abundances of the natal gas from which the star was created, after corrections to the observed carbon abundance due to stellar evolution effects.

TABLE A.1
OBSERVATION LOG FOR THE FOURTH DATA RELEASE OF THE
RPA

Stellar ID	RA	Dec	<i>V</i> mag ^a	MJD	Exp	S/N	RV _{helio}		RV _{err}	Source ^b
							(s)	4129 Å	(km s ⁻¹)	
J00002416–1107454	00 00 24.0	−11 07 44.4	12.0	58080.06763	3123	40	−106.81		0.21	S
J00023429–1924590	00 02 34.3	−19 24 59.0	10.9	58077.04492	1100	28	−100.36		0.22	R
J00041581–5815524	00 04 15.8	−58 15 52.5	10.9	58075.05943	1100	25	+184.69		0.27	R
J00062986–5049319	00 06 29.8	−50 49 30.0	10.5	58074.10377	906	42	+214.56		0.39	SH
J00093394–1857008	00 09 34.0	−18 57 01.1	11.2	58081.06715	1200	46	−67.34		0.23	R
J00154806–6253207	00 15 48.1	−62 53 20.7	11.0	58075.02570	1200	28	+204.55		0.44	R
J00172430–3333151	00 17 24.3	−33 33 15.1	12.2	57985.00459	1200	25	−17.33		0.28	R
J00182832–3900338	00 18 28.3	−39 00 32.4	11.2	58076.02986	1400	31	+346.12		0.21	R
J00223225–4839449	00 22 32.2	−48 39 43.2	11.1	58075.04273	1200	27	+243.54		0.20	R
J00374325–1204391	00 37 43.3	−12 04 39.2	11.1	57985.00459	800	35	−27.84		0.41	R
J00410929–0328595	00 41 09.1	−03 28 58.8	11.5	58075.07915	1600	32	−42.17		0.24	H
J00413026–4058547	00 41 30.3	−40 58 54.6	11.3	58077.06495	1540	36	+354.36		1.81	R

TABLE A.1 (CONTINUED)

Stellar ID	RA	Dec	<i>V</i> mag ^a	MJD	Exp	S/N	RV _{helio}	RV _{err}	Source ^b
J00442897–1017497	00 44 28.8	−10 17 49.2	10.8	58076.04883	1152	33	−2.74	0.16	H
J00452879–5846450	00 45 28.7	−58 46 45.1	10.6	58076.06452	900	32	+184.17	0.57	R
J00482431–1041309	00 48 24.2	−10 41 31.2	10.8	58077.02930	1000	32	−88.81	0.23	R
J00584386–3005576	00 58 43.7	−30 05 56.4	10.7	58077.08440	1000	49	+27.36	0.83	H
J01083959–2857013	01 08 39.6	−28 57 01.5	12.6	57985.00459	1010	20	+139.24	0.55	R
J01094330–5907230	01 09 43.2	−59 07 22.8	12.2	58078.07975	2700	32	+65.47	0.29	S
J01213447–2528002	01 21 34.5	−25 28 01.2	11.7	57985.00459	900	27	+33.17	0.26	R
J01265856+0135153	01 26 58.6	+01 35 13.2	12.7	58078.11736	3000	21	−221.38	0.92	H
J01311599–4016510	01 31 16.0	−40 16 51.2	11.1	57985.00459	800	35	−33.31	0.38	R
J01321981–3040512	01 32 19.8	−30 40 52.1	10.8	57985.00459	1000	43	−94.60	0.22	R
J01352315–0817533	01 35 23.2	−08 17 53.5	10.9	58080.09427	900	36	+84.45	0.30	R
J01371888–1729037	01 37 19.0	−17 29 02.4	9.7	58077.09636	400	38	−204.31	0.55	D
J01373857–2618131	01 37 38.6	−26 18 13.3	11.4	57985.00459	683	20	−91.61	0.53	S
J01425232–4657481	01 42 52.3	−46 57 48.5	11.2	58081.08651	1006	40	+131.29	0.16	RS
J01425445–0904162	01 42 54.5	−09 04 15.6	9.6	58081.09799	400	44	−60.18	0.19	M
J01451383–4302313	01 45 13.8	−43 02 31.3	12.2	58081.11611	2193	36	+114.91	0.15	R

TABLE A.1 (CONTINUED)

Stellar ID	RA	Dec	<i>V</i> mag ^a	MJD	Exp	S/N	RV _{helio}	RV _{err}	Source ^b
J01493760–4551222	01 49 37.6	−45 51 22.3	10.4	57985.00459	700	26	+66.11	0.51	RH
J02070641–5009166	02 07 06.4	−50 09 16.6	11.2	57985.00459	654	21	+109.52	0.28	R
J02212400–4056480	02 21 24.0	−40 56 48.0	13.8	58078.15299	2400	18	−80.50	0.29	S
J02215117–5933316	02 21 51.1	−59 33 32.4	11.7	58079.10877	1800	33	+14.69	0.29	H
J02215557–5410143	02 21 55.6	−54 10 14.4	10.4	57985.00459	456	29	+128.94	0.85	R
J02215793–2130429	02 21 57.8	−21 30 43.2	10.5	58080.11086	700	48	+104.89	0.13	R
J02230804–3129531	02 23 07.9	−31 29 52.8	11.5	58080.13146	1600	42	+62.55	0.44	R
J02265832–0749596	02 26 58.4	−07 49 59.7	10.5	57985.00459	800	42	−39.47	0.22	R
J02275765–4808083	02 27 57.8	−48 08 09.4	11.3	57985.00459	714	35	+33.56	0.80	R
J02515281–3717316	02 51 52.8	−37 17 31.6	10.4	57985.00459	800	39	+35.04	0.31	R
J02515281–3717316	02 51 52.8	−37 17 31.6	10.4	57985.00459	800	39	+35.04	0.31	R
J02570028–3024374	02 57 00.2	−30 24 36.0	10.3	58081.15912	691	57	+106.21	0.24	R
J03142084–1035112	03 14 20.9	−10 35 09.6	12.7	58080.19114	3600	29	+241.24	0.10	H
J03190629–0819306	03 19 06.2	−08 19 30.0	11.1	58079.18352	1000	34	+293.47	0.61	R
J03210882–3944213	03 21 08.9	−39 44 20.4	10.8	58079.23196	2400	43	+97.31	0.26	R
J03362087–4830299	03 36 20.9	−48 30 30.0	12.9	57985.00459	832	16	+142.02	0.38	S

TABLE A.1 (CONTINUED)

Stellar ID	RA	Dec	<i>V</i> mag ^a	MJD	Exp	S/N	RV _{helio}	RV _{err}	Source ^b
J03422816–6500355	03 42 28.2	−65 00 35.8	11.0	58081.17478	1400	37	+113.58	0.21	R
J03425812–3047217	03 42 58.1	−30 47 21.9	10.9	57985.00459	500	30	+296.96	0.62	R
J04012191–2635058	04 01 21.8	−26 35 06.0	10.6	58078.17787	600	45	+7.37	0.41	H
J04014897–3757533	04 01 49.0	−37 57 53.4	11.6	57985.00459	800	29	+156.55	0.17	R
J04182158–2323391	04 18 21.6	−23 23 38.4	10.1	58081.19374	600	44	+50.40	0.26	R
J04263084–4058516	04 26 30.8	−40 58 51.7	12.1	58078.19383	1587	31	+122.72	0.26	R
J04315411–0632100	04 31 54.1	−06 32 11.2	11.3	58081.20728	1108	41	+209.37	0.27	R
J04350131–0959363	04 35 01.2	−09 59 34.8	13.0	58078.23106	3000	28	+193.93	0.12	SH
J04411241–6518438	04 41 12.5	−65 18 44.4	...	58081.22080	600	52	+288.28	1.27	R
J04520910–6209121	04 52 09.2	−62 09 12.2	10.2	58080.21959	600	38	+164.78	0.41	RS
J05311779–5810048	05 31 17.8	−58 10 04.7	12.4	58080.23988	2400	29	+129.19	0.31	R
J05381700–7516207	05 38 17.0	−75 16 20.6	11.2	58081.26521	1934	22	+58.73	0.34	R
J05383296–5904280	05 38 33.0	−59 04 28.0	...	58081.28257	600	56	+189.02	0.37	R
J05514213–3327337	05 51 42.1	−33 27 33.8	11.8	58079.29115	3000	20	+103.68	0.16	R
J05521578–3953184	05 52 15.8	−39 53 18.6	11.5	58080.26635	1600	38	+104.12	0.29	R
J05564771–6639054	05 56 47.8	−66 39 05.0	10.1	58081.29338	700	40	+201.58	0.33	R

TABLE A.1 (CONTINUED)

Stellar ID	RA	Dec	<i>V</i> mag ^a	MJD	Exp	S/N	RV _{helio}	RV _{err}	Source ^b
J06014757–5951510	06 01 47.6	−59 51 51.4	10.3	58080.28231	600	46	+246.53	0.22	R
J06055404–3306288	06 05 54.0	−33 06 29.0	13.2	58081.32967	2501	19	+157.40	0.29	R
J06090353–7122260	06 09 03.6	−71 22 26.0	11.2	58078.25958	1200	27	+186.94	0.74	R
J06195001–5312114	06 19 50.0	−53 12 11.7	11.4	58078.27529	993	35	+130.70	0.33	R
J06290787–6709523	06 29 07.9	−67 09 52.4	12.4	58080.30953	3600	23	+67.10	0.49	R
J06320130–2026538	06 32 01.2	−20 26 52.8	10.0	58080.33765	500	47	+109.82	0.35	R
J06332771–3519240	06 33 27.8	−35 19 25.1	11.5	57822.06214	1501	46	+190.97	0.15	R
J06401317–3540444	06 40 13.1	−35 40 44.0	12.1	57821.07370	3067	52	+138.18	0.12	R
J06420823–5116448	06 42 08.1	−51 16 44.0	11.1	58078.29254	1513	47	+15.43	0.27	R
J06592949–5406125	06 59 29.4	−54 06 12.0	11.7	57818.01264	1800	36	+311.14	0.13	R
J07052028–3343242	07 05 20.3	−33 43 24.2	11.7	57818.04772	3600	70	+399.39	0.09	R
J07103110–7121522	07 10 31.2	−71 21 51.5	10.9	58081.33733	2000	32	+247.88	0.43	R
J07123398–4814049	07 12 33.9	−48 14 04.0	11.6	57820.07360	1800	34	+353.16	0.13	R
J07161594–5135248	07 16 15.9	−51 35 24.9	10.1	57818.07437	400	35	+311.33	0.08	R
J07202253–3358518	07 20 22.6	−33 58 52.0	10.8	57818.08385	700	46	+74.98	0.12	R
J07265723–5647500	07 26 57.2	−56 47 50.5	12.3	58079.33009	3000	23	+71.75	0.62	R

TABLE A.1 (CONTINUED)

Stellar ID	RA	Dec	<i>V</i> mag ^a	MJD	Exp	S/N	RV _{helio}	RV _{err}	Source ^b
J07352232–4425010	07 35 22.4	−44 25 02.1	10.7	57818.09539	800	54	+177.92	0.08	R
J07393021–5548171	07 39 30.2	−55 48 17.2	...	57818.10662	500	29	+333.67	0.09	R
J07411443–4339360	07 41 14.5	−43 39 35.5	11.1	57822.08183	1200	45	+475.50	0.05	R
J07482433–4831405	07 48 24.3	−48 31 40.4	11.3	57819.06302	1500	37	+314.12	0.22	R
J07501424–4123454	07 50 14.2	−41 23 45.1	11.1	57822.09901	1200	37	+400.60	0.07	R
J08015897–5752032	08 01 59.0	−57 52 02.8	10.3	57820.11631	600	31	+139.75	0.06	R
J08032084–5856521	08 03 20.8	−58 56 52.3	11.2	57822.11678	1298	37	+130.62	0.10	R
J08134364–2332528	08 13 43.7	−23 32 52.8	11.0	58079.85258	1847	44	+129.90	0.26	R
J08155667–2204105	08 15 56.7	−22 04 10.8	11.4	57820.10080	1500	48	+263.58	0.06	R
J08311233–6013195	08 31 12.4	−60 13 19.5	11.0	57819.08080	1000	28	+441.53	0.09	R
J08393460–2122069	08 39 34.6	−21 22 07.6	10.5	57818.11722	700	50	+140.53	0.06	R
J08594093–1415151	08 59 40.9	−14 15 15.1	11.9	57818.14538	3600	53	+383.58	0.05	R
J09214783–0214582	09 21 47.8	−02 14 58.4	10.7	57819.09478	800	31	+87.10	0.06	R
J09255655–3450373	09 25 56.6	−34 50 37.5	11.5	57894.96311	1800	16	+203.06	0.39	R
J09261133–1526232	09 26 11.3	−15 26 23.2	10.7	57821.10107	1000	55	+386.19	0.08	R
J09284944–0738585	09 28 49.5	−07 38 58.5	11.0	57822.15905	1000	32	+129.86	0.06	R

TABLE A.1 (CONTINUED)

Stellar ID	RA	Dec	<i>V</i> mag ^a	MJD	Exp	S/N	RV _{helio}	RV _{err}	Source ^b
J09310102–0304052	09 31 01.0	−03 04 05.0	10.5	57818.18263	700	49	+122.02	0.20	R
J09364069–2038386	09 36 40.7	−20 38 38.8	10.5	57818.19310	600	45	+273.76	0.07	R
J09471921–4127042	09 47 19.2	−41 27 04.0	7.9	57820.12775	800	147	+79.96	0.13	R
J09574607–3923072	09 57 46.1	−39 23 07.3	11.1	57821.11650	1200	48	+127.44	0.09	R
J10025125–4331098	10 02 51.2	−43 31 09.9	13.2	57895.02066	4500	16	+233.46	1.53	BS
J10080064–1008523	10 08 00.6	−10 08 52.0	10.7	57819.12613	1800	55	+145.60	0.09	R
J10082492–2314124	10 08 24.9	−23 14 12.3	10.9	57818.20447	900	49	+131.58	0.06	R
J10121964–3221347	10 12 19.6	−32 21 34.0	11.1	57819.14706	1200	43	+363.48	0.18	R
J10162157–2959521	10 16 21.5	−29 59 52.0	11.7	57822.14043	1700	49	+406.74	0.08	R
J10174884–4818125	10 17 48.8	−48 18 12.0	12.2	57820.14248	1200	27	+198.14	0.27	R
J10191573–1924464	10 19 15.7	−19 24 46.4	11.2	57821.15172	1200	36	+84.28	0.05	R
J10194932–4900584	10 19 49.3	−49 00 58.3	11.7	57822.20572	1689	36	+261.40	0.07	R
J10251539–3554026	10 25 15.4	−35 54 03.6	10.8	57892.99330	900	20	+248.87	0.45	R
J10302845–7543299	10 30 28.4	−75 43 29.0	11.5	57894.98408	1200	12	+263.78	0.54	R
J10344785–4823544	10 34 47.9	−48 23 54.5	11.6	57819.16783	1800	46	+274.43	0.13	R
J10345348–1117221	10 34 53.5	−11 17 22.1	10.9	57822.23440	1204	36	+185.34	0.07	R

TABLE A.1 (CONTINUED)

Stellar ID	RA	Dec	<i>V</i> mag ^a	MJD	Exp	S/N	RV _{helio}	RV _{err}	Source ^b
J10362687–3746174	10 36 26.9	−37 46 19.2	11.1	57893.95780	900	12	+143.95	0.99	R
J10401894–4106124	10 40 18.9	−41 06 12.8	11.3	57821.13413	1400	51	−31.80	0.15	R
J10540994–1347522	10 54 09.8	−13 47 52.8	12.8	57893.98725	3600	16	+180.23	0.77	H
J10550634–1908359	10 55 06.2	−19 08 34.8	12.9	57893.02632	3600	18	+14.23	0.58	H
J10563033–3428423	10 56 30.3	−34 28 42.0	12.1	57819.18831	1200	26	+243.87	0.25	R
J10581140–2634179	10 58 11.4	−26 34 18.1	10.3	57818.21647	600	40	+117.59	0.04	R
J11014865–3749526	11 01 48.7	−37 49 52.6	11.0	57818.22997	1200	36	+260.88	0.09	R
J11142319–3208509	11 14 23.2	−32 08 50.8	10.7	57819.20226	800	38	+328.19	0.08	R
J11265122–1805295	11 26 51.3	−18 05 29.0	11.2	57819.21877	1500	65	+89.87	0.10	R
J11301705–1449325	11 30 17.0	−14 49 32.7	11.7	57820.16193	1600	46	−28.21	0.18	R
J11325299–2913137	11 32 53.0	−29 13 13.7	10.8	57819.28669	800	36	+72.28	0.05	R
J11370170–5401298	11 37 01.7	−54 01 30.0	10.8	57819.24545	800	25	+111.86	0.06	R
J11373800–5202251	11 37 38.0	−52 02 24.9	11.8	57822.26749	1674	36	+300.57	0.11	R
J11404726–0833030	11 40 47.3	−08 33 03.2	10.7	57821.18023	750	51	+172.22	0.10	R
J11404944–1615396	11 40 49.4	−16 15 39.6	10.7	57821.16887	800	45	+174.97	0.08	R
J11444480–1128167	11 44 44.7	−11 28 16.0	...	57821.19660	400	59	+162.15	0.29	R

TABLE A.1 (CONTINUED)

Stellar ID	RA	Dec	<i>V</i> mag ^a	MJD	Exp	S/N	RV _{helio}	RV _{err}	Source ^b
J11515010–0545441	11 51 50.1	−05 45 44.6	8.1	57818.27185	150	38	+234.22	0.17	R
J12044314–2911051	12 04 43.2	−29 11 06.0	9.2	57895.05280	300	17	+25.49	0.23	M
J12050944–1204531	12 05 09.4	−12 04 53.2	10.1	57822.24766	600	39	+116.09	0.07	R
J12062488–4741150	12 06 24.9	−47 41 14.9	11.1	57895.06525	1200	14	+136.99	1.24	R
J12070990–3653243	12 07 09.9	−36 53 24.5	10.1	57821.20523	500	38	+138.72	0.05	R
J12100070–3130359	12 10 00.7	−31 30 36.0	10.7	57822.28569	956	47	+335.42	0.08	RH
J12102259–4902190	12 10 22.6	−49 02 19.3	10.3	57818.27970	600	19	+247.28	0.07	R
J12170912–2721034	12 17 09.1	−27 21 03.6	12.1	57895.08941	2400	16	+301.50	0.83	H
J12192034–1721547	12 19 20.3	−17 21 54.0	12.1	57894.03746	3600	21	−75.34	0.35	R
J12232106–5305536	12 23 21.1	−53 05 53.4	10.5	57818.29191	700	24	+266.08	0.08	R
J12341308–3149577	12 34 13.1	−31 49 58.4	10.2	57819.32186	600	51	+205.90	0.04	R
J12405721–4051430	12 40 57.2	−40 51 43.3	11.2	57821.23027	1200	48	+247.33	0.16	R
J12424489–1315032	12 42 44.8	−13 15 03.0	10.3	57820.24560	500	65	−7.81	0.18	R
J12535742–3801355	12 53 57.4	−38 01 35.0	10.9	57818.30473	1000	46	+172.82	0.13	R
J12571667–4335318	12 57 16.7	−43 35 31.6	10.5	57820.25497	600	49	+136.67	0.10	R
J12572833–5125217	12 57 28.3	−51 25 21.7	11.9	57821.25217	2099	35	+41.62	0.22	R

TABLE A.1 (CONTINUED)

Stellar ID	RA	Dec	<i>V</i> mag ^a	MJD	Exp	S/N	RV _{helio}	RV _{err}	Source ^b
J13085850–2712188	13 08 58.5	−27 12 18.9	13.0	57820.23438	1000	16	+111.10	0.21	R
J13101305–3342369	13 10 13.1	−33 42 36.9	10.9	57818.31885	1000	36	+30.24	0.08	R
J13214178–4320055	13 21 41.8	−43 20 05.5	11.4	57821.28414	1102	38	+201.63	0.09	R
J13241428–1806211	13 24 14.2	−18 06 21.0	11.5	57820.28893	2400	64	−44.62	0.18	RH
J13315746–1929446	13 31 57.5	−19 29 44.5	10.6	57822.29866	800	49	−1.29	0.04	R
J13330890–4654079	13 33 08.9	−46 54 07.9	12.5	57821.30725	2400	32	−15.90	0.46	BS
J13335283–2623539	13 33 52.8	−26 23 53.0	11.1	57820.31262	1200	61	+62.39	0.10	R
J13421261–1417354	13 42 12.6	−14 17 35.5	10.2	57820.32500	500	36	+159.75	0.09	R
J13530579–4438041	13 53 05.8	−44 38 04.0	12.2	57820.34541	2626	47	−21.43	0.35	RS
J13573542–3032486	13 57 35.4	−30 32 48.0	12.5	57818.33441	1200	25	−26.83	0.20	R
J14030859–3214014	14 03 08.6	−32 14 01.4	11.0	57820.36802	1000	40	+190.88	0.09	R
J14032900–5250429	14 03 29.0	−52 50 42.0	10.6	57895.10913	400	13	+111.24	0.23	R
J14091000–3013572	14 09 10.0	−30 13 57.7	10.7	57819.33436	800	51	+48.65	0.11	R
J14155955–3219255	14 15 59.6	−32 19 25.5	11.5	57895.12702	2069	15	−162.59	0.20	RM
J14165685+1215598	14 16 56.9	+12 15 59.8	12.9	57894.10118	4500	18	−87.15	0.82	B
J14180866–2842077	14 18 08.7	−28 42 07.9	10.7	57818.34850	800	36	+171.49	0.15	R

TABLE A.1 (CONTINUED)

Stellar ID	RA	Dec	<i>V</i> mag ^a	MJD	Exp	S/N	RV _{helio}	RV _{err}	Source ^b
J14254628–1546301	14 25 46.3	−15 46 30.2	10.9	57820.38971	900	33	+14.24	0.17	R
J14283907–2044594	14 28 39.1	−20 44 59.5	10.6	57821.35007	600	43	+51.64	0.18	R
J14354680–1124122	14 35 46.8	−11 24 12.3	10.1	57821.34193	400	37	−16.85	0.16	R
J14392683–1949132	14 39 26.8	−19 49 13.0	11.3	57818.38764	1400	37	+84.29	0.21	R
J14435196–2106283	14 43 52.0	−21 06 28.2	10.9	57819.36272	1000	38	+29.81	0.06	R
J14533307–4428301	14 53 33.1	−44 28 30.1	10.9	57819.37776	1000	45	+53.89	0.25	RS
J14560449–3950349	14 56 04.5	−39 50 34.7	11.1	57821.38213	1200	37	−3.37	0.19	R
J14592981–3852558	14 59 29.8	−38 52 56.0	11.1	57821.33048	1100	36	+300.95	0.11	R
J15023852–4602066	15 02 38.5	−46 02 06.6	11.1	57821.36366	1200	45	−32.06	0.25	R
J15062866–1428038	15 06 28.6	−14 28 04.0	11.3	57822.32766	1201	42	+3.16	0.25	R
J15141994–4359554	15 14 19.9	−43 59 55.3	11.7	57895.19105	2400	11	+148.50	0.97	R
J15155734–1054220	15 15 57.4	−10 54 22.1	11.0	57822.31208	993	41	+145.02	0.04	R
J15230675–7930072	15 23 06.7	−79 30 07.3	13.2	57894.17468	4500	16	+125.42	0.77	B
J15293404–3906241	15 29 34.1	−39 06 25.2	11.4	57895.22589	3097	14	+154.28	0.48	M
J15320193–2211091	15 32 01.9	−22 11 09.3	12.1	57985.00459	900	22	+308.61	0.97	R
J15360493+0247300	15 36 04.9	+02 47 30.0	12.7	57894.23740	4500	16	−20.03	0.23	B

TABLE A.1 (CONTINUED)

Stellar ID	RA	Dec	<i>V</i> mag ^a	MJD	Exp	S/N	RV _{helio}	RV _{err}	Source ^b
J15573010–2939228	15 57 30.1	−29 39 22.7	13.1	57893.23442	3600	16	+123.03	0.84	BS
J15582703–1136532	15 58 27.0	−11 36 53.3	10.4	57822.34808	700	30	−248.84	0.06	R
J16064231–1632461	16 06 42.3	−16 32 46.1	...	57822.33961	400	35	−185.30	0.09	RM
J16122832–0848083	16 12 28.3	−08 48 08.4	10.6	57985.00459	1000	35	−1.94	0.23	R
J16285613–1014576	16 28 56.1	−10 14 57.7	10.5	57822.36005	800	47	+60.45	0.15	R
J16524315–6719521	16 52 43.1	−67 19 52.2	12.9	57893.28977	3600	18	+90.67	0.71	B
J17013206–5507454	17 01 32.1	−55 07 45.7	13.4	57985.00459	1071	13	+33.07	0.59	B
J17383643–5358288	17 38 36.4	−53 58 28.8	11.1	57822.38750	908	30	+20.20	0.18	R
J17405736–5339473	17 40 57.4	−53 39 47.4	...	57985.00459	900	29	+23.36	0.60	R
J18050641–4907579	18 05 06.4	−49 07 58.0	11.1	57985.00459	780	21	+162.66	0.30	R
J18272347–5133001	18 27 23.5	−51 33 00.2	10.9	57895.32768	2400	13	−73.69	0.22	R
J18114680–2126085	18 11 46.8	−21 26 09.0	9.7	57985.00459	600	40	+77.38	0.28	R
J18301354–4555101	18 30 13.6	−45 55 10.1	12.1	57894.29405	3290	21	+60.15	0.28	R
J19050116–1949280	19 05 01.2	−19 49 28.4	10.2	57985.00459	1200	56	+95.31	0.35	R
J19175585–5440147	19 17 55.8	−54 40 14.0	10.8	57985.00459	780	38	+48.08	0.54	R
J19232941–4425432	19 23 29.4	−44 25 43.5	11.1	57985.00459	800	23	+258.81	0.28	R

TABLE A.1 (CONTINUED)

Stellar ID	RA	Dec	<i>V</i> mag ^a	MJD	Exp	S/N	RV _{helio}	RV _{err}	Source ^b
J19345326–3236567	19 34 53.3	−32 36 57.0	11.1	57985.00459	520	28	+206.14	0.32	R
J19441170–3526278	19 44 11.7	−35 26 28.3	10.4	57985.00459	500	28	+59.16	0.28	R
J19445483–4039459	19 44 54.7	−40 39 46.8	10.6	58019.01533	1400	52	+92.74	0.30	R
J19451414–1729269	19 45 14.1	−17 29 27.9	9.2	57985.00459	450	60	+46.23	0.80	R
J19510180–6331111	19 51 01.8	−63 31 11.1	10.5	58019.03464	1000	36	+254.49	0.33	R
J19584974–1812109	19 58 49.7	−18 12 10.8	...	57894.33395	300	18	−121.26	0.34	D
J20000364–3301351	20 00 03.6	−33 01 35.3	11.3	58019.05892	2400	39	−58.36	0.15	R
J20005766–2541488	20 00 57.6	−25 41 49.1	10.9	58019.10853	1600	48	+150.37	0.18	R
J20080083–2759265	20 08 00.8	−27 59 26.6	10.9	57985.00459	876	32	−82.24	0.46	R
J20100948–4408274	20 10 09.5	−44 08 27.5	12.8	57985.00459	1200	20	+1.77	0.30	B
J20103193–3558546	20 10 31.9	−35 58 54.7	11.4	58021.00083	1600	43	+124.94	0.30	R
J20152296–3740178	20 15 22.9	−37 40 18.2	11.8	57985.00459	753	24	−19.42	0.27	R
J20194310–3158163	20 19 43.1	−31 58 16.7	11.2	58020.01044	1600	58	−130.00	0.30	R
J20233743–1659533	20 23 37.4	−16 59 53.5	11.7	58020.03586	2189	51	−141.72	0.23	R
J20302849–4531164	20 30 28.5	−45 31 16.8	10.1	57894.38071	500	16	−1.52	0.40	R
J20305648–3446521	20 30 56.5	−34 46 52.2	10.9	57985.00459	1200	34	−13.82	0.22	R

TABLE A.1 (CONTINUED)

Stellar ID	RA	Dec	<i>V</i> mag ^a	MJD	Exp	S/N	RV _{helio}	RV _{err}	Source ^b
J20411424–4654315	20 41 14.2	−46 54 31.5	...	57894.40613	3323	17	−64.47	0.33	R
J20435776–4408037	20 43 57.8	−44 08 02.4	11.4	58021.02347	1699	29	+42.09	0.25	R
J20453454–1431151	20 45 34.5	−14 31 15.3	10.7	58020.05788	1010	56	−74.25	0.21	R
J20504869–3355289	20 50 48.7	−33 55 28.9	11.1	58022.01645	1300	47	−153.72	0.22	R
J20554594–3155159	20 55 45.9	−31 55 16.0	10.8	57985.00459	508	31	−151.07	0.19	R
J21003824–0539171	21 00 38.2	−05 39 17.2	10.8	58021.04304	1000	35	−113.59	0.37	R
J21055865–4919336	21 05 58.7	−49 19 33.7	10.9	58020.07484	1102	37	+207.72	0.19	R
J21080151–6555366	21 08 01.4	−65 55 37.2	...	58020.09119	1098	29	+81.27	0.27	R
J21103411–6331354	21 10 34.2	−63 31 36.3	10.8	58022.03397	1013	46	−122.35	0.23	R
J21314253–1459110	21 31 42.5	−14 59 11.2	12.1	57985.00459	1109	24	+11.39	0.30	R
J21402305–1227035	21 40 23.0	−12 27 03.6	11.0	58019.13698	1400	39	−127.50	0.23	H
J21462219–0512324	21 46 22.2	−05 12 32.4	10.7	58022.04924	900	40	−310.46	0.25	L
J22115488–2847382	22 11 54.9	−28 47 38.3	10.4	57985.00459	813	40	−128.54	0.63	R
J22125424–0235414	22 12 54.3	−02 35 42.0	12.2	57985.00459	900	25	−103.40	0.40	R
J22161170–5319492	22 16 11.7	−53 19 49.4	10.9	57985.00459	714	38	+88.90	1.71	R
J22190836–2333467	22 19 08.3	−23 33 46.8	10.9	58020.10816	1100	55	−41.70	0.23	R

TABLE A.1 (CONTINUED)

Stellar ID	RA	Dec	<i>V</i> mag ^a	MJD	Exp	S/N	RV _{helio}	RV _{err}	Source ^b
J22223324–1314488	22 22 33.2	−13 14 49.0	10.8	57985.00459	600	29	+26.96	0.25	R
J22233596–5301145	22 23 36.0	−53 01 14.8	10.0	57985.00459	1003	40	+146.88	0.26	R
J22371623–1608005	22 37 16.3	−16 08 01.4	10.6	58019.15677	1181	61	−0.74	0.34	R
J22372037–4741375	22 37 20.4	−47 41 37.5	12.4	57985.00459	1109	21	−138.25	0.26	RH
J22373316–4341181	22 37 33.1	−43 41 18.5	11.0	58020.12455	1100	52	−11.16	0.23	R
J22585069–3923437	22 58 50.7	−39 23 43.7	12.9	57985.00459	800	19	−55.60	0.40	B
J23060975–6107368	23 06 09.8	−61 07 36.8	11.0	58074.02543	1200	34	+54.28	0.33	RH
J23181358–6252270	23 18 13.5	−62 52 27.1	11.1	58074.05629	1200	33	+188.70	0.40	R
J23242766–2728055	23 24 27.6	−27 28 04.8	10.6	58019.18943	1200	52	−133.11	0.26	R
J23254164–2356206	23 25 41.6	−23 56 20.9	10.1	58074.06961	500	38	+74.19	0.21	RM
J23285061–0432368	23 28 50.6	−04 32 34.8	11.5	58074.08497	1504	31	−34.94	0.34	H
J2330336–4437127	23 33 03.4	−44 37 13.1	10.0	57985.00459	1200	74	+94.53	0.29	RH
J23342332–2748003	23 34 23.3	−27 48 00.3	12.6	58078.03508	3600	28	−50.35	0.35	R
J23425814–4327352	23 42 58.1	−43 27 35.2	11.4	58081.02092	1600	46	+48.53	0.22	R
J23434113–6019223	23 43 41.1	−60 19 22.6	12.9	58079.02857	3170	22	+208.99	2.13	SH
J23475942–5701184	23 47 59.4	−57 01 18.6	11.7	58081.04474	2000	35	+40.74	0.31	R

TABLE A.1 (CONTINUED)

Stellar ID	RA	Dec	<i>V</i> mag ^a	MJD	Exp	S/N	RV _{helio}	RV _{err}	Source ^b
J23490902–2447176	23 49 09.1	–24 47 17.4	12.1	58080.03000	2700	44	–164.58	0.22	R
J23552837+0421179	23 55 28.4	+04 21 18.0	9.9	57985.00459	1000	55	–217.70	0.41	L

^aRAVE DR5 *V* magnitudes are from [Munari et al. \(2014\)](#), B&B are from [Henden et al. \(2015\)](#).

^bR: RAVE ([Kordopatis et al. 2013](#); [Kunder et al. 2017](#)), B: B&B ([Schlaufman and Casey 2014](#)), L: LAMOST ([Deng et al. 2012](#)), S: SkyMapper ([Wolf et al. 2018](#)), M: [Meléndez et al. \(2016\)](#), H: Hamburg/ESO ([Christlieb et al. 2008](#)), D: SAGA Database ([Suda et al. 2017](#)).

TABLE A.2
MODEL ATMOSPHERIC PARAMETERS

Stellar ID	T_{eff}	$\log g$	[Fe/H]	$\sigma_{[\text{Fe}/\text{H}]}$	$N_{\text{Fe I}}$	$N_{\text{Fe II}}$	ξ
	(K)	(cgs)					(km s $^{-1}$)
J00002416–1107454	4693	1.37	−2.40	0.12	90	26	2.11
J00023429–1924590	4400	1.15	−2.22	0.14	32	15	2.97
J00041581–5815524	4375	1.50	−2.32	0.17	30	12	2.81
J00062986–5049319	4647	0.75	−2.59	0.15	86	27	2.36
J00093394–1857008	4815	1.78	−1.85	0.14	115	27	1.56
J00154806–6253207	4725	1.78	−2.30	0.15	60	16	2.09
J00172430–3333151	4764	1.73	−2.29	0.13	69	16	2.02
J00182832–3900338	4639	1.34	−1.75	0.13	60	17	2.09
J00223225–4839449	4648	1.40	−1.75	0.15	102	21	2.15
J00374325–1204391	4695	1.31	−2.40	0.13	98	23	1.98
J00410929–0328595	4898	1.78	−2.53	0.15	84	15	2.21
J00413026–4058547	4605	1.19	−2.57	0.17	78	22	2.17
J00442897–1017497	4672	1.31	−2.35	0.15	101	24	2.07
J00452879–5846450	4754	1.27	−2.22	0.16	96	26	2.02
J00482431–1041309	4764	1.08	−2.45	0.15	83	26	2.43
J00584386–3005576	4833	1.65	−3.50	0.15	78	12	1.50
J01083959–2857013	4936	2.01	−2.84	0.13	49	9	1.39
J01094330–5907230	4714	1.13	−2.46	0.15	80	27	2.03
J01213447–2528002	4551	1.05	−2.61	0.14	79	21	2.33
J01265856+0135153	4355	0.52	−3.39	0.20	33	11	2.11
J01311599–4016510	4824	1.63	−2.17	0.13	97	23	2.05
J01321981–3040512	5175	2.87	−2.13	0.12	101	22	1.57

TABLE A.2 (CONTINUED)

Stellar ID	T _{eff}	log <i>g</i>	[Fe/H]	$\sigma_{\text{[Fe/H]}}$	<i>N</i> Fe I	<i>N</i> Fe II	ξ
J01352315–0817533	4733	1.52	−2.06	0.14	84	24	1.77
J01371888–1729037	4381	0.66	−2.55	0.15	68	23	2.82
J01373857–2618131	4579	1.03	−2.80	0.15	51	13	2.09
J01425232–4657481	5126	2.60	−2.04	0.14	100	19	1.67
J01425445–0904162	4662	1.59	−1.73	0.14	156	24	1.98
J01451383–4302313	4910	1.83	−2.09	0.15	105	23	1.97
J01493760–4551222	4965	1.50	−2.72	0.10	49	16	2.50
J02070641–5009166	4526	0.98	−2.15	0.14	46	16	2.68
J02212400–4056480	4797	0.94	−2.52	0.15	46	16	1.93
J02215117–5933316	5119	2.85	−2.68	0.16	77	13	2.58
J02215557–5410143	5842	3.53	−2.09	0.13	85	18	1.54
J02215793–2130429	4806	1.50	−1.98	0.12	87	18	1.83
J02230804–3129531	4757	1.52	−1.82	0.16	111	26	1.93
J02265832–0749596	5088	2.74	−1.94	0.11	100	22	1.66
J02275765–4808083	5884	3.58	−2.80	0.16	67	7	1.60
J02515281–3717316	4660	0.83	−2.33	0.13	82	22	2.27
J02570028–3024374	4833	1.84	−2.09	0.13	106	23	1.44
J03142084–1035112	4769	1.15	−3.75	0.12	37	7	2.11
J03190629–0819306	4751	1.45	−2.24	0.14	94	24	1.84
J03210882–3944213	4671	1.18	−1.91	0.16	149	32	2.24
J03362087–4830299	4948	2.12	−2.75	0.14	44	15	1.52
J03422816–6500355	4976	2.29	−2.16	0.13	143	25	2.05
J03425812–3047217	5381	1.66	−2.35	0.12	52	19	1.64
J04012191–2635058	4856	1.93	−2.17	0.13	104	27	1.78
J04014897–3757533	4797	1.02	−2.28	0.13	97	23	2.32

TABLE A.2 (CONTINUED)

Stellar ID	T _{eff}	log <i>g</i>	[Fe/H]	$\sigma_{\text{[Fe/H]}}$	<i>N</i> Fe I	<i>N</i> Fe II	ξ
J04182158–2323391	4633	1.37	−1.76	0.15	92	27	1.86
J04263084–4058516	4612	1.37	−2.43	0.15	72	18	2.00
J04315411–0632100	5274	3.39	−2.18	0.13	83	13	1.28
J04350131–0959363	4839	1.80	−2.87	0.14	70	14	2.57
J04411241–6518438	5008	2.36	−2.47	0.12	85	16	1.45
J04420818–3421138	5005	2.12	−1.94	0.15	49	18	1.99
J04520910–6209121	4623	1.15	−2.78	0.12	67	17	2.15
J05311779–5810048	5141	2.58	−2.33	0.11	65	21	1.78
J05381700–7516207	4968	2.08	−1.83	0.13	85	20	1.91
J05383296–5904280	5824	2.03	−2.53	0.14	69	18	2.84
J05514213–3327337	4718	1.62	−2.42	0.15	36	15	2.04
J05521578–3953184	4705	1.55	−2.34	0.15	89	21	2.00
J05564771–6639054	4711	1.67	−2.01	0.13	82	21	1.89
J06014757–5951510	5274	3.18	−2.08	0.12	91	20	1.61
J06055404–3306288	5354	2.68	−1.93	0.15	65	13	2.08
J06090353–7122260	4878	1.51	−2.73	0.11	63	13	1.94
J06195001–5312114	5212	3.04	−2.06	0.13	87	19	1.59
J06290787–6709523	4616	1.05	−2.73	0.15	63	15	2.81
J06320130–2026538	5067	2.52	−1.56	0.11	147	23	1.63
J06332771–3519240	5224	3.15	−1.84	0.14	108	22	1.33
J06401317–3540444	4942	2.26	−2.38	0.14	102	18	1.21
J06420823–5116448	4707	1.40	−2.64	0.12	83	18	1.79
J06592949–5406125	4887	1.89	−1.86	0.11	87	24	1.96
J07052028–3343242	4802	1.52	−2.37	0.13	155	20	1.80
J07103110–7121522	5167	2.94	−1.47	0.11	80	18	1.75

TABLE A.2 (CONTINUED)

Stellar ID	T _{eff}	log <i>g</i>	[Fe/H]	$\sigma_{\text{[Fe/H]}}$	<i>N</i> Fe I	<i>N</i> Fe II	ξ
J07123398–4814049	4490	0.86	−3.03	0.15	118	24	2.37
J07161594–5135248	4575	1.15	−1.86	0.15	159	29	2.06
J07202253–3358518	5040	2.22	−1.60	0.12	138	26	1.78
J07265723–5647500	4916	1.95	−1.93	0.13	67	15	1.90
J07352232–4425010	5245	3.06	−1.58	0.11	141	18	1.30
J07393021–5548171	4426	1.39	−1.74	0.15	135	24	2.37
J07411443–4339360	4974	2.18	−1.87	0.10	69	20	1.39
J07482433–4831405	5329	1.46	−2.10	0.10	87	21	1.90
J07501424–4123454	5021	2.21	−1.87	0.14	97	30	1.80
J08015897–5752032	4622	1.24	−1.72	0.11	60	27	2.11
J08032084–5856521	5158	2.75	−1.73	0.14	95	22	1.57
J08134364–2332528	4836	1.33	−1.72	0.15	79	32	2.03
J08155667–2204105	4877	1.95	−1.82	0.14	133	33	1.71
J08311233–6013195	5153	2.44	−1.47	0.12	103	29	1.79
J08393460–2122069	4779	1.66	−1.94	0.12	172	25	1.98
J08594093–1415151	4876	2.04	−1.46	0.14	152	22	1.82
J09214783–0214582	4788	1.59	−1.99	0.12	101	25	1.94
J09255655–3450373	4619	1.55	−1.80	0.14	77	22	2.04
J09261133–1526232	5004	2.19	−1.69	0.14	112	26	1.80
J09284944–0738585	4760	2.02	−1.23	0.14	92	22	1.76
J09310102–0304052	6026	3.80	−1.70	0.14	93	23	1.48
J09364069–2038386	4778	1.71	−1.78	0.14	158	19	1.95
J09471921–4127042	4680	0.83	−2.67	0.16	85	24	2.39
J09574607–3923072	4903	1.64	−1.69	0.14	99	24	2.28
J10025125–4331098	4788	0.94	−2.87	0.14	53	19	2.64

TABLE A.2 (CONTINUED)

Stellar ID	T _{eff}	log <i>g</i>	[Fe/H]	$\sigma_{\text{[Fe/H]}}$	<i>N</i>	Fe I	<i>N</i>	Fe II	ξ
J10080064–1008523	4727	1.16	−1.91	0.14	75	24			2.21
J10082492–2314124	4898	2.10	−1.97	0.14	157	23			1.97
J10121964–3221347	4595	0.88	−2.68	0.15	105	26			2.52
J10162157–2959521	4939	2.11	−1.99	0.13	99	23			1.81
J10174884–4818125	5003	2.18	−1.84	0.14	81	23			1.35
J10191573–1924464	4564	2.03	−1.11	0.17	67	20			1.96
J10194932–4900584	5013	2.09	−1.50	0.14	114	32			1.79
J10251539–3554026	4888	1.52	−1.52	0.15	30	18			1.70
J10302845–7543299	4684	0.89	−2.18	0.14	48	16			2.45
J10344785–4823544	4927	1.82	−2.08	0.13	128	29			1.74
J10345348–1117221	4548	1.25	−1.77	0.17	91	26			2.43
J10362687–3746174	4597	1.19	−1.73	0.16	66	24			1.92
J10401894–4106124	4958	2.17	−1.55	0.15	114	33			1.63
J10540994–1347522	4710	1.20	−2.93	0.13	55	17			2.20
J10550634–1908359	4752	1.45	−3.03	0.13	46	14			2.85
J10563033–3428423	4467	0.69	−2.69	0.16	61	17			2.19
J10581140–2634179	4520	1.18	−1.85	0.14	92	18			2.02
J11014865–3749526	4452	0.95	−2.26	0.15	86	19			2.49
J11142319–3208509	4451	0.86	−2.36	0.15	97	23			2.57
J11265122–1805295	5054	2.46	−2.59	0.12	129	21			1.84
J11301705–1449325	4947	2.11	−2.73	0.13	174	21			1.86
J11325299–2913137	4435	1.12	−1.97	0.19	90	26			2.09
J11370170–5401298	4466	1.25	−1.80	0.14	70	22			2.42
J11373800–5202251	5053	2.21	−2.21	0.14	94	23			2.00
J11404726–0833030	5118	2.65	−1.52	0.13	108	26			1.51

TABLE A.2 (CONTINUED)

Stellar ID	T _{eff}	log <i>g</i>	[Fe/H]	$\sigma_{\text{[Fe/H]}}$	<i>N</i> Fe I	<i>N</i> Fe II	ξ
J11404944–1615396	4697	1.52	−1.67	0.14	84	25	2.19
J11444480–1128167	5289	3.08	−2.24	0.15	105	20	1.32
J11515010–0545441	4391	1.22	−1.74	0.14	53	18	3.46
J12044314–2911051	4465	0.92	−2.35	0.15	73	23	2.49
J12050944–1204531	4358	0.85	−1.80	0.14	47	22	2.06
J12062488–4741150	4584	1.03	−2.35	0.14	75	28	2.66
J12070990–3653243	4604	1.51	−1.64	0.17	93	21	2.24
J12100070–3130359	4669	1.21	−2.57	0.13	92	24	2.16
J12102259–4902190	4822	1.49	−1.74	0.13	66	13	1.95
J12170912–2721034	4935	1.76	−2.82	0.14	73	20	2.01
J12192034–1721547	4752	1.48	−2.74	0.12	75	17	1.93
J12232106–5305536	4676	1.07	−2.12	0.20	49	23	2.05
J12341308–3149577	4772	2.05	−1.34	0.13	78	24	1.86
J12405721–4051430	5163	2.83	−1.48	0.11	76	20	1.71
J12424489–1315032	5867	3.51	−1.91	0.12	106	24	1.62
J12535742–3801355	4773	1.36	−2.37	0.14	100	27	2.01
J12571667–4335318	4845	1.93	−1.97	0.14	110	30	1.54
J12572833–5125217	4699	1.49	−2.36	0.12	76	18	2.07
J13085850–2712188	4487	1.05	−2.38	0.21	66	22	2.32
J13101305–3342369	4594	1.28	−2.01	0.14	103	17	2.12
J13214178–4320055	4892	1.36	−2.17	0.13	77	17	2.87
J13241428–1806211	4741	1.38	−2.59	0.14	124	22	1.89
J13315746–1929446	5077	2.62	−1.15	0.14	100	30	1.52
J13330890–4654079	4591	0.79	−3.02	0.16	73	17	2.14
J13335283–2623539	4811	1.89	−2.24	0.13	110	26	1.60

TABLE A.2 (CONTINUED)

Stellar ID	T _{eff}	log <i>g</i>	[Fe/H]	$\sigma_{\text{[Fe/H]}}$	<i>N</i> Fe I	<i>N</i> Fe II	ξ
J13421261–1417354	4542	1.07	−1.63	0.18	97	29	2.44
J13530579–4438041	4576	0.84	−3.31	0.15	45	18	2.85
J13573542–3032486	5289	2.49	−2.12	0.16	59	11	1.85
J14030859–3214014	4470	1.08	−2.39	0.21	103	22	2.20
J14032900–5250429	5121	2.65	−1.86	0.12	79	21	1.57
J14091000–3013572	5166	2.82	−1.80	0.11	100	22	1.59
J14155955–3219255	4486	1.00	−2.58	0.18	72	18	2.81
J14165685+1215598	4802	1.38	−2.74	0.15	47	11	2.55
J14180866–2842077	4639	1.18	−2.50	0.13	86	19	2.35
J14254628–1546301	4305	0.64	−2.26	0.15	65	25	2.20
J14283907–2044594	4815	1.79	−1.60	0.15	85	25	1.82
J14354680–1124122	5079	2.68	−1.10	0.16	82	24	1.84
J14392683–1949132	5072	2.22	−2.27	0.16	63	19	1.98
J14435196–2106283	4486	1.04	−1.93	0.19	103	25	2.49
J14533307–4428301	4701	1.00	−2.56	0.13	101	27	2.28
J14560449–3950349	4612	1.36	−1.74	0.19	75	23	2.18
J14592981–3852558	4484	0.83	−2.40	0.16	39	20	2.38
J15023852–4602066	4806	1.66	−2.23	0.14	83	27	2.09
J15062866–1428038	5278	3.16	−2.23	0.13	85	18	1.35
J15141994–4359554	4589	0.73	−2.43	0.15	60	15	2.55
J15155734–1054220	4856	1.68	−1.71	0.13	88	25	2.09
J15230675–7930072	4737	1.07	−2.55	0.20	47	11	1.93
J15293404–3906241	4492	0.66	−2.75	0.15	50	14	3.07
J15320193–2211091	4868	1.23	−2.37	0.13	81	16	2.15
J15360493+0247300	4779	1.81	−2.42	0.15	48	14	2.47

TABLE A.2 (CONTINUED)

Stellar ID	T _{eff}	log <i>g</i>	[Fe/H]	$\sigma_{\text{[Fe/H]}}$	<i>N</i> Fe I	<i>N</i> Fe II	ξ
J15573010–2939228	5562	3.59	−1.74	0.15	32	8	2.13
J15582703–1136532	4736	1.46	−1.61	0.13	47	20	1.68
J16064231–1632461	4444	1.13	−2.17	0.18	138	21	2.10
J16122832–0848083	4492	1.12	−2.04	0.16	85	25	1.97
J16285613–1014576	5012	1.68	−1.90	0.13	112	26	1.81
J16524315–6719521	5333	1.90	−2.58	0.17	28	9	2.30
J17013206–5507454	5094	1.80	−2.10	0.15	53	8	1.91
J17383643–5358288	4671	0.87	−2.23	0.14	69	26	2.42
J17414840–5340354	4580	1.17	−2.14	0.15	88	23	2.27
J18050641–4907579	4430	1.03	−2.58	0.18	64	13	2.44
J18114680–2126085	4646	2.12	−0.97	0.13	51	21	1.78
J18272347–5133001	4583	1.53	−1.85	0.15	80	20	2.37
J18301354–4555101	5035	1.89	−2.98	0.14	44	9	1.86
J19050116–1949280	4780	1.40	−1.82	0.12	71	19	2.03
J19175585–5440147	4738	1.28	−2.75	0.12	85	19	2.05
J19232941–4425432	4437	1.01	−2.07	0.13	40	16	2.42
J19345326–3236567	4634	1.16	−2.17	0.14	72	14	2.20
J19441170–3526278	4513	0.99	−2.13	0.15	57	22	2.48
J19445483–4039459	4500	1.16	−1.92	0.13	61	24	1.87
J19451414–1729269	4631	1.23	−2.63	0.13	82	22	2.16
J19510180–6331111	4721	1.60	−2.09	0.14	101	25	1.74
J19584974–1812109	4785	1.53	−2.99	0.10	79	17	1.94
J20000364–3301351	4474	1.12	−1.89	0.14	79	27	2.06
J20005766–2541488	4731	1.69	−2.01	0.12	73	22	1.76
J20080083–2759265	4481	1.00	−2.16	0.14	58	22	2.12

TABLE A.2 (CONTINUED)

Stellar ID	T _{eff}	log <i>g</i>	[Fe/H]	$\sigma_{\text{[Fe/H]}}$	<i>N</i> Fe I	<i>N</i> Fe II	ξ
J20100948–4408274	4698	1.02	−2.78	0.12	51	15	2.20
J20103193–3558546	4931	1.04	−2.56	0.11	71	22	2.15
J20152296–3740178	4747	1.58	−2.73	0.12	70	16	2.04
J20194310–3158163	4927	2.29	−2.16	0.12	102	21	1.51
J20233743–1659533	4635	1.43	−2.57	0.13	75	17	1.80
J20305648–3446521	4571	1.15	−2.47	0.13	53	17	2.25
J20411424–4654315	4647	1.30	−2.30	0.15	85	18	2.56
J20435776–4408037	4410	0.86	−1.85	0.14	49	20	2.05
J20453454–1431151	4582	1.01	−2.81	0.13	81	21	2.02
J20504869–3355289	4549	1.09	−2.63	0.14	73	21	2.33
J20554594–3155159	4581	0.94	−2.67	0.13	61	17	2.26
J21003824–0539171	4872	1.13	−2.27	0.11	68	17	2.03
J21055865–4919336	4633	1.30	−2.27	0.14	75	21	2.30
J21080151–6555366	4428	1.07	−2.40	0.14	53	20	2.76
J21103411–6331354	5066	2.75	−2.07	0.12	93	20	1.44
J21314253–1459110	4927	1.93	−1.97	0.12	71	16	1.83
J21402305–1227035	4621	1.30	−3.09	0.15	85	16	1.86
J21462219–0512324	4723	1.19	−1.69	0.13	63	18	1.97
J22115488–2847382	4710	1.78	−2.62	0.12	78	15	2.03
J22125424–0235414	5187	2.99	−2.09	0.11	82	19	1.58
J22161170–5319492	5112	1.53	−2.51	0.12	79	19	2.50
J22190836–2333467	4743	1.46	−2.54	0.14	84	22	1.95
J22223324–1314488	4613	1.09	−2.46	0.13	66	19	2.44
J22233596–5301145	4692	1.40	−2.41	0.12	81	22	2.25
J22371623–1608005	6175	3.86	−2.10	0.13	78	16	1.96

TABLE A.2 (CONTINUED)

Stellar ID	T _{eff}	log <i>g</i>	[Fe/H]	$\sigma_{\text{[Fe/H]}}$	<i>N</i> Fe I	<i>N</i> Fe II	ξ
J22372037–4741375	4499	1.07	−2.97	0.19	46	18	2.12
J22373316–4341181	4707	1.73	−2.47	0.13	77	20	1.70
J22585069–3923437	4901	1.61	−2.45	0.12	68	21	1.91
J23060975–6107368	4669	1.33	−2.28	0.15	80	22	2.03
J23181358–6252270	4554	1.03	−2.40	0.10	69	18	1.89
J23242766–2728055	4743	1.59	−2.40	0.11	83	20	1.96
J23254164–2356206	4647	1.28	−1.88	0.14	84	25	2.15
J23285061–0432368	4792	1.60	−1.95	0.14	75	24	1.84
J23330336–4437127	4716	1.08	−2.60	0.11	85	23	2.32
J23342332–2748003	4617	1.05	−2.35	0.14	59	16	2.14
J23425814–4327352	4867	1.99	−2.16	0.11	83	24	1.67
J23434113–6019223	4660	1.47	−3.05	0.11	32	6	2.54
J23475942–5701184	4668	0.88	−2.33	0.13	67	26	2.45
J23490902–2447176	5248	2.73	−2.18	0.10	75	19	1.81
J23552837+0421179	4528	0.97	−2.51	0.15	92	21	2.26

TABLE A.3

NEUTRON-CAPTURE ABUNDANCES AND SUBCLASS

ASSIGNMENTS

Stellar ID	[Fe/H]	[C/Fe]	[C/Fe] _c	[Sr/Fe]	[Ba/Fe]	[Eu/Ba]	Class
J00002416-1107454	-2.40	-0.33	+0.24	-0.32	-0.27	+0.50	<i>r</i> -I
J00023429-1924590	-2.22	-0.64	+0.06	+0.08	-0.27	+0.56	<i>r</i> -I
J00041581-5815524	-2.32	-0.66	-0.16	+0.72	+0.30	+0.95	<i>r</i> -II
J00062986-5049319	-2.59	-0.65	+0.11	-0.45	-0.70	-0.15	non-RPE
J00093394-1857008	-1.85	-0.17	+0.06	+0.13	+0.23	+0.46	<i>r</i> -I
J00154806-6253207	-2.30	-0.55	-0.33	+0.30	+0.08	+0.40	<i>r</i> -I
J00172430-3333151	-2.29	-0.07	+0.23	+0.35	+0.05	+0.59	<i>r</i> -I
J00182832-3900338	-1.75	-0.35	+0.14	+0.28	+0.07	+0.57	<i>r</i> -I
J00223225-4839449	-1.75	-0.25	+0.20	-0.05	+0.10	+0.65	<i>r</i> -I
J00374325-1204391	-2.40	-0.20	+0.42	0.00	-0.27	+0.28	non-RPE
J00410929-0328595	-2.53	+0.24	+0.46	-0.16	-0.49	+0.12	non-RPE
J00413026-4058547	-2.57	-0.49	+0.20	+0.04	-0.27	+0.38	<i>r</i> -I
J00442897-1017497	-2.35	-0.25	+0.36	-0.08	-0.07	+0.47	<i>r</i> -I
J00452879-5846450	-2.22	-0.25	+0.37	+0.28	+0.12	+0.57	<i>r</i> -I
J00482431-1041309	-2.45	-0.25	+0.47	+0.25	+0.09	+0.45	<i>r</i> -I
J00584386-3005576	-3.50	+0.43	+0.66	-1.12	<-0.15	<+0.30	...
J01083959-2857013	-2.84	+0.10	+0.13	+0.46	-0.13	<+0.50	...
J01094330-5907230	-2.46	-0.17	+0.51	+0.08	-0.49	+0.01	limited- <i>r</i>
J01213447-2528002	-2.61	-0.50	+0.24	+0.13	-0.30	+0.30	<i>r</i> -I
J01265856+0135153	-3.39	-0.92	-0.20	-0.77	-0.93	<0.00	non-RPE
J01311599-4016510	-2.17	-0.10	+0.27	+0.18	-0.12	+0.53	<i>r</i> -I
J01321981-3040512	-2.13	-0.15	-0.14	+0.07	+0.03	+0.42	<i>r</i> -I

TABLE A.3 (CONTINUED)

Stellar ID	[Fe/H]	[C/Fe]	[C/Fe] _c	[Sr/Fe]	[Ba/Fe]	[Eu/Ba]	Class
J01352315–0817533	−2.06	−0.16	+0.28	+0.57	+1.02	+0.43	<i>s</i>
J01371888–1729037	−2.55	−0.85	−0.07	−0.18	−0.31	+0.33	<i>r</i> -I
J01373857–2618131	−2.80	−0.15	+0.57	0.00	+0.03	+0.62	<i>r</i> -I
J01425232–4657481	−2.04	+0.02	+0.03	+0.22	−0.13	+0.22	non-RPE
J01425445–0904162	−1.73	−0.55	−0.15	+0.30	+0.35	+0.83	<i>r</i> -II
J01451383–4302313	−2.09	−0.20	−0.02	−0.25	−0.15	+0.13	non-RPE
J01493760–4551222	−2.72	−0.10	+0.36	−0.40	−0.05	+0.30	<i>r</i> -I
J02070641–5009166	−2.15	−0.80	−0.04	+0.13	+0.20	+0.65	<i>r</i> -I
J02212400–4056480	−2.52	+0.20	+0.83	−0.18	−0.18	+0.46	<i>r</i> -I
J02215117–5933316	−2.68	+0.25	+0.26	+0.25	−0.18	<+0.50	...
J02215557–5410143	−2.09	0.00	0.00	+0.22	+0.42	<+0.80	...
J02215793–2130429	−1.98	−0.59	−0.11	+0.24	+0.14	+0.18	non-RPE
J02230804–3129531	−1.82	−0.30	+0.12	+0.15	+0.10	+0.45	<i>r</i> -I
J02265832–0749596	−1.94	−0.05	−0.04	+0.23	+0.08	+0.56	<i>r</i> -I
J02515281–3717316	−2.33	−0.40	+0.34	−0.33	−0.22	+0.33	<i>r</i> -I
J02570028–3024374	−2.09	+0.15	+0.33	−0.03	+0.03	+0.55	<i>r</i> -I
J03142084–1035112	−3.75	+0.76	+1.45	−1.52	<−0.35	<+0.55	...
J03190629–0819306	−2.24	−0.32	+0.21	−0.12	−0.55	−0.15	non-RPE
J03210882–3944213	−1.91	−0.60	+0.03	+0.20	+0.13	+0.55	<i>r</i> -I
J03422816–6500355	−2.16	+0.05	+0.06	+0.33	+0.40	+1.05	<i>r</i> -II
J03425812–3047217	−2.35	<0.00	...	+0.75	+0.55	+0.67	<i>r</i> -I
J04012191–2635058	−2.17	+0.03	+0.13	+0.13	+0.15	+0.38	<i>r</i> -I
J04014897–3757533	−2.28	−0.30	+0.42	+0.07	+0.17	+0.18	non-RPE
J04182158–2323391	−1.76	−0.44	+0.06	+0.19	+0.13	+0.48	<i>r</i> -I
J04263084–4058516	−2.43	−0.60	−0.01	+0.02	+0.07	+0.40	<i>r</i> -I

TABLE A.3 (CONTINUED)

Stellar ID	[Fe/H]	[C/Fe]	[C/Fe] _c	[Sr/Fe]	[Ba/Fe]	[Eu/Ba]	Class
J04315411–0632100	−2.18	−0.05	−0.05	+0.05	−0.10	+0.30	<i>r</i> -I
J04350131–0959363	−2.87	+0.05	+0.20	−0.70	−0.75	<+0.20	non-RPE
J04411241–6518438	−2.47	−0.14	−0.13	+0.24	−0.21	+0.29	non-RPE
J04420818–3421138	−1.94	+1.80	+1.83	+0.50	+1.38	+0.60	CEMP- <i>s</i>
J04520910–6209121	−2.78	−0.19	+0.49	−0.14	−0.14	+0.46	<i>r</i> -I
J05311779–5810048	−2.33	+0.17	+0.18	−0.13	−0.11	+0.65	<i>r</i> -I
J05381700–7516207	−1.83	+0.01	+0.04	+0.46	+0.23	+0.53	<i>r</i> -I
J05383296–5904280	−2.53	<+0.80	...	+1.15	+0.76	+1.28	<i>r</i> -II
J05514213–3327337	−2.42	−0.27	+0.11	+0.30	−0.13	+0.49	<i>r</i> -I
J05521578–3953184	−2.34	−0.22	+0.24	+0.23	−0.04	+0.41	<i>r</i> -I
J05564771–6639054	−2.01	−0.45	−0.12	+0.10	+0.08	+0.45	<i>r</i> -I
J06014757–5951510	−2.08	+0.01	+0.01	+0.24	−0.12	+0.26	non-RPE
J06055404–3306288	−1.93	+1.03	+1.05	+1.03	+1.13	+0.93	non-RPE
J06090353–7122260	−2.73	−0.08	+0.38	−0.16	−0.45	+0.32	<i>r</i> -I
J06195001–5312114	−2.06	+0.30	+0.31	+1.00	−0.03	+0.73	<i>r</i> -II
J06290787–6709523	−2.73	−0.44	+0.30	−0.44	−0.17	+0.46	<i>r</i> -I
J06320130–2026538	−1.56	−0.05	−0.03	+1.44	+0.15	+0.70	<i>r</i> -I
J06332771–3519240	−1.84	+0.02	+0.03	+0.12	+0.02	+0.45	<i>r</i> -I
J06401317–3540444	−2.38	−0.10	−0.09	+0.24	+0.05	+0.38	<i>r</i> -I
J06420823–5116448	−2.64	+0.15	+0.65	−0.02	−0.43	+0.05	non-RPE
J06592949–5406125	−1.86	+0.50	+0.62	+0.63	+0.80	+0.43	non-RPE
J07103110–7121522	−1.47	0.00	+0.02	+0.61	+0.33	+1.05	<i>r</i> -II
J07161594–5135248	−1.86	−0.47	+0.13	+0.21	+0.28	+0.46	<i>r</i> -I
J07202253–3358518	−1.60	+0.11	+0.13	+0.49	+0.68	+1.44	<i>r</i> -II
J07265723–5647500	−1.93	+0.04	+0.14	+0.07	+0.10	+0.65	<i>r</i> -I

TABLE A.3 (CONTINUED)

Stellar ID	[Fe/H]	[C/Fe]	[C/Fe] _c	[Sr/Fe]	[Ba/Fe]	[Eu/Ba]	Class
J07352232–4425010	-1.58	-0.01	0.00	+0.24	+0.39	+0.79	<i>r</i> -II
J07393021–5548171	-1.74	-0.95	-0.40	+0.35	+0.50	+0.63	<i>r</i> -I
J07411443–4339360	-1.87	+0.05	+0.06	+0.02	+0.13	+0.50	<i>r</i> -I
J07482433–4831405	-2.10	+0.06	+0.51	+0.36	+0.34	+0.06	non-RPE
J07501424–4123454	-1.87	+0.17	+0.18	+0.15	+0.27	+0.59	<i>r</i> -I
J08015897–5752032	-1.72	-0.35	+0.17	+0.20	+0.15	+0.55	<i>r</i> -I
J08032084–5856521	-1.73	+0.01	+0.03	+0.24	+0.26	+0.49	<i>r</i> -I
J08134364–2332528	-1.72	-0.40	+0.10	+0.10	+0.28	+0.32	<i>r</i> -I
J08155667–2204105	-1.82	-0.13	-0.03	+0.11	+0.21	+0.57	<i>r</i> -I
J08311233–6013195	-1.47	+0.04	+0.06	-0.06	-0.39	+0.14	non-RPE
J08393460–2122069	-1.94	-0.20	+0.14	+0.15	+0.13	+0.42	<i>r</i> -I
J08594093–1415151	-1.46	-0.27	-0.20	+0.13	+0.35	+0.52	<i>r</i> -I
J09214783–0214582	-1.99	-0.12	+0.26	+0.38	0.00	+0.23	non-RPE
J09255655–3450373	-1.80	-0.46	-0.04	+0.39	+0.22	+0.62	<i>r</i> -I
J09261133–1526232	-1.69	+0.01	+0.03	+0.06	+0.28	+0.43	<i>r</i> -I
J09284944–0738585	-1.23	0.00	+0.07	+0.45	+0.32	+0.60	<i>r</i> -I
J09310102–0304052	-1.70	+0.08	+0.08	+0.36	+0.36	+0.33	non-RPE
J09364069–2038386	-1.78	-0.35	-0.05	+0.15	+0.12	+0.48	<i>r</i> -I
J09471921–4127042	-2.67	-0.42	+0.32	-1.57	-0.89	-0.45	non-RPE
J09574607–3923072	-1.69	-0.06	+0.24	+0.22	+0.21	+0.55	<i>r</i> -I
J10025125–4331098	-2.87	-0.25	+0.49	-0.36	-0.71	+0.42	<i>r</i> -I
J10080064–1008523	-1.91	+0.42	+0.79	+0.47	+1.19	+0.37	<i>s</i>
J10082492–2314124	-1.97	0.00	+0.02	+0.15	+0.23	+0.40	<i>r</i> -I
J10121964–3221347	-2.68	-0.55	+0.20	-0.20	-0.07	+0.55	<i>r</i> -I
J10162157–2959521	-1.99	+0.01	+0.03	+0.14	-0.06	+0.22	non-RPE

TABLE A.3 (CONTINUED)

Stellar ID	[Fe/H]	[C/Fe]	[C/Fe] _c	[Sr/Fe]	[Ba/Fe]	[Eu/Ba]	Class
J10174884–4818125	−1.84	+0.01	+0.02	+0.24	+0.06	+0.28	non-RPE
J10191573–1924464	−1.11	−0.32	−0.23	+0.63	+0.73	+0.75	<i>r</i> -II
J10194932–4900584	−1.50	−0.05	−0.02	+0.20	+0.22	+0.45	<i>r</i> -I
J10251539–3554026	−1.52	+0.05	+0.35	+0.40	+0.60	+0.47	non-RPE
J10302845–7543299	−2.18	−0.52	+0.21	−0.07	+0.08	+0.53	<i>r</i> -I
J10344785–4823544	−2.08	0.00	+0.20	+0.18	−0.35	−0.08	limited- <i>r</i>
J10345348–1117221	−1.77	−0.65	−0.07	+0.05	−0.32	+0.35	<i>r</i> -I
J10362687–3746174	−1.73	−0.51	+0.06	+0.22	+0.32	+0.60	<i>r</i> -I
J10401894–4106124	−1.55	0.00	+0.02	+0.13	+0.35	+0.82	<i>r</i> -II
J10540994–1347522	−2.93	<−0.20	...	−1.14	−1.27	<+0.30	non-RPE
J10563033–3428423	−2.69	−0.43	+0.32	−0.68	−1.28	−0.63	limited- <i>r</i>
J10581140–2634179	−1.85	−0.60	+0.02	+0.10	+0.15	+0.20	non-RPE
J11014865–3749526	−2.26	−0.70	+0.07	+0.10	−0.12	+0.50	<i>r</i> -I
J11142319–3208509	−2.36	−0.80	−0.01	+0.05	−0.35	+0.23	non-RPE
J11265122–1805295	−2.59	−0.01	0.00	+0.12	−0.28	+0.04	non-RPE
J11325299–2913137	−1.97	−0.90	−0.21	+0.18	−0.02	+0.15	non-RPE
J11370170–5401298	−1.80	−0.80	−0.19	+0.05	+0.10	+0.63	<i>r</i> -I
J11373800–5202251	−2.21	+0.13	+0.14	−0.24	−0.49	+0.09	non-RPE
J11404726–0833030	−1.52	+0.03	+0.05	+0.11	+0.36	+0.55	<i>r</i> -I
J11404944–1615396	−1.67	−0.40	+0.02	+0.20	+0.27	+0.88	<i>r</i> -II
J11515010–0545441	−1.74	−1.20	−0.54	+0.20	+0.62	+0.23	non-RPE
J12044314–2911051	−2.35	−0.67	+0.11	+0.28	+0.33	+0.71	<i>r</i> -II
J12050944–1204531	−1.80	−0.80	−0.11	+0.23	+0.17	+0.25	non-RPE
J12062488–4741150	−2.35	−0.63	+0.13	0.00	−0.35	−0.11	non-RPE
J12070990–3653243	−1.64	−0.50	−0.06	+0.10	−0.10	+0.40	<i>r</i> -I

TABLE A.3 (CONTINUED)

Stellar ID	[Fe/H]	[C/Fe]	[C/Fe] _c	[Sr/Fe]	[Ba/Fe]	[Eu/Ba]	Class
J12100070–3130359	−2.57	−0.22	+0.45	−0.07	−0.25	+0.26	non-RPE
J12102259–4902190	−1.74	−0.05	+0.34	+0.15	+0.23	+0.58	<i>r</i> -I
J12170912–2721034	−2.82	+0.34	+0.53	+0.01	−0.51	+0.22	non-RPE
J12192034–1721547	−2.74	+0.23	+0.67	−0.12	−0.52	+0.11	non-RPE
J12232106–5305536	−2.12	−0.09	+0.52	−0.19	−0.29	−0.04	non-RPE
J12341308–3149577	−1.34	−0.20	−0.13	+0.35	+0.18	+0.35	<i>r</i> -I
J12405721–4051430	−1.48	+0.05	+0.07	+0.20	+0.22	+0.45	<i>r</i> -I
J12424489–1315032	−1.91	+0.25	+0.25	+0.20	+0.20	<+0.50	...
J12535742–3801355	−2.37	−0.01	+0.55	−0.06	−0.14	+0.53	<i>r</i> -I
J12571667–4335318	−1.97	−0.05	+0.05	+0.05	+0.15	+0.30	<i>r</i> -I
J12572833–5125217	−2.36	−0.30	+0.20	+0.15	0.00	−0.13	non-RPE
J13085850–2712188	−2.38	−0.60	+0.15	+0.25	−0.30	+0.20	limited- <i>r</i>
J13101305–3342369	−2.01	−0.60	+0.01	+0.40	+0.08	+0.53	<i>r</i> -I
J13214178–4320055	−2.17	−0.30	+0.26	−0.05	+0.15	+0.58	<i>r</i> -I
J13241428–1806211	−2.59	−0.01	+0.53	−0.06	−0.51	−0.01	non-RPE
J13315746–1929446	−1.15	+0.09	+0.11	+0.29	+0.44	+0.51	<i>r</i> -I
J13330890–4654079	−3.02	+0.05	+0.78	0.00	−0.17	+0.49	<i>r</i> -I
J13421261–1417354	−1.63	−0.61	−0.02	+0.09	−0.24	−0.16	non-RPE
J13530579–4438041	−3.31	<−0.20	...	−0.29	−1.07	<+0.60	...
J13573542–3032486	−2.12	+0.30	+0.31	−0.38	−0.45	<+0.40	...
J14032900–5250429	−1.86	−0.05	−0.04	+0.15	+0.10	+0.38	<i>r</i> -I
J14091000–3013572	−1.80	−0.05	−0.04	+0.30	+0.30	+0.24	non-RPE
J14155955–3219255	−2.58	−0.81	−0.03	−0.11	−0.26	+0.47	<i>r</i> -I
J14165685+1215598	−2.74	+0.13	+0.65	−0.31	−1.04	−0.01	non-RPE
J14254628–1546301	−2.26	−0.45	+0.29	−0.15	−0.28	+0.25	non-RPE

TABLE A.3 (CONTINUED)

Stellar ID	[Fe/H]	[C/Fe]	[C/Fe] _c	[Sr/Fe]	[Ba/Fe]	[Eu/Ba]	Class
J14283907–2044594	−1.60	−0.60	−0.33	+0.15	+0.27	+0.29	non-RPE
J14354680–1124122	−1.10	−0.05	−0.03	+0.38	+0.42	+0.72	<i>r</i> -II
J14392683–1949132	−2.27	+1.05	+1.07	+0.60	+0.32	+0.25	non-RPE
J14435196–2106283	−1.93	−0.95	−0.23	+0.18	−0.45	−0.30	limited- <i>r</i>
J14533307–4428301	−2.56	−0.80	−0.02	−0.15	−0.78	−0.26	limited- <i>r</i>
J14560449–3950349	−1.74	−0.60	−0.08	+0.20	−0.07	+0.08	non-RPE
J14592981–3852558	−2.40	−0.95	−0.16	+0.23	+0.13	+0.93	<i>r</i> -II
J15023852–4602066	−2.23	−0.16	+0.20	−0.26	−0.61	−0.16	non-RPE
J15062866–1428038	−2.23	−0.08	−0.08	+0.17	−0.01	+0.65	<i>r</i> -I
J15141994–4359554	−2.43	−0.31	+0.43	+0.11	−0.32	+0.02	non-RPE
J15155734–1054220	−1.71	+0.02	+0.29	+0.44	+0.52	+0.66	<i>r</i> -I
J15230675–7930072	−2.55	+0.28	+0.87	+0.71	−0.43	+0.36	non-RPE
J15293404–3906241	−2.75	<−0.80	...	−0.36	−0.16	+0.34	<i>r</i> -I
J15320193–2211091	−2.37	−0.45	+0.22	−0.05	+0.03	+0.15	non-RPE
J15360493+0247300	−2.42	−0.28	−0.10	+0.12	−0.86	+0.22	non-RPE
J15573010–2939228	−1.74	<0.00	...	+0.26	−0.05	... ^a	...
J15582703–1136532	−1.61	−0.14	+0.25	+0.19	+0.81	+0.39	non-RPE
J16524315–6719521	−2.58	<+0.50	...	−0.08	<−1.00	<+0.70	...
J17013206–5507454	−2.10	+0.43	+0.63	+0.04	−0.10	<+0.30	non-RPE
J17383643–5358288	−2.23	−0.73	+0.04	−0.03	−0.01	+0.55	<i>r</i> -I
J17414840–5340354	−2.14	−0.55	+0.12	+0.25	0.00	+0.63	<i>r</i> -I
J18050641–4907579	−2.58	−0.70	+0.06	+0.10	+0.15	+0.73	<i>r</i> -II
J18272347–5133001	−1.85	−0.47	−0.02	+0.43	+0.18	+0.56	<i>r</i> -I
J18301354–4555101	−2.98	+1.63	+1.71	−0.77	+0.09	<+0.80	CEMP
J19232941–4425432	−2.07	−0.95	−0.20	+0.05	0.00	+0.38	<i>r</i> -I

TABLE A.3 (CONTINUED)

Stellar ID	[Fe/H]	[C/Fe]	[C/Fe] _c	[Sr/Fe]	[Ba/Fe]	[Eu/Ba]	Class
J19345326–3236567	−2.17	−0.40	+0.26	+0.15	+0.07	+0.63	<i>r</i> -I
J19441170–3526278	−2.13	−0.70	+0.04	+0.25	+0.25	+0.40	<i>r</i> -I
J19445483–4039459	−1.92	−0.27	+0.31	+0.21	+0.13	+0.33	<i>r</i> -I
J19451414–1729269	−2.63	−0.25	+0.41	+0.25	−0.03	+0.55	<i>r</i> -I
J19510180–6331111	−2.09	−0.09	+0.29	+0.39	+0.36	+0.36	non-RPE
J19584974–1812109	−2.99	+0.13	+0.52	−0.92	−0.77	<+0.20	...
J20000364–3301351	−1.89	−0.85	−0.18	+0.20	+0.02	+0.90	<i>r</i> -II
J20005766–2541488	−2.01	−0.05	+0.27	+0.60	+0.35	+0.40	<i>r</i> -I
J20080083–2759265	−2.16	−0.75	+0.01	+0.25	0.00	+0.35	<i>r</i> -I
J20100948–4408274	−2.78	0.00	+0.72	−0.30	−0.50	+0.13	non-RPE
J20103193–3558546	−2.56	−0.20	+0.52	+0.18	−0.03	+0.38	<i>r</i> -I
J20152296–3740178	−2.73	+0.10	+0.46	−0.55	−0.30	+0.13	non-RPE
J20194310–3158163	−2.16	−0.02	−0.01	+0.31	+0.16	+0.46	<i>r</i> -I
J20233743–1659533	−2.57	−0.57	−0.02	+0.23	−0.07	+0.50	<i>r</i> -I
J20305648–3446521	−2.47	−0.55	+0.16	−0.10	−0.10	+0.28	non-RPE
J20411424–4654315	−2.30	−0.30	+0.32	+0.02	−0.02	+0.88	<i>r</i> -II
J20435776–4408037	−1.85	−0.70	−0.01	+0.20	+0.15	+0.78	<i>r</i> -II
J20453454–1431151	−2.81	−0.22	+0.51	+0.13	−0.12	+0.31	<i>r</i> -I
J20504869–3355289	−2.63	−0.34	+0.38	+0.24	−0.06	+0.62	<i>r</i> -I
J20554594–3155159	−2.67	−0.45	+0.30	+0.02	−0.05	+0.67	<i>r</i> -I
J21003824–0539171	−2.27	−0.15	+0.50	+0.20	−0.13	+0.38	<i>r</i> -I
J21055865–4919336	−2.27	−0.50	+0.13	−0.05	+0.12	+0.67	<i>r</i> -I
J21080151–6555366	−2.40	−0.22	+0.49	+0.21	−0.25	+0.18	non-RPE
J21103411–6331354	−2.07	−0.15	−0.14	+0.20	−0.08	+0.10	non-RPE
J21314253–1459110	−1.97	0.00	+0.10	−0.38	−0.20	−0.05	non-RPE

TABLE A.3 (CONTINUED)

Stellar ID	[Fe/H]	[C/Fe]	[C/Fe] _c	[Sr/Fe]	[Ba/Fe]	[Eu/Ba]	Class
J21402305–1227035	−3.09	+0.04	+0.62	+1.59	−0.26	<0.00	limited- <i>r</i>
J21462219–0512324	−1.69	−0.47	+0.08	+0.21	+0.33	+0.45	<i>r</i> -I
J22115488–2847382	−2.62	−0.30	−0.11	+0.05	+0.06	+0.28	non-RPE
J22125424–0235414	−2.09	−0.16	−0.15	−0.27	+0.21	+0.34	<i>r</i> -I
J22161170–5319492	−2.51	−0.15	+0.31	+0.20	+0.31	+0.59	<i>r</i> -I
J22190836–2333467	−2.54	−0.13	+0.39	+0.27	+0.24	+0.87	<i>r</i> -II
J22223324–1314488	−2.46	−0.80	−0.05	0.00	−0.47	−0.04	non-RPE
J22233596–5301145	−2.41	+0.80	+1.15	−0.35	−0.28	+0.23	non-RPE
J22371623–1608005	−2.10	+0.35	+0.35	0.00	+0.15	<+1.00	...
J22372037–4741375	−2.97	−0.20	+0.54	0.00	+0.10	+0.84	<i>r</i> -II
J22373316–4341181	−2.47	−0.21	+0.06	+0.14	−0.06	+0.40	<i>r</i> -I
J22585069–3923437	−2.45	+0.15	+0.53	−0.18	−0.18	+0.02	non-RPE
J23060975–6107368	−2.28	−0.36	+0.25	+0.09	−0.14	+0.31	<i>r</i> -I
J23181358–6252270	−2.40	−0.22	+0.48	+0.23	−0.04	+0.16	non-RPE
J23242766–2728055	−2.40	+0.07	+0.49	+0.27	+0.32	+0.55	<i>r</i> -I
J23254164–2356206	−1.88	−0.47	+0.10	+0.06	+0.19	+0.42	<i>r</i> -I
J23285061–0432368	−1.95	+0.05	+0.41	−0.10	0.00	+0.53	<i>r</i> -I
J23330336–4437127	−2.60	−0.55	+0.18	−0.08	−0.26	+0.16	non-RPE
J23342332–2748003	−2.35	−0.24	+0.47	+0.39	−0.06	+0.71	<i>r</i> -II
J23425814–4327352	−2.16	−0.24	−0.18	+0.19	−0.01	+0.36	<i>r</i> -I
J23434113–6019223	−3.05	<−0.50	...	−1.89	−1.34	<+0.50	...
J23475942–5701184	−2.33	−0.55	+0.21	−0.08	−0.07	+0.45	<i>r</i> -I
J23490902–2447176	−2.18	+0.17	+0.18	−0.03	−0.16	+0.65	<i>r</i> -I
J23552837+0421179	−2.51	−0.45	+0.30	+0.07	−0.33	+0.06	non-RPE

^aCasey and Schlaufman (2015) have also analyzed this star and find [Eu/Fe] < +0.50.

APPENDIX B

DETAILED MCMC RESULTS FOR THE FIRST NEUTRON STAR MERGERS

B.1 MCMC Results by EOS

Tables B.1–B.6 summarize the MCMC results for each star in Table 8.2 using different EOSs. Each table shows the model output abundance ratio that corresponds to the optimal combination of neutron star masses M_1 and M_2 . Also tabulated are the remnant lifetimes and total ejecta masses associated with each M_1 - M_2 solution.

TABLE B.1

INDIVIDUAL RESULTS USING H4

ID	[Zr/Dy] model	[Th/Dy] model	M_1 (M $_{\odot}$)	M_2 (M $_{\odot}$)	τ (ms)	m_{wind} (10 $^{-3}$ M $_{\odot}$)	m_{dyn} (10 $^{-3}$ M $_{\odot}$)
1	0.23	0.07	1.36 $^{+0.001}_{-0.001}$	1.23 $^{+0.013}_{-0.012}$	115	42.41	1.22
2	-0.16	0.23	1.42 $^{+0.006}_{-0.006}$	1.14 $^{+0.009}_{-0.006}$	181	42.90	4.23
3	-0.20	-0.03	1.40 $^{+0.004}_{-0.004}$	1.12 $^{+0.004}_{-0.003}$	∞	43.35	3.45
4	-0.19	-0.22	1.42 $^{+0.018}_{-0.022}$	1.15 $^{+0.024}_{-0.022}$	156	42.75	4.10
5	-0.14	0.14	1.42 $^{+0.010}_{-0.009}$	1.15 $^{+0.020}_{-0.012}$	156	42.75	4.10
6	-0.32	-0.01	1.40 $^{+0.001}_{-0.000}$	1.33 $^{+0.000}_{-0.010}$	15	36.85	3.01
7	-0.43	-0.04	1.48 $^{+0.010}_{-0.009}$	1.10 $^{+0.007}_{-0.007}$	134	42.59	8.49
8	-0.42	0.01	1.42 $^{+0.023}_{-0.005}$	1.08 $^{+0.003}_{-0.004}$	∞	43.52	5.33
9	-0.79	-0.23	1.62 $^{+0.002}_{-0.002}$	1.07 $^{+0.030}_{-0.032}$	26	39.22	18.93

TABLE B.1 (CONTINUED)

ID	[Zr/Dy]	[Th/Dy]	M_1	M_2	τ	m_{wind}	m_{dyn}
	model	model	(M_\odot)	(M_\odot)	(ms)	($10^{-3} M_\odot$)	($10^{-3} M_\odot$)
10	-0.64	0.22	$1.46^{+0.009}_{-0.010}$	$1.42^{+0.010}_{-0.011}$	2	18.48	4.74
11	-0.46	0.01	$1.46^{+0.032}_{-0.015}$	$1.08^{+0.012}_{-0.007}$	246	43.15	7.83
12	-0.50	-0.21	$1.42^{+0.009}_{-0.009}$	$1.38^{+0.010}_{-0.011}$	6	30.26	3.83
13	-0.70	-0.10	$1.59^{+0.010}_{-0.047}$	$1.14^{+0.076}_{-0.114}$	15	36.85	13.65
14	-0.41	0.31	$1.46^{+0.007}_{-0.007}$	$1.30^{+0.012}_{-0.012}$	10	34.45	4.54
15	-0.78	0.07	$1.61^{+0.037}_{-0.054}$	$1.00^{+0.135}_{-0.012}$	85	41.99	22.52
16	-0.94	0.02	$1.69^{+0.033}_{-0.111}$	$0.96^{+0.075}_{-0.033}$	47	40.87	32.45
17	-0.86	0.01	$1.48^{+0.011}_{-0.008}$	$1.45^{+0.003}_{-0.018}$	1	10.22	5.16
18	-0.75	-0.09	$1.60^{+0.017}_{-0.078}$	$1.03^{+0.171}_{-0.022}$	63	41.49	19.82
19	-0.82	0.11	$1.61^{+0.025}_{-0.050}$	$0.98^{+0.009}_{-0.005}$	115	42.41	23.93
20	-0.85	-0.24	$1.64^{+0.045}_{-0.007}$	$1.13^{+0.040}_{-0.168}$	8	33.51	17.05
21	-0.95	0.42	$1.74^{+0.013}_{-0.074}$	$1.00^{+0.130}_{-0.103}$	13	36.11	33.00
22	-0.96	0.16	$1.72^{+0.015}_{-0.091}$	$0.98^{+0.116}_{-0.067}$	23	38.70	33.19
23	-0.87	0.17	$1.65^{+0.035}_{-0.076}$	$0.96^{+0.219}_{-0.005}$	85	41.99	28.93
24	-0.21	-0.14	$1.40^{+0.002}_{-0.002}$	$1.12^{+0.003}_{-0.001}$	∞	43.35	3.45
25	-0.76	-0.14	$1.60^{+0.011}_{-0.047}$	$1.03^{+0.035}_{-0.018}$	63	41.49	19.82
26	-1.02	-0.23	$1.72^{+0.009}_{-0.009}$	$0.96^{+0.138}_{-0.023}$	30	39.69	35.07
27	-0.79	0.09	$1.62^{+0.016}_{-0.010}$	$1.19^{+0.025}_{-0.049}$	5	29.03	13.32
28	-0.83	0.26	$1.47^{+0.019}_{-0.002}$	$1.46^{+0.009}_{-0.017}$	1	10.22	5.12
29	-0.88	-0.18	$1.65^{+0.020}_{-0.053}$	$1.00^{+0.146}_{-0.030}$	47	40.87	25.76
30	-0.99	-0.46	$1.71^{+0.023}_{-0.100}$	$0.96^{+0.116}_{-0.052}$	35	40.12	34.20

TABLE B.2
INDIVIDUAL RESULTS USING DD2

ID	[Zr/Dy]	[Th/Dy]	M_1	M_2	τ	m_{wind}	m_{dyn}
	model	model	(M _⊕)	(M _⊕)	(ms)	(10 ⁻³ M _⊕)	(10 ⁻³ M _⊕)
1	0.19	0.02	1.28 ^{+0.009} _{-0.012}	1.23 ^{+0.015} _{-0.025}	∞	44.08	0.84
2	-0.16	0.17	1.32 ^{+0.032} _{-0.009}	1.31 ^{+0.006} _{-0.090}	∞	43.69	2.71
3	-0.19	-0.06	1.32 ^{+0.036} _{-0.010}	1.31 ^{+0.010} _{-0.086}	∞	43.69	2.71
4	-0.18	-0.29	1.33 ^{+0.020} _{-0.020}	1.27 ^{+0.038} _{-0.154}	∞	43.83	2.45
5	-0.15	0.08	1.34 ^{+0.006} _{-0.028}	1.25 ^{+0.058} _{-0.121}	∞	43.87	2.55
6	-0.32	0.08	1.39 ^{+0.010} _{-0.036}	1.31 ^{+0.050} _{-0.150}	∞	43.15	3.99
7	-0.45	-0.13	1.43 ^{+0.019} _{-0.020}	1.38 ^{+0.026} _{-0.203}	∞	41.08	4.91
8	-0.41	-0.04	1.40 ^{+0.042} _{-0.006}	1.39 ^{+0.013} _{-0.187}	∞	41.63	4.61
9	-0.79	-0.30	1.58 ^{+0.006} _{-0.007}	1.24 ^{+0.025} _{-0.014}	∞	40.76	10.79
10	-0.63	0.25	1.56 ^{+0.022} _{-0.032}	1.50 ^{+0.005} _{-0.064}	212	18.66	5.92
11	-0.48	-0.06	1.46 ^{+0.007} _{-0.031}	1.36 ^{+0.069} _{-0.070}	∞	40.76	5.37
12	-0.48	-0.15	1.43 ^{+0.042} _{-0.013}	1.41 ^{+0.024} _{-0.138}	∞	40.04	5.03
13	-0.70	-0.07	1.57 ^{+0.031} _{-0.056}	1.32 ^{+0.160} _{-0.136}	∞	37.59	8.41
14	-0.40	0.39	1.44 ^{+0.025} _{-0.016}	1.40 ^{+0.025} _{-0.098}	∞	40.04	5.09
15	-0.78	0.03	1.52 ^{+0.029} _{-0.008}	1.11 ^{+0.043} _{-0.020}	∞	43.69	12.28
16	-0.96	-0.00	1.62 ^{+0.009} _{-0.006}	1.11 ^{+0.015} _{-0.012}	∞	42.77	18.20
17	-0.84	0.01	1.56 ^{+0.020} _{-0.015}	1.13 ^{+0.017} _{-0.019}	∞	43.25	13.75
18	-0.74	-0.13	1.59 ^{+0.018} _{-0.016}	1.42 ^{+0.043} _{-0.016}	∞	26.06	7.07
19	-0.84	0.03	1.58 ^{+0.006} _{-0.007}	1.16 ^{+0.022} _{-0.007}	∞	42.62	13.60
20	-0.90	-0.20	1.54 ^{+0.002} _{-0.001}	1.07 ^{+0.011} _{-0.011}	∞	43.79	15.20
21	-0.94	0.43	1.58 ^{+0.013} _{-0.012}	1.56 ^{+0.013} _{-0.012}	78	6.74	5.61
22	-0.96	0.16	1.72 ^{+0.007} _{-0.032}	1.31 ^{+0.027} _{-0.017}	∞	23.24	13.53

TABLE B.2 (CONTINUED)

ID	[Zr/Dy]	[Th/Dy]	M_1	M_2	τ	m_{wind}	m_{dyn}
	model	model	(M_\odot)	(M_\odot)	(ms)	($10^{-3} M_\odot$)	($10^{-3} M_\odot$)
23	-0.85	0.13	$1.66^{+0.009}_{-0.022}$	$1.35^{+0.006}_{-0.019}$	∞	26.06	10.20
24	-0.19	-0.16	$1.32^{+0.006}_{-0.005}$	$1.30^{+0.007}_{-0.006}$	∞	43.74	2.58
25	-0.76	-0.18	$1.61^{+0.015}_{-0.039}$	$1.45^{+0.017}_{-0.076}$	212	18.66	6.91
26	-1.03	-0.26	$1.58^{+0.008}_{-0.009}$	$1.56^{+0.008}_{-0.009}$	78	6.74	5.61
27	-0.79	0.17	$1.62^{+0.032}_{-0.099}$	$1.35^{+0.094}_{-0.241}$	∞	30.94	9.11
28	-0.85	0.31	$1.66^{+0.030}_{-0.019}$	$1.34^{+0.063}_{-0.018}$	∞	27.38	10.50
29	-0.88	-0.20	$1.64^{+0.030}_{-0.007}$	$1.33^{+0.048}_{-0.074}$	∞	30.94	10.22
30	-0.99	-0.47	$1.62^{+0.014}_{-0.009}$	$1.09^{+0.014}_{-0.013}$	∞	43.03	19.30

TABLE B.3
INDIVIDUAL RESULTS USING ALF2

ID	[Zr/Dy]	[Th/Dy]	M_1	M_2	τ	m_{wind}	m_{dyn}
	model	model	(M_\odot)	(M_\odot)	(ms)	($10^{-3} M_\odot$)	($10^{-3} M_\odot$)
1	0.20	0.02	$1.26^{+0.006}_{-0.006}$	$1.22^{+0.008}_{-0.015}$	∞	43.52	0.79
2	-0.16	0.19	$1.39^{+0.019}_{-0.053}$	$1.24^{+0.044}_{-0.047}$	133	40.85	4.34
3	-0.19	-0.07	$1.38^{+0.033}_{-0.049}$	$1.30^{+0.044}_{-0.127}$	64	38.64	4.02
4	-0.19	-0.24	$1.39^{+0.005}_{-0.037}$	$1.27^{+0.033}_{-0.050}$	86	39.65	4.24
5	-0.14	0.10	$1.38^{+0.011}_{-0.047}$	$1.26^{+0.040}_{-0.044}$	115	40.48	4.00
6	-0.30	0.11	$1.42^{+0.029}_{-0.060}$	$1.19^{+0.088}_{-0.013}$	179	41.47	5.86
7	-0.45	-0.08	$1.46^{+0.012}_{-0.029}$	$1.16^{+0.009}_{-0.007}$	155	41.17	8.16
8	-0.42	-0.02	$1.44^{+0.019}_{-0.040}$	$1.16^{+0.009}_{-0.008}$	208	41.74	7.25

TABLE B.3 (CONTINUED)

ID	[Zr/Dy]	[Th/Dy]	M_1	M_2	τ	m_{wind}	m_{dyn}
	model	model	(M_\odot)	(M_\odot)	(ms)	($10^{-3} M_\odot$)	($10^{-3} M_\odot$)
9	-0.79	-0.27	$1.58^{+0.028}_{-0.043}$	$1.06^{+0.040}_{-0.008}$	115	40.48	19.07
10	-0.62	0.30	$1.40^{+0.008}_{-0.005}$	$1.02^{+0.010}_{-0.020}$	∞	43.86	9.06
11	-0.46	0.01	$1.48^{+0.009}_{-0.006}$	$1.16^{+0.005}_{-0.006}$	115	40.48	9.09
12	-0.49	-0.10	$1.47^{+0.007}_{-0.075}$	$1.15^{+0.005}_{-0.016}$	155	41.17	8.90
13	-0.69	-0.04	$1.52^{+0.021}_{-0.010}$	$1.08^{+0.003}_{-0.003}$	208	41.74	14.19
14	-0.39	0.43	$1.48^{+0.012}_{-0.018}$	$1.16^{+0.013}_{-0.009}$	115	40.48	9.09
15	-0.80	-0.03	$1.60^{+0.004}_{-0.004}$	$1.20^{+0.013}_{-0.021}$	12	27.44	13.30
16	-0.95	0.02	$1.68^{+0.015}_{-0.071}$	$1.00^{+0.012}_{-0.027}$	64	38.64	30.71
17	-0.85	0.04	$1.59^{+0.062}_{-0.027}$	$1.02^{+0.113}_{-0.005}$	179	41.47	22.32
18	-0.74	-0.08	$1.58^{+0.006}_{-0.019}$	$1.08^{+0.020}_{-0.006}$	86	39.65	17.93
19	-0.84	0.02	$1.64^{+0.009}_{-0.057}$	$1.09^{+0.045}_{-0.066}$	31	35.19	21.12
20	-0.89	-0.17	$1.63^{+0.018}_{-0.046}$	$1.02^{+0.015}_{-0.008}$	99	40.09	25.27
21	-0.95	0.40	$1.72^{+0.008}_{-0.013}$	$1.03^{+0.032}_{-0.067}$	24	33.35	31.09
22	-0.95	0.14	$1.50^{+0.004}_{-0.004}$	$1.42^{+0.005}_{-0.004}$	2	8.28	5.84
23	-0.84	0.17	$1.62^{+0.043}_{-0.025}$	$1.02^{+0.075}_{-0.009}$	115	40.48	24.53
24	-0.20	-0.16	$1.38^{+0.003}_{-0.003}$	$1.30^{+0.005}_{-0.009}$	64	38.64	4.02
25	-0.77	-0.14	$1.56^{+0.013}_{-0.040}$	$1.06^{+0.012}_{-0.005}$	155	41.17	17.75
26	-1.02	-0.26	$1.71^{+0.009}_{-0.029}$	$1.02^{+0.085}_{-0.053}$	31	35.19	31.24
27	-0.78	0.15	$1.62^{+0.010}_{-0.010}$	$1.14^{+0.024}_{-0.096}$	20	32.32	17.06
28	-0.84	0.31	$1.66^{+0.008}_{-0.035}$	$1.06^{+0.057}_{-0.049}$	36	36.00	24.46
29	-0.88	-0.17	$1.59^{+0.039}_{-0.034}$	$1.02^{+0.013}_{-0.006}$	179	41.47	22.32
30	-0.99	-0.46	$1.50^{+0.012}_{-0.007}$	$0.96^{+0.011}_{-0.016}$	∞	43.66	19.41

TABLE B.4
INDIVIDUAL RESULTS USING LS220

ID	[Zr/Dy]	[Th/Dy]	M_1	M_2	τ	m_{wind}	m_{dyn}
	model	model	(M _⊕)	(M _⊕)	(ms)	(10 ⁻³ M _⊕)	(10 ⁻³ M _⊕)
1	0.23	0.02	1.22 ^{+0.009} _{-0.009}	1.20 ^{+0.011} _{-0.010}	∞	43.33	0.71
2	-0.16	0.18	1.33 ^{+0.012} _{-0.026}	1.26 ^{+0.050} _{-0.015}	193	38.72	3.75
3	-0.19	-0.04	1.33 ^{+0.017} _{-0.046}	1.29 ^{+0.019} _{-0.055}	124	36.78	3.95
4	-0.18	-0.30	1.29 ^{+0.030} _{-0.018}	1.28 ^{+0.024} _{-0.018}	261	39.75	3.23
5	-0.15	0.09	1.30 ^{+0.015} _{-0.020}	1.29 ^{+0.007} _{-0.030}	193	38.72	3.50
6	-0.31	0.07	1.40 ^{+0.014} _{-0.051}	1.26 ^{+0.013} _{-0.072}	69	33.26	5.31
7	-0.44	-0.10	1.44 ^{+0.016} _{-0.085}	1.18 ^{+0.068} _{-0.064}	124	36.78	7.46
8	-0.42	-0.02	1.43 ^{+0.018} _{-0.020}	1.18 ^{+0.061} _{-0.018}	143	37.49	7.09
9	-0.79	-0.28	1.54 ^{+0.042} _{-0.056}	1.06 ^{+0.040} _{-0.011}	166	38.13	16.27
10	-0.64	0.17	1.48 ^{+0.002} _{-0.001}	1.27 ^{+0.008} _{-0.011}	19	20.72	7.18
11	-0.48	-0.09	1.44 ^{+0.006} _{-0.006}	1.26 ^{+0.012} _{-0.015}	38	28.47	6.30
12	-0.48	-0.13	1.42 ^{+0.054} _{-0.011}	1.15 ^{+0.084} _{-0.013}	261	39.75	7.23
13	-0.70	-0.14	1.40 ^{+0.014} _{-0.014}	1.38 ^{+0.014} _{-0.015}	12	15.49	5.23
14	-0.39	0.42	1.44 ^{+0.018} _{-0.027}	1.16 ^{+0.013} _{-0.011}	166	38.13	7.85
15	-0.79	-0.01	1.42 ^{+0.008} _{-0.008}	1.38 ^{+0.009} _{-0.008}	9	12.03	5.37
16	-0.96	0.02	1.65 ^{+0.015} _{-0.069}	0.99 ^{+0.035} _{-0.015}	92	35.16	27.86
17	-0.84	0.02	1.53 ^{+0.088} _{-0.085}	1.03 ^{+0.084} _{-0.036}	∞	40.19	17.22
18	-0.75	-0.17	1.42 ^{+0.009} _{-0.005}	1.37 ^{+0.004} _{-0.015}	11	13.75	5.37
19	-0.83	0.05	1.59 ^{+0.019} _{-0.040}	1.04 ^{+0.067} _{-0.020}	107	36.01	20.37
20	-0.90	-0.18	1.60 ^{+0.020} _{-0.070}	1.02 ^{+0.013} _{-0.011}	124	36.78	22.28
21	-0.95	0.44	1.50 ^{+0.009} _{-0.010}	0.93 ^{+0.015} _{-0.013}	∞	43.23	21.15
22	-0.97	0.18	1.65 ^{+0.018} _{-0.045}	0.97 ^{+0.088} _{-0.011}	124	36.78	29.54

TABLE B.4 (CONTINUED)

ID	[Zr/Dy]	[Th/Dy]	M_1	M_2	τ	m_{wind}	m_{dyn}
	model	model	(M_\odot)	(M_\odot)	(ms)	($10^{-3} M_\odot$)	($10^{-3} M_\odot$)
23	-0.84	0.05	$1.44^{+0.010}_{-0.026}$	$1.37^{+0.035}_{-0.010}$	8	10.37	5.56
24	-0.20	-0.14	$1.32^{+0.029}_{-0.051}$	$1.30^{+0.012}_{-0.073}$	124	36.78	3.88
25	-0.76	-0.16	$1.54^{+0.030}_{-0.039}$	$1.07^{+0.077}_{-0.016}$	143	37.49	15.77
26	-1.02	-0.25	$1.64^{+0.009}_{-0.021}$	$0.97^{+0.003}_{-0.015}$	143	37.49	28.82
27	-0.78	0.19	$1.56^{+0.036}_{-0.045}$	$1.04^{+0.104}_{-0.011}$	166	38.13	18.53
28	-0.87	0.24	$1.42^{+0.010}_{-0.012}$	$1.40^{+0.010}_{-0.013}$	7	8.79	5.39
29	-0.88	-0.19	$1.57^{+0.050}_{-0.031}$	$1.02^{+0.090}_{-0.007}$	193	38.72	20.35
30	-0.98	-0.48	$1.54^{+0.007}_{-0.007}$	$1.26^{+0.009}_{-0.008}$	9	12.03	8.97

TABLE B.5
INDIVIDUAL RESULTS USING MPA1

ID	[Zr/Dy]	[Th/Dy]	M_1	M_2	τ	m_{wind}	m_{dyn}
	model	model	(M_\odot)	(M_\odot)	(ms)	($10^{-3} M_\odot$)	($10^{-3} M_\odot$)
1	0.23	0.02	$1.20^{+0.004}_{-0.004}$	$1.15^{+0.014}_{-0.011}$	∞	44.15	0.74
2	-0.16	0.17	$1.27^{+0.011}_{-0.031}$	$1.16^{+0.078}_{-0.020}$	∞	44.03	2.72
3	-0.20	-0.06	$1.27^{+0.015}_{-0.025}$	$1.17^{+0.069}_{-0.055}$	∞	44.01	2.74
4	-0.18	-0.28	$1.24^{+0.011}_{-0.007}$	$1.22^{+0.009}_{-0.015}$	∞	43.96	2.46
5	-0.14	0.08	$1.24^{+0.013}_{-0.008}$	$1.22^{+0.013}_{-0.011}$	∞	43.96	2.46
6	-0.31	0.08	$1.31^{+0.014}_{-0.024}$	$1.24^{+0.049}_{-0.067}$	∞	43.52	3.91
7	-0.46	-0.12	$1.36^{+0.031}_{-0.025}$	$1.34^{+0.012}_{-0.232}$	∞	40.97	4.96
8	-0.42	-0.04	$1.35^{+0.019}_{-0.018}$	$1.21^{+0.120}_{-0.006}$	∞	43.44	4.86

TABLE B.5 (CONTINUED)

ID	[Zr/Dy]	[Th/Dy]	M_1	M_2	τ	m_{wind}	m_{dyn}
	model	model	(M_\odot)	(M_\odot)	(ms)	($10^{-3} M_\odot$)	($10^{-3} M_\odot$)
9	-0.79	-0.30	$1.50^{+0.005}_{-0.004}$	$1.16^{+0.006}_{-0.009}$	∞	42.04	10.99
10	-0.63	0.25	$1.48^{+0.004}_{-0.004}$	$1.21^{+0.016}_{-0.010}$	∞	41.28	8.78
11	-0.48	-0.06	$1.38^{+0.016}_{-0.013}$	$1.36^{+0.013}_{-0.032}$	∞	39.41	5.17
12	-0.49	-0.15	$1.38^{+0.026}_{-0.013}$	$1.36^{+0.012}_{-0.090}$	∞	39.41	5.17
13	-0.69	-0.07	$1.49^{+0.019}_{-0.018}$	$1.22^{+0.071}_{-0.040}$	∞	40.63	8.86
14	-0.41	0.39	$1.39^{+0.015}_{-0.030}$	$1.32^{+0.048}_{-0.125}$	∞	40.63	5.25
15	-0.80	0.02	$1.50^{+0.009}_{-0.007}$	$1.43^{+0.008}_{-0.017}$	∞	19.74	5.54
16	-0.95	-0.00	$1.50^{+0.005}_{-0.006}$	$1.47^{+0.015}_{-0.004}$	∞	13.16	5.21
17	-0.86	0.01	$1.58^{+0.006}_{-0.098}$	$1.28^{+0.018}_{-0.215}$	∞	29.80	9.82
18	-0.74	-0.14	$1.48^{+0.007}_{-0.006}$	$1.16^{+0.012}_{-0.014}$	∞	42.44	10.16
19	-0.81	0.03	$1.48^{+0.010}_{-0.008}$	$1.46^{+0.009}_{-0.008}$	∞	18.11	5.30
20	-0.89	-0.21	$1.30^{+0.006}_{-0.005}$	$0.78^{+0.007}_{-0.012}$	∞	44.24	15.08
21	-0.93	0.44	$1.50^{+0.007}_{-0.007}$	$1.48^{+0.008}_{-0.007}$	∞	11.57	5.15
22	-0.94	0.16	$1.30^{+0.010}_{-0.008}$	$0.73^{+0.002}_{-0.010}$	∞	44.25	18.87
23	-0.86	0.13	$1.58^{+0.013}_{-0.009}$	$1.19^{+0.070}_{-0.026}$	∞	37.80	13.13
24	-0.21	-0.16	$1.26^{+0.011}_{-0.023}$	$1.21^{+0.021}_{-0.055}$	∞	43.93	2.74
25	-0.76	-0.19	$1.46^{+0.016}_{-0.015}$	$1.11^{+0.020}_{-0.016}$	∞	43.36	10.88
26	-1.01	-0.26	$1.54^{+0.009}_{-0.005}$	$1.02^{+0.007}_{-0.012}$	∞	43.44	19.62
27	-0.78	0.17	$1.56^{+0.005}_{-0.005}$	$1.30^{+0.022}_{-0.088}$	∞	29.80	8.72
28	-0.84	0.31	$1.50^{+0.033}_{-0.016}$	$1.05^{+0.043}_{-0.018}$	∞	43.52	15.49
29	-0.86	-0.21	$1.57^{+0.018}_{-0.005}$	$1.28^{+0.025}_{-0.079}$	∞	30.97	9.55
30	-0.99	-0.47	$1.58^{+0.011}_{-0.020}$	$1.07^{+0.017}_{-0.013}$	∞	42.25	19.12

TABLE B.6
INDIVIDUAL RESULTS USING SFHO

ID	[Zr/Dy]	[Th/Dy]	M_1	M_2	τ	m_{wind}	m_{dyn}
	model	model	(M _⊕)	(M _⊕)	(ms)	(10 ⁻³ M _⊕)	(10 ⁻³ M _⊕)
1	0.24	0.01	1.16 ^{+0.007} _{-0.006}	1.12 ^{+0.014} _{-0.008}	∞	43.80	0.71
2	-0.17	0.17	1.21 ^{+0.023} _{-0.012}	1.19 ^{+0.006} _{-0.055}	∞	42.54	2.72
3	-0.20	-0.06	1.22 ^{+0.012} _{-0.018}	1.17 ^{+0.023} _{-0.032}	∞	42.72	2.69
4	-0.18	-0.28	1.20 ^{+0.013} _{-0.012}	1.18 ^{+0.013} _{-0.019}	∞	42.88	2.42
5	-0.14	0.08	1.20 ^{+0.012} _{-0.010}	1.18 ^{+0.013} _{-0.012}	∞	42.88	2.42
6	-0.31	0.08	1.26 ^{+0.009} _{-0.012}	1.19 ^{+0.027} _{-0.155}	∞	41.30	3.66
7	-0.45	-0.11	1.35 ^{+0.017} _{-0.043}	1.24 ^{+0.031} _{-0.009}	250	31.73	5.35
8	-0.42	-0.03	1.34 ^{+0.016} _{-0.066}	1.25 ^{+0.045} _{-0.022}	250	31.73	5.14
9	-0.80	-0.32	1.36 ^{+0.000} _{-0.000}	1.36 ^{+0.000} _{-0.001}	37	10.66	5.17
10	-0.62	0.26	1.46 ^{+0.005} _{-0.040}	1.17 ^{+0.032} _{-0.035}	137	26.28	9.25
11	-0.48	-0.05	1.37 ^{+0.016} _{-0.059}	1.22 ^{+0.040} _{-0.098}	250	31.73	5.89
12	-0.49	-0.13	1.38 ^{+0.006} _{-0.066}	1.24 ^{+0.021} _{-0.122}	159	27.77	5.89
13	-0.72	-0.08	1.36 ^{+0.014} _{-0.011}	1.35 ^{+0.003} _{-0.021}	43	12.38	5.17
14	-0.40	0.39	1.31 ^{+0.076} _{-0.007}	1.22 ^{+0.074} _{-0.100}	∞	37.34	4.69
15	-0.79	0.03	1.50 ^{+0.011} _{-0.066}	1.10 ^{+0.062} _{-0.018}	215	30.50	13.22
16	-0.97	0.00	1.40 ^{+0.011} _{-0.007}	0.87 ^{+0.020} _{-0.010}	∞	43.85	19.04
17	-0.85	0.01	1.38 ^{+0.007} _{-0.004}	0.93 ^{+0.017} _{-0.010}	∞	43.62	14.13
18	-0.74	-0.12	1.46 ^{+0.011} _{-0.020}	1.12 ^{+0.006} _{-0.006}	290	32.87	10.80
19	-0.83	0.03	1.52 ^{+0.006} _{-0.036}	1.09 ^{+0.046} _{-0.014}	185	29.18	14.56
20	-0.91	-0.20	1.52 ^{+0.011} _{-0.009}	1.06 ^{+0.012} _{-0.002}	290	32.87	16.03
21	-0.97	0.41	1.42 ^{+0.005} _{-0.003}	1.33 ^{+0.003} _{-0.013}	24	6.07	5.55
22	-0.97	0.17	1.56 ^{+0.004} _{-0.002}	1.02 ^{+0.002} _{-0.001}	290	32.87	20.49

TABLE B.6 (CONTINUED)

ID	[Zr/Dy]	[Th/Dy]	M_1	M_2	τ	m_{wind}	m_{dyn}
	model	model	(M_\odot)	(M_\odot)	(ms)	($10^{-3} M_\odot$)	($10^{-3} M_\odot$)
23	-0.86	0.13	$1.30^{+0.008}_{-0.008}$	$0.79^{+0.012}_{-0.015}$	∞	44.20	15.36
24	-0.20	-0.16	$1.21^{+0.023}_{-0.018}$	$1.18^{+0.019}_{-0.062}$	∞	42.72	2.60
25	-0.75	-0.17	$1.47^{+0.022}_{-0.057}$	$1.12^{+0.069}_{-0.021}$	250	31.73	11.20
26	-0.98	-0.27	$1.42^{+0.009}_{-0.008}$	$1.32^{+0.013}_{-0.008}$	28	7.47	5.65
27	-0.78	0.18	$1.51^{+0.004}_{-0.026}$	$1.10^{+0.011}_{-0.013}$	185	29.18	13.66
28	-0.84	0.32	$1.54^{+0.007}_{-0.042}$	$1.07^{+0.051}_{-0.015}$	185	29.18	16.50
29	-0.89	-0.20	$1.53^{+0.012}_{-0.050}$	$1.08^{+0.018}_{-0.015}$	185	29.18	15.51
30	-1.01	-0.46	$1.59^{+0.006}_{-0.059}$	$1.03^{+0.058}_{-0.019}$	159	27.77	21.51

B.2 Model Variations

This section displays the ADMC results as total mass distributions and individual M_1 - M_2 solutions (where applicable) for all variations discussed in Section 8.5. Figures B.1 shows the mass distributions when the r -II stars are removed, while Figure B.2 shows the same distributions when the results are rescaled by Galactic [Eu/Fe] distributions. The results varying the ejecta composition are shown next; Figures B.3 and B.4 display the individual mass combinations and total mass distribution when the dynamical ejecta contributions some limited- r material (an increase of 1.8 dex to the final Zr abundance). Figures B.5 and B.6 show the results when the initial neutron-richness of the disk wind ejecta is decreased by about 10% (Y_e increased by 0.03). Lastly, Figure B.7 and B.8 show the mass results when no prior is supplied to the MCMC.

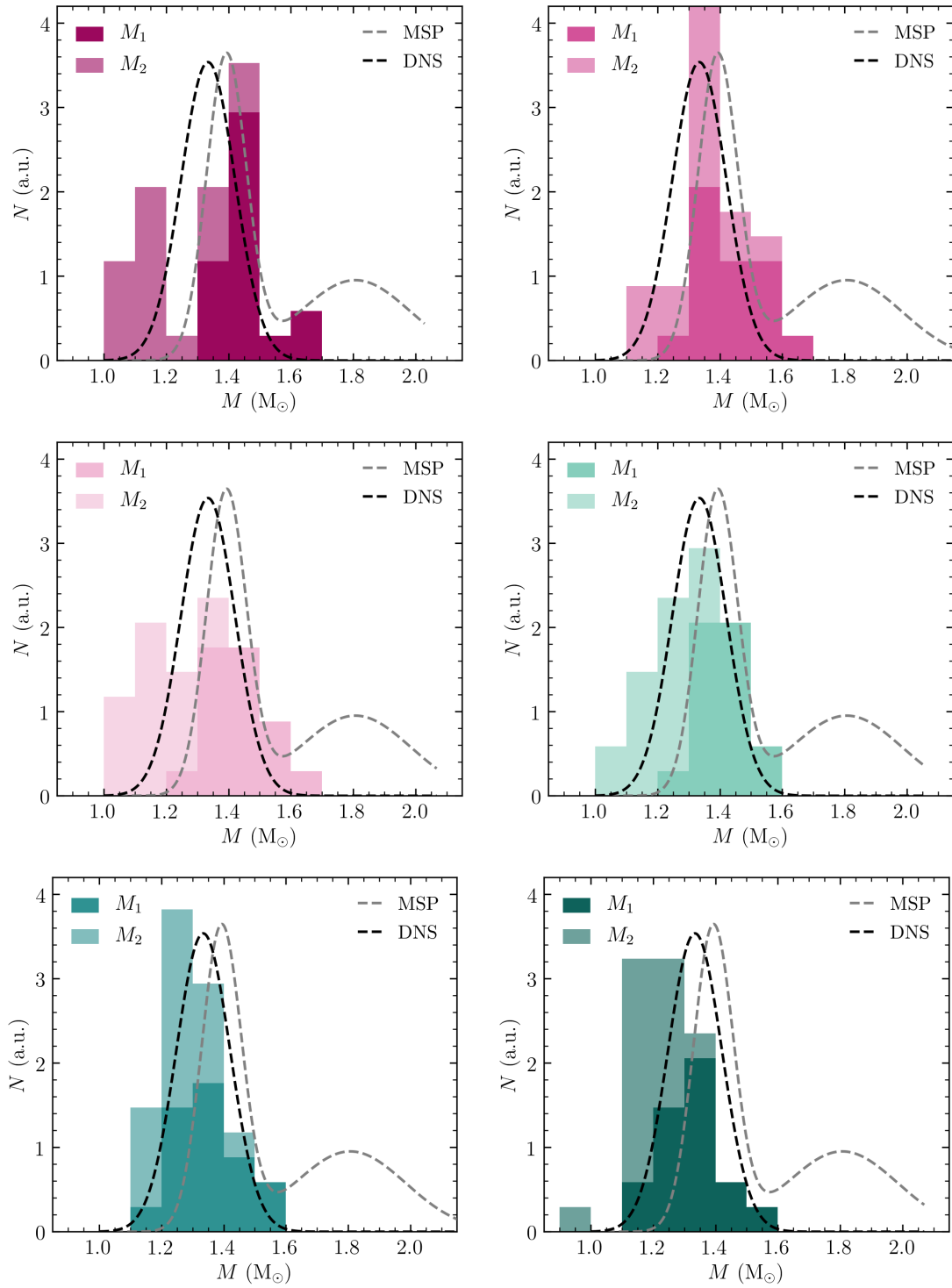


Figure B.1. Scaled mass distributions for each EOS choice when r -II stars are removed.

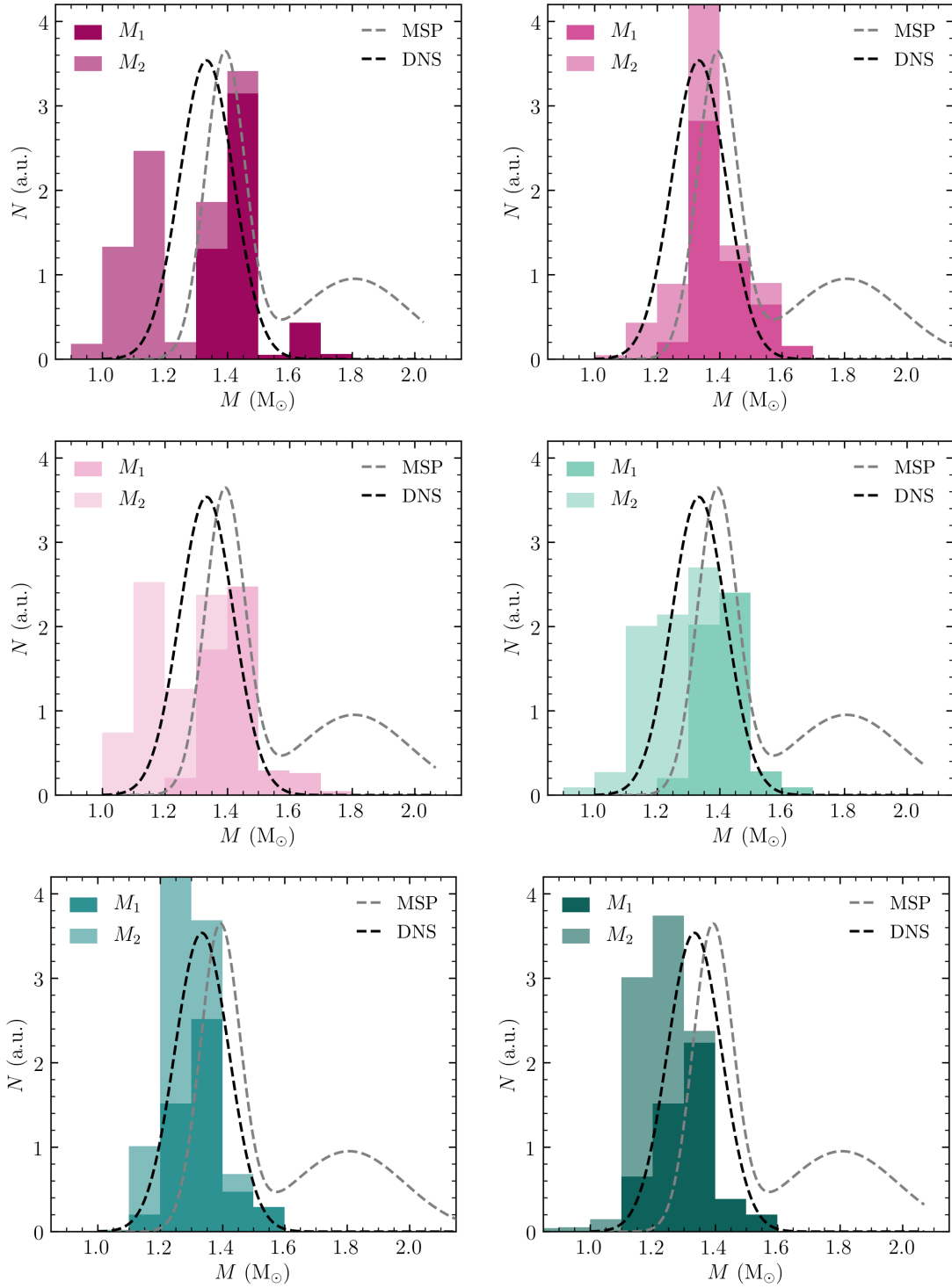


Figure B.2. Scaled mass distributions for each EOS choice, re-weighted by the [Eu/Fe] distributions of RPA measurements.

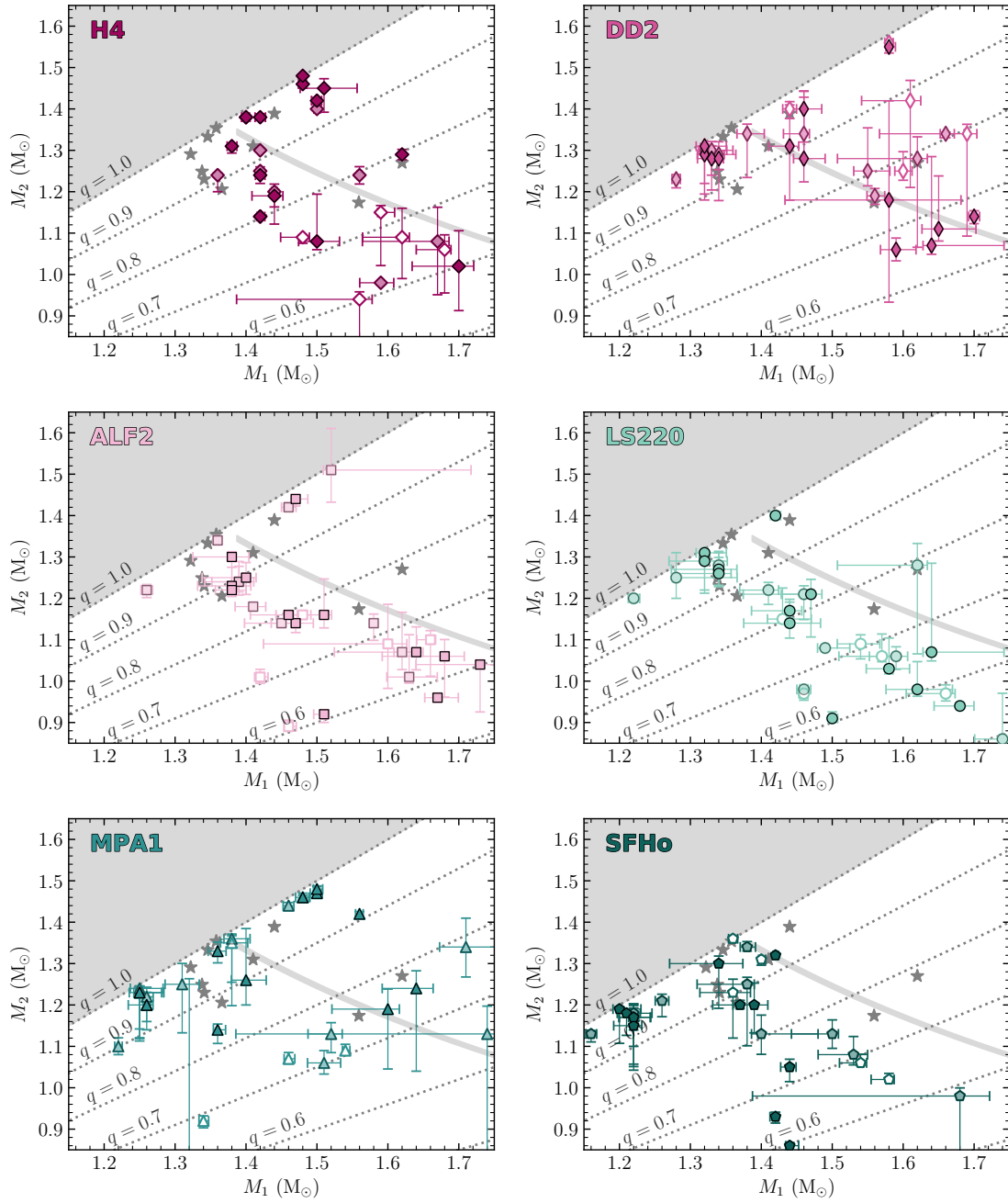


Figure B.3. Mass results for each EOS choice when the Zr abundance of the dynamical ejecta is increased by 1.8 dex.

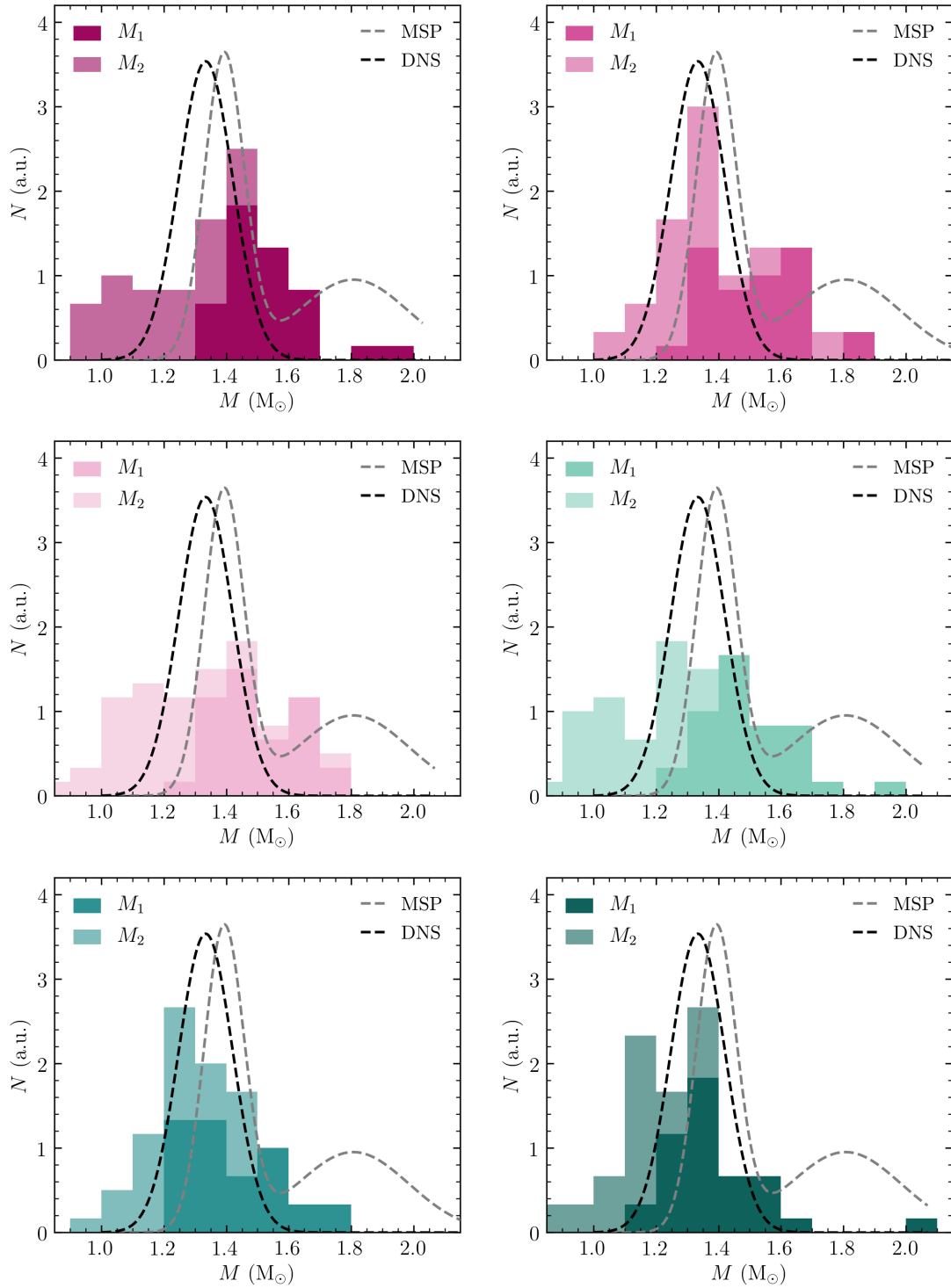


Figure B.4. Scaled mass distributions in arbitrary units for each EOS choice when the Zr abundance of the dynamical ejecta is increased by 1.8 dex.

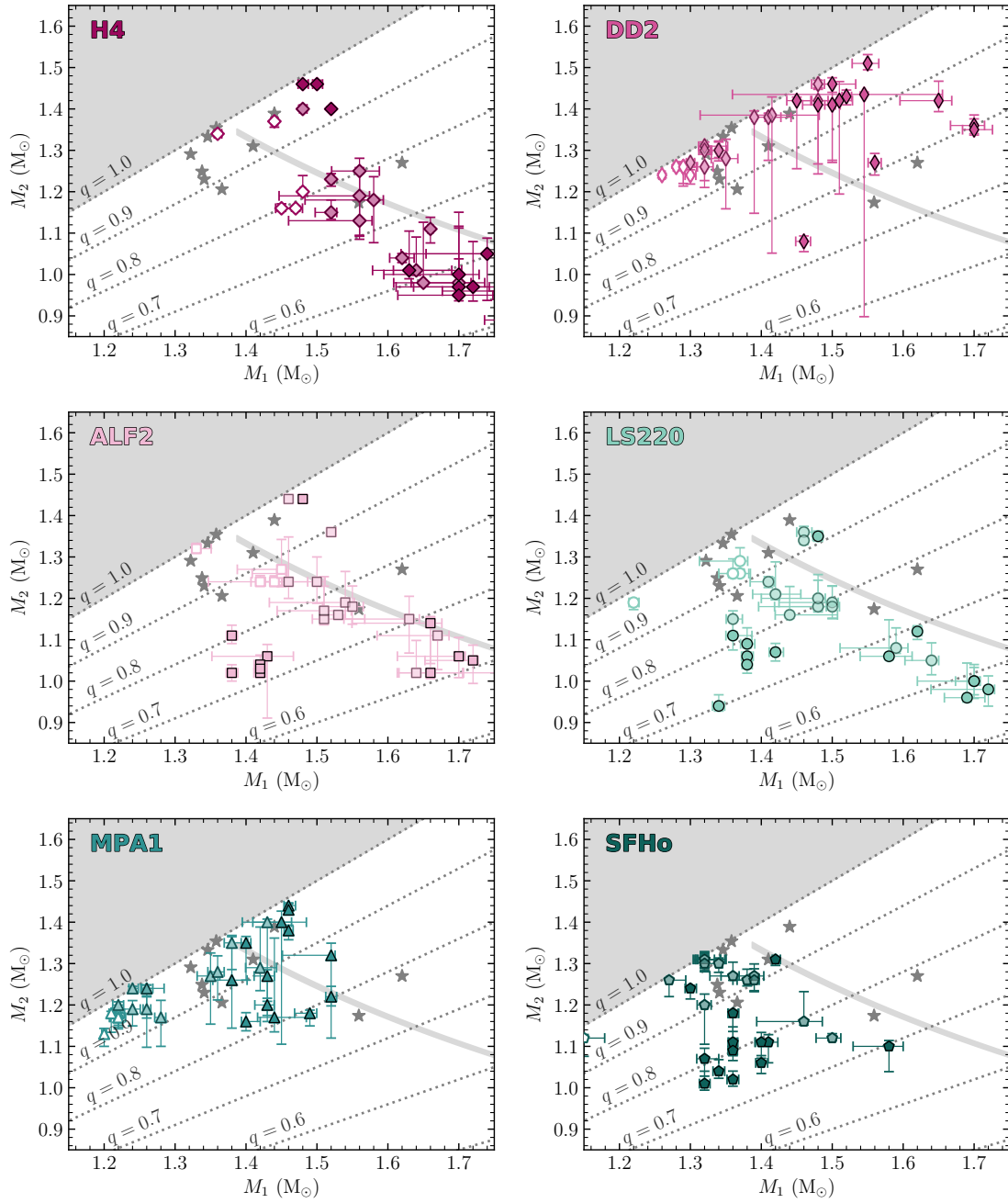


Figure B.5. Mass results for each EOS choice when the Y_e of the disk wind is effectively shifted by 0.03.

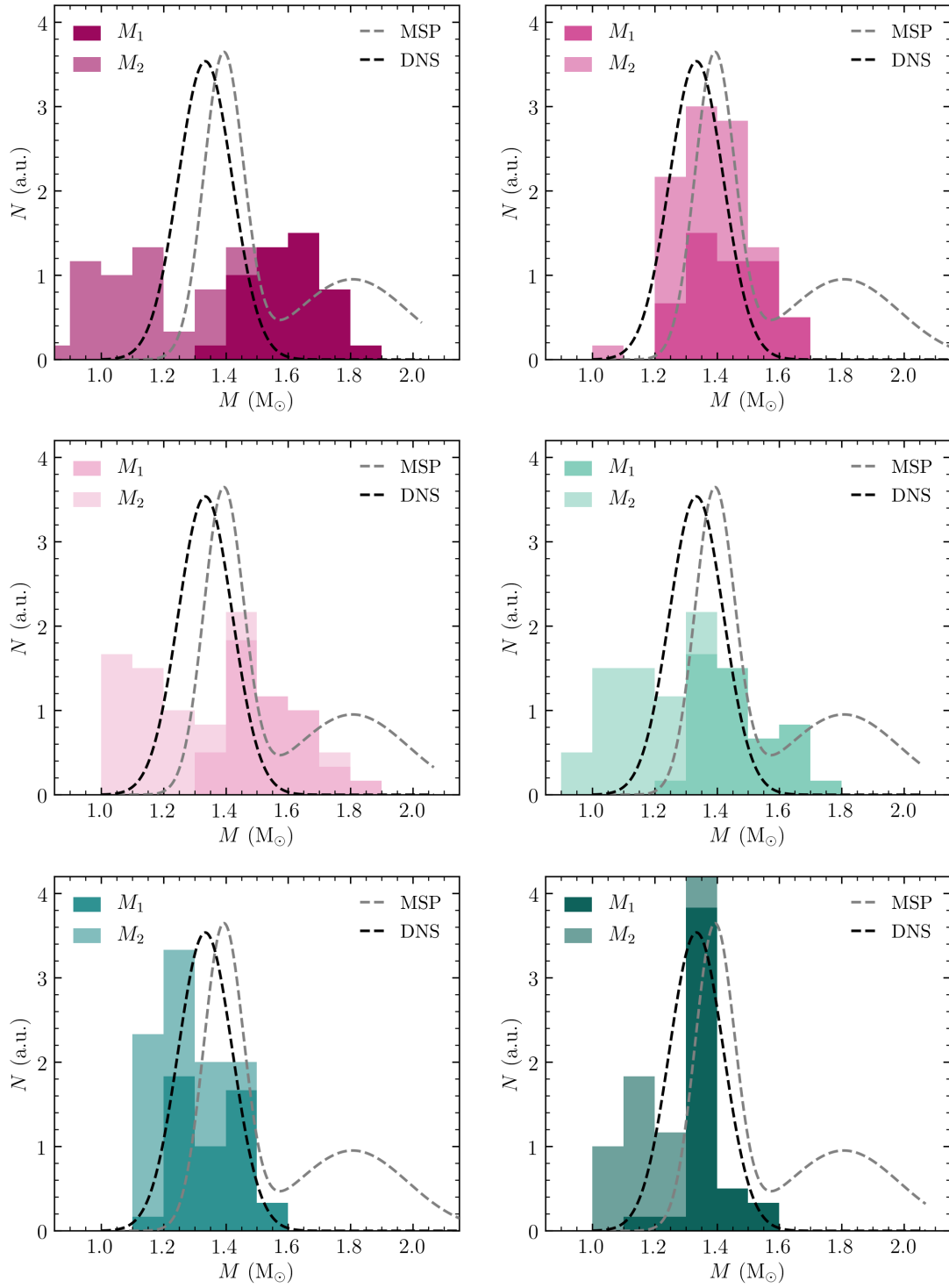


Figure B.6. Scaled mass distributions when the Y_e of the disk wind is effectively shifted by 0.03.

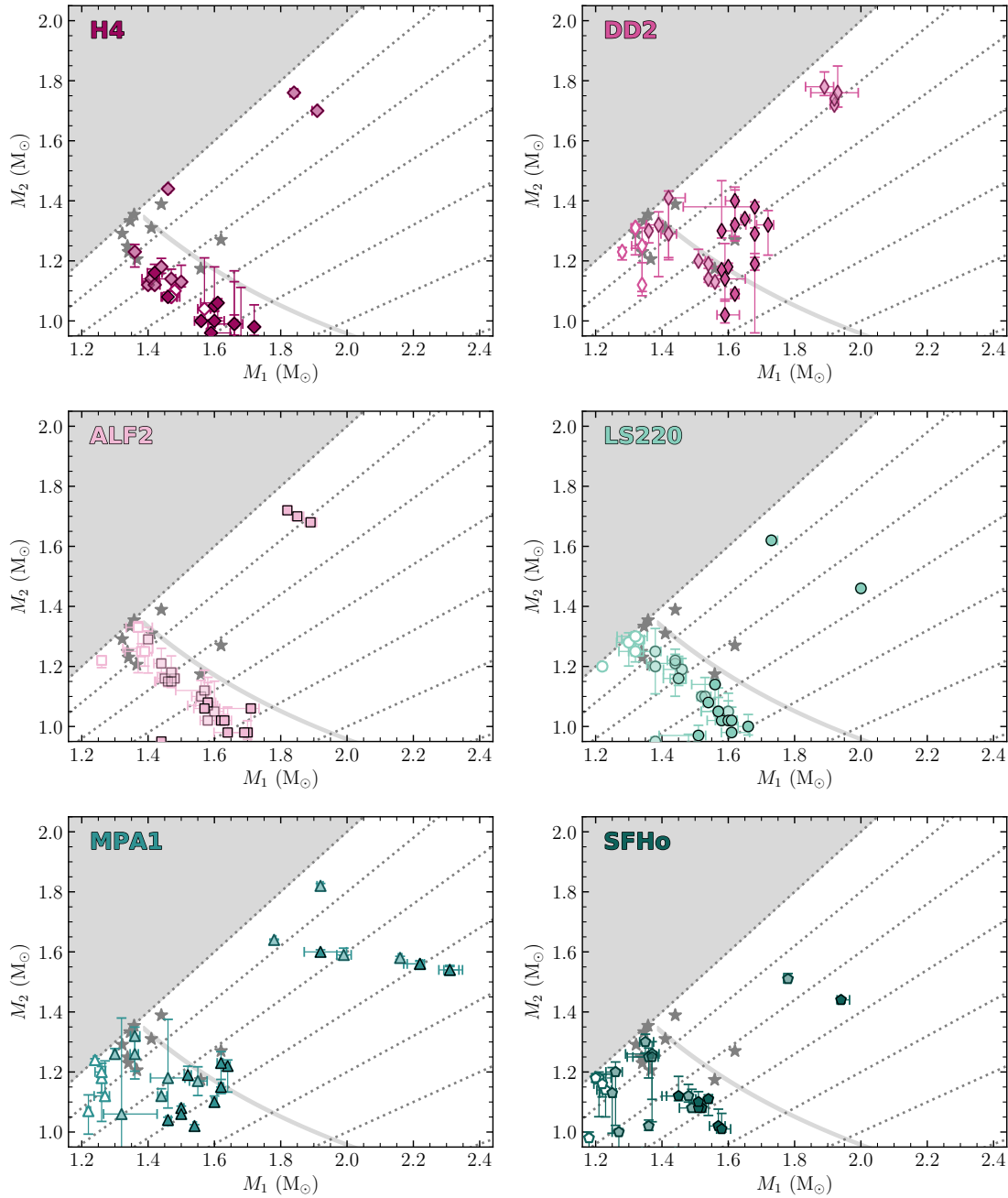


Figure B.7. Mass results for each EOS choice when the prior is removed.

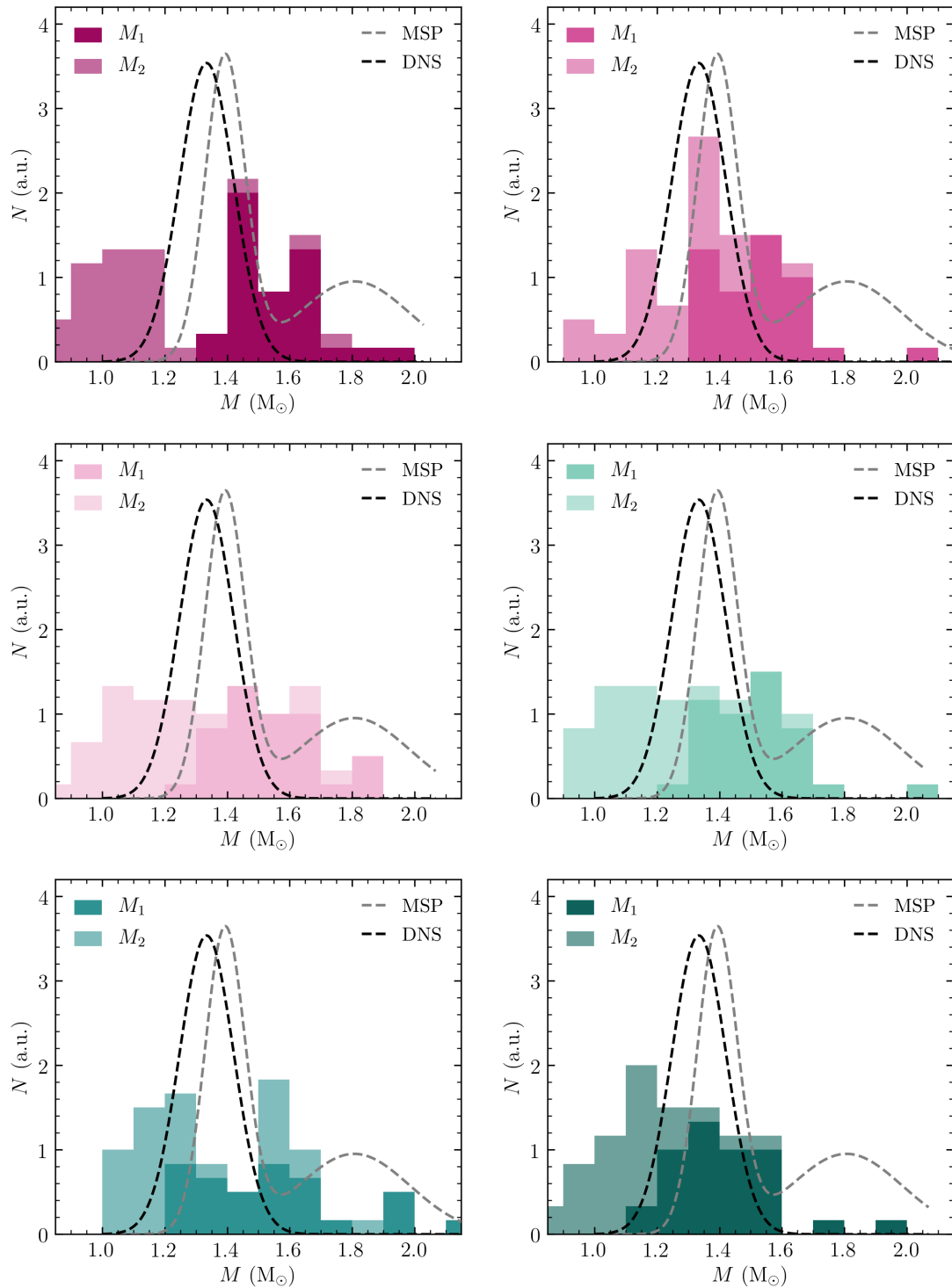


Figure B.8. Scaled mass distributions when the prior is removed.

BIBLIOGRAPHY

- B. P. Abbott, R. Abbott, T. D. Abbott, F. Acernese, K. Ackley, C. Adams, T. Adams, P. Addesso, R. X. Adhikari, V. B. Adya, et al. GW170817: Observation of Gravitational Waves from a Binary Neutron Star Inspiral. *PhRvL*, 119(16):161101, [Oct. 2017](#).
- A. Abohalima and A. Frebel. JINAbase—A Database for Chemical Abundances of Metal-poor Stars. *ApJS*, 238(2):36, [Oct. 2018](#).
- H. Akaike. Maximum likelihood identification of gaussian autoregressive moving average models. *Biometrika*, 60(2):255–265, 1973.
- M. Alford, M. Braby, M. Paris, and S. Reddy. Hybrid Stars that Masquerade as Neutron Stars. *ApJ*, 629(2):969–978, [Aug. 2005](#).
- A. Alonso, S. Arribas, and C. Martínez-Roger. The effective temperature scale of giant stars (F0-K5). II. Empirical calibration of T_{eff} versus colours and [Fe/H]. *A&AS*, 140:261–277, [Dec. 1999](#).
- S. M. Andrievsky, F. Spite, S. A. Korotin, P. François, M. Spite, P. Bonifacio, R. Cayrel, and V. Hill. NLTE strontium abundance in a sample of extremely metal poor stars and the Sr/Ba ratio in the early Galaxy. *A&A*, 530:A105, [June 2011](#).
- J. Antoniadis, P. C. C. Freire, N. Wex, T. M. Tauris, R. S. Lynch, M. H. van Kerkwijk, M. Kramer, C. Bassa, V. S. Dhillon, T. Driebe, et al. A Massive Pulsar in a Compact Relativistic Binary. *Science*, 340(6131):448, [Apr. 2013](#).
- J. Antoniadis, T. M. Tauris, F. Ozel, E. Barr, D. J. Champion, and P. C. C. Freire. The millisecond pulsar mass distribution: Evidence for bimodality and constraints on the maximum neutron star mass. *arXiv e-prints*, art. arXiv:1605.01665, May 2016.
- W. Aoki, S. Honda, K. Sadakane, and N. Arimoto. First Determination of the Actinide Thorium Abundance for a Red Giant of the Ursa Minor Dwarf Galaxy. *PASJ*, 59:L15–L19, [June 2007](#).
- A. Aprahamian, R. Surman, A. Frebel, G. C. McLaughlin, A. Arcones, A. B. Balantekin, J. Barnes, T. C. Beers, E. M. Holmbeck, J. Yoon, et al. FRIB and the GW170817 Kilonova. *arXiv e-prints*, art. arXiv:1809.00703, Sept. 2018.

- A. Arcones and F.-K. Thielemann. Neutrino-driven wind simulations and nucleosynthesis of heavy elements. *Journal of Physics G Nuclear Physics*, 40(1):013201, [Jan. 2013](#).
- A. Arcones, H.-T. Janka, and L. Scheck. Nucleosynthesis-relevant conditions in neutrino-driven supernova outflows. I. Spherically symmetric hydrodynamic simulations. *A&A*, 467:1227–1248, [June 2007](#).
- D. Argast, M. Samland, F.-K. Thielemann, and Y.-Z. Qian. Neutron star mergers versus core-collapse supernovae as dominant r-process sites in the early Galaxy. *A&A*, 416:997–1011, [Mar. 2004](#).
- C. Arlandini, F. Käppeler, K. Wissak, R. Gallino, M. Lugaro, M. Busso, and O. Straniero. Neutron Capture in Low-Mass Asymptotic Giant Branch Stars: Cross Sections and Abundance Signatures. *ApJ*, 525:886–900, [Nov. 1999](#).
- M. Arnould, S. Goriely, and K. Takahashi. The r-process of stellar nucleosynthesis: Astrophysics and nuclear physics achievements and mysteries. *Physics Reports*, 450:97–213, [Sept. 2007](#).
- M. Asplund, N. Grevesse, A. J. Sauval, and P. Scott. The Chemical Composition of the Sun. *ARA&A*, 47:481–522, [Sept. 2009](#).
- G. Audi, F. G. Kondev, M. Wang, W. J. Huang, and S. Naimi. The NUBASE2016 evaluation of nuclear properties. *Chinese Physics C*, 41(3):030001, [Mar. 2017](#).
- P. S. Barklem, N. Christlieb, T. C. Beers, V. Hill, M. S. Bessell, J. Holmberg, B. Marsteller, S. Rossi, F.-J. Zickgraf, and D. Reimers. The Hamburg/ESO R-process enhanced star survey (HERES). II. Spectroscopic analysis of the survey sample. *A&A*, 439:129–151, [Aug. 2005](#).
- K. Bechtol, A. Drlica-Wagner, E. Balbinot, A. Pieres, J. D. Simon, B. Yanny, B. Santiago, R. H. Wechsler, J. Frieman, A. R. Walker, et al. Eight New Milky Way Companions Discovered in First-year Dark Energy Survey Data. *ApJ*, 807(1):50, [July 2015](#).
- T. C. Beers and N. Christlieb. The Discovery and Analysis of Very Metal-Poor Stars in the Galaxy. *ARA&A*, 43:531–580, [Sept. 2005](#).
- T. C. Beers, G. W. Preston, and S. A. Shectman. A search for stars of very low metal abundance. I. *AJ*, 90:2089–2102, [Oct. 1985](#).
- T. C. Beers, G. W. Preston, and S. A. Shectman. A search for stars of very low metal abundance. II. *AJ*, 103:1987–2034, [June 1992](#).
- T. C. Beers, N. Christlieb, J. E. Norris, M. S. Bessell, R. Wilhelm, C. Allende Prieto, B. Yanny, C. Rockosi, H. J. Newberg, S. Rossi, and Y. S. Lee. The Metallicity Distribution Function of the Halo of the Milky Way. In V. Hill, P. Francois, and

- F. Primas, editors, *From Lithium to Uranium: Elemental Tracers of Early Cosmic Evolution*, volume 228 of *IAU Symposium*, pages 175–183, [Jan. 2005](#).
- T. C. Beers, J. E. Norris, V. M. Placco, Y. S. Lee, S. Rossi, D. Carollo, and T. Masseron. Population Studies. XIII. A New Analysis of the Bidelman-MacConnell “Weak-metal” Stars—Confirmation of Metal-poor Stars in the Thick Disk of the Galaxy. *ApJ*, 794:58, [Oct. 2014](#).
- T. C. Beers, V. M. Placco, D. Carollo, S. Rossi, Y. S. Lee, A. Frebel, J. E. Norris, S. Dietz, and T. Masseron. Bright Metal-Poor Stars from the Hamburg/ESO Survey. II. A Chemodynamical Analysis. *ApJ*, 835:81, [Jan. 2017](#).
- E. Berger, P. A. Price, S. B. Cenko, A. Gal-Yam, A. M. Soderberg, M. Kasliwal, D. C. Leonard, P. B. Cameron, D. A. Frail, S. R. Kulkarni, et al. The afterglow and elliptical host galaxy of the short γ -ray burst GRB 050724. *Nature*, 438(7070): 988–990, [Dec. 2005](#).
- T. J. Bernatowicz and E. Zinner. Astrophysical implications of the laboratory study of presolar materials. In *American Institute of Physics Conference Series*, volume 402 of *American Institute of Physics Conference Series*, Mar. 1997.
- J. Beun, G. C. McLaughlin, R. Surman, and W. R. Hix. Fission cycling in a supernova r process. *PhRvC*, 77:035804, [Mar 2008](#). URL <https://link.aps.org/doi/10.1103/PhysRevC.77.035804>.
- L. Bovard, D. Martin, F. Guercilena, A. Arcones, L. Rezzolla, and O. Korobkin. r -process nucleosynthesis from matter ejected in binary neutron star mergers. *PhRvD*, 96(12):124005, [Dec. 2017](#).
- K. Brauer, A. P. Ji, A. Frebel, G. A. Dooley, F. A. Gómez, and B. W. O’Shea. The Origin of r-process Enhanced Metal-poor Halo Stars In Now-destroyed Ultra-faint Dwarf Galaxies. *ApJ*, 871:247, [Feb. 2019](#).
- T. M. Brown, J. Tumlinson, M. Geha, J. D. Simon, L. C. Vargas, D. A. VandenBerg, E. N. Kirby, J. S. Kalirai, R. J. Avila, M. Gennaro, et al. The Quenching of the Ultra-faint Dwarf Galaxies in the Reionization Era. *ApJ*, 796(2):91, [Dec. 2014](#).
- E. M. Burbidge, G. R. Burbidge, W. A. Fowler, and F. Hoyle. Synthesis of the Elements in Stars. *Reviews of Modern Physics*, 29:547–650, [1957](#).
- M. Cain, A. Frebel, M. Gull, A. P. Ji, V. M. Placco, T. C. Beers, J. Meléndez, R. Ezzeddine, A. R. Casey, T. T. Hansen, I. U. Roederer, and C. Sakari. The R-Process Alliance: Chemical Abundances for a Trio of r-process-enhanced Stars—One Strong, One Moderate, and One Mild. *ApJ*, 864(1):43, [Sept. 2018](#).
- A. G. W. Cameron. Nuclear Reactions in Stars and Nucleogenesis. *PASP*, 69:201, [June 1957](#).

- A. G. W. Cameron. Some Nucleosynthesis Effects Associated with r-Process Jets. *ApJ*, 587:327–340, [Apr. 2003](#).
- A. G. W. Cameron, J. J. Cowan, and J. W. Truran. The Waiting Point Approximation in R-Process Calculations. *Ap&SS*, 91(2):235–243, [Apr. 1983](#).
- D. Carollo, P. B. Tissera, T. C. Beers, D. Gudin, B. K. Gibson, K. C. Freeman, and A. Monachesi. The Origin of the Milky Way’s Halo Age Distribution. *ApJL*, 859(1):L7, [May 2018](#).
- L. Casagrande, I. Ramírez, J. Meléndez, M. Bessell, and M. Asplund. An absolutely calibrated T_{eff} scale from the infrared flux method. Dwarfs and subgiants. *A&A*, 512:A54, [Mar. 2010](#).
- A. R. Casey and K. C. Schlaufman. Chemistry of the Most Metal-poor Stars in the Bulge and the $z \gtrsim 10$ Universe. *ApJ*, 809(2):110, [Aug. 2015](#).
- F. Castelli and R. L. Kurucz. New Grids of ATLAS9 Model Atmospheres. *Symposium - International Astronomical Union*, 2003.
- A. Choplin. *The early generations of rotating massive stars and the origin of carbon-enhanced metal-poor stars*. PhD thesis, Oct. 2018.
- R. Chornock, E. Berger, D. Kasen, P. S. Cowperthwaite, M. Nicholl, V. A. Villar, K. D. Alexander, P. K. Blanchard, T. Eftekhari, W. Fong, et al. The Electromagnetic Counterpart of the Binary Neutron Star Merger LIGO/Virgo GW170817. IV. Detection of Near-infrared Signatures of r-process Nucleosynthesis with Gemini-South. *ApJL*, 848:L19, [Oct. 2017](#).
- N. Christlieb, T. C. Beers, P. S. Barklem, M. Bessell, V. Hill, J. Holmberg, A. J. Korn, B. Marsteller, L. Mashonkina, Y. Z. Qian, et al. The Hamburg/ESO R-process Enhanced Star survey (HERES). I. Project description, and discovery of two stars with strong enhancements of neutron-capture elements. *A&A*, 428:1027–1037, [Dec. 2004](#).
- N. Christlieb, T. Schörck, A. Frebel, T. C. Beers, L. Wisotzki, and D. Reimers. The stellar content of the Hamburg/ESO survey. IV. Selection of candidate metal-poor stars. *A&A*, 484:721–732, [June 2008](#).
- F. W. Clarke. The relative abundance of the chemical elements. *Bulletin of the Philosophical Society of Washington*, 11:135–143, 1889.
- D. D. Clayton. *Principles of stellar evolution and nucleosynthesis*. 1968.
- D. D. Clayton and R. A. Ward. s-process studies: xenon and krypton isotopic abundances. *ApJ*, 224:1000–1006, [Sept. 1978](#).
- D. D. Clayton, W. A. Fowler, T. E. Hull, and B. A. Zimmerman. Neutron capture chains in heavy element synthesis. *Annals of Physics*, 12(3):331–408, [Mar. 1961](#).

- B. Côté, C. L. Fryer, K. Belczynski, O. Korobkin, M. Chruścińska, N. Vassh, M. R. Mumpower, J. Lippuner, T. M. Sprouse, R. Surman, and R. Wollaeger. The Origin of r-process Elements in the Milky Way. *ApJ*, 855:99, Mar. 2018.
- B. Côté, M. Eichler, A. Arcones, C. J. Hansen, P. Simonetti, A. Frebel, C. L. Fryer, M. Pignatari, M. Reichert, K. Belczynski, and F. Matteucci. Neutron Star Mergers Might Not Be the Only Source of r-process Elements in the Milky Way. *ApJ*, 875(2):106, Apr. 2019.
- M. W. Coughlin, T. Dietrich, B. Margalit, and B. D. Metzger. Multimessenger Bayesian parameter inference of a binary neutron star merger. *MNRAS*, 489(1):L91–L96, Oct. 2019.
- J. J. Cowan, F.-K. Thielemann, and J. W. Truran. The R-process and nucleochronology. *Physics Reports*, 208:267–394, Nov. 1991.
- J. J. Cowan, B. Pfeiffer, K.-L. Kratz, F.-K. Thielemann, C. Sneden, S. Burles, D. Tytler, and T. C. Beers. R-Process Abundances and Chronometers in Metal-poor Stars. *ApJ*, 521:194–205, Aug. 1999.
- J. J. Cowan, C. Sneden, S. Burles, I. I. Ivans, T. C. Beers, J. W. Truran, J. E. Lawler, F. Primas, G. M. Fuller, B. Pfeiffer, and K.-L. Kratz. The Chemical Composition and Age of the Metal-poor Halo Star BD +17°3248. *ApJ*, 572(2):861–879, June 2002.
- P. S. Cowperthwaite, E. Berger, V. A. Villar, B. D. Metzger, M. Nicholl, R. Chornock, P. K. Blanchard, W. Fong, R. Margutti, M. Soares-Santos, et al. The Electromagnetic Counterpart of the Binary Neutron Star Merger LIGO/Virgo GW170817. II. UV, Optical, and Near-infrared Light Curves and Comparison to Kilonova Models. *ApJL*, 848(2):L17, Oct. 2017.
- R. H. Cyburt, A. M. Amthor, R. Ferguson, Z. Meisel, K. Smith, S. Warren, A. Heger, R. D. Hoffman, T. Rauscher, A. Sakharuk, H. Schatz, F. K. Thielemann, and M. Wiescher. The jina reaclib database: Its recent updates and impact on type-i x-ray bursts. *ApJS*, 189(1):240, 2010. URL <http://stacks.iop.org/0067-0049/189/i=1/a=240>.
- Z. G. Dai and T. Lu. γ -Ray Bursts and Afterglows from Rotating Strange Stars and Neutron Stars. *PhRvL*, 81(20):4301–4304, Nov. 1998.
- Z. G. Dai, X. Y. Wang, X. F. Wu, and B. Zhang. X-ray Flares from Postmerger Millisecond Pulsars. *Science*, 311(5764):1127–1129, Feb. 2006.
- L. Dardelet, C. Ritter, P. Prado, E. Heringer, C. Higgs, S. Sandalski, S. Jones, P. Denissenkov, K. Venn, M. Bertolli, M. Pignatari, P. Woodward, and F. Herwig. i process and cemp-s+ r stars. In Z. Elekes and Z. Fülöp, editors, *Proceedings, 13th International Symposium on Nuclei in the Cosmos (NIC XIII)*, volume NICXIII of *Nuclei in the Cosmos*, page 145, July 2015.

- M. D. Delano and A. G. W. Cameron. Nucleosynthesis in Neutron Rich Supernova Ejecta. *Ap&SS*, 10(2):203–226, [Feb. 1971](#).
- P. Demarque, J.-H. Woo, Y.-C. Kim, and S. K. Yi. Y^2 Isochrones with an Improved Core Overshoot Treatment. *ApJS*, 155:667–674, [Dec. 2004](#).
- L.-C. Deng, H. J. Newberg, C. Liu, J. L. Carlin, T. C. Beers, L. Chen, Y.-Q. Chen, N. Christlieb, C. J. Grillmair, P. Guhathakurta, et al. LAMOST Experiment for Galactic Understanding and Exploration (LEGUE) — The survey’s science plan. *Research in Astronomy and Astrophysics*, 12(7):735–754, [July 2012](#).
- T. Dietrich and M. Ujevic. Modeling dynamical ejecta from binary neutron star mergers and implications for electromagnetic counterparts. *Classical and Quantum Gravity*, 34(10):105014, [May 2017](#).
- T. Dietrich, S. Bernuzzi, M. Ujevic, and B. Brügmann. Numerical relativity simulations of neutron star merger remnants using conservative mesh refinement. *PhRvD*, 91(12):124041, [June 2015](#).
- I. Dillmann, D. Abriola, and B. Singh. Recent activities for β -decay half-lives and β -delayed neutron emission of very neutron-rich isotopes. In S. Jeong, N. Imai, H. Miyatake, and T. Kajino, editors, *American Institute of Physics Conference Series*, volume 1594 of *American Institute of Physics Conference Series*, pages 332–338, [May 2014](#).
- M. R. Drout, A. L. Piro, B. J. Shappee, C. D. Kilpatrick, J. D. Simon, C. Contreras, D. A. Coulter, R. J. Foley, M. R. Siebert, N. Morrell, et al. Light curves of the neutron star merger GW170817/SSS17a: Implications for r-process nucleosynthesis. *Science*, 358(6370):1570–1574, [Dec. 2017](#).
- J. Duflo and A. P. Zuker. Microscopic mass formulas. *PhRvC*, 52:R23–R27, [July 1995](#).
- M. Eichler, A. Arcones, A. Kelic, O. Korobkin, K. Langanke, T. Marketin, G. Martinez-Pinedo, I. Panov, T. Rauscher, S. Rosswog, C. Winteler, N. T. Zinner, and F.-K. Thielemann. The Role of Fission in Neutron Star Mergers and Its Impact on the r-Process Peaks. *ApJ*, 808:30, [July 2015](#).
- M. Eichler, W. Sayar, A. Arcones, and T. Rauscher. Probing the Production of Actinides under Different r-process Conditions. *ApJ*, 879(1):47, [July 2019](#).
- P. A. Evans, S. B. Cenko, J. A. Kennea, S. W. K. Emery, N. P. M. Kuin, O. Korobkin, R. T. Wollaeger, C. L. Fryer, K. K. Madsen, F. A. Harrison, et al. Swift and NuSTAR observations of GW170817: Detection of a blue kilonova. *Science*, 358 (6370):1565–1570, [Dec. 2017](#).
- R. Ezzeddine, A. Frebel, and B. Plez. Ultra-metal-poor Stars: Spectroscopic Determination of Stellar Atmospheric Parameters Using Iron Non-LTE Line Abundances. *ApJ*, 847:142, [Oct. 2017](#).

- R. Ezzeddine, K. Rasmussen, A. Frebel, A. Chiti, K. Hinojisa, V. M. Placco, I. U. Roederer, A. P. Ji, T. C. Beers, T. T. Hansen, C. M. Sakari, and J. Melendez. The R-process Alliance: First Magellan/MIKE Release from the Southern Search for R-Process-enhanced Stars. *arXiv e-prints*, art. arXiv:2006.07731, June 2020.
- K. Farouqi, K.-L. Kratz, B. Pfeiffer, T. Rauscher, F.-K. Thielemann, and J. W. Truran. Charged-particle and Neutron-capture Processes in the High-entropy Wind of Core-collapse Supernovae. *ApJ*, 712:1359–1377, Apr. 2010.
- R. Fernández, D. Kasen, B. D. Metzger, and E. Quataert. Outflows from accretion discs formed in neutron star mergers: effect of black hole spin. *MNRAS*, 446: 750–758, Jan. 2015.
- R. Fernández, E. Quataert, K. Kashiyama, and E. R. Coughlin. Mass ejection in failed supernovae: variation with stellar progenitor. *MNRAS*, 476(2):2366–2383, May 2018.
- D. Foreman-Mackey, D. W. Hogg, D. Lang, and J. Goodman. emcee: The mcmc hammer. *PASP*, 125(925):306–312, Mar 2013. ISSN 1538-3873. URL <http://dx.doi.org/10.1086/670067>.
- P. François, L. Monaco, P. Bonifacio, C. Moni Bidin, D. Geisler, and L. Sbordone. Abundance ratios of red giants in low-mass ultra-faint dwarf spheroidal galaxies. *A&A*, 588:A7, Apr. 2016.
- J. Fraunhofer. Bestimmung des Brechungs- und des Farbenzerstreuungs-Vermögens verschiedener Glasarten, in Bezug auf die Vervollkommnung achromatischer Fernröhre. *Annalen der Physik*, 56(7):264–313, Jan. 1817.
- A. Frebel. From Nuclei to the Cosmos: Tracing Heavy-Element Production with the Oldest Stars. *Annual Review of Nuclear and Particle Science*, 68(1):237–269, Oct. 2018.
- A. Frebel and J. E. Norris. *Metal-Poor Stars and the Chemical Enrichment of the Universe*, volume 5, page 55. 2013.
- A. Frebel, A. R. Casey, H. R. Jacobson, and Q. Yu. Deriving Stellar Effective Temperatures of Metal-poor Stars with the Excitation Potential Method. *ApJ*, 769:57, May 2013.
- A. Frebel, J. D. Simon, and E. N. Kirby. Segue 1: An Unevolved Fossil Galaxy from the Early Universe. *ApJ*, 786(1):74, May 2014.
- C. Freiburghaus, S. Rosswog, and F.-K. Thielemann. R-Process in Neutron Star Mergers. *ApJ*, 525:L121–L124, Nov. 1999.
- Gaia Collaboration, A. G. A. Brown, A. Vallenari, T. Prusti, J. H. J. de Bruijne, F. Mignard, R. Drimmel, C. Babusiaux, C. A. L. Bailer-Jones, U. Bastian, et al.

- Gaia Data Release 1. Summary of the astrometric, photometric, and survey properties. *A&A*, 595:A2, [Nov. 2016](#).
- Gaia Collaboration, A. G. A. Brown, A. Vallenari, T. Prusti, J. H. J. de Bruijne, C. Babusiaux, C. A. L. Bailer-Jones, M. Biermann, D. W. Evans, L. Eyer, et al. Gaia Data Release 2. Summary of the contents and survey properties. *A&A*, 616: A1, [Aug. 2018](#).
- K. K. Gilroy, C. Sneden, C. A. Pilachowski, and J. J. Cowan. Abundances of neutron capture elements in Population II stars. *ApJ*, 327:298–320, [Apr. 1988](#).
- V. Goldschmidt. The distribution of the chemical elements. *Nature*, 124(3114):15–17, 1929. ISSN 00280836.
- V. M. Goldschmidt. Geochemische verteilungsgesetze der elemente. ix. die mengenverhaltnisse der elemente und der atom-arten. *Skrifter Norske Videnskaps-Akademie Oslo, I. Mat.-Naturv. Klasse*, 4:1–148, 1938.
- G. A. Gontcharov. Pulkovo Compilation of Radial Velocities for 35 495 Hipparcos stars in a common system. *Astronomy Letters*, 32(11):759–771, [Nov. 2006](#).
- S. Goriely, N. Chamel, and J. M. Pearson. Skyrme-Hartree-Fock-Bogoliubov Nuclear Mass Formulas: Crossing the 0.6MeV Accuracy Threshold with Microscopically Deduced Pairing. *PhRvL*, 102(15):152503, [Apr. 2009](#).
- S. Goriely, A. Bauswein, and H.-T. Janka. r-process Nucleosynthesis in Dynamically Ejected Matter of Neutron Star Mergers. *ApJ*, 738:L32, [Sept. 2011](#).
- S. Goriely, N. Chamel, and J. M. Pearson. Further explorations of Skyrme-Hartree-Fock-Bogoliubov mass formulas. XIII. The 2012 atomic mass evaluation and the symmetry coefficient. *PhRvC*, 88(2):024308, [Aug. 2013](#).
- S. Goriely, A. Bauswein, O. Just, E. Pllumbi, and H.-T. Janka. Impact of weak interactions of free nucleons on the r-process in dynamical ejecta from neutron star mergers. *MNRAS*, 452:3894–3904, [Oct. 2015](#).
- M. Gull, A. Frebel, M. G. Cain, V. M. Placco, A. P. Ji, C. Abate, R. Ezzeddine, A. I. Karakas, T. T. Hansen, C. Sakari, et al. The R-Process Alliance: Discovery of the First Metal-poor Star with a Combined r- and s-process Element Signature. *ApJ*, 862(2):174, [Aug. 2018](#).
- M. Hampel, R. J. Stancliffe, M. Lugaro, and B. S. Meyer. The Intermediate Neutron-capture Process and Carbon-enhanced Metal-poor Stars. *ApJ*, 831(2):171, [Nov. 2016](#).
- C. J. Hansen, F. Primas, H. Hartman, K.-L. Kratz, S. Wanajo, B. Leibundgut, K. Farouqi, O. Hallmann, N. Christlieb, and H. Nilsson. Silver and palladium help unveil the nature of a second r-process. *A&A*, 545:A31, [Sept. 2012](#).

- T. T. Hansen, J. D. Simon, J. L. Marshall, T. S. Li, D. Carollo, D. L. DePoy, D. Q. Nagasawa, R. A. Bernstein, A. Drlica-Wagner, F. B. Abdalla, et al. An r-process Enhanced Star in the Dwarf Galaxy Tucana III. *ApJ*, 838(1):44, [Mar. 2017](#).
- T. T. Hansen, E. M. Holmbeck, T. C. Beers, V. M. Placco, I. U. Roederer, A. Frebel, C. M. Sakari, J. D. Simon, and I. B. Thompson. The R-process Alliance: First Release from the Southern Search for R-process-enhanced Stars in the Galactic Halo. *ApJ*, 858:92, [May 2018](#).
- W. Hayek, U. Wiesendahl, N. Christlieb, K. Eriksson, A. J. Korn, P. S. Barklem, V. Hill, T. C. Beers, K. Farouqi, B. Pfeiffer, and K. L. Kratz. The Hamburg/ESO R-process enhanced star survey (HERES). IV. Detailed abundance analysis and age dating of the strongly r-process enhanced stars CS 29491-069 and HE 1219-0312. *A&A*, 504(2):511–524, [Sept. 2009](#).
- A. A. Henden, S. Levine, D. Terrell, and D. L. Welch. APASS - The Latest Data Release. In *American Astronomical Society Meeting Abstracts #225*, volume 225 of *American Astronomical Society Meeting Abstracts*, page 336.16, Jan. 2015.
- V. Hill, B. Plez, R. Cayrel, T. C. Beers, B. Nordström, J. Andersen, M. Spite, F. Spite, B. Barbuy, P. Bonifacio, E. Depagne, P. François, and F. Primas. First stars. I. The extreme r-element rich, iron-poor halo giant CS 31082-001. Implications for the r-process site(s) and radioactive cosmochronology. *A&A*, 387:560–579, [May 2002](#).
- V. Hill, N. Christlieb, T. C. Beers, P. S. Barklem, K.-L. Kratz, B. Nordström, B. Pfeiffer, and K. Farouqi. The Hamburg/ESO R-process Enhanced Star survey (HERES). XI. The highly r-process-enhanced star CS 29497-004. *A&A*, 607: A91, [Nov. 2017](#).
- E. M. Holmbeck, T. C. Beers, I. U. Roederer, V. M. Placco, T. T. Hansen, C. M. Sakari, C. Sneden, C. Liu, Y. S. Lee, J. J. Cowan, and A. Frebel. The R-Process Alliance: 2MASS J09544277+5246414, the Most Actinide-enhanced R-II Star Known. *ApJL*, 859:L24, [June 2018](#).
- E. M. Holmbeck, A. Frebel, G. C. McLaughlin, M. R. Mumpower, T. M. Sprouse, and R. Surman. Actinide-rich and Actinide-poor r-process-enhanced Metal-poor Stars Do Not Require Separate r-process Progenitors. *ApJ*, 881(1):5, [Aug. 2019a](#).
- E. M. Holmbeck, T. M. Sprouse, M. R. Mumpower, N. Vassh, R. Surman, T. C. Beers, and T. Kawano. Actinide Production in the Neutron-rich Ejecta of a Neutron Star Merger. *ApJ*, 870(1):23, [Jan. 2019b](#).
- E. M. Holmbeck, T. T. Hansen, T. C. Beers, V. M. Placco, D. D. Whitten, K. C. Rasmussen, I. U. Roederer, R. Ezzeddine, C. M. Sakari, A. Frebel, et al. The R-Process Alliance: Fourth Data Release from the Search for r-Process-Enhanced Stars in the Galactic Halo. *arXiv e-prints*, art. arXiv:2007.00749, July 2020.

- S. Honda, W. Aoki, T. Kajino, H. Ando, T. C. Beers, H. Izumiura, K. Sadakane, and M. Takada-Hidai. Spectroscopic Studies of Extremely Metal-Poor Stars with the Subaru High Dispersion Spectrograph. II. The r-Process Elements, Including Thorium. *ApJ*, 607:474–498, [May 2004](#).
- S. Honda, W. Aoki, Y. Ishimaru, S. Wanajo, and S. G. Ryan. Neutron-Capture Elements in the Very Metal Poor Star HD 122563. *ApJ*, 643:1180–1189, [June 2006](#).
- C. J. Horowitz, A. Arcones, B. Côté, I. Dillmann, W. Nazarewicz, I. U. Roederer, H. Schatz, A. Aprahamian, D. Atanasov, A. Bauswein, et al. r-process nucleosynthesis: connecting rare-isotope beam facilities with the cosmos. *Journal of Physics G Nuclear Physics*, 46(8):083001, [Aug. 2019](#).
- K. Hotokezaka, K. Kiuchi, K. Kyutoku, T. Muranushi, Y.-i. Sekiguchi, M. Shibata, and K. Taniguchi. Remnant massive neutron stars of binary neutron star mergers: Evolution process and gravitational waveform. *PhRvD*, 88(4):044026, [Aug. 2013](#).
- K. Hotokezaka, P. Beniamini, and T. Piran. Neutron star mergers as sites of r-process nucleosynthesis and short gamma-ray bursts. *International Journal of Modern Physics D*, 27(13):1842005, [Jan. 2018](#).
- F. Hoyle. The synthesis of the elements from hydrogen. *MNRAS*, 106:343, [Jan. 1946](#).
- J. Iben, I. Thermal pulses: p-capture, alpha -capture, s-process nucleosynthesis; and convective mixing in a star of intermediate mass. *ApJ*, 196:525–547, [Mar. 1975](#).
- M. N. Ishigaki, M. Chiba, and W. Aoki. Chemical Abundances of the Milky Way Thick Disk and Stellar Halo. I. Implications of $[\alpha/\text{Fe}]$ for Star Formation Histories in Their Progenitors. *ApJ*, 753(1):64, [July 2012](#).
- I. I. Ivans, J. Simmerer, C. Sneden, J. E. Lawler, J. J. Cowan, R. Gallino, and S. Bisterzo. Near-Ultraviolet Observations of HD 221170: New Insights into the Nature of r-Process-rich Stars. *ApJ*, 645(1):613–633, [July 2006](#).
- A. P. Ji and A. Frebel. From Actinides to Zinc: Using the Full Abundance Pattern of the Brightest Star in Reticulum II to Distinguish between Different r-process Sites. *ApJ*, 856:138, [Apr. 2018](#).
- A. P. Ji, A. Frebel, A. Chiti, and J. D. Simon. R-process enrichment from a single event in an ancient dwarf galaxy. *Nature*, 531:610–613, [Mar. 2016a](#).
- A. P. Ji, A. Frebel, J. D. Simon, and A. Chiti. Complete Element Abundances of Nine Stars in the r-process Galaxy Reticulum II. *ApJ*, 830:93, [Oct. 2016b](#).
- A. P. Ji, A. Frebel, J. D. Simon, and M. Geha. High-resolution Spectroscopy of Extremely Metal-poor Stars in the Least-evolved Galaxies: Boötes II. *ApJ*, 817(1):41, [Jan. 2016c](#).

- A. P. Ji, M. R. Drout, and T. T. Hansen. The Lanthanide Fraction Distribution in Metal-poor Stars: A Test of Neutron Star Mergers as the Dominant r-process Site. *ApJ*, 882(1):40, [Sept. 2019](#).
- J. A. Johnson. Abundances of 30 Elements in 23 Metal-Poor Stars. *ApJS*, 139(1):219–247, [Mar. 2002](#).
- O. Just, A. Bauswein, R. Ardevol Pulpillo, S. Goriely, and H. T. Janka. Comprehensive nucleosynthesis analysis for ejecta of compact binary mergers. *MNRAS*, 448(1):541–567, [Mar. 2015](#).
- D. Kasen, B. Metzger, J. Barnes, E. Quataert, and E. Ramirez-Ruiz. Origin of the heavy elements in binary neutron-star mergers from a gravitational-wave event. *Nature*, 551:80–84, [Nov. 2017](#).
- W. Kastaun and F. Galeazzi. Properties of hypermassive neutron stars formed in mergers of spinning binaries. *PhRvD*, 91(6):064027, [Mar. 2015](#).
- L. Kaufman and P. J. Rousseeuw. *Finding groups in data. an introduction to cluster analysis*. 1990.
- T. Kawano, R. Capote, S. Hilaire, and P. Chau Huu-Tai. Statistical Hauser-Feshbach theory with width-fluctuation correction including direct reaction channels for neutron-induced reactions at low energies. *PhRvC*, 94(1):014612, [July 2016](#).
- D. D. Kelson. *The Fundamental Plane of Early-Type Galaxies in the Intermediate Redshift Cluster CL1358+62*. PhD thesis, University of California, Santa Cruz, Jan. 1998.
- D. D. Kelson. Optimal Techniques in Two-dimensional Spectroscopy: Background Subtraction for the 21st Century. *PASP*, 115:688–699, [June 2003](#).
- D. D. Kelson, G. D. Illingworth, P. G. van Dokkum, and M. Franx. The Evolution of Early-Type Galaxies in Distant Clusters. II. Internal Kinematics of 55 Galaxies in the z=0.33 Cluster CL 1358+62. *ApJ*, 531:159–183, [Mar. 2000](#).
- C. D. Kilpatrick, R. J. Foley, D. Kasen, A. Murguia-Berthier, E. Ramirez-Ruiz, D. A. Coulter, M. R. Drout, A. L. Piro, B. J. Shappee, K. Boutsia, et al. Electromagnetic evidence that SSS17a is the result of a binary neutron star merger. *Science*, 358(6370):1583–1587, [Dec. 2017](#).
- E. N. Kirby, J. D. Simon, M. Geha, P. Guhathakurta, and A. Frebel. Uncovering Extremely Metal-Poor Stars in the Milky Way’s Ultrafaint Dwarf Spheroidal Satellite Galaxies. *ApJL*, 685(1):L43, [Sept. 2008](#).
- G. Kirchhoff. Ueber die Fraunhofer’schen Linien. *Annalen der Physik*, 185(1):148–150, [Jan. 1860](#).

- M. W. Kirson. An empirical study of the Duflo-Zuker mass formula. *NuPhA*, 893: 27–42, [Nov. 2012](#).
- T. Kodama and K. Takahashi. R-process nucleosynthesis and nuclei far from the region of β -stability. *NuPhA*, 239:489–510, [Mar. 1975](#).
- S. E. Koposov, V. Belokurov, G. Torrealba, and N. W. Evans. Beasts of the Southern Wild: Discovery of Nine Ultra Faint Satellites in the Vicinity of the Magellanic Clouds. *ApJ*, 805(2):130, [June 2015](#).
- G. Kordopatis, G. Gilmore, M. Steinmetz, C. Boeche, G. M. Seabroke, A. Siebert, T. Zwitter, J. Binney, P. de Laverny, A. Recio-Blanco, et al. The Radial Velocity Experiment (RAVE): Fourth Data Release. *AJ*, 146(5):134, [Nov. 2013](#).
- O. Korobkin, S. Rosswog, A. Arcones, and C. Winteler. On the astrophysical robustness of the neutron star merger r-process. *MNRAS*, 426:1940–1949, [Nov. 2012](#).
- K.-L. Kratz, J.-P. Bitouzet, F.-K. Thielemann, P. Moeller, and B. Pfeiffer. Isotopic r-Process Abundances and Nuclear Structure Far from Stability: Implications for the r-Process Mechanism. *ApJ*, 403:216, [Jan. 1993](#).
- K.-L. Kratz, B. Pfeiffer, and F.-K. Thielemann. Nuclear-structure input to r-process calculations. *NuPhA*, 630:352–367, [Feb. 1998](#).
- K.-L. Kratz, K. Farouqi, and P. Möller. A High-entropy-wind r-process Study Based on Nuclear-structure Quantities from the New Finite-range Droplet Model Frdm(2012). *ApJ*, 792:6, [Sept. 2014](#).
- C. J. Krüger and F. Foucart. Estimates for disk and ejecta masses produced in compact binary mergers. *PhRvD*, 101(10):103002, [May 2020](#).
- A. Kunder, G. Kordopatis, M. Steinmetz, T. Zwitter, P. J. McMillan, L. Casagrande, H. Enke, J. Wojno, M. Valentini, C. Chiappini, et al. The Radial Velocity Experiment (RAVE): Fifth Data Release. *AJ*, 153(2):75, [Feb. 2017](#).
- B. D. Lackey, M. Nayyar, and B. J. Owen. Observational constraints on hyperons in neutron stars. *PhRvD*, 73(2):024021, [Jan. 2006](#).
- J. M. Lattimer. The Nuclear Equation of State and Neutron Star Masses. *Annual Review of Nuclear and Particle Science*, 62(1):485–515, [Nov. 2012](#).
- J. M. Lattimer and D. N. Schramm. Black-hole-neutron-star collisions. *ApJL*, 192: L145–L147, [Sept. 1974](#).
- J. M. Lattimer and D. F. Swesty. A generalized equation of state for hot, dense matter. *NuPhA*, 535(2):331–376, [Dec. 1991](#).

- Y. S. Lee, T. C. Beers, T. Sivarani, C. Allende Prieto, L. Koesterke, R. Wilhelm, P. Re Fiorentin, C. A. L. Bailer-Jones, J. E. Norris, C. M. Rockosi, et al. The SEGUE Stellar Parameter Pipeline. I. Description and Comparison of Individual Methods. *AJ*, 136:2022–2049, [Nov. 2008a](#).
- Y. S. Lee, T. C. Beers, T. Sivarani, J. A. Johnson, D. An, R. Wilhelm, C. Allende Prieto, L. Koesterke, P. Re Fiorentin, C. A. L. Bailer-Jones, et al. The SEGUE Stellar Parameter Pipeline. II. Validation with Galactic Globular and Open Clusters. *AJ*, 136:2050–2069, [Nov. 2008b](#).
- Y. S. Lee, T. C. Beers, T. Masseron, B. Plez, C. M. Rockosi, J. Sobeck, B. Yanny, S. Lucatello, T. Sivarani, V. M. Placco, and D. Carollo. Carbon-enhanced Metal-poor Stars in SDSS/SEGUE. I. Carbon Abundance Estimation and Frequency of CEMP Stars. *AJ*, 146:132, [Nov. 2013](#).
- S. N. Liddick, A. Spyrou, B. P. Crider, F. Naqvi, A. C. Larsen, M. Guttormsen, M. Mumpower, R. Surman, G. Perdikakis, D. L. Bleuel, et al. Experimental Neutron Capture Rate Constraint Far from Stability. *PhRvL*, 116(24):242502, [June 2016](#).
- K. Lind, M. Bergemann, and M. Asplund. Non-LTE line formation of Fe in late-type stars - II. 1D spectroscopic stellar parameters. *MNRAS*, 427(1):50–60, [Nov. 2012](#).
- J. Lippuner and L. F. Roberts. SkyNet: A Modular Nuclear Reaction Network Library. *ApJS*, 233:18, [Dec. 2017](#).
- J. Lippuner, R. Fernández, L. F. Roberts, F. Foucart, D. Kasen, B. D. Metzger, and C. D. Ott. Signatures of hypermassive neutron star lifetimes on r-process nucleosynthesis in the disc ejecta from neutron star mergers. *MNRAS*, 472:904–918, [Nov. 2017](#).
- C. Liu, L.-C. Deng, J. L. Carlin, M. C. Smith, J. Li, H. J. Newberg, S. Gao, F. Yang, X.-X. Xue, Y. Xu, et al. The K Giant Stars from the LAMOST Survey Data. I. Identification, Metallicity, and Distance. *ApJ*, 790:110, [Aug. 2014](#).
- M. Liu, N. Wang, Y. Deng, and X. Wu. Further improvements on a global nuclear mass model. *PhRvC*, 84(1):014333, [July 2011](#).
- M. Lucca and L. Sagunski. The lifetime of binary neutron star merger remnants. *Journal of High Energy Astrophysics*, 27:33–37, [Aug. 2020](#).
- D. Lunney, J. M. Pearson, and C. Thibault. Recent trends in the determination of nuclear masses. *Reviews of Modern Physics*, 75(3):1021–1082, [Aug. 2003](#).
- T. Malik, N. Alam, M. Fortin, C. Providênciac, B. K. Agrawal, T. K. Jha, B. Kumar, and S. K. Patra. GW170817: Constraining the nuclear matter equation of state from the neutron star tidal deformability. *PhRvC*, 98(3):035804, [Sept. 2018](#).

- A. Malkus, G. C. McLaughlin, and R. Surman. Symmetric and standard matter neutrino resonances above merging compact objects. *PhRvD*, 93(4):045021, [Feb. 2016](#).
- T. Marketin, L. Huther, and G. Martínez-Pinedo. Large-scale evaluation of β -decay rates of r -process nuclei with the inclusion of first-forbidden transitions. *PhRvC*, 93:025805, [Feb 2016](#). URL <https://link.aps.org/doi/10.1103/PhysRevC.93.025805>.
- D. Martin, A. Perego, W. Kastaun, and A. Arcones. The role of weak interactions in dynamic ejecta from binary neutron star mergers. *Classical and Quantum Gravity*, 35(3):034001, [Feb. 2018](#).
- G. Martínez-Pinedo, T. Fischer, A. Lohs, and L. Huther. Charged-Current Weak Interaction Processes in Hot and Dense Matter and its Impact on the Spectra of Neutrinos Emitted from Protoneutron Star Cooling. *PhRvL*, 109(25):251104, [Dec. 2012](#).
- L. Mashonkina, N. Christlieb, P. S. Barklem, V. Hill, T. C. Beers, and A. Velichko. The Hamburg/ESO R-process enhanced star survey (HERES). V. Detailed abundance analysis of the r-process enhanced star HE 2327-5642. *A&A*, 516:A46, [June 2010](#).
- L. Mashonkina, N. Christlieb, and K. Eriksson. The Hamburg/ESO R-process Enhanced Star survey (HERES). X. HE 2252-4225, one more r-process enhanced and actinide-boost halo star. *A&A*, 569:A43, [Sept. 2014](#).
- G. J. Mathews and J. J. Cowan. New insights into the astrophysical r-process. *Nature*, 345:491–494, [June 1990](#).
- G. J. Mathews, G. Bazan, and J. J. Cowan. Evolution of Heavy-Element Abundances as a Constraint on Sites for Neutron-Capture Nucleosynthesis. *ApJ*, 391:719, [June 1992](#).
- G. J. Mathews, M. Meixner, J. P. Olson, I. S. Suh, T. Kajino, T. Maruyama, J. Hidaka, C. Y. Ryu, M. K. Cheoun, and N. Q. Lan. Updates of the nuclear equation of state for core-collapse supernovae and neutron stars: effects of 3-body forces, QCD, and magnetic fields. In *Journal of Physics Conference Series*, volume 445 of *Journal of Physics Conference Series*, page 012023, [July 2013](#).
- G. Matijević, C. Chiappini, E. K. Grebel, R. F. G. Wyse, T. Zwitter, O. Bienaymé, J. Bland -Hawthorn, K. C. Freeman, B. K. Gibson, G. Gilmore, et al. Very metal-poor stars observed by the RAVE survey. *A&A*, 603:A19, [July 2017](#).
- A. McWilliam. Barium Abundances in Extremely Metal-poor Stars. *AJ*, 115:1640–1647, [Apr. 1998](#).
- J. Meléndez, V. M. Placco, M. Tucci-Maia, I. Ramírez, T. S. Li, and G. Perez. 2MASS J18082002-5104378: The brightest ($V = 11.9$) ultra metal-poor star. *A&A*, 585:L5, [Jan. 2016](#).

- J. d. J. Mendoza-Temis, M.-R. Wu, K. Langanke, G. Martínez-Pinedo, A. Bauswein, and H.-T. Janka. Nuclear robustness of the r process in neutron-star mergers. *PhRvC*, 92(5):055805, [Nov. 2015](#).
- B. D. Metzger and R. Fernández. Red or blue? A potential kilonova imprint of the delay until black hole formation following a neutron star merger. *MNRAS*, 441(4):3444–3453, [July 2014](#).
- B. D. Metzger, A. L. Piro, and E. Quataert. Time-dependent models of accretion discs formed from compact object mergers. *MNRAS*, 390:781–797, [Oct. 2008](#).
- B. S. Meyer. Decompression of initially cold neutron star matter - A mechanism for the r-process? *ApJ*, 343:254–276, [Aug. 1989](#).
- B. S. Meyer. The r-, s-, and p-Processes in Nucleosynthesis. *ARA&A*, 32:153–190, [1994](#).
- B. S. Meyer, G. J. Mathews, W. M. Howard, S. E. Woosley, and R. D. Hoffman. R-process nucleosynthesis in the high-entropy supernova bubble. *ApJ*, 399:656–664, [Nov. 1992](#).
- J. M. Miller, T. M. Sprouse, C. L. Fryer, B. R. Ryan, J. C. Dolence, M. R. Mumpower, and R. Surman. Full Transport General Relativistic Radiation Magnetohydrodynamics for Nucleosynthesis in Collapsars. *arXiv e-prints*, art. arXiv:1912.03378, Dec. 2019.
- P. Möller, J. R. Nix, W. D. Myers, and W. J. Swiatecki. Nuclear Ground-State Masses and Deformations. *Atomic Data and Nuclear Data Tables*, 59:185, [Jan. 1995](#).
- P. Möller, W. D. Myers, H. Sagawa, and S. Yoshida. New Finite-Range Droplet Mass Model and Equation-of-State Parameters. *PhRvL*, 108(5):052501, [Feb. 2012](#).
- P. Möller, A. J. Sierk, T. Ichikawa, A. Iwamoto, and M. Mumpower. Fission barriers at the end of the chart of the nuclides. *PhRvC*, 91(2):024310, [Feb. 2015](#).
- P. Möller, A. J. Sierk, T. Ichikawa, and H. Sagawa. Nuclear ground-state masses and deformations: FRDM(2012). *Atomic Data and Nuclear Data Tables*, 109:1–204, [May 2016](#).
- P. Möller, M. R. Mumpower, T. Kawano, and W. D. Myers. Nuclear properties for astrophysical and radioactive-ion-beam applications (II). *Atomic Data and Nuclear Data Tables*, 125:1–192, [Jan. 2019](#).
- P. Mösta, L. F. Roberts, G. Halevi, C. D. Ott, J. Lippuner, R. Haas, and E. Schnetter. r-process Nucleosynthesis from Three-dimensional Magnetorotational Core-collapse Supernovae. *ApJ*, 864:171, [Sept. 2018](#).

- M. R. Mumpower, G. C. McLaughlin, and R. Surman. The Rare Earth Peak: An Overlooked r-process Diagnostic. *ApJ*, 752:117, June 2012.
- M. R. Mumpower, R. Surman, D.-L. Fang, M. Beard, P. Möller, T. Kawano, and A. Aprahamian. Impact of individual nuclear masses on r-process abundances. *PhRvC*, 92(3):035807, Sept. 2015.
- M. R. Mumpower, T. Kawano, and P. Möller. Neutron- γ competition for β -delayed neutron emission. *PhRvC*, 94(6):064317, Dec. 2016a.
- M. R. Mumpower, R. Surman, G. C. McLaughlin, and A. Aprahamian. The impact of individual nuclear properties on r-process nucleosynthesis. *Progress in Particle and Nuclear Physics*, 86:86–126, Jan. 2016b.
- M. R. Mumpower, G. C. McLaughlin, R. Surman, and A. W. Steiner. The Rare Earth Peak and the Astrophysical Location of the r Process. In S. Kubono, T. Kajino, S. Nishimura, T. Isobe, S. Nagataki, T. Shima, and Y. Takeda, editors, *14th International Symposium on Nuclei in the Cosmos (NIC2016)*, page 020614, 2017.
- M. R. Mumpower, T. Kawano, T. M. Sprouse, N. Vassh, E. M. Holmbeck, R. Surman, and P. Möller. β -delayed Fission in r-process Nucleosynthesis. *ApJ*, 869(1):14, Dec. 2018.
- U. Munari, A. Henden, A. Frigo, T. Zwitter, O. Bienaymé, J. Bland-Hawthorn, C. Boeche, K. C. Freeman, B. K. Gibson, G. Gilmore, et al. APASS Landolt-Sloan BVgri Photometry of RAVE Stars. I. Data, Effective Temperatures, and Reddenings. *AJ*, 148(5):81, Nov. 2014.
- H. Müther, M. Prakash, and T. L. Ainsworth. The nuclear symmetry energy in relativistic Brueckner-Hartree-Fock calculations. *Physics Letters B*, 199(4):469–474, Dec. 1987.
- N. Nishimura, T. Takiwaki, and F.-K. Thielemann. The r-process Nucleosynthesis in the Various Jet-like Explosions of Magnetorotational Core-collapse Supernovae. *ApJ*, 810:109, Sept. 2015.
- K. Otsuki, G. J. Mathews, and T. Kajino. r-Process abundance universality and actinide cosmochronology. *NewA*, 8(8):767–776, Nov. 2003.
- I. V. Panov and H. T. Janka. On the dynamics of proto-neutron star winds and r-process nucleosynthesis. *A&A*, 494(3):829–844, Feb. 2009.
- I. V. Panov and F. K. Thielemann. Fission and the r-Process: Competition between Neutron-Induced and Beta-Delayed Fission. *Astronomy Letters*, 30:647–655, Sept. 2004.
- L. Pasquini and H. Lindgren. Chromospheric activity in population II binaries. *A&A*, 283:179–188, Mar. 1994.

- A. Perego, S. Rosswog, R. M. Cabezón, O. Korobkin, R. Käppeli, A. Arcones, and M. Liebendörfer. Neutrino-driven winds from neutron star merger remnants. *MNRAS*, 443:3134–3156, [Oct. 2014](#).
- A. Perego, D. Radice, and S. Bernuzzi. AT 2017gfo: An Anisotropic and Three-component Kilonova Counterpart of GW170817. *ApJL*, 850(2):L37, [Dec. 2017](#).
- I. Petermann, K. Langanke, G. Martínez-Pinedo, I. V. Panov, P.-G. Reinhard, and F.-K. Thielemann. Have superheavy elements been produced in nature? *European Physical Journal A*, 48:122, [Sept. 2012](#).
- E. Pian, P. D’Avanzo, S. Benetti, M. Branchesi, E. Brocato, S. Campana, E. Cappellaro, S. Covino, V. D’Elia, J. P. U. Fynbo, et al. Spectroscopic identification of r-process nucleosynthesis in a double neutron-star merger. *Nature*, 551(7678): 67–70, [Nov. 2017](#).
- J. Piekarewicz and M. Centelles. Incompressibility of neutron-rich matter. *PhRvC*, 79(5):054311, [May 2009](#).
- T. Piran, E. Nakar, and S. Rosswog. The electromagnetic signals of compact binary mergers. *MNRAS*, 430:2121–2136, [Apr. 2013](#).
- V. M. Placco, A. Frebel, T. C. Beers, and R. J. Stancliffe. Carbon-enhanced Metal-poor Star Frequencies in the Galaxy: Corrections for the Effect of Evolutionary Status on Carbon Abundances. *ApJ*, 797:21, [Dec. 2014](#).
- V. M. Placco, E. M. Holmbeck, A. Frebel, T. C. Beers, R. A. Surman, A. P. Ji, R. Ezzeddine, S. D. Points, C. C. Kaleida, T. T. Hansen, C. M. Sakari, and A. R. Casey. RAVE J203843.2-002333: The First Highly R-process-enhanced Star Identified in the RAVE Survey. *ApJ*, 844:18, [July 2017](#).
- V. M. Placco, T. C. Beers, R. M. Santucci, J. Chanamé, M. P. Sepúlveda, J. Coronado, S. D. Points, C. C. Kaleida, S. Rossi, G. Kordopatis, et al. Spectroscopic Validation of Low-metallicity Stars from RAVE. *AJ*, 155(6):256, [June 2018](#).
- V. M. Placco, R. M. Santucci, T. C. Beers, J. Chanamé, M. P. Sepúlveda, J. Coronado, S. Rossi, Y. S. Lee, E. Starkenburg, K. Youakim, et al. The R-Process Alliance: Spectroscopic Follow-up of Low-metallicity Star Candidates from the Best & Brightest Survey. *ApJ*, 870(2):122, [Jan. 2019](#).
- Planck Collaboration, P. A. R. Ade, N. Aghanim, M. I. R. Alves, C. Armitage-Caplan, M. Arnaud, M. Ashdown, F. Atrio-Barandela, J. Aumont, H. Aussel, et al. Planck 2013 results. I. Overview of products and scientific results. *A&A*, 571:A1, [Nov. 2014](#).
- N. Prantzos. The metallicity distribution of the halo and the satellites of the Milky Way in the hierarchical merging paradigm. *A&A*, 489(2):525–532, [Oct. 2008](#).

- J. Prael, T. A. Thompson, and R. D. Hoffman. Nucleosynthesis in Outflows from the Inner Regions of Collapsars. *ApJ*, 606:1006–1018, May 2004.
- Y. Z. Qian and G. J. Wasserburg. Where, oh where has the r-process gone? *PhR*, 442(1-6):237–268, Apr. 2007.
- Y. Z. Qian and S. E. Woosley. Nucleosynthesis in Neutrino-driven Winds. I. The Physical Conditions. *ApJ*, 471:331, Nov. 1996.
- D. Radice, A. Perego, K. Hotokezaka, S. A. Fromm, S. Bernuzzi, and L. F. Roberts. Binary Neutron Star Mergers: Mass Ejection, Electromagnetic Counterparts, and Nucleosynthesis. *ApJ*, 869(2):130, Dec. 2018a.
- D. Radice, A. Perego, F. Zappa, and S. Bernuzzi. GW170817: Joint Constraint on the Neutron Star Equation of State from Multimessenger Observations. *ApJL*, 852(2):L29, Jan. 2018b.
- J. Ren, N. Christlieb, and G. Zhao. The Hamburg/ESO R-process Enhanced Star survey (HERES). VII. Thorium abundances in metal-poor stars. *A&A*, 537:A118, Jan. 2012.
- L. F. Roberts, S. Reddy, and G. Shen. Medium modification of the charged-current neutrino opacity and its implications. *PhRvC*, 86(6):065803, Dec. 2012.
- I. U. Roederer. Are There Any Stars Lacking Neutron-capture Elements? Evidence from Strontium and Barium. *AJ*, 145:26, Jan. 2013.
- I. U. Roederer, C. Sneden, I. B. Thompson, G. W. Preston, and S. A. Shectman. Characterizing the Chemistry of the Milky Way Stellar Halo: Detailed Chemical Analysis of a Metal-poor Stellar Stream. *ApJ*, 711(2):573–596, Mar. 2010.
- I. U. Roederer, J. E. Lawler, J. S. Sobeck, T. C. Beers, J. J. Cowan, A. Frebel, I. I. Ivans, H. Schatz, C. Sneden, and I. B. Thompson. New Hubble Space Telescope Observations of Heavy Elements in Four Metal-Poor Stars. *ApJS*, 203(2):27, Dec. 2012.
- I. U. Roederer, G. W. Preston, I. B. Thompson, S. A. Shectman, and C. Sneden. Neutron-capture Nucleosynthesis in the First Stars. *ApJ*, 784:158, Apr. 2014a.
- I. U. Roederer, G. W. Preston, I. B. Thompson, S. A. Shectman, C. Sneden, G. S. Burley, and D. D. Kelson. A Search for Stars of Very Low Metal Abundance. VI. Detailed Abundances of 313 Metal-poor Stars. *AJ*, 147:136, June 2014b.
- I. U. Roederer, M. Mateo, J. I. Bailey, III, Y. Song, E. F. Bell, J. D. Crane, S. Loebman, D. L. Nidever, E. W. Olszewski, S. A. Shectman, I. B. Thompson, M. Valluri, and M. G. Walker. Detailed Chemical Abundances in the r-process-rich Ultra-faint Dwarf Galaxy Reticulum 2. *AJ*, 151:82, Mar. 2016.

- I. U. Roederer, K. Hattori, and M. Valluri. Kinematics of Highly r-process-enhanced Field Stars: Evidence for an Accretion Origin and Detection of Several Groups from Disrupted Satellites. *AJ*, 156(4):179, Oct. 2018a.
- I. U. Roederer, C. M. Sakari, V. M. Placco, T. C. Beers, R. Ezzeddine, A. Frebel, and T. T. Hansen. The R-Process Alliance: A Comprehensive Abundance Analysis of HD 222925, a Metal-poor Star with an Extreme R-process Enhancement of [Eu/H] = -0.14. *ApJ*, 865(2):129, Oct. 2018b.
- S. Rosswog, T. Piran, and E. Nakar. The multimessenger picture of compact object encounters: binary mergers versus dynamical collisions. *MNRAS*, 430:2585–2604, Apr. 2013.
- S. Rosswog, J. Sollerman, U. Feindt, A. Goobar, O. Korobkin, R. Wollaeger, C. Fremling, and M. M. Kasliwal. The first direct double neutron star merger detection: Implications for cosmic nucleosynthesis. *A&A*, 615:A132, July 2018.
- G. R. Ruchti, J. P. Fulbright, R. F. G. Wyse, G. F. Gilmore, O. Bienaymé, J. Bland -Hawthorn, B. K. Gibson, E. K. Grebel, A. Helmi, U. Munari, et al. Observational Properties of the Metal-poor Thick Disk of the Milky Way and Insights into its Origins. *ApJ*, 737(1):9, Aug. 2011.
- H. N. Russell. On the Composition of the Sun's Atmosphere. *ApJ*, 70:11, July 1929.
- M. Safarzadeh, E. Ramirez-Ruiz, J. J. Andrews, P. Macias, T. Fragos, and E. Scannapieco. r-process Enrichment of the Ultra-faint Dwarf Galaxies by Fast-merging Double-neutron Stars. *ApJ*, 872:105, Feb. 2019.
- C. M. Sakari, V. M. Placco, E. M. Farrell, I. U. Roederer, G. Wallerstein, T. C. Beers, R. Ezzeddine, A. Frebel, T. Hansen, E. M. Holmbeck, et al. The R-Process Alliance: First Release from the Northern Search for r-process-enhanced Metal-poor Stars in the Galactic Halo. *ApJ*, 868(2):110, Dec. 2018a.
- C. M. Sakari, V. M. Placco, T. Hansen, E. M. Holmbeck, T. C. Beers, A. Frebel, I. U. Roederer, K. A. Venn, G. Wallerstein, C. E. Davis, E. M. Farrell, and D. Yong. The r-process Pattern of a Bright, Highly r-process-enhanced Metal-poor Halo Star at [Fe/H]~−2. *ApJL*, 854(2):L20, Feb. 2018b.
- C. M. Sakari, I. U. Roederer, V. M. Placco, T. C. Beers, R. Ezzeddine, A. Frebel, T. Hansen, C. Sneden, J. J. Cowan, G. Wallerstein, et al. The R-Process Alliance: Discovery of a Low- α , r-process-enhanced Metal-poor Star in the Galactic Halo. *ApJ*, 874(2):148, Apr. 2019.
- K. Sato, K. Nakazawa, and S. Ikeuchi. Formation of Elements in Neutron Rich Ejected Matter of Supernovae. *Progress of Theoretical Physics*, 49(4):1166–1183, Apr. 1973.

- H. Schatz, R. Toenjes, B. Pfeiffer, T. C. Beers, J. J. Cowan, V. Hill, and K.-L. Kratz. Thorium and Uranium Chronometers Applied to CS 31082-001. *ApJ*, 579:626–638, Nov. 2002.
- E. F. Schlafly and D. P. Finkbeiner. Measuring Reddening with Sloan Digital Sky Survey Stellar Spectra and Recalibrating SFD. *ApJ*, 737:103, Aug. 2011.
- K. C. Schlaufman and A. R. Casey. The Best and Brightest Metal-poor Stars. *ApJ*, 797(1):13, Dec. 2014.
- K. C. Schlaufman, C. M. Rockosi, C. Allende Prieto, T. C. Beers, D. Bizyaev, H. Brewington, Y. S. Lee, V. Malanushenko, E. Malanushenko, D. Oravetz, et al. Insight into the Formation of the Milky Way Through Cold Halo Substructure. I. The ECHOS of Milky Way Formation. *ApJ*, 703:2177–2204, Oct. 2009.
- D. N. Schramm. Explosive r-PROCESS Nucleosynthesis. *ApJ*, 185:293–302, Oct. 1973.
- L. Searle and R. Zinn. Compositions of halo clusters and the formation of the galactic halo. *ApJ*, 225:357–379, Oct. 1978.
- P. A. Seeger, W. A. Fowler, and D. D. Clayton. Nucleosynthesis of Heavy Elements by Neutron Capture. *ApJS*, 11:121, Feb. 1965.
- B. J. Shappee, J. D. Simon, M. R. Drout, A. L. Piro, N. Morrell, J. L. Prieto, D. Kasen, T. W. S. Holoién, J. A. Kollmeier, D. D. Kelson, et al. Early spectra of the gravitational wave source GW170817: Evolution of a neutron star merger. *Science*, 358(6370):1574–1578, Dec. 2017.
- A. Siebert, M. E. K. Williams, A. Siviero, W. Reid, C. Boeche, M. Steinmetz, J. Fulbright, U. Munari, T. Zwitter, F. G. Watson, et al. The RAdial Velocity Experiment (RAVE): Third Data Release. *AJ*, 141(6):187, June 2011.
- D. M. Siegel, J. Barnes, and B. D. Metzger. Collapsars as a major source of r-process elements. *Nature*, 569(7755):241–244, May 2019.
- C. Siqueira Mello, V. Hill, B. Barbuy, M. Spite, F. Spite, T. C. Beers, E. Caffau, P. Bonifacio, R. Cayrel, P. François, H. Schatz, and S. Wanajo. High-resolution abundance analysis of very metal-poor r-I stars. *A&A*, 565:A93, May 2014.
- M. F. Skrutskie, R. M. Cutri, R. Stiening, M. D. Weinberg, S. Schneider, J. M. Carpenter, C. Beichman, R. Capps, T. Chester, J. Elias, et al. The Two Micron All Sky Survey (2MASS). *AJ*, 131(2):1163–1183, Feb. 2006.
- S. J. Smartt, T. W. Chen, A. Jerkstrand, M. Coughlin, E. Kankare, S. A. Sim, M. Fraser, C. Inserra, K. Maguire, K. C. Chambers, et al. A kilonova as the electromagnetic counterpart to a gravitational-wave source. *Nature*, 551(7678):75–79, Nov. 2017.

- C. Sneden. The nitrogen abundance of the very metal-poor star HD 122563. *ApJ*, 184:839–849, Sept. 1973.
- C. Sneden. Abundances in halo population stars. In K. Nomoto and J. W. Truran, editors, *Cosmic Chemical Evolution*, volume 187 of *IAU Symposium*, pages 81–90, 2002.
- C. Sneden and M. Parthasarathy. The r- and s- process nuclei in the early history of the galaxy : HD 122563. *ApJ*, 267:757–778, Apr. 1983.
- C. Sneden, G. W. Preston, A. McWilliam, and L. Searle. Ultrametal-poor halo stars: The remarkable spectrum of CS 22892-052. *ApJL*, 431:L27–L30, Aug. 1994.
- C. Sneden, J. J. Cowan, J. E. Lawler, I. I. Ivans, S. Burles, T. C. Beers, F. Primas, V. Hill, J. W. Truran, G. M. Fuller, B. Pfeiffer, and K.-L. Kratz. The Extremely Metal-poor, Neutron Capture-rich Star CS 22892-052: A Comprehensive Abundance Analysis. *ApJ*, 591:936–953, July 2003.
- C. Sneden, J. J. Cowan, and R. Gallino. Neutron-Capture Elements in the Early Galaxy. *ARA&A*, 46:241–288, Sept. 2008.
- J. S. Sobeck, R. P. Kraft, C. Sneden, G. W. Preston, J. J. Cowan, G. H. Smith, I. B. Thompson, S. A. Shectman, and G. S. Burley. The Abundances of Neutron-capture Species in the Very Metal-poor Globular Cluster M15: A Uniform Analysis of Red Giant Branch and Red Horizontal Branch Stars. *AJ*, 141:175, June 2011.
- C. Soubiran, G. Jasniewicz, L. Chemin, F. Crifo, S. Udry, D. Hestroffer, and D. Katz. The catalogue of radial velocity standard stars for Gaia. I. Pre-launch release. *A&A*, 552:A64, Apr. 2013.
- M. Spite and F. Spite. Nucleosynthesis in the Galaxy and the chemical composition of old halo stars. *A&A*, 67:23–31, June 1978.
- T. M. Sprouse, R. Navarro Perez, R. Surman, M. R. Mumpower, G. C. McLaughlin, and N. Schunck. Propagation of statistical uncertainties of Skyrme mass models to simulations of r -process nucleosynthesis. *PhRvC*, 101(5):055803, May 2020.
- A. W. Steiner, M. Hempel, and T. Fischer. Core-collapse Supernova Equations of State Based on Neutron Star Observations. *ApJ*, 774:17, Sept. 2013a.
- A. W. Steiner, J. M. Lattimer, and E. F. Brown. The Neutron Star Mass-Radius Relation and the Equation of State of Dense Matter. *ApJL*, 765(1):L5, Mar. 2013b.
- M. Steinmetz, T. Zwitter, A. Siebert, F. G. Watson, K. C. Freeman, U. Munari, R. Campbell, M. Williams, G. M. Seabroke, R. F. G. Wyse, et al. The Radial Velocity Experiment (RAVE): First Data Release. *AJ*, 132(4):1645–1668, Oct. 2006.

- M. Steinmetz, T. Zwitter, G. Matijevic, A. Siviero, and U. Munari. A Comparison between RAVE DR5 and Gaia DR2 Radial Velocities. *Research Notes of the American Astronomical Society*, 2(4):194, [Oct. 2018](#).
- M. Steinmetz, G. Guiglion, P. J. McMillan, G. Matijevic, H. Enke, G. Kordopatis, T. Zwitter, M. Valentini, C. Chiappini, L. Casagrande, et al. The Sixth Data Release of the Radial Velocity Experiment (RAVE) – II: Stellar Atmospheric Parameters, Chemical Abundances and Distances. *arXiv e-prints*, art. arXiv:2002.04512, Feb. 2020.
- T. Suda, J. Hidaka, W. Aoki, Y. Katsuta, S. Yamada, M. Y. Fujimoto, Y. Ohtani, M. Masuyama, K. Noda, and K. Wada. Stellar Abundances for Galactic Archaeology Database. IV. Compilation of stars in dwarf galaxies. *PASJ*, 69:76, [Oct. 2017](#).
- H. E. Suess and H. C. Urey. Abundances of the Elements. *Reviews of Modern Physics*, 28(1):53–74, [Jan. 1956](#).
- R. Surman and G. C. McLaughlin. Neutrinos and Nucleosynthesis in Gamma-Ray Burst Accretion Disks. *ApJ*, 603:611–623, [Mar. 2004](#).
- R. Surman and G. C. McLaughlin. Neutrino Interactions in the Outflow from Gamma-Ray Burst Accretion Disks. *ApJ*, Jan. 2005.
- R. Surman, J. Beun, G. C. McLaughlin, S. Kane, and W. R. Hix. The role of neutrinos in r-process nucleosynthesis in supernovae and gamma-ray bursts. *Journal of Physics G Nuclear Physics*, 35(1):014059, [Jan. 2008](#).
- W. J. Swiatecki. Systematics of Spontaneous Fission Half-Lives. *Physical Review*, 100:937–938, [Nov. 1955](#).
- K. Takahashi, J. Witti, and H. T. Janka. Nucleosynthesis in neutrino-driven winds from protoneutron stars II. The r-process. *A&A*, 286:857–869, June 1994.
- M. Tanaka, Y. Utsumi, P. A. Mazzali, N. Tominaga, M. Yoshida, Y. Sekiguchi, T. Morokuma, K. Motohara, K. Ohta, K. S. Kawabata, et al. Kilonova from post-merger ejecta as an optical and near-Infrared counterpart of GW170817. *PASJ*, 69(6):102, [Dec. 2017](#).
- N. R. Tanvir, A. J. Levan, A. S. Fruchter, J. Hjorth, R. A. Hounsell, K. Wiersema, and R. L. Tunnicliffe. A ‘kilonova’ associated with the short-duration γ -ray burst GRB 130603B. *Nature*, 500(7464):547–549, [Aug. 2013](#).
- N. R. Tanvir, A. J. Levan, C. González-Fernández, O. Korobkin, I. Mandel, S. Rosswog, J. Hjorth, P. D’Avanzo, A. S. Fruchter, C. L. Fryer, et al. The Emergence of a Lanthanide-rich Kilonova Following the Merger of Two Neutron Stars. *ApJL*, 848(2):L27, [Oct. 2017](#).

- Y. Tarumi, N. Yoshida, and S. Inoue. R-process enrichment in ultrafaint dwarf galaxies. *MNRAS*, 494(1):120–128, Mar. 2020.
- T. M. Tauris, M. Kramer, P. C. C. Freire, N. Wex, H. T. Janka, N. Langer, P. Podsiadlowski, E. Bozzo, S. Chaty, M. U. Kruckow, et al. Formation of Double Neutron Star Systems. *ApJ*, 846(2):170, Sept. 2017.
- F. K. Thielemann, J. Metzinger, and H. V. Klapdor. Beta-delayed fission and neutron emission: Consequences for the astrophysical r-process and the age of the galaxy. *Zeitschrift fur Physik A Hadrons and Nuclei*, 309(4):301–317, Dec. 1983.
- F.-K. Thielemann, A. Arcones, R. Käppeli, M. Liebendörfer, T. Rauscher, C. Winterer, C. Fröhlich, I. Dillmann, T. Fischer, G. Martinez-Pinedo, et al. What are the astrophysical sites for the r-process and the production of heavy elements? *Progress in Particle and Nuclear Physics*, 66:346–353, Apr. 2011.
- F. K. Thielemann, M. Eichler, I. V. Panov, and B. Wehmeyer. Neutron Star Mergers and Nucleosynthesis of Heavy Elements. *Annual Review of Nuclear and Particle Science*, 67:253–274, Oct. 2017.
- T. A. Thompson, A. Burrows, and B. S. Meyer. The Physics of Proto-Neutron Star Winds: Implications for r-Process Nucleosynthesis. *ApJ*, 562(2):887–908, Dec. 2001.
- D. Tody. IRAF in the Nineties. In R. J. Hanisch, R. J. V. Brissenden, and J. Barnes, editors, *Astronomical Data Analysis Software and Systems II*, volume 52 of *Astronomical Society of the Pacific Conference Series*, page 173, Jan. 1993.
- C. Travaglio, R. Gallino, E. Arnone, J. Cowan, F. Jordan, and C. Sneden. Galactic Evolution of Sr, Y, And Zr: A Multiplicity of Nucleosynthetic Processes. *ApJ*, 601:864–884, Feb. 2004.
- E. Troja, L. Piro, H. van Eerten, R. T. Wollaeger, M. Im, O. D. Fox, N. R. Butler, S. B. Cenko, T. Sakamoto, C. L. Fryer, et al. The X-ray counterpart to the gravitational-wave event GW170817. *Nature*, 551(7678):71–74, Nov. 2017.
- J. W. Truran and J. Iben, I. On s-process nucleosynthesis in thermally pulsing stars. *ApJ*, 216:797–810, Sept. 1977.
- J. W. Truran, A. G. W. Cameron, and A. Gilbert. The approach to nuclear statistical equilibrium. *Canadian Journal of Physics*, 44:563, Jan. 1966.
- J. W. Truran, J. J. Cowan, C. A. Pilachowski, and C. Sneden. Probing the Neutron-Capture Nucleosynthesis History of Galactic Matter. *PASP*, 114(802):1293–1308, Dec. 2002.
- R. G. Tull, P. J. MacQueen, C. Sneden, and D. L. Lambert. The high-resolution cross-dispersed echelle white-pupil spectrometer of the McDonald Observatory 2.7-m telescope. *PASP*, 107:251–264, Mar. 1995.

- J. Tumlinson. Chemical Evolution in Hierarchical Models of Cosmic Structure. II. The Formation of the Milky Way Stellar Halo and the Distribution of the Oldest Stars. *ApJ*, 708:1398–1418, [Jan. 2010](#).
- S. Typel, G. Röpke, T. Klähn, D. Blaschke, and H. H. Wolter. Composition and thermodynamics of nuclear matter with light clusters. *PhRvC*, 81(1):015803, [Jan. 2010](#).
- N. Vassh, R. Vogt, R. Surman, J. Randrup, T. M. Sprouse, M. R. Mumpower, P. Jaffke, D. Shaw, E. M. Holmbeck, Y. Zhu, and G. C. McLaughlin. Using excitation-energy dependent fission yields to identify key fissioning nuclei in r-process nucleosynthesis. *Journal of Physics G Nuclear Physics*, 46(6):065202, [June 2019](#).
- G. Wallerstein, J. Iben, Icko, P. Parker, A. M. Boesgaard, G. M. Hale, A. E. Champagne, C. A. Barnes, F. Käppeler, V. V. Smith, R. D. Hoffman, et al. Synthesis of the elements in stars: forty years of progress. *Reviews of Modern Physics*, 69(4): 995–1084, [Oct. 1997](#).
- S. Wanajo. The r-process in Proto-neutron-star Wind Revisited. *ApJL*, 770:L22, [June 2013](#).
- S. Wanajo and Y. Ishimaru. r-process calculations and Galactic chemical evolution. *NuPhA*, 777:676–699, [Oct. 2006](#).
- S. Wanajo, N. Itoh, Y. Ishimaru, S. Nozawa, and T. C. Beers. The r-Process in the Neutrino Winds of Core-Collapse Supernovae and U-Th Cosmochronology. *ApJ*, 577:853–865, [Oct. 2002](#).
- S. Wanajo, S. Goriely, M. Samyn, and N. Itoh. The r-Process in Supernovae: Impact of New Microscopic Mass Formulae. *ApJ*, 606:1057–1069, [May 2004](#).
- S. Wanajo, Y. Sekiguchi, N. Nishimura, K. Kiuchi, K. Kyutoku, and M. Shibata. Production of All the r-process Nuclides in the Dynamical Ejecta of Neutron Star Mergers. *ApJL*, 789:L39, [July 2014](#).
- G. J. Wasserburg, M. Busso, and R. Gallino. Abundances of Actinides and Short-lived Nonactinides in the Interstellar Medium: Diverse Supernova Sources for the r-Processes. *ApJL*, 466:L109, [Aug. 1996](#).
- J. Westin, C. Sneden, B. Gustafsson, and J. J. Cowan. The r-Process-enriched Low-Metallicity Giant HD 115444. *ApJ*, 530:783–799, [Feb. 2000](#).
- J. C. Wheeler, C. Sneden, and J. Truran, James W. Abundance ratios as a function of metallicity. *ARA&A*, 27:279–349, [Jan. 1989](#).
- M. Wiescher, F. Käppeler, and K. Langanke. Critical Reactions in Contemporary Nuclear Astrophysics. *ARA&A*, 50:165–210, [Sept. 2012](#).

- B. Willman, M. R. Blanton, A. A. West, J. J. Dalcanton, D. W. Hogg, D. P. Schneider, N. Wherry, B. Yanny, and J. Brinkmann. A New Milky Way Companion: Unusual Globular Cluster or Extreme Dwarf Satellite? *AJ*, 129(6):2692–2700, [June 2005a](#).
- B. Willman, J. J. Dalcanton, D. Martinez-Delgado, A. A. West, M. R. Blanton, D. W. Hogg, J. C. Barentine, H. J. Brewington, M. Harvanek, S. J. Kleinman, et al. A New Milky Way Dwarf Galaxy in Ursa Major. *ApJL*, 626(2):L85–L88, [June 2005b](#).
- C. Winteler, R. Käppeli, A. Perego, A. Arcones, N. Vasset, N. Nishimura, M. Liebendörfer, and F.-K. Thielemann. Magnetorotationally Driven Supernovae as the Origin of Early Galaxy r-process Elements? *ApJL*, 750:L22, [May 2012](#).
- C. Wolf, C. A. Onken, L. C. Luvaal, B. P. Schmidt, M. S. Bessell, S.-W. Chang, G. S. Da Costa, D. Mackey, T. Martin-Jones, S. J. Murphy, et al. SkyMapper Southern Survey: First Data Release (DR1). *PASA*, 35:e010, [Feb. 2018](#).
- W. H. Wollaston. Xii. a method of examining refractive and dispersive powers, by prismatic reflection. *Philosophical Transactions of the Royal Society of London*, (92):365–380, 1802.
- S. E. Woosley, J. R. Wilson, G. J. Mathews, R. D. Hoffman, and B. S. Meyer. The r-process and neutrino-heated supernova ejecta. *ApJ*, 433:229–246, [Sept. 1994](#).
- J. Yoon, T. C. Beers, S. Dietz, Y. S. Lee, V. M. Placco, G. Da Costa, S. Keller, C. I. Owen, and M. Sharma. Galactic Archeology with the AEGIS Survey: The Evolution of Carbon and Iron in the Galactic Halo. *ApJ*, 861(2):146, [July 2018](#).
- Z. Yuan, G. C. Myeong, T. C. Beers, N. W. Evans, Y. S. Lee, P. Banerjee, D. Gudin, K. Hattori, H. Li, T. Matsuno, et al. Dynamical Relics of the Ancient Galactic Halo. *ApJ*, 891(1):39, [Mar. 2020](#).
- V. I. Zagrebaev, A. V. Karpov, I. N. Mishustin, and W. Greiner. Production of heavy and superheavy neutron-rich nuclei in neutron capture processes. *PhRvC*, 84(4):044617, [Oct. 2011](#).
- H. Zhang, J. Dong, N. Ma, G. Royer, J. Li, and H. Zhang. An improved nuclear mass formula with a unified prescription for the shell and pairing corrections. *NuPhA*, 929:38–53, [Sept. 2014](#).
- Y. Zhu, R. T. Wollaeger, N. Vassh, R. Surman, T. M. Sprouse, M. R. Mumpower, P. Möller, G. C. McLaughlin, O. Korobkin, T. Kawano, et al. Californium-254 and Kilonova Light Curves. *ApJL*, 863(2):L23, [Aug. 2018](#).
- E. Zinner. Stellar Nucleosynthesis and the Isotopic Composition of Presolar Grains from Primitive Meteorites. *Annual Review of Earth and Planetary Sciences*, 26: 147–188, [Jan. 1998](#).

T. Zwitter, J. Kos, A. Chiavassa, S. Buder, G. Traven, K. Čotar, J. Lin, M. Asplund, J. Bland-Hawthorn, A. R. Casey, et al. The GALAH survey: accurate radial velocities and library of observed stellar template spectra. *MNRAS*, 481(1):645–654, Nov. 2018.

*This document was prepared & typeset with pdfL^AT_EX, and formatted with
NDDiss2_ε classfile (v3.2017.2[2017/05/09])*